Crack Closure and Enhanced Autogenous Healing of Structural Concrete Using Shape Memory Polymers

Doctor of Philosophy (PhD) Thesis

Oliver Robert Teall

School of Engineering, Cardiff University

2016

Summary

Self-healing concrete has the potential to significantly reduce the life cycle cost of concrete structures. The ability for concrete to undergo autogenous self-healing is largely dependent upon the width of the cracks in the material. Shape memory polymers (SMP) can be used to close cracks in concrete and produce a compressive stress across crack faces, enhancing the load recovery associated with this healing process.

Previous proof of concept studies used commercially available SMP strips to close cracks within small scale mortar beams. Within this thesis, specifically manufactured high shrinkage polymer samples are refined and tested. An SMP tendon system is developed which is capable of activation via electrical heating. This system is incorporated into structural concrete beam samples with and without steel reinforcement. Crack closure is successfully achieved and the system's performance assessed with suggestions for future development. Enhanced autogenous healing of structural concrete using SMP strips is confirmed by comparing the mechanical load recovery of samples cured for one, three and six months.

The SMP tendons are applied at full-scale, alongside three other self-healing techniques investigated as part of the Materials 4 Life project, to assess their performance in the field. A life cycle cost assessment of self-healing concrete is undertaken using a bridge deck slab as a case study, concluding that a self-healing concrete capable of repeated healing cycles has the potential to significantly reduce costs over a 120-year design life.

DECLARATION

This work has not been submitted in substance for any other degree or award at this or any other university or place of learning, nor is being submitted concurrently in candidature for any degree or other award.

Signed …… Date …….

STATEMENT 1

This thesis is being submitted in partial fulfilment of the requirements for the degree of Doctor of Philosophy (PhD)

Signed …… Date …….

STATEMENT 2

This thesis is the result of my own independent work/investigation, except where otherwise stated, and the thesis has not been edited by a third party beyond what is permitted by Cardiff University's Policy on the Use of Third Party Editors by Research Degree Students. Other sources are acknowledged by explicit references. The views expressed are my own.

Signed …… Date …….

STATEMENT 3

I hereby give consent for my thesis, if accepted, to be available online in the University's Open Access repository and for inter-library loan, and for the title and summary to be made available to outside organisations.

Signed …… Date …….

Acknowledgements

I would firstly like to express my gratitude to Professor Bob Lark and Dr Diane Gardner for their support and guidance throughout my PhD studies. Their willingness to help solve any and all challenges helps to smooth out the somewhat bumpy road to completing a PhD. Many thanks also to Professor Tony Jefferson, who's genuine enthusiasm and ability to solve complex problems was of great help. The research within this thesis forms part of the Materials 4 Life project, funded by the Engineering and Physical Science Research Council (EP/K026631/1), who I thank for their contribution.

I would like to thank both Andrea Green and Tim Embley for their ongoing encouragement and assistance, particularly in engaging with industry and making sure the research was promoted widely. Without their work, and the financial support of Costain Group Plc., I would not have been offered this opportunity and would not be where I am today.

Many thanks also to the Costain team on the A465, in particular Bruce Richards for having the foresight to support the research from the very beginning, and Toby Bedford who was always on the end of the phone whenever needed and was instrumental in getting the site trials up and running. I would also like to express my sincere thanks to Barry Woodman and Andy Bannister for supporting the Materials 4 Life project and making the Costain-Cardiff collaboration possible.

Thanks to all my friends and colleagues from Cardiff University for sharing the journey, with a special mention to Martins for his undying enthusiasm and positivity, as captured by his saying: 'tomorrow is another step towards failure'. Thanks also to Dr Rob Davies, who I look forward to working with in the future in his new capacity at the University. My PhD certainly wouldn't have been what it was without the help received from both of you.

Many thanks to the lab technicians, particularly Ian, Rich, Carl and Jack, who were always happy to help out with setting up the next experiment, regardless of whatever strange new request we had.

Finally, and for many reasons, I would like to thank my wife Adriana. For the countless times she sat through practice presentations, and had to listen to me explain my PhD topic around a dinner table. For the love and support she has shown throughout, and for giving me the encouragement I needed when the finish line seemed far away. Thank you for pushing me to be the best I can be. Juntos, lograremos nuestros sueños.

Publications

The author is named on the following journal papers and conference proceedings, and presented at two of the conferences as first author:

1. Teall, O.R.; Pilegis, M.; Sweeney, J.; Gough, T.; Thompson, G.; Jefferson, A.; Lark, R.; Gardner, D. Development of High Shrinkage Polyethylene Terephthalate (PET) Shape Memory Polymer Tendons for Concrete Crack Closure. Journal of Smart Materials and Structures Vol. 26, 4, 2017

2. Teall, O. R.; Pilegis, M.; Jefferson, A. D.; Lark, R. J.; Gardner, D. R. 2015. Shape Memory Polymer (SMP) Prestressing System to Enhance the Autogenous Healing of Structural Concrete. Fifth International Conference on Self-Healing Materials, 2015, Durham NC, USA.

3. Teall, O. R.; Davies, R. E.; Pilegis, M.; Kanellopoulos, A.; Sharma, T.; Paine, K.; Jefferson, A.; Lark, R.; Gardner, D.; Al-Tabbaa, A. 2016. Self-Healing Concrete Full-Scale Site Trials. 11th fib International PhD Symposium in Civil Engineering, 29-31st August 2016, University of Tokyo, Japan.

4. Pilegis, M.; Teall, O. R.; Hazelwood, T.; Jefferson, A. D.; Gardner, D. R.; Lark, R. J. 2015. Delayed concrete pre-stressing with shape memory polymer tendons. fib Symposium 2015, Copenhagen, Denmark.

Contents

List of Figures

List of Tables

Chapter 1. Introduction

1.1. WHY WE USE CONCRETE

Concrete, a mix of cement, water, sand, coarse aggregates and admixtures, has been used in one form or another since the days of the Bedouins in southern Syria and northern Jordan in around 6500BC (Gromicko and Shepard, 2016). The Romans were well known for their concrete structures, such as the 2000-year old Pantheon in Rome topped by what remains the world's largest unreinforced concrete dome (Mitchell Crow, 2008). Today, concrete is the most abundantly used construction material in the world. An estimated 11 billion metric tonnes of concrete are produced globally on an annual basis (Imbabi et al., 2012).

Concrete generally has good compressive strength, durability, thermal insulation and fire resistance properties (Imbabi et al., 2012). As well as these properties, one of the reasons for its enduring success is its versatility, in terms of both the constituent materials and the wide range of potential applications. Mix designs can be adjusted to provide vastly different final properties, such as compressive strengths ranging from 2MPa to 200MPa (FIB, 2012). Concrete has been used in almost every type of structure imaginable, from the tallest structure in the world (Burj Khalifa in Dubai) (PJSC, 2016) to the longest and deepest railway tunnel ever built (Gotthard Base tunnel in Switzerland) (Grey, 2016).

A second reason for the popularity of concrete is its low cost. One cubic metre of concrete in the UK typically costs between £65-85 (Quotes, 2016). Cement is produced relatively cheaply worldwide, and aggregates can often be sourced locally, allowing concrete to remain a low-cost material almost regardless of where the construction is taking place.

1.2. CONCRETE DURABILITY AND THE PRINCIPLE OF SELF-HEALING

Unreinforced concrete structures can last thousands of years, as demonstrated by ancient Roman structures such as the Coliseum. Its low tensile strength, however, has led to the incorporation of reinforcing steel into modern concrete.

Reinforced concrete structures, used since the early 1850's in the UK and France (Shaeffer, 1992), enable the material to be used in a much wider variety of applications, such as cantilever sections and long-span bridges where high tensile loads are present. However, unprotected steel will corrode over time in aggressive environments. Corrosive materials such as chlorides and sulphates penetrating the surface of the concrete and causing reinforcement corrosion is the cause of well over 90% of concrete durability problems (Mitchell Crow, 2008). The repair of reinforced concrete structures can come with high associated costs. In the UK, £50.3Bn was spent on repair and maintenance in 2015, making up 35% of the total value of UK construction output (ONS, 2015).

Cracking in reinforced concrete structures is a common phenomenon, with a variety of causes as indicated in Figure 1.1. It is generally accepted that the presence of cracks has a negative impact on the durability of concrete by providing paths for corrosive materials to the embedded steel (Van Breugel, 2007, Van den Heede et al., 2014).

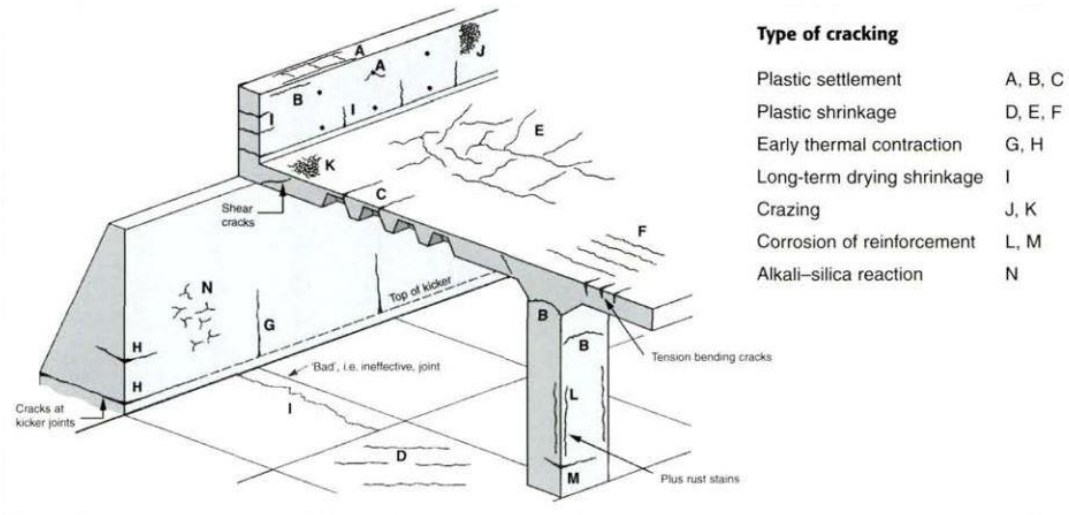

Figure 1.1: Illustration of the various types of non-structural cracking (Society, 2010).

The limitation of crack widths in concrete structures is specified within BS EN 1992-1-1:2004 for both durability and aesthetic purposes (BSI, 2014). This is achieved by imposing a minimum level of steel reinforcement while limiting the maximum spacing and maximum bar diameter used. Alternatively, pre-stressing techniques may be used to ensure that no section of the concrete is in tension.

The principle of self-healing materials is one of damage management, as presented by Van der Zwaag (2007) in his book *Self Healing Materials*. This strategy incorporates techniques to give the material an in-built capacity to self-heal. In this way, cracks are no longer a durability issue as they can be healed over time, theoretically leading to the indefinite service life of structures.

1.3. ENHANCING SELF-HEALING WITH SHAPE MEMORY POLYMERS

Concrete is capable of natural or 'autogenous' healing in certain conditions, discussed in detail in Section 2.2. There are also several potential approaches to introducing 'autonomic' healing techniques into cementitious materials, discussed in Section 2.6. In all cases, the width of the crack is a fundamental factor which affects the self-healing process (De Rooij et al., 2013).

Shape memory polymers (SMP) have been proposed as a method to enhance self-healing by producing a compressive stress across cracks in concrete (Jefferson et al., 2010, Dunn et al., 2011, Isaacs et al., 2013). This is based on the premise of reducing crack widths and the evidence, provided initially by Heide and Schlangen (2007), that a compressive stress applied across the crack faces enhances the load recovery observed in healed concrete samples. To date, experiments have been carried out at small scale using mortar beams specimens, confined to the laboratory. The next step was to scale the technique up, using materials capable of higher shrinkage forces to develop a system capable of deployment in full scale structures.

1.4. AIMS AND OBJECTIVES OF THE RESEARCH

The aims of the research were to further develop the shape memory polymer crack closure system proposed by Jefferson et al. (2010) for structural concrete and test this both within a laboratory environment and at full scale. The specific research objectives are detailed below:

1. Refine and develop a high shrinkage shape memory polymer material to enable it to be used in concrete.
2. Refine and develop an SMP system to close cracks and enhance autogenous self-healing in structural concrete elements.
3. Test the SMP system and its ability to enhance autonomous self-healing at full scale.
4. Complete a life cycle cost comparison of self-healing concrete in a real-world application.

1.5. OUTLINE OF THE THESIS

This thesis reports the experimental work undertaken to develop and test a shape memory polymer crack closure system for structural concrete elements.

A review of the state of the art of self-healing is detailed in Chapter 2, focusing on autogenous and enhanced autogenous healing techniques. A review of the latest shape memory polymer research relevant to the proposed application is included, followed by a summary of autonomic self-healing systems and previous applications of self-healing technology at full scale.

The results of tests on a number of specially manufactured shape memory Polyethylene Terephthalate (PET) samples are presented in Chapter 3 and compared against the commercially available PET strip samples used in previous experiments. Tests on the restrained shrinkage stress, free shrinkage, tensile strength, Young's modulus and alkalinity resistance of the most promising PET filament samples are discussed and the results analysed in terms of the material's proposed use within concrete.

In Chapter 4, a programme of work in which PET strip samples are introduced into concrete beam samples cracked in three-point bending to enhance autogenous healing over 1, 3 and 6 months is described. The development of SMP tendons using the PET filaments tested in Chapter 3, along with an electrical activation system and sleeve method to activate, protect and de-bond the filaments from the surrounding concrete is also presented. These tendons were then tested both outside the concrete (for restrained shrinkage stress) and within reinforced and unreinforced concrete beams to close induced cracks and the results of these tests are presented and discussed in the context of their use as a mechanism for closing cracks in RC structures.

The design, construction and testing of a full-scale site trial of the SMP system alongside autonomous self-healing systems (developed separately as part of the Materials for Life research project) is described in Chapter 5. The tendons were incorporated into a trial panel, constructed on a live construction project, which was loaded and monitored alongside four other panels. The performance of the system is assessed with reference to the laboratory testing in Chapter 4.

Chapter 6 introduces a life cycle cost assessment of a theoretical self-healing concrete in highways bridge decks. A preliminary study using historical cost data is described, followed by a case study analysis using a modified version of the Structures Asset Management Planning Toolkit (SAMPT) cost model. The results of the case study are presented along with a sensitivity analysis of the model.

Finally, the conclusions of the thesis and recommendations for future work are presented in Chapter 7, with reference to the aims and objectives of the research.

Chapter 2. State-of-the-Art Review

2.1. KEY DEFINITIONS

2.1.1. Self-healing, self-sealing & repair of cementitious materials

Self-healing in cementitious materials is a widely researched topic, but is also the subject of significant debate regarding its definition. Self-healing and self-tightening (which will be referred to as self-sealing within this thesis) have been identified by Heide and Schlangen (2007) as two mechanisms within the field of self-healing concrete. They define self-sealing as the process by which a crack is blocked via the transportation of material fluids flowing through it, and self-healing as a chemical reaction which connects the two crack surfaces.

The authors do not specify the recovery of material properties such as elastic modulus or flexural strength as a requirement for self-healing, stating that within self-healing research "the recovering (sic) of mechanical properties of the material is almost never investigated". Neville (2002) agrees, stating that "the strength of the healed concrete is rarely of interest and has not often been determined". This creates ambiguities within self-healing concrete research, in which a crack which has been sealed via chemical reaction could be termed as 'healed' despite no recovery in performance. While in recent years, several studies have used the recovery of mechanical performance as a measurement of self-healing (Isaacs et al., 2013, Yang et al., 2011, Li et al., 2013b), the majority of studies within the literature rely on a reduction in crack width or permeability (Edvardsen, 1999, Reinhardt and Jooss, 2003, Ahn and Kishi, 2010, Wiktor and Jonkers, 2011, Van Tittelboom et al., 2011, De Rooij et al., 2013, Sahmaran et al., 2013, Wang et al., 2014, Palin et al., 2015).

A second definition of self-healing is proposed by De Rooij et al. (2013) as "any process by the material itself involving the recovery and hence improvement of performance after an earlier action that has reduced the performance of the material". This then distinguishes healing

(recovery of performance) from sealing (blocking of cracks) by requiring some improvement of performance to have taken place. Using this definition, a crack which has been sealed and has resulted in a decrease in the permeability of the concrete could be said to have self-healed, so long as decreased permeability is accepted as an improvement of performance.

It therefore depends on the performance specifications under investigation as to whether a recovery of concrete properties can be considered as self-healing. If, for example, the permeability of concrete has been increased due to cracking which in turn leads to a higher risk of reinforcement corrosion, a subsequent decrease of permeability could be classed as self-healing as this leads to an improvement of the material's performance. Similarly, a recovery of mechanical properties such as flexural strength following structural cracking would also be categorised as self-healing. This performance-based definition of self-healing will be adopted throughout this thesis.

For self-healing to occur the healing process must be carried out by the material itself, either autogenically or engineered through the introduction of specific constituents, as discussed in section 2.1.2. Once the material is required to be replaced or added to, the process is no longer self-healing but should be defined as repair (De Rooij et al., 2013). Repair is defined as the restoration of performance through the addition of external materials and effort.

2.1.2. Self-healing: autogenous & autonomic

Following detailed discussions within the RILEM Technical Committee 221-SHC (De Rooij et al., 2013) to define the categories of self-healing within concrete, self-healing processes were grouped into autogenous and autonomic.

Autogenous or 'self-generated' healing involves material components which could also otherwise be present when not specifically designed for self-healing. Autogenic healing mechanisms in concrete include the continued hydration of cement within the material and the

precipitation of calcium carbonate ($CaCO_3$) on the crack faces. Autonomic (defined as 'involuntary or unconscious') healing involves specific materials included for the purpose of self-healing which would *not* otherwise be present. Autonomic techniques typically make use of adhesive repair agents embedded in the cementitious matrix; be these within protective microcapsules or provided through a pre-formed vascular flow network (Isaacs et al., 2012, De Rooij et al., 2013).

Within this thesis, shape memory polymers are used as a crack closure mechanism to improve the autogenous self-healing of concrete. This approach will be categorised as enhanced autogenous healing. The definition of autonomic self-healing as proposed by the RILEM technical committee will be used to refer to the healing techniques used within the on-site trial application of self-healing concrete, discussed in more detail in section 2.6.

2.1.3. Smart & intelligent materials

Bogue (2014) identified that, despite wide coverage within technical literature, smart and intelligent materials still do not have a single agreed definition. According to De Rooij et al. (2013), smart materials respond and change in reaction to the environment in which they are situated and include examples such as piezoelectric materials, temperature-responsive polymers and shape memory materials. They go on to define intelligent materials as those which incorporate information as well as their fundamental material properties to enable them to respond to external stimuli in a regulated manner; including materials such as living tissue and bone. The difference between smart and intelligent materials in this context is then defined by the material's ability to gather, combine and process information before reacting accordingly.

However, Bogue (2014) suggested defining smart materials based on the actual response; i.e. smart materials are those which provide a means for a composite material or structure to achieve 'smart behaviour', such as self-healing or shape changing capabilities.

Shape memory polymers, investigated within this thesis, can be categorised as smart materials based on both of these interpretations: the polymers are able to respond to external temperature changes with a change in basic shape, and are used as a mechanism to introduce smart behaviour (enhanced autogenous self-healing) into concrete elements.

2.1.4. Smart structures

Smart structures, as opposed to smart materials, are engineered composites of basic materials which exhibit some sensing and actuation properties due to the properties of their individual components (De Rooij et al., 2013). Self-healing concrete can therefore be classed as a smart structure, but one which is made up of a number of basic and smart materials. In previous work by Isaacs (2011) and Joseph (2008), self-healing cementitious materials have also been defined in this category.

To be classed as an intelligent rather than a smart structure, self-healing concrete must be able to regulate the degree of self-healing or to monitor the application or effectiveness of self-healing processes (De Rooij et al., 2013). While this is a long-term aim of self-healing concrete development, within this thesis a 'smart' rather than 'intelligent' response is investigated.

2.1.5. Shape-memory polymers: material and key terminology

Shape memory materials (SMM) can retain a memory of their 'permanent', or lowest energy, shape when subjected to stress under which they are deformed into a new, 'temporary' shape. This changing of shape from permanent to temporary is referred to as 'programming' the material (Lendlein and Kelch, 2002).

Shape memory polymers (SMP), discussed in more detail in section 2.4, are a type of SMM which exhibit shape memory properties derived from their material structure, morphology, manufacturing process and programming regime. A drawing process is typically used to achieve

the temporary shape. Upon an appropriate external stimulus, these materials will then return to their permanent shape. Specifically, the SMP considered within this thesis are activated via heat, and are therefore defined as thermoresponsive (Lendlein and Kelch, 2002).

Key parameters relating to SMP properties include the draw ratio, draw rate, degree of crystallinity and orientation, and these are defined below:

Draw ratio: The ratio of cross-sectional area of the polymer before and after the drawing process. e.g. a draw ratio of 4 indicates a 4-fold reduction in area when the polymer was drawn.

Draw rate: The rate at which the polymer is drawn in units of length over time.

Degree of crystallinity: The percentage of the polymer structure made up of ordered, crystalline regions. The degree of crystallinity affects the optical, mechanical, thermal and chemical properties of the polymer (Carraher, 2005).

Orientation: The degree to which the polymer chains are preferentially ordered in one direction (anisotropic) (Carraher, 2005).

2.2. AUTOGENOUS SELF-HEALING IN CEMENTITIOUS MATERIALS

2.2.1. Introduction

While there have been numerous studies on the autogenous self-healing of cementitious materials, the method of measurement of healing has not been consistent. Several studies have measured the physical reduction in crack width to quantify self-healing (Wiktor and Jonkers, 2011, Van Tittelboom et al., 2012, Palin et al., 2015). Others have measured the recovery of permeability (Edvardsen, 1999, Reinhardt and Jooss, 2003) or the recovery of stiffness and load capacity (Yang et al., 2009, Isaacs et al., 2013, Heide and Schlangen, 2007). In addition, the majority of experiments have been carried out on mortar beams (Wiktor and Jonkers, 2011, Van

Tittelboom et al., 2012, Palin et al., 2015, De Rooij et al., 2013), while some have used concrete containing coarse aggregates (Heide and Schlangen, 2007) or fibres (Yang et al., 2009).

The lack of a standard method to test and quantify self-healing has led to contradictory conclusions regarding the principal mechanisms for self-healing and the conditions under which it can take place. This section references a number of key studies, highlighting agreed conclusions and areas of disagreement.

2.2.2. Principal mechanisms

It is generally agreed that the main two processes which contribute to self-healing in cementitious materials are the precipitation of calcium carbonate ($CaCO_3$) on crack faces, and the continued hydration and swelling of cement within the material. As well as these two major contributors, it has been suggested that physical clogging through the transportation of material by water travelling through the crack also aid crack closure. These different causes are represented as a reduction in crack width for a through-crack in Figure 2.1 (Isaacs, 2011, De Rooij et al., 2013).

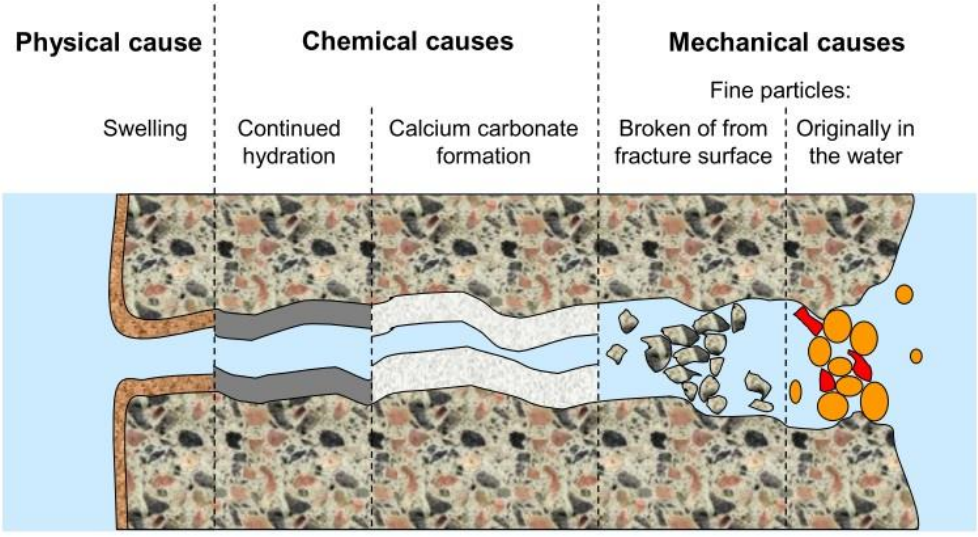

Figure 2.1: Different causes leading to autogenic self-healing (De Rooij et al., 2013).

The precipitation of $CaCO_3$ on the crack faces is due to a reaction between the calcium ions Ca^{2+} derived from the calcium hydroxide ($Ca(OH)_2$) within the concrete, and the carbonates CO_3^{2-} within water (Edvardsen, 1999, De Rooij et al., 2013). Edvardsen (1999) argues that this mechanism is by far the most important contributor to self-healing within concrete cracks, demonstrating by experimentation that this reaction is dependent upon temperature, pH and concentration of the reactants.

However, according to Van Tittelboom and De Belie (2013), the most effective autogenous self-healing mechanism depends on the concrete age at the time of cracking. Ongoing hydration is dominant in young concrete due to the abundant availability of unhydrated cement, with $CaCO_3$ precipitation becoming more important with increasing age.

The dominant mechanism for self-healing also depends upon the size of the crack being healed. According to De Rooij et al. (2013), ongoing hydration cannot be responsible for a complete self-closing of a crack, and its effect becomes minor with crack widths above 0.1mm.

Evidence that the physical clogging of flow paths via the movement of fragments suspended in liquid cannot be the dominant factor in the self-healing of cementitious materials is presented by Hearn (1998). The author explains how during experiments in which water was replaced by propan-2-ol as a permeant, self-healing was completely absent. As the liquid's viscosity is close to that of water, this demonstrates that the transport of external materials into the crack has little influence on the concrete's ability to heal.

From the literature it is apparent that self-healing via continued hydration of cement is only dominant in cementitious materials when: 1) there is a significant quantity of available unhydrated cement, probably due to a high initial cement content such as within the mortar beam specimens tested by Van Tittelboom et al. (2012); 2) where crack widths are limited to below 0.1mm, and 3) in cracking at an early age. In all other cases, the precipitation of $CaCO_3$ seems to be the most influential mechanism for autogenous self-healing (Wiktor and Jonkers, 2011, Palin et al., 2015, Edvardsen, 1999, Yang et al., 2009).

2.2.3. Conditions for autogenous healing

All studies agree that the two most important factors for autogenous self-healing are the presence of water and the size of the crack. The age of the concrete at first cracking and the concrete mix proportions also have an effect (Isaacs et al., 2013, De Rooij et al., 2013, Heide and Schlangen, 2007, Mihashi and Nishiwaki, 2012, Jefferson et al., 2010).

Presence of water

All of the principal mechanisms discussed in section 2.2.2 require the presence of water for autogenous self-healing to take place. In previous studies this has been supplied through submersion of samples (continuous or via wet/dry cycles) (Wiktor and Jonkers, 2011, Van Tittelboom et al., 2012, Palin et al., 2015, Yang et al., 2011) or the flow of water in a through-crack (Edvardsen, 1999, Reinhardt and Jooss, 2003).

Without water, no self-healing is observed. A high relative humidity (RH) has been found to be insufficient to induce autogenous healing, even at up to 95% RH with curing time of 3 months. (De Rooij et al., 2013, Isaacs et al., 2013, Heide and Schlangen, 2007).

Age at first cracking

Heide and Schlangen (2007) investigated the effect of the age of the concrete at cracking and the subsequent healing due to ongoing hydration when cured in water. They found a clear decrease in strength recovery with increased age of cracking, with little healing attributed to ongoing hydration for samples cracked 72 hours after casting. This agrees with the conclusions made by Neville (2002) that ongoing hydration is the primary cause of autogenous healing only in “very young concrete, in which the fracture is jagged so that it exposes some hydrated parts of cement”. However, the definition of ‘very young’ in this context is not given. In general, the

younger the concrete, the more unhydrated cement it contains and therefore the higher the regain of strength through healing (Neville, 2012).

Experiments by Yang et al. (2011) found that, contrary to expectations, autogenous self-healing of engineered cementitious composites (ECC) samples damaged after 6 months was superior to the healing observed for samples damaged after just 3 days. Their samples had high cement and fly ash content (578kg/m³ Portland cement and 694kg/m³ Fly ash), low water cement ratio (0.25) and 2% volume Poly(vinyl alcohol) (PVA) fibres. Healing was measured as recovery of stiffness using resonant frequency equipment before and after wetting and drying cycles over 24 hours. It was concluded that, while all samples were damaged via uniaxial tensile loading to the same strain, in the younger samples this resulted in fewer, but larger, cracks. These ranged from 24-35 microns depending on the damage level (strain) used. In more mature ECC samples, cracked at 90 days, the average crack width was lower, at between 13-18 microns. Results from this paper are shown in Figure 2.2.

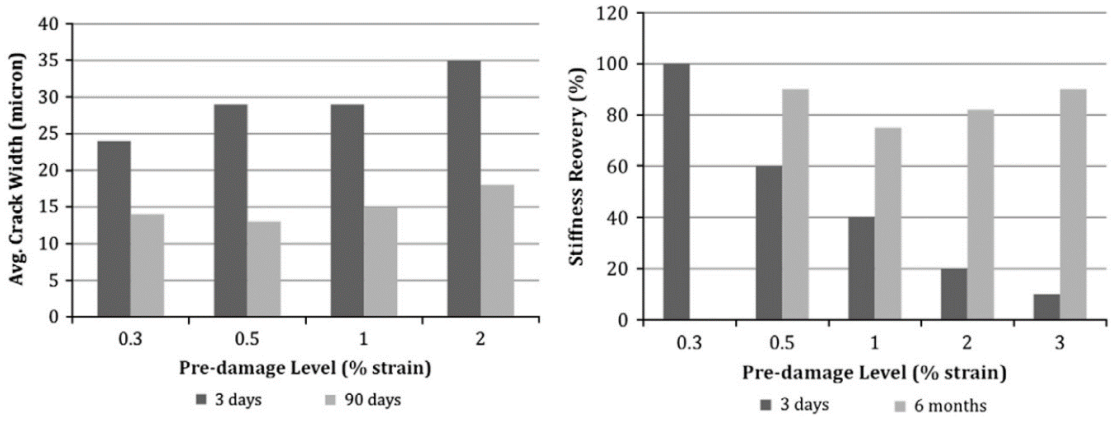

Figure 2.2: (a) average crack width against pre-damage level for ECC samples cracked at 3 and 90 days, (b) stiffness recovery of against pre-damage level for ECC samples cracked at 3 days and 6 months (Yang et al., 2011).

This suggests that the crack width is a more important factor than the age of the samples for autogenous self-healing. The results may also have been influenced by the delayed pozzolanic reaction of the fly ash, which would have continued beyond the 3 days at which the sample was damaged. The influence of cement type is discussed further in the following section.

Cement type

Sahmaran et al. (2013) observed improved self-healing in ECC samples containing Ground Granulated Blastfurnace Slag (GGBS) compared to those containing Portland cement (PC) alone. The authors identified the main mechanism of healing as calcite precipitation, with cracks up to 0.1mm healed in GGBS as opposed to 0.05mm for PC specimens.

This agrees with Palin et al. (2015), who found that a cement mortar mix containing 66-80% GGBS by mass of cement could heal cracks up to 0.41mm when submerged in fresh water, compared to the 0.17mm cracks healed in a PC mix. The authors attribute the added $CaCO_3$ precipitation to a steady leaching of ions due to the fine pore structure of the mortar sample containing GGBS.

Van Tittelboom et al. (2012) also found that the use of GGBS and Pulverised Fly Ash (PFA) improved the autogenous healing efficiency of mortar beam samples as measured by a reduction in water permeability. Of the two, GGBS cement resulted in the largest improvement over PC. However, the authors attributed the healing to continued hydration, concluding that in the case in which the precipitation of $CaCO_3$ is the principal mechanism of healing, PC mortar beams produce better results than those containing GGBS, contradictory to the results of Sahmaran et al. (2013) and Palin et al. (2015) (Van Tittelboom et al., 2012).

According to Neville (2012), as GGBS consumes $Ca(OH)_2$ during hydration, there is no pore-blocking formation of $CaCO_3$ when high proportions are used within the cement mix. This supports the conclusions of Van Tittelboom et al. (2012) but does not account for the results observed by Palin et al. (2015) and Sahmaran et al. (2013).

The addition of GGBS therefore appears to result in improved self-healing within cementitious materials, although the principal healing mechanism is unclear. The addition of PFA results in some improved healing where ongoing hydration is the main mechanism.

Self-healing is less apparent in concrete containing silica fume (SF) than in concrete without SF (De Rooij et al., 2013). The most probable cause of this is that the addition of SF results in a higher proportion of calcium silicate hydrates (C-S-H), and a reduced quantity of $Ca(OH)_2$, formed within the concrete (Construction, 1985). This $Ca(OH)_2$ provides the calcium ions required for the precipitation of $CaCO_3$ on the crack faces. The addition of SF also contributes to an improved distribution of cement particles in the mix, improving hydration and reducing the availability of unhydrated cement for self-healing. This could have an impact on the self-healing properties of high-strength concretes.

However, experiments by Granger et al. (2007) on high performance cementitious beams containing SF show a significant recovery of flexural strength when cured in water for between 1-20 weeks after cracking. The beams tested used a water-cement ratio of 0.2, intentionally leaving a large quantity of unhydrated cement within the matrix. It can therefore be concluded that while SF decreases the potential for autogenous self-healing within cementitious materials, with a sufficient quantity of unhydrated cement this self-healing is still possible.

Crack size

A comparison of the maximum crack width at which autogenic healing occurs, from a number of sources within the literature, is presented in Figure 2.3. A summary of each of the experiments detailed in these sources is shown in Table 2.1.

From the references compared, it is generally agreed that 100% autogenic self-healing can only occur with crack widths below 0.25mm. However, it should be noted that as the studies in some cases measured self-healing as a reduction in crack widths and in others as a reduction in permeability or resonance frequency, the definition of '100% healing' will be different in each case. For example, Edvardsen (1999) defined 'complete healing' as when the flow of water through the sample had stopped entirely, while Yang et al. (2011) defined it as a recovery of

resonance frequency of the sample to values associated with undamaged 'virgin' specimens. There is no indication that these two measurements are equivalent.

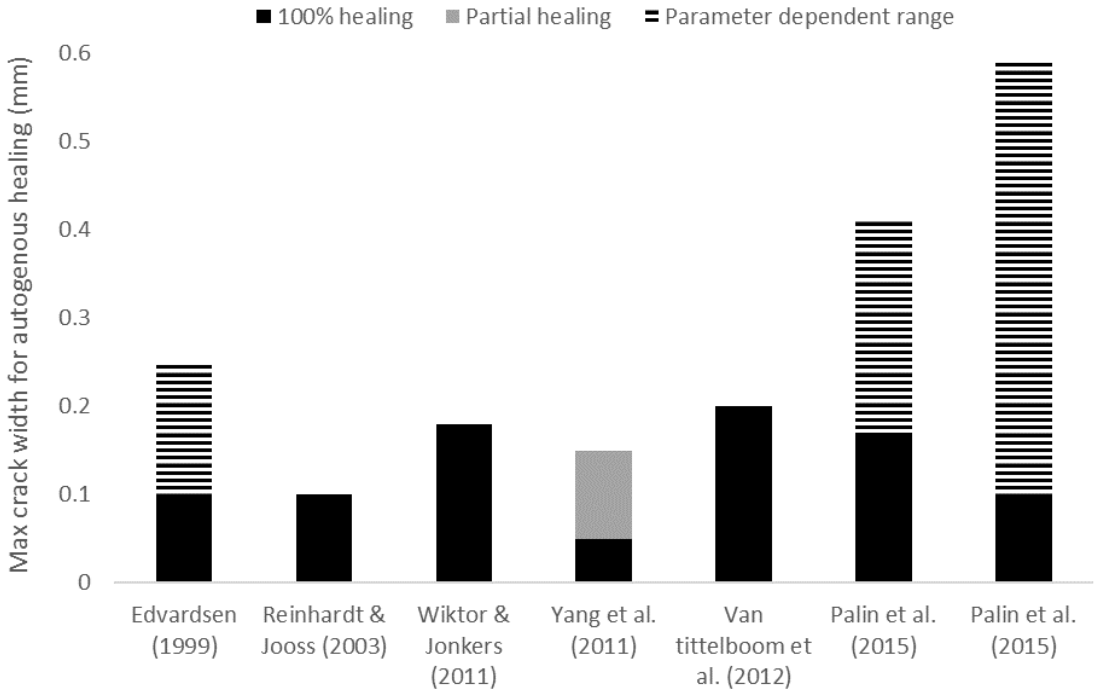

Figure 2.3: Comparison of references on the maximum crack width for autogenic healing.

A notable exception to the maximum crack width of 0.25mm is the result of tests carried out by Palin et al. (2015), in which specimens submerged in fresh water and sea water were seen to heal cracks of up to 0.41 mm and 0.59 mm respectively. The best healing results in fresh water were from samples containing high quantities of GGBS cement (494 kg/m^3 CEM III/B) (reference 6 in Table 2.1). Conversely, in reference 7, the largest crack widths were healed in specimens containing PC. However, this was accompanied by drastic drops in compressive strength due to the dissolution of calcium hydroxide and formation of magnesium silicate hydrate within the sample.

Reference 4 (Yang et al., 2011) reports smaller maximum crack widths for autogenous healing than other sources, despite testing early age (3 day) samples in comparison with the 24 day samples tested by the majority of the sources included. Significantly, these results are based upon the percentage recovery of stiffness as measured through resonance frequency tests, as

opposed to a reduction in crack widths. Heide and Schlangen (2007) found that for self-healing via ongoing hydration to result in strength recovery, a compressive stress was required to ensure the crack faces are in either in contact with each other, or the distance between the faces is small enough to allow healing to occur. Crack widths as small as 0.05mm resulted in very little self-healing, as measured by strength recovery, through ongoing hydration.

Table 2.1: Summary of compared autogenous healing experiments from the literature.

Ref.	Source	Max crack width	Material	Healing definition	Main mechanism	Age at cracking	Curing regime	Additional factors
1	Edvardsen (1999)	0.1-0.25mm	Small concrete beams, various cements	Reduction in permeability	$CaCO_3$ precipitation	unspecified	5-20 weeks fresh water flow through crack	Range depending on crack movement and hydraulic gradient
2	Reinhardt and Jooss (2003)	0.1mm	High Performance Concrete with CEM II/A-L	Reduction in permeability	Unclear	28 days	350 hours fresh water flow through crack	
3	Wiktor and Jonkers (2011)	0.18mm	CEM I Mortar beams	Crack width reduction	$CaCO_3$ precipitation	56 days	100 days submersion in fresh water	
4	Yang et al. (2011)	0.05mm for 100%, 0.15mm partial	ECC with CEM I & PVA fibres	Resonance frequency & permeability recovery	$CaCO_3$ precipitation	3 days	wet-dry cycles (water & air), 24hrs per cycle, 10 cycles	
5	Van Tittelboom et al. (2012)	0.2mm	CEM I Mortar beams	Crack width reduction	$CaCO_3$ precipitation & ongoing hydration	28 days	42 days submersion in fresh water	
6	Palin et al. (2015)	0.17mm - 0.41mm	CEM I Mortar beams & CEM III/B Mortar beams	Crack width reduction	$CaCO_3$ precipitation	28 days	56 days submersion in fresh water	Range dependent on cement type
7	Palin et al. (2015)	0.1mm - 0.59mm	CEM I Mortar beams & CEM III/B Mortar beams	Crack width reduction	$CaCO_3$ and brucite-aragonite precipitation	28 days	56 days submersion in sea water	Range dependent on cement type. Significant reduction in compressive strength after submersion

It appears therefore that while crack widths up to 0.25mm may be sealed autogenously, self-healing as measured by strength or stiffness recovery requires much smaller crack widths of less than 0.05mm.

Aggregates

Angular coarse aggregates, which offer a larger surface area, are more effective than smooth coarse aggregates for self-healing purposes (De Rooij et al., 2013). This may be due to an increase in void content within the concrete when using angular aggregate, which could contain unhydrated cement. As smooth aggregates may be used to improve concrete consistency compared to angular aggregates when using the same quantity of cement paste, or to reduce the quantity of cement paste required, this should be taken into account when considering the use of self-healing concretes within industry.

Summary

A significant limitation to autogenous healing is the crack width range over which full healing can take place, particularly if the recovery of mechanical strength and stiffness is used as a measurement of self-healing. The requirement for water within the crack faces also limits where autogenous healing may occur.

The use of GGBS and PFA within concrete has been found to improve the self-healing response, particularly in early-age cracking, due to their slower hydration properties and the improved fine pore structure of the concrete.

The vast majority of studies into autogenous healing of cementitious materials have been undertaken on mortar beam specimens, containing no coarse aggregates (Van Tittelboom et al., 2012, De Rooij et al., 2013, Wiktor and Jonkers, 2011, Palin et al., 2015). This may have a significant effect on the resulting self-healing, as there is a much larger surface area of exposed cementitious matrix in mortar beams due to the absence of large aggregate particles.

Areas in which further study are needed include the recovery of the mechanical properties of self-healed samples and the use of structural concrete mixes containing coarse aggregates. Both of these areas are addressed within this thesis.

2.3. ENHANCED AUTOGENOUS SELF-HEALING IN CEMENTITIOUS MATERIALS

As autogenous healing is primarily a result of ongoing hydration, the precipitation of $CaCO_3$ or a combination of these two processes, any method which improves the performance of these processes will enhance the autogenous self-healing capability of a cementitious material. This includes the supply of additional pozzolanic or latent hydraulic materials into the cementitious matrix and the reduction or restriction of crack widths (Van Tittelboom and De Belie, 2013).

2.3.1. Crack control using fibres

Methods to restrict crack widths within concrete commonly include the introduction of steel or polymer fibres. Steel cord fibres have been found to corrode within concrete cracks, making them less effective as a crack control mechanism for self-healing purposes (Homma et al., 2009).

Engineered cementitious composite (ECC) materials contain polymer fibres, typically 2% by volume, which help to reduce the appearance of single cracks and distribute any micro-cracks throughout the material, resulting in a smaller average crack width compared to concrete reinforced with conventional steel bars. ECC can be designed to reduce average crack widths to as low as 0.03mm (Yang et al., 2009, De Rooij et al., 2013)

Victor Li and colleagues from 1998 onwards (Li et al., 1998, Van Tittelboom and De Belie, 2013) developed ECC first using polyethylene (PE) and later poly vinyl alcohol (PVA) fibres. They found that, as well as restricting crack widths, the fibres also aided autogenous healing by providing a surface on which healing products are deposited when bridging a crack. These healing products both block the cracks and result in a recovery of stiffness as measured by resonance frequency tests (Yang et al., 2009, Yang et al., 2011, De Rooij et al., 2013)

The healing products for ECC samples were identified by Kan et al. (2010) as a combination of C-S-H and $CaCO_3$, with C-S-H dominant for crack widths below 0.015mm. As the formation of additional C-S-H through ongoing hydration is associated with strength regain in self-healing

cementitious materials (Heide and Schlangen, 2007), this is probably the cause of the regain in stiffness within ECC samples.

A typical ECC mix contains 570kg/m³ PC and 684kg/m³ PFA (De Rooij et al., 2013), high proportions compared to conventional reinforced concrete. While contributing to self-healing by ongoing hydration, this results in a higher level of embodied CO_2 and increased material cost compared to more conventional mixes. Given the UK government's aim, set out in 'Construction 2025' (Government, 2013), to achieve a 50% reduction in greenhouse gas emissions and 33% lower initial construction costs in the built environment by 2025, a solution which produces the same benefits as ECC while reducing the cement content would be desirable.

2.3.2. Effect of compressive stress on crack healing

The application of a compressive stress on the crack faces has been shown to improve strength recovery with autogenous healing (Neville, 2012). Heide and Schlangen (2007) investigated the autogenous self-healing of submerged concrete samples subjected to an applied compressive stress following three-point bending to induce cracks. They found that with a compressive stress of 1N/mm^2 on the crack face, the stiffness and strength of the concrete specimen was recovered, while without this stress the strength recovery was minor, as shown in Figure 2.4. While it appears from Figure 2.4 that a compressive stress of 2N/mm^2 produced a higher strength recovery than 1N/mm^2, the authors concluded that compressive stresses above 1N/mm^2 brought no further benefit to the self-healing system, perhaps due to the uncertainty in the results.

However, within this purely laboratory-based study, the compressive force was generated using a spring loading device. While useful as proof of concept, there is no suggestion by the authors of a system to replicate this compression within a practical case. Previous investigations using shape memory polymers to produce a compressive stress across crack faces in discussed in the following section.

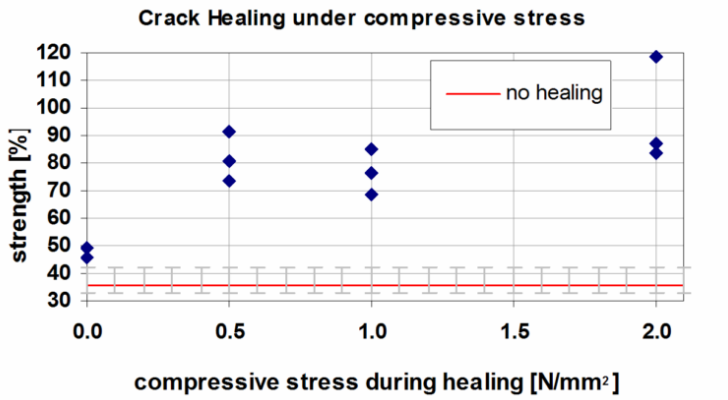

Figure 2.4: Relative strength after autogenous crack healing with applied compressive stress (Heide and Schlangen, 2007).

In addition, the beams used within the study were small in size (40x40x160mm) and made from a concrete mix containing river gravel aggregates no larger than 8mm in diameter (Heide and Schlangen, 2007). Further tests on different structural mixes would be beneficial to determine whether a similar effect is observed. The healing period used within the study was two weeks from initial cracking (time of initial cracking was varied from between 18 to 72 hours) and the main mechanism for healing was identified as ongoing hydration; later initial cracking and longer healing periods may yield different results as ongoing hydration will become less of a factor with precipitation of $CaCO_3$ increasingly influential (De Rooij et al., 2013).

2.3.3. Crack closure using shape memory polymers

Shape memory polymers have been proposed as a method to enhance autogenous healing within concrete through the closure of cracks and the production of a compressive stress across the crack faces (Jefferson et al., 2010). Shape memory polymers are discussed at length in section 2.4.

Proof of concept experiments carried out by Jefferson et al. (2010) and Isaacs et al. (2013) used drawn Polyethylene Terephthalate (PET) tape to close cracks in prismatic hollow mortar beam specimens, making use of the shrinkage stress generated by the material's retraction upon heating.

Preliminary screening tests were undertaken by Jefferson et al. (2010) to determine the most effective polymer to use within the system. These tests were based on a set of essential criteria for the material properties based on their proposed use, including a minimum restrained shrinkage stress of 20MPa and an activation temperature between 60-100°C (Dunn et al., 2011). Tests were carried out on six different semi-crystalline polymers, the details of which can be seen in Table 2.2 below. The specimens, each 280mm in length, were heated from ambient temperature (25°C) at a rate of 1°C per minute until failure. This resulted in PET Shrink tite being chosen as the most viable option, having generated a shrinkage stress of over 31.5MPa, while none of the other specimens tested reached above 15MPa.

Table 2.2: Polymer screening samples (Jefferson et al., 2010).

Name	Polymer	Description	Form	Area[1] (mm^2)	Supplier
PP Pure	PP	Oriented PP tape coextruded with PP-PE copolymer	Tape	0.126	Lankhorst
PP Armordon	PP	Oriented PP tape coextruded with PP-PE copolymer	Tape	0.224	Don & Low
PP Lotrak	PP	Oriented PP tape	Tape	0.10	Don & Low
PE Certran	PE	Melt spun PE continuous filament yarn	Yarn	0.061	University of Leeds
PP Multiprof	PP	Oriented PP tape coextruded with heat sealing layer, fibrillate	Fibrillated Tape	0.24	Lankhorst
PET Shrink tite	PET	Oriented PET tape	Tape	0.10	Aerovac

[1]Area = original cross-sectional area of specimen

PET Shrink tite was then subjected to additional testing to investigate the restrained stresses developed when heating to 90°C. This temperature was chosen as it was just below the temperature at which damage to cementitious materials is expected. PET samples of width 6mm, thickness 3.45mm and length 450mm were formed from 75 layered strips, which were then bonded at each end by applying heat locally to melt the polymer strips together. These were then loaded into a specially prepared jig and heated using an environmental chamber. The average peak stress from three tests on the PET specimens was 33.5MPa, with a coefficient of variation of 2.05% (Jefferson et al., 2010).

Further testing on the PET tape was then carried out by Dunn et al. (2011). The purpose of these tests was to study the shrinkage behaviour of the PET material and the effects of the geometry, temperature and soak time (time at constant temperature for each incremental increase) on its mechanical properties. The conclusions of these tests were that the glass transition temperature (at which shrinkage begins) of the material, as shown by changes in young's modulus, is approximately 70 °C and that the highest peak stress is generated by heating the material above this temperature to 90°C for 15 minutes, before allowing the PET to cool.

PET shrink tite samples were placed within prismatic hollow mortar beam samples, 25x25x150mm in dimension with a 10x10mm void running through the centre, to investigate their potential as a crack closure system. Mortar beams containing water:cement:sand contents of 306kg/m^3:510kg/m^3:1530kg/m^3 (or 0.6:1:3 by weight) were cast with a central void, into which tendons of cross-sectional area 20.7mm^2 were placed and externally anchored. The tendons made up 3.9% of the cross-sectional area of the un-notched mortar beam. The sample set-up can be seen in Figure 2.5. A three-stage test was carried out, consisting of 3-point loading to form a 0.3mm width crack, dry heating in an oven at 90°C to activate the PET specimens and a second round of 3-point loading to failure. Conclusions from these tests were that activation of the tendons closed the cracks and applied a pre-stress of between 1.5 – 2MPa on the mortar beam specimens (Jefferson et al., 2010).

Tests by Isaacs et al. (2013) followed on from this work by repeating the mortar beam experiments using varied heating and curing regimes to investigate the possibility of enhanced autogenous healing. These tests used identical hollow mortar beam & PET tendon specimens and followed the same 3-stage testing regime. One specimen was dry heated followed by curing in water at 20°C, a second heated and cured via steam, and a third activated in water (heated to 90°C) and allowed to cool to ambient temperature in the same environment for curing. The heating activation methods and healing regimes used are described in more detail in Table 2.3 below.

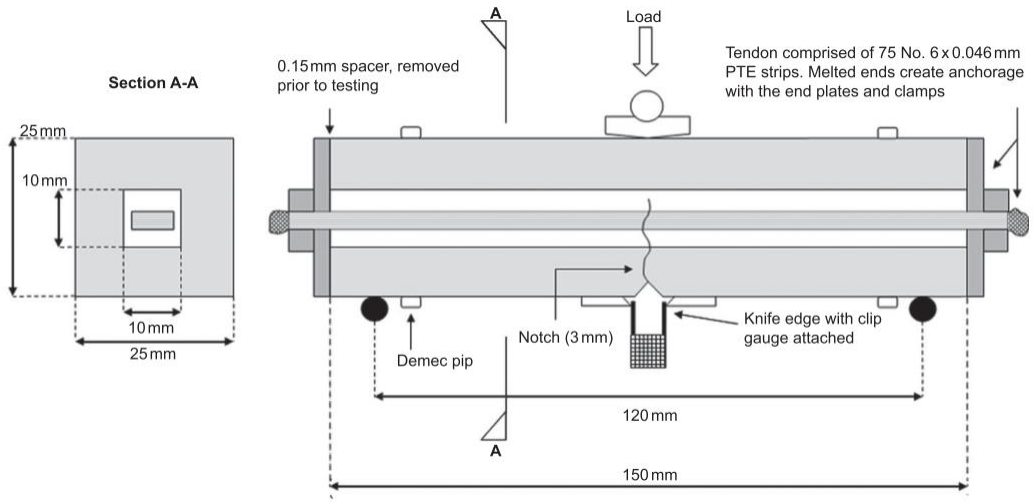

Figure 2.5:Hollow mortar beam specimens used in tests by Jefferson et al. (2010) and Isaacs et al. (2013) (Isaacs et al., 2013).

Table 2.3: Heating activation methods and healing regimes (Isaacs et al., 2013).

AH regime	Heat activation method stage 2a Description	Temp (°C)	Time (h)	Healing regime stage 2b Description	Time (h)
1	Dry heat activation	90	18	Cured in water at ambient temperature (approx. 20°C)	48
2	Steam heat activation	90[1]	18	Specimens left in steam chamber with steam production turned off and chamber allowed to return to ambient conditions	48
3	Water heat activation	90	18	Specimens left in water tank with temperature allowed to return to ambient conditions	48

[1]The atmospheric temperature was measured at 90°C and the water in the tank was heated to 100°C in order to produce steam conditions.

The paper concludes, as did Jefferson et al. (2010), that the PET tendons can close cracks in prismatic mortar beam specimens and impart a pre-stress upon them. It also concludes that of the three regimes tested, regimes 1 and 2 (dry heat activation and water curing, and steam heat activation and curing) demonstrate effective autogenous healing, with 80% strength recovery of the specimens when the PET were removed following curing and prior to testing to failure (Isaacs et al., 2013).

However, these experiments are at a small scale within a laboratory setting, and make use of mortar beams rather than structural concrete. Further investigation should therefore incorporate structural mix designs as well as reinforced concrete using larger samples to assess the feasibility of the system within construction. As suggested by Isaacs (2011), larger specimens

may require polymers which generate larger shrinkage stresses for lower concrete volume replacement. It is therefore important to continue investigating different polymer forms and materials for use within the system.

A suitable activation technique for the polymers is also required. Jefferson et al. (2010) suggest that the use of ovens to activate the PET shrinktite is regarded as a temporary solution by stating that "It is envisaged that in later versions of the system, activation will be achieved via an electrical supply". The importance of this element is reiterated by Mihashi and Nishiwaki (2012) in their review of the experiments, by pointing out that to heat an entire structure for polymer activation would require too much energy, suggesting that without a direct activation method the system is unfeasible. While oven activation may be feasible for small, pre-cast elements, an alternative activation method is required for larger elements or those cast in-situ.

There is the potential to increase the restrained shrinkage stress of the polymer, and thereby reduce the area of concrete replaced. This is discussed in more detail in section 2.4.3. The layered strips are also not very practical to install. A rigid section which could be placed easily into concrete or tied onto reinforcing bars would be preferable.

Isaacs (2011) notes that these experiments form the 'preliminary' and 'product' levels in the development of a self-healing concrete system using shape memory polymers. Here he is making reference to the four common milestones to product commercialisation as described by Ghosh (2009) in relation to self-healing materials; idea generation (preliminary), laboratory implementation (product), pilot line up scaling (process) and industrial applications (marketing).

Following these milestones, the work described within this thesis focusses on the process level of this system's development. Experimental work includes the testing of various shape memory PET samples to determine their restrained shrinkage stress, and the incorporation of a polymer system into unreinforced and reinforced structural concrete beams to close cracks and enhance autogenous healing. An electrical activation system is also developed and the system tested at a structural scale.

2.4. SHAPE MEMORY POLYMERS

2.4.1. Introduction to shape memory polymers

SMPs are materials which respond to external stimuli by altering their physical shapes. The most common stimulus used to provoke this change is direct heat, leading to a temperature change of the polymer. This form of SMP is known as thermoresponsive, and the ability for the material to undergo this shape change is referred to as the shape memory effect (SME) (Xie, 2011).

The SME is not unique to polymers; in fact, shape memory alloys (SMAs) are currently the most commonly used SMM. However, the first widely recognised recording of a SME within polymers was in 1941 in a United States Patent by Vernon, who claimed a material made from methacrylic acid ester resin had ‘‘elastic memory’’ and could resume its original shape upon heating (Xie, 2011); which according to Liu et al. (2007) is earlier than the first record of a SMA, in 1951. Contradictory evidence is presented by Huang et al. (2010), who state that the SME was observed in a Gold-Cadmium (AuCd) alloy as early as 1932, but concede that this property was not widely recognised for its potential within SMAs until 1971 when significant recoverable strain was observed in a Nickel-Titanium (NiTi) alloy.

What is clear is that SMAs, while being utilised within several industries, in particular within medical and aerospace applications, have significant limitations when compared to SMPs. These include a lower percentage of recoverable strain (typically less than 8% for SMAs compared to over 800% for SMPs), higher stiffness and less flexible transition temperatures. Tailoring material properties is also easier with SMPs, and the cycle of programming and recovery can be much faster. SMAs are generally much more expensive than SMPs and can contain metals with significant toxicity (Liu et al., 2007, Sun et al., 2011, Behl and Lendlein, 2007, Zhao et al., 2015).

To date, the main applications for SMPs are within heat shrink tubing for electrical wires and in a growing capacity within the biomedical and aerospace industries (Xie, 2011, Liu et al., 2014, Xu and Song, 2011). SMP applications are discussed in more detail in section 2.4.5.

2.4.2. Shape memory effect

The SME observed in alloys and in polymers differs entirely. SMAs rely on the reversible thermal transition between martensitic and austenitic crystalline phases. In polymers the process is primarily entropic; it is not an intrinsic property of the polymers themselves but rather depends upon a combination of polymer morphology and specific programming (Xie, 2011, Sun et al., 2011, Behl and Lendlein, 2007).

The most common form of SME in polymers is referred to by Xie (2011) as the 'dual shape memory effect', in which the polymer exhibits one 'permanent' and one 'temporary' macroscopic shape. This is known as one-way memory and is demonstrated by Figure 2.6. It is possible for some polymers to perform reversible or 'two-way' shape memory, differing from one-way memory in that an external mechanical manipulation phase is not required to achieve the temporary shape. Triple-shape memory polymers also exist, in which two temporary shapes can be created within one shape memory cycle. A detailed discussion around the material cause of these shape memory effects is, however, outside the scope of this thesis which will focus on the more common one-way memory.

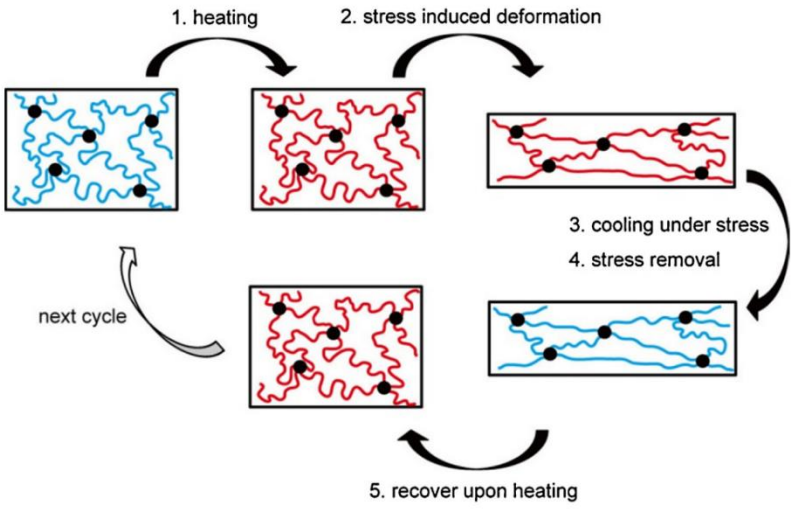

Figure 2.6: The molecular mechanism of the dual-SME. Black dots: cross-links; blue lines: molecular chains of low mobility below T_g; red lines: molecular chains of high mobility above T_g (Zhao et al., 2015).

The SME within polymers derives from the entropic state of the material's molecular chains. Upon manufacture via injection moulding (or similar processes), the permanent shape of the

polymer is formed, in which its molecular chains adopt conformations with the highest entropy (highest degree of disorder). When heated above a certain material dependent transition temperature, often referred to as the glass transition temperature and denoted as T_{trans} or T_g, and placed under an external deformation load, the polymer chains are changed to a lower entropy state as the polymer is strained. This is possible above T_g as at this point the polymer network exhibits entropic elastic behaviour. These two states, above and below T_g within amorphous and semi-crystalline polymers are often known as the glassy and rubber-like states respectively. The external load introduces molecular chain orientation into the polymer. Upon cooling in the strained state, the polymer's temporary shape is retained due to the freezing of the molecular chain segments. When reheated above T_g, molecular mobility is regained and, if unrestrained, the molecular chains will return to their highest entropy state and the polymer will therefore return to its permanent shape (Xie, 2011, Behl and Lendlein, 2007, Ward and Sweeney, 2013, Sweeney et al., 2014).

The majority of polymers have the capacity to exhibit the SME described above. The mechanism behind the SME is the dual domain system, in which an 'elastic' segment is always hard while a second 'transition' segment can be stiff or ductile depending on the appropriate stimulus. Therefore, to be able to demonstrate the effect, two main requirements must be adhered to: firstly, the polymer must be able to undergo a reversible thermal transition for temporary shape fixing and recovery. As polymers are in general intrinsically viscoelastic with at least one such thermal phase transition, most if not all polymers meet this first requirement (Xie, 2011, Huang et al., 2010, Sun et al., 2011).

The second requirement is for the polymer to exhibit a cross-linking network which functions as the elastic segment and sets the permanent shape, acting as the polymer's 'memory' in the SME process. The cross-links in the polymer chains are referred to interchangeably as netpoints, and can be physical (intermolecular interactions) or chemical (covalent bonds). Without these cross-links, upon heating above the transition temperature and exerting a deformation force on the

polymer the material would undergo long-range chain slippage; thus changing macroscopic shape with little or no change in polymer chain conformation. This results in unrecoverable strains as the entropic change which drives macroscopic shape recovery is absent. This chain slippage can be stopped almost completely by cross-linking, the linkage points acting as anchors in the polymer chain network (Xie, 2011, Lendlein and Kelch, 2002, Behl and Lendlein, 2007).

According to (Xie, 2011), SMPs can generally be defined as one of four categories: Chemically cross-linked glassy polymers; chemically cross-linked semi-crystalline polymers; physically cross-linked glassy polymers and physically cross-linked semi-crystalline polymers.

Chemical cross-links can be achieved through additives to the polymer network. The resulting polymer is then a thermosetting polymer as the cross-linking agent is normally activated via heating and upon further heating the polymer will not soften or flow. Physical cross-linking can occur when very long molecules in linear polymers become entangled, or when chain-branching occurs where a secondary chain initiates from a point on the main chain (Ward and Sweeney, 2013).

Glassy, or amorphous, polymers are those which form a disordered structure when cooled from the melt. Examples include polymethyl methacrylate, polystyrene and rapidly cooled (melt-quenched) polyethylene terephthalate. Semi-crystalline polymers are those which display both amorphous and crystalline regions. This may occur in drawn polymers, including polyethylene terephthalate in which small regions of crystallites form within an oriented amorphous structure (Ward and Sweeney, 2013, Dunn, 2010).

2.4.3. Restrained shrinkage stress

If the SMP, having been programmed into a temporary shape, is then heated above T_g while restrained, the recovery stress of the SMP can be utilised. Considering an SMP which has been programmed in tension, which will therefore shrink upon activation, this stress can be referred

to as the restrained shrinkage stress. The majority of experimental investigations into SMPs focuses on shape recovery rather than the magnitude of shrinkage stress (Souri et al., 2015). Our fundamental understanding of the restrained shrinkage stress generated by SMPs is therefore currently at an early stage, despite several experimental explorations of the phenomena (Xie, 2011, Volk et al., 2011, Koerner et al., 2004, Miaudet et al., 2007).

Sun et al. (2011) performed a number of experiments, using mainly polymethyl methacrylate, to maximise the restrained shrinkage stress generated by the SME in polymers. They found that a key parameter which determined the final stress achieved was the temperature at which the SMP had been programmed.

A schematic of the relationship between the programming temperature and the maximum recovery stress (so named as the stress considered is compressive, not tensile) as presented by Sun et al. (2011) is shown in Figure 2.7. T_a to T_d refer to increasing programming temperatures; T_a is at the start of the polymer's glass transition range (polymer in a 'glassy' state), T_d is at the end of the range (polymer in a 'rubbery' state). T_b and T_c are intermediate values between these temperatures.

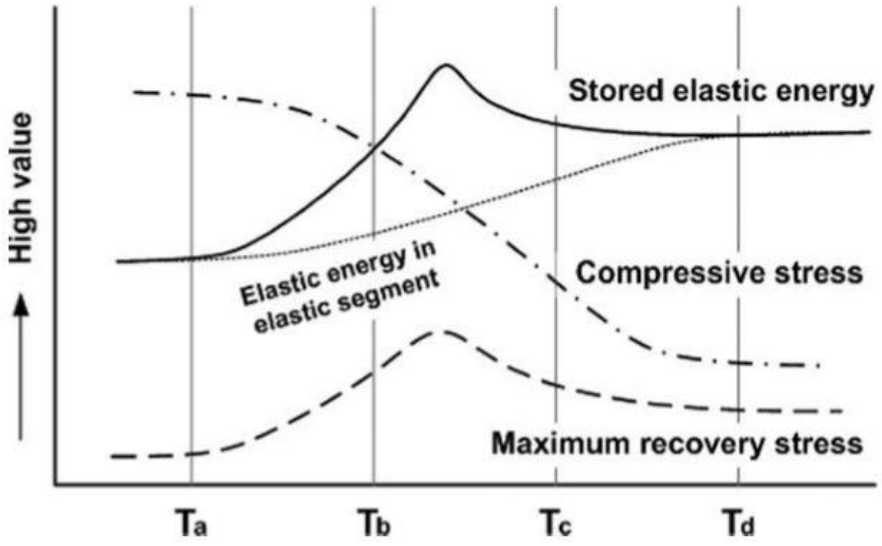

Figure 2.7: Schematic comparison of the maximum recovery stress in samples programmed at different temperatures (Sun et al., 2011).Compressive stress refers to the stress required to deform the polymer to a given strain (i.e. proportional to the young's modulus).

The maximum recovery stress is proportional to the total stored elastic energy, which is made up of contributions from both the elastic and transitional segments. The energy in the elastic segment increases with programming temperature as the recoverable strain in the polymer increases (caused by a reduction in the instant recovery strain during programing, explained in detail in Sun et al. (2011)), while the energy in the transitional segment decreases with increasing temperature due to the drop in young's modulus of the polymer across the glass transition range. This energy is represented in Figure 2.7 by the compressive stress required to programme the polymer (Sun et al., 2011)

The authors concluded that by selecting the right programming temperature within the glass transition range, a much higher maximum shrinkage stress than is usually observed can be achieved. They also noted that the maximum value for this stress upon reheating generally occurs at or near the programming temperature initially used. This phenomenon they refer to as the temperature memory effect (TME) (Sun et al., 2011).

This conclusion concurs with observations by Xie (2011), who found that the same material deformed to the same strain but at different programming temperatures could show a variation in final restrained shrinkage stress by a factor of 4-5.

Bonner et al. (2010) found that keeping a constant programming temperature while increasing the programming strain, rate of strain or draw ratio also results in higher restrained shrinkage stress, as this increases the elastic energy stored by the polymer. The authors suggest that the ratio between the restrained shrinkage stress and the total stress stored within the polymer, which for an elastic solid should be 1, depends upon the viscoelastic behaviour of the SMP being investigated. Within their experiments on spun samples of an amorphous lactide based copolymer with 35% weight of calcium carbonate, they found this ratio to be between 0.7 and 0.8, and that this ratio did not change with varying drawing temperature, strain rate or draw ratio.

The stored energy in the transitional segment of SMPs is limited by the relatively low elastic modulus of the material in the rubbery state (above T_g). The restrained shrinkage stress exhibited by unmodified SMPs generally ranges from a few tenths of a megapascal to a few tens of megapascals, depending on the material and programming regime used (Meng and Hu, 2009, Xu and Song, 2011, Xie, 2011).

Efforts to improve the rubbery state elastic modulus have included increasing the cross-linking density and the incorporation of fillers into the polymer matrix. Common fillers include carbon nanotubes (CNTs) and carbon nanofibres (CNFs), as well as glass or Kevlar fibres, carbon powders and silicon carbide (SiC) particles (Xu and Song, 2011, Meng and Hu, 2009). These fillers may also allow the use of alternative activation techniques for the polymer, as discussed in section 2.4.4.

Experiments carried out by Miaudet et al. (2007) on polyvinyl alcohol (PVA) with large fractions (around 20% weight) of CNTs achieved restrained shrinkage stresses as high as 130MPa. This is almost comparable to the typical stresses achieved by SMAs (200-800 MPa for NiTi alloys). Koerner et al. (2004) carried out experiments on shape memory polyurethane with 1-5% weight of CNFs, resulting in increases in restrained shrinkage stress by up to 50% compared to the unmodified polymer.

However, the addition of CNTs reduces the shape recovery ratio of the PVA (Miaudet et al., 2007, Xie, 2011). It should also be noted that, in general, inconsistent results have been seen with nano-scale fillers, possibly due to the complexity involved in the preparation of composite materials. Final properties depend on processing techniques, filler dispersion, orientation and size, interfacial adhesion, aspect ratio and matrix nature (Meng and Hu, 2009, Loos, 2011). While the use of composite shape memory materials can result in higher restrained shrinkage stresses, the current cost of CNTs (anywhere between $0.5-2000 USD/g (Loos, 2016)) may be prohibitive for their use within a concrete crack closure system.

2.4.4. Activation methods

Although the most common form of activation for a SMP is direct heat, the polymers can be triggered by various forms of external stimuli including light (UV and infrared) and chemical change (moisture, solvent and pH) (Xie, 2011, Huang et al., 2010). Thermoresponsive polymers themselves can be activated by methods other than direct heat. One example is by illumination with infrared light. This concept has been demonstrated previously in a laser-activated polyurethane medical device (Behl and Lendlein, 2007).

Forming SMP composites allows indirect heating by a variety of mechanisms, including joule heating (through the inclusion of conductive elements), induction heating through energy dissipation via hysteresis upon applying an alternating magnetic / electric field or heating through radiation (Huang et al., 2010, Mather et al., 2009, Xu and Song, 2011). The heat transfer properties of the SMP can be enhanced through the incorporation of conductive fillers such as conductive ceramics, carbon black and CNTs. Alternative activation methods can include a change in pH as well as contact with specific ions or enzymes (Behl and Lendlein, 2007, Meng and Hu, 2009).

Lu et al. (2014) investigated the potential for the shape recovery of a polyurethane-based SMP resin through joule heating, by creating a nanocomposite consisting of four layers of CNF nanopaper and resin. The nanopaper itself conducted the electricity, with the multi-layering approach improving the bond between the two materials to allow heat transfer. This resulted in successful shape recovery using a 30 V electricity supply. This, however, would be an expensive approach and would almost certainly alter the mechanical properties of the polymer, which were not investigated within the paper.

Remote activation of SMP composites via a magnetic field was investigated by Yakacki et al. (2009), using methacrylate-based thermoset SMP networks which were synthesised with varying amounts of Fe_3O_4 magnetite nanoparticles. They successfully heated the specimens through exposure to an alternating magnetic field for 5 minutes, inducing shape recovery.

Remote activation is an attractive option for the use of SMPs within concrete, however the incorporation of the magnetite reduced the crosslinking density and rubbery modulus of the polymer which would reduce the maximum restrained shrinkage stress of the material. The polymer also exhibited more brittle behaviour with increasing nanoparticle additions which would be undesirable within the tensile zone of concrete (Yakacki et al., 2009, Meng and Hu, 2009).

One method of altering the activation behaviour of SMPs is the shifting of their transformational temperature via molecular interaction with a surrounding solvent. Yu et al. (2011) investigated the effect of water absorption of polyurethane SMPs on their glass transition temperatures, concluding that reductions from a T_g of 67°C to 5°C can be achieved after exposure to 100% relative humidity for 96 hours. However, this exposure also reduced failure stresses by 500% and decreased shape recovery and recovery stresses of the material (Yu et al., 2011, Mather et al., 2009). For the proposed application within concrete this would not, therefore, be a feasible option.

The literature discussed above will inform the development of a shape memory polymer activation system within this thesis.

2.4.5. Applications

One of the earliest commercial applications for SMPs was in heat shrink tubing, most notably within electronics. The tubing is placed over exposed wiring and heated, causing lateral shrinkage and creating an insulative layer around the wire (CableOrganiser.com, 2014).

Over the last decade, potential biomedical applications have contributed to a large increase in SMP interest, examples of which include active medical devices such as a laser-activated device for the mechanical removal of blood clots (Xie, 2011, Behl and Lendlein, 2007). However, uses for SMPs have also been found in a wide range of other areas, such as smart textiles, high

performance water vapour permeability materials, heat shrinkable electronics packaging, sensors and actuators, self-deployable structures in spacecraft and micro-systems (solution, emulsion, film, foam and bulk) (Meng and Hu, 2009).

Many of these applications, especially those within the aerospace industry, have involved the development of shape memory polymer composites (SMPC) to change the SMP properties. Examples of SMPC applications within the aerospace industry include hinges, truss booms, reflector antennas, morphing structures, lunar habitats and mandrel fabrication. SMPCs seem likely to play increasingly important role in aerospace in the future (Liu et al., 2014).

Work undertaken by Jefferson et al. (2010), Dunn et al. (2011), Isaacs et al. (2013) and Hazelwood et al. (2015) have all focused on the application of shape memory polymers as a crack closure system within concrete beams. This utilises the uniaxial restrained shrinkage stress of the polymer to produce a compressive stress onto the concrete. These experiments and how they relate to the current thesis are discussed in more detail in section 2.3.3.

2.5. POLY(ETHYLENE) TEREPHTHALATE

2.5.1. Introduction

Polyethylene terephthalate (PET) is the most common thermoplastic polyester and is therefore often known simply as 'polyester'. It is a clear, strong and lightweight polymer commonly used for packaging food and beverages (PETRA, 2014). PET is used as the shape memory polymer within this thesis for concrete crack closure following on from previous studies, discussed in section 2.3.3.

First synthesised in North America in the mid-1940s, PET is formed from ethylene glycol (EG) (converted into bis-hydroxyethyl-terephthalate (BHET)), and either terephthalic acid (TA) or dimethyl terephthalate (DMT). Both methods remove the excess EG to form PET. The resulting PET strands are then extruded, cooled and cut into small pellets, known as PET resin. This resin

can then be heated into a molten liquid, which may be extruded or moulded into the desired shape (PETRA, 2014, Dunn, 2010).

The most abundant use of PET is in plastic bottles used as beverage containers. Research and development on its use in this application began in the late 1960's and intensified during the early 1970's when the technology for blow-stretch moulding of PET was developed. The PET industry in general, including bottle manufacturing as well as machine manufacturing and resin production, has seen huge expansion since the early 1980's. PET fibre, film and engineered product applications have also enjoyed steady growth. Today, the PET resin, machine and product manufacturing industries are a substantial part of world commerce. (PTI, 2011, PETRA, 2014).

A desirable property of PET, and one of the reasons for its widespread use as a replacement for alternative materials, is its recyclability. PET is completely recyclable through washing and re-melting, or by chemical breakdown into component materials to form new resin. It can also be crushed and mixed in small proportions (no more than 20% weight) with virgin PET resins. It is the most recycled plastic worldwide, commonly reformed into new bottles and jars, carpet, clothing, industrial strapping, rope, automotive parts, fibrefill and protective packaging (PETRA, 2014, Dunn, 2010).

2.5.2. Structure and properties

PET can exist in both amorphous and semi-crystalline states; a variety of microstructures can be developed in PET depending on the processing and preparation techniques used. Molten PET can be cooled into either the amorphous or semi-crystalline state due to its slow crystallisation kinetics. The degree of crystallinity of the end product therefore depends on the cooling rate of the polymer in the moulding or extrusion process (Gorlier et al., 2001). The crystallinity of PET can vary from as low as 30% to over 90% (Ward and Sweeney, 2013).

As well as occurring during polymer cooling, strain induced crystallisation will also arise during the tensile drawing of PET. The extent of this effect is dependent upon the draw ratio, rate and drawing temperature, discussed in section 2.5.3.

The degree of crystallinity and the size and distribution of crystallites within PET can significantly influence the thermal, mechanical, optical and permeation properties of the material (Chen et al., 1998, Dunn, 2010, Dusunceli and Colak, 2008). The crystal regions restrict the internal mobility of the material, causing brittle failure mechanisms over the more ductile behaviour associated with amorphous PET (Torres et al., 2000). This generally results in increasing yield stress and a decrease in strain hardening with increasing degree of crystallinity (Rastogi et al., 2004).

The amorphous phase of PET actually consists of two fractions, known as the Mobile Amorphous Fraction (MAF) and the Rigid Amorphous Fraction (RAF) (Rastogi et al., 2004, Chen et al., 1998).

The 3-phase model of PET with MAF, RAF and crystalline phases (as presented by Rastogi et al. (2004)) demonstrates the complex relationship between the microstructure and solid properties of PET, a detailed discussion of which is outside the scope of this thesis. However, an important factor to consider is the effect of PET crystallinity on the shape memory properties of the material.

As previously discussed, the shape memory effect in polymers relies upon the recovery of strains through the interaction between physical or chemical cross-links and the polymer chain segments. In PET, the SME is driven by the molecular mobility of the amorphous phase. Crystalline regions in the polymer matrix produce fixed points which prevent strain recovery. Crystallinity in shape memory polymers should therefore be reduced to achieve maximum strain recovery (Alves et al., 2002, Hoff and Pelzbauer, 1990, Schwartz and Saraf, 2003, Mody et al., 2001). Increasing the cooling rate, or producing thin cross-sections, would help to minimise crystallisation in shape memory PET.

Crystallinity also affects the glass transition temperature (T_g) of PET. In their study using differential scanning calorimetry (DSC), Alves et al. (2002) found the T_g of amorphous PET samples to be 71°C with a relatively narrow transition range. With increasing crystallinity, higher T_g values of up to 92°C were observed, with a broader transition range. This was attributed to the crystals causing a reduction in the mobility of polymer chain segments.

2.5.3. Drawing and orientation

The shape memory effect in PET can be programmed through the drawing process, which orientates the polymer chains and introduces recoverable strains. Orientation processes can significantly enhance the properties of polymers, including the mechanical, impact, optical and barrier properties, by altering the microstructure (Matthews et al., 1998). Variables including the draw ratio, rate and temperature affect the extent of orientation.

In amorphous polymers, drawing produces preferential alignment of the microstructure in the direction of drawing. In semi-crystalline PET, drawing produces both molecular orientation and small regions of three-dimensional crystallites (Ward and Sweeney, 2013).

Higher levels of orientation can be achieved through increasing the draw ratio and strain rate during drawing (Lu and Hay, 2001). However, increasing the draw ratio of PET also increases the strain-induced crystallisation observed in the drawn polymer, which acts to restrict shape recovery. Hoff and Pelzbauer (1990) observed that, at draw ratios above 5-10, a crystalline skeleton is formed within the polymer which then improves with increasing draw ratio. This agreed with later observations by Ajji et al. (1997), who investigated the crystallinity of PET following tensile drawing, roll drawing and die drawing processes. The authors found that for all the processes used, crystallinity was seen to increase with draw ratio.

Increases in strain rate have also been observed to increase the crystallinity of the resultant PET. Mody et al. (2001) carried out experiments on PET film, finding that higher strain rates minimise

the shape relaxation process by developing a more dimensionally stable crystalline phase through strain-induced crystallisation. The authors found that the relationship between the shrinkage, crystallinity, amorphous orientation and draw ratio (referred to as extension ratio) was non-linear, as shown by Figure 2.8. This relationship was attributed to the changing structure of PET with increasing extension ratio. At a ratio below 2, stretching results in orientation of the amorphous phase only, with resulting increase in shrinkage upon testing. As the extension is increased, strain-induced crystallisation begins, which prevents shrinkage in the amorphous phase. At higher extension ratios (above 3), shrinkage begins to increase again due to the influence of oriented tie-chains between strain-induced crystallites (Mody et al., 2001).

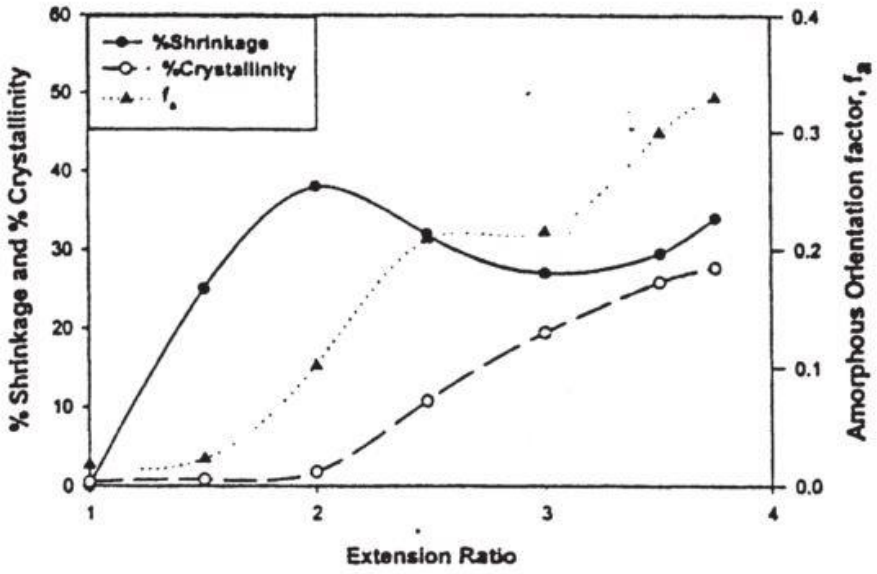

Figure 2.8: The relationships of shrinkage, crystallinity, and amorphous orientation factor to extension ratio (draw ratio) of PET stretched at 200%/sec at 100°C (Mody et al., 2001).

The relationship between the draw ratio, strain rate and crystallinity in PET also changes depending on the temperature at which the polymer has been drawn. Experiments by Rietsch et al. (1979) investigated the tensile drawing behaviour of PET when drawn between 20-80°C. They found that, when drawn below T_g (approximated as 66°C), the PET would neck to create a thinner section towards the midpoint of the sample, in which permanent deformations were localised. Above T_g, however, the sample would strain uniformly. Due to this effect, when

drawing below the glass transition temperature the draw ratio changes across the neck of the sample, producing complex results.

Above T_g, an increase in drawing temperature was shown to increase both the percentage volume of crystallinity and the size of the crystals in the resulting PET, in non-quenched samples (Vigny et al., 1999).

To maximise the shape memory effect, therefore, the drawing temperature should be minimised to reduce strain-induced crystallinity, while ensuring that the PET can still be drawn uniformly. A more complex relationship exists between the draw ratio, strain rate and orientation for which the appropriate values will depend on the proposed application. Previous experiments undertaken on shape memory PET for its inclusion in self-healing concrete are described in section 2.3.3.

2.5.4. PET in concrete

In addition to the PET crack closure system discussed in section 2.3.3, several studies have been completed into the use of waste PET within concrete as fine aggregates, fibres or formed into resins for use as a replacement binder material (Pacheco-Torgal et al., 2012, Choi et al., 2009, Azhdarpour et al., 2016).

The use of waste PET as a fine aggregate to replace river sand within concrete was studied by Choi et al. (2009), who found that increasing amount of PET resulted in proportional increases in workability, reduced density and a decrease in compressive strength of 6%, 16% and 30% with 25%, 50% and 75% replacement respectively. In a similar study, Azhdarpour et al. (2016) observed an improvement in compressive and tensile strength of concrete samples with up to 10% replacement of fine aggregate with PET, with increasing proportions resulting in a reversal of this trend.

Kim et al. (2008) found PET fibres reduced plastic shrinkage in mortar beam samples when a 0.25% volume fraction is introduced, with no further increase with additional volume of fibres up to 1%. In concrete samples, Borg et al. (2016) observed reductions in plastic shrinkage of up to 68.7% with a 1.5% volume fraction of fibres compared to a control mix. The authors also found that mixes containing PET fibres reached higher peak loads and had higher residual strengths when subjected to flexural 3-point bend tests. However, the fibre-reinforced samples demonstrated a reduction in compressive strength of between 0.5 to 8.5% (Borg et al., 2016).

PET fibres have also been found to degrade over time in concrete due to the alkaline environment. Pelisser et al. (2012) found that after 150 days, the PET fibres within concrete had degraded and become brittle, resulting in a loss in any improvement in mechanical properties observed at earlier ages. This degradation continued, leading to an increase in porosity of the fibre-reinforced samples compared to the control sample after 1 year. This agreed with an earlier study by Silva et al. (2005), who observed a gradual reduction in toughness of PET fibre-reinforced mortars due to alkaline hydrolysis, confirmed by fourier transform infrared spectroscopy (FT-IR) and scanning electron microscope (SEM) analysis of PET fibres immersed in alkaline solution for 150 days. This has important implications for a PET crack closure system; the polymer will need to be protected from the alkaline environment to ensure degradation does not occur.

Polymer concrete can be manufactured by using a polymer binder to replace cement and water. It was used as early as 1958 in the US to produce building cladding and was seen to have great potential as a repair material. This was due to its rapid curing, excellent bond to concrete and steel reinforcement and exceptional strength and durability. It also exhibits improved resistance to chlorine-based acidic solutions and sulphate attack. Due to these properties, polymer concrete is mostly used for repair and adhesion in practice (Fowler, 1999, Rebeiz, 1995, Saribiyik et al., 2013).

Resins for polymer concrete are commonly made from methacrylate, polyester, epoxy, vinylester or furan. While epoxy resins produce a concrete with better mechanical properties and improved durability compared to polyester resins, the latter are the most commonly used resin system due to their low cost and wide availability (Bedi et al., 2013). Rebeiz (1995) used recycled PET waste to produce a polyester resin for use within a polymer concrete containing fly ash, sand and gravel. The concrete demonstrated ultimate compressive strengths two to three times greater than Portland cement concrete, and achieved more than 80% of its final strength in one day.

However, the same study by Rebeiz (1995) found a reduction in compressive strength of the polymer concrete by approximately 45% when heated to 60°C. This is a drawback common to polymer use in concrete more generally, including the use of fibre-reinforced polymers, which can restrict polymer use to structures which are not required to be fire resistant (Fowler, 1999, Nigro et al., 2014).

In addition, the high cost of resin binders makes polymer concrete expensive in comparison with Portland cement materials (Rebeiz, 1995). The cost of polymers can range from 10 to 100 times that of Portland cement, resulting in a considerably higher cost per unit volume despite cement having a specific gravity around two and a half times that of polymer materials (Fowler, 1999). The inclusion of polymers into concrete would therefore need to be counteracted by its beneficial effect on concrete properties. This topic is considered in more detail in Chapter 6.

2.6. AUTONOMOUS SELF-HEALING IN CEMENTITIOUS MATERIALS

Autonomous self-healing systems involve the addition of new materials or elements into the concrete to induce a healing response. While the majority of the work within this thesis focuses on enhanced autogenous healing, autonomous self-healing techniques are incorporated into

the on-site trial application described in Chapter 5 and as such a review of their main characteristics is warranted here.

This section includes a review on the introduction of healing agents into concrete through microcapsules or vascular flow networks. A brief summary of other autonomous self-healing systems is included as section 2.6.2.

2.6.1. Delivery systems for healing agents

Healing solutions have been introduced into cementitious materials through continuous hollow brittle tubes/fibres or as discrete capsules. Healing agents used have included cyanoacrylate (Dry, 1994), two-part methyl-methacrylate (MMA) adhesive (Dry and McMillan, 1996), sodium silicate solution (Huang and Ye, 2011) and epoxy resins (Li et al., 2013a).

The use of encapsulated healing agents within concrete dates back to the early 1990's, when Dry (1994) used hollow brittle glass fibres filled with cyanoacrylate to heal cracks in mortar beam specimens. The use of glass tubes or fibres to deliver air-cured chemical adhesives into cracks in beams was also investigated by Thao et al. (2009), Joseph et al. (2007) and Van Tittelboom and De Belie (2009).

Joseph et al. (2007) and Van Tittelboom and De Belie (2009) observed that cyanoacrylate did not travel successfully from sealed glass tubes onto the crack face, either due to curing within the tubes or a negative air pressure acting against its flow. As an alternative solution, channels (open to atmospheric pressure) can be formed in the concrete to allow the external introduction of healing agents. Joseph et al. (2010) conducted a later series of experiments using glass capillary tubes extending outside the length of mortar beam samples. The set-up for these experiments is shown in Figure 2.9. Cyanoacrylate was introduced using syringes, resulting in successful healing of the samples following three-point bend tests.

However, glass tubes are fragile, which can result in accidental failures during assembly within concrete structures. In addition, Thao et al. (2009) found that with cyanoacrylate only partial crack healing had taken place due to the availability of air on the surface of the beams, but not further within the crack. To avoid this issue, two-part healing solutions can be used, requiring a second component to initiate the curing process.

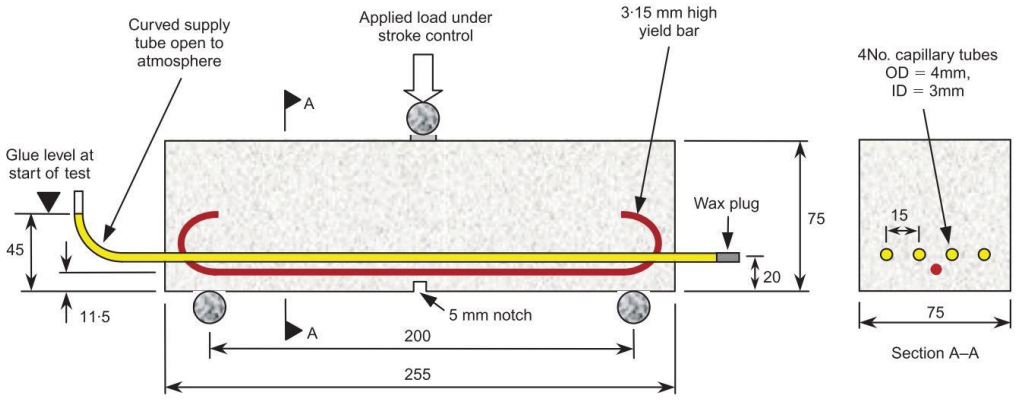

Figure 2.9: Delivery system using glass tubes open to atmospheric pressure (Joseph et al., 2010).

Dry and McMillan (1996) developed a two-part system using methylmethacrylate (MMA) adhesive delivered in three channels within a mortar beam specimen. The channels were formed using steel rods, removed 24 hrs after casting, and the channels then coated with waterproof sealant and plugged at either end. This was successful in releasing the healing agent into the crack, resulting in crack healing. This same system was tested at a much larger scale in full scale bridge decks, as discussed in section 2.7.

Huang and Ye (2011) investigated the delivery of sodium silicate solution as a healing agent into ECC beams in 5mm diameter capsules. The capsules were formed by storing the solution in sponge before sealing with wax. They found that the sodium silicate was successfully delivered into the crack, resulting in an improved recovery of mechanical properties compared to control samples. However, the ECC containing the capsules exhibited a flexural strength approximately 27% lower than controls. In this case the capsules were placed by hand rather than mixed into the ECC.

Li et al. (2013a) introduced polystyrene-divinylbenzene microcapsules, between 100-150µm in diameter, containing epoxy resin into cement paste samples. The authors found that 1-2% microcapsules by weight of cement produced voids within the samples which reduced their strength, and that healing efficiency depended upon the amount and size of cracks in relation to the volume of healing agent released by breakage of the capsules.

Hilloulin et al. (2014) developed polymeric capsules which could be made to survive the mixing process. Capsules 50mm in length and inner diameter between 1.1-4mm made from poly(lactic acid) (PLA), polystyrene (PS) and Poly(methyl methacrylate/n-butyl methacrylate) (P(MMA/n-BMA)) were introduced into concrete at temperatures above their glass transition temperatures to avoid brittle behaviours. This resulted in improved survivability of the mixing process compared to mixing at room temperature. However, they found compatibility issues with the capsules and the healing agents used (two-part polyurethane-based) which began to harden within the capsules. They also found that only some capsules subsequently broke during 3-point bending up to 0.4mm crack width.

To summarise, work by Dry (1994), Thao et al. (2009) and Joseph et al. (2007) focussed on the internal delivery of healing agents through brittle tube or channel systems, which in some cases were unsuccessful due to hardening of the healing agent before cracking or a negative air pressure acting against the flow of the agent into the crack. This system also delivers a finite quantity of healing agent into a crack and does not allow 'repeated healing' to occur.

Capsule-based delivery systems, particularly microcapsules (to reduce the effect on compressive strength of samples), show potential as autonomous self-healing systems but present several challenges. Firstly, the capsules must be able to be mixed within concrete without breaking, while maintaining the ability to release their healing cargos when cracking occurs. Secondly, the cargo must not harden within the capsules and once released must be able to successfully heal the cracks.

Ongoing research being conducted as part of the “Materials for Life” project (EPSRC reference EP/K026631/1) follows on from experiments by Joseph et al. (2010) into an external delivery system for healing agents, by investigating the potential for a 2D network of channels in cementitious materials (Davies et al., 2015). In addition, the project includes research into various shell and cargo materials to develop an autonomous self-healing microcapsule system.

2.6.2. Alternative autonomous self-healing systems

Bacteria healing systems: There have been various studies on micro-organisms as self-healing initiators within concrete. These may be embedded in expanded clay particles (Wiktor and Jonkers, 2011), encapsulated in polymer microcapsules (Wang et al., 2014) or introduced directly to cementitious materials along with a liquid medium (Luo et al., 2015). A range of bacterial strains have been investigated, a detailed analysis of which is outside scope of this review. The use of bacterial systems has the potential for repeated and long-term healing. However, the use of living organisms brings challenges such as survivability in the environmental conditions (particularly high alkalinity and varying temperature) within cementitious materials. Bacterial systems also require a supply of nutrients to feed the live bacteria to produce healing materials.

Super-absorbent polymers: One proposed system is the introduction of super-absorbent polymers (SAP) into the cementitious material. These materials absorb water during the mixing process, then dry out after the mix has hardened, leaving voids within the concrete or mortar. When cracks occur, they are more likely to pass through these voids. With water ingress, the SAP swell beyond their original dimensions during mixing, so long as the water has a low ionic concentration. This blocks the cracks, reducing permeability. During dry periods, the SAP shrink and release water to aid the precipitation of calcium carbonate and ongoing hydration (Van Tittelboom and De Belie, 2013).

Expansive crystalline admixtures: Expansive additives in concrete, which form crystals upon the ingress of water into the crack, can be used to heal cracks (Van Tittelboom and De Belie, 2013, Liberato et al., 2016). These systems vary in the crystals produced, with some promising results. An area where further investigation is needed is on the production of in-crack stress and micro cracking around the swelling agents (Van Tittelboom and De Belie, 2013).

2.7. ON-SITE APPLICATION OF SELF-HEALING CONCRETE

Despite the fact that self-healing concrete techniques have been the subject of research since the early 1990's, there have been very few tests conducted outside of a laboratory environment (Dry, 1994, De Rooij et al., 2013).

Dry (2001) undertook experiments on the self-repair of drying shrinkage cracks and structural load-induced cracks in full-scale concrete bridge decks. Adhesive-filled fibres were embedded into bridge decks and compared to a control deck. The author concluded that the embedded fibres successfully released the adhesives which resulted in the repair of structural cracks and a higher strength upon second loading compared to the control.

Wiktor and Jonkers (2015) carried out a field study using a bacteria-based repair system in a parking garage. While the application was as a repair technique rather than self-healing, the studied mechanism of crack sealing through bacteria has also been proposed for a self-healing system as discussed in section 2.6.2.

In their study, two bacterial repair solutions were spray applied to a concrete slab in the garage with existing cracks. The first solution contained sodium silicate (as an alkaline buffer), sodium gluconate (as a carbon source for the bacteria) and alkaliphilic bacteria. The second contained calcium nitrate (as a calcium source for $CaCO_3$ precipitation, and as a nitrate source for denitrification as an anaerobic sealing process) and alkaliphilic bacteria (Wiktor and Jonkers, 2015).

The cracked area to which both solutions were applied was compared to an untreated area in terms of resistance to freeze-thaw and icing salts (using cored samples) and permeability from a visual assessment of how much water flowed through the slab when 5L of tap water was poured on the areas from above.

The field study concluded that the solutions resulted in an improvement in resistance to freeze thaw and de-icing salts (although all cores demonstrated very poor resistance), and that the treated area showed significantly reduced leakage of water compared to the untreated area (Wiktor and Jonkers, 2015). However, it is not clear whether the bacteria were the cause of these changes. One potential cause for the reduction in permeability was the sodium silicate buffer, which as the authors mention, is expected to form a gel to seal the crack within a few hours of application. A buffer-only control was not included as part of the study.

Biodegradable plastic capsules made from bacteria and calcium lactate have reportedly been introduced into concrete for the purposes of self-healing in a lifeguard station structure in the Netherlands (Johnson, 2015). However, at the time of writing no peer-reviewed papers have been published which include any findings from this field study.

The question remains as to whether the autonomous self-healing techniques investigated in laboratory studies, as well as enhanced autogenous self-healing systems, can function in a full-scale site environment. Chapter 5 seeks to address this question.

2.8. CONCLUSIONS FROM CHAPTER 2

- The principal mechanisms of autogenous self-healing of cementitious materials, $CaCO_3$ precipitation and the ongoing hydration of cement, require the presence of water within the crack and complete healing is limited to crack widths below 0.25mm. The majority of existing studies have monitored crack sealing through the reduction in crack width or

regain in permeability; autogenous healing measured as a regain in mechanical properties is less common.

- Enhanced autogenous healing through the reduction of crack widths has previously been achieved, primarily by introducing polymer fibres to create engineered cementitious composites. Jefferson et al. (2010), Dunn et al. (2011) and Isaacs et al. (2013) have developed a shape memory polymer crack closure system to impart a compressive stress onto concrete cracks, thereby enhancing the strength regain through autogenous healing. Experiments to date have used small mortar beam specimens, with polymer activation by placing the samples in an oven. Larger, structural concrete specimen tests are now required to assess the feasibility of this system in practice, along with improvements to the polymer system including the production of higher restrained shrinkage stress and an activation system suitable for in situ-application.
- The shape memory effect (SME) in shape memory polymers can be improved through changes to the programming (drawing) regime. Key variables include the temperature, draw ratio and draw rate. For PET, the degree of crystallinity also has an effect on the SME observed upon activation. Maximising the restrained shrinkage stress of PET is of importance within this thesis, to reduce the area of concrete replaced by the SMP system whilst applying sufficient stress to close cracks in concrete. It would also be beneficial to produce a rigid polymer system which is more practical to install in both unreinforced and reinforced concrete structures.
- There have been limited full-scale tests of self-healing concrete systems. Adhesive-filled fibres (Dry, 2001), a bacterial-based repair solution (Wiktor and Jonkers, 2015) and a bacterial self-healing concrete (Johnson, 2015) have been applied to full-scale structures. Of the three, only the fibres have produced conclusive results of self-healing through the proposed mechanism.
- The identified gap within the literature which this thesis seeks to address is the scalability and practical application of the shape memory polymer crack closure system

developed by Jefferson et al. (2010), Dunn et al. (2011) and Isaacs et al. (2013). This will be achieved through experimental and development work on the system's use within larger structural concrete members, both in the laboratory and at full-scale, and the ability to activate the polymers directly in-situ (i.e. without the need to place cementitious specimens into an oven).

Chapter 3. Developing a High Shrinkage Shape Memory Polymer Material

3.1. INTRODUCTION

This chapter describes the development and testing of high shrinkage shape memory polymer material for use in a concrete crack closure system. Previous experiments carried out by Jefferson et al. (2010), Dunn et al. (2011) and Isaacs et al. (2013) made use of PET strips to generate restrained shrinkage stresses, thereby closing cracks in small scale mortar beams. Whilst the crack closure system has been demonstrated successfully at this scale, it has been suggested that for larger structural concrete applications, higher shrinkage stresses than those previously observed are required for the crack closure system to be viable (Isaacs, 2011, Hazelwood et al., 2015).

Higher restrained shrinkage stress would allow a reduction in the area of polymer required to impart the same compression force on to the concrete element. This is particularly important to reduce the volume of concrete replaced by the polymer material, which can weaken the structural member.

In addition, the PET strips used in the original experiments were cut and layered before being placed within the beams. A new polymer form which is easier to set up within concrete elements would be a significant improvement on the previous time-consuming process.

The development of a new polymer for use within the crack closure system has been conducted in collaboration with Bradford University. Polymer experts at Bradford used their die-drawing equipment to manufacture samples for testing in Cardiff University laboratories. This chapter details the specification of and experiments undertaken to investigate the mechanical and shape memory properties of these samples, comparing them to the PET strips used in previous work.

The polymer samples tested, with the exclusion of the commercially available PET strips, are bespoke and have been produced at Bradford University for the purpose of assessing their potential for use within the concrete crack closure system. SMPs have never before been manufactured specifically for this purpose. Maximising the polymer restrained shrinkage stress and improving the polymer's ease of use within a cementitious system is the long-term objective of the work described in this chapter.

3.2. MATERIAL MANUFACTURING DETAILS

The information in the following sections (3.2.1 to 3.2.3) relates to work undertaken by Bradford University to manufacture the samples used for testing and is included here for reference. Originally, rigid, hollow tube samples were produced for ease of handling and use. It was then proposed to include smaller filament samples (either hollow or solid) within the tubes in an attempt to improve the shrinkage stress generated. These filaments were also manufactured and tested outside of tube samples. This resulted in the four sample types shown in Figure 3.1.

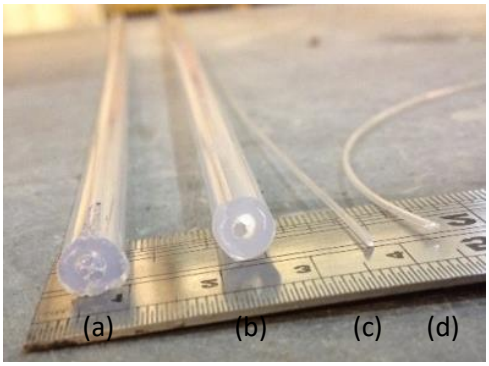

Figure 3.1: Manufactured PET samples: (a) tube with filaments, (b) tube, (c) solid filament, (d) filament tube.

3.2.1. PET solid filament and filament tube

For the PET solid filaments and filament tube, a commercial grade of PET (Dow Lighter C93), recommended for injection moulding, stretch blow moulding and thermoforming, was obtained in granular form. It was first made into fibres by melt extrusion. This was done using a single-

screw Killion S1748 25mm extruder operating at a screw speed of 15rpm and a screw pressure of 30bar. The maximum melt temperature in the extruder was 280°C and the die head was at 270°C; above the 260°C melting temperature of PET (Göschel, 1996), while avoiding thermal degradation of the material through excessive temperature (Sciences, 2011). The material was extruded through a circular die of 4mm internal diameter at a rate of 5m/min. On exit from the die it was cooled in a glycerol bath at room temperature. The final diameter of the cooled product was 1.8mm.

The second stage of the process was to introduce molecular orientation into the fibres. The technique of die-drawing was used, as described for polymers by Coates and Ward (1981). Fibre at room temperature was pulled through a 1.5m length fan-assisted oven with a controlled air temperature. On exit from the oven, it entered a converging conical die with cone angle 30° and final diameter 1mm, held at a constant temperature. After the die the fibre was gripped by a caterpillar-type haul-off device operating at a constant linear speed.

Since the highest levels of orientation are associated with the highest haul-off speeds and lowest temperatures, the caterpillar speed was set at its maximum 1m/min and both the oven and die temperatures were lowered in 1°C increments from 80°C until stress whitening and failure of the fibre were observed at 75°C. The die temperature was then raised incrementally until satisfactory fibre was produced; the final settings were thus 75°C in the oven and 80°C in the die.

After exiting the die, further drawing took place during cooling between the die and the caterpillar, resulting in a final diameter of 0.9mm, corresponding to a draw ratio of 4.0. At the start of the process the haul-off force was measured as 80N, and this reduced to a steady load of 50N as the process stabilised; these loads correspond to stresses of 99 and 62MPa respectively, to be compared with the yield strength of 55MPa according to the manufacturer's data sheet.

3.2.2. PET tube

The outer cylinder was made from the same grade of PET as with the filaments described above. Tubes were extruded using the same Killion extruder operating at a screw speed of 70rpm and a pressure of 200bar. The maximum temperature in the extruder was 280°C and the die head was at 260°C. Extrusion was through a circular section die of diameter 14mm, with a central internal pin of diameter 4mm to create the central hole. The haul-off speed was 500mm/min and final dimensions were outer diameter 13mm and inner diameter 6mm.

The tubes were then die-drawn from 1m lengths through a 30° conical die with an exit diameter of 7mm. Otherwise, the die-drawing equipment was as used for the drawing of the filaments described above. Both the die and oven air temperatures were set at 75°C. The initial haul-off speed was 40mm/min, and was increased during the die-drawing process to reach the maximum draw ratio. The tube's final outer diameter was 6.61mm on average, corresponding to a draw ratio of 3.9.

3.2.3. PET tube with filaments

An alternative system was studied that consisted of PET filaments inside hollow PET tubes. This was assembled in its initial isotropic state (see configuration in Figure 3.2) and then the complete assembly was die-drawn.

Both the internal fibres and the tubes within this system were extruded from Tergal grade T74F9 PET. The source material was changed (for the *solid filament*, *filament tube* and *tube* samples) to Dow Lighter C93 for reasons of reliability of supply. Extruder and die temperatures were both 280°C, with extrusion through a 2.5mm spinneret at a screw speed of 5.4rpm to achieve a final fibre diameter of 1.2mm. The outer cylinder was manufactured following the same process described for the PET tube samples.

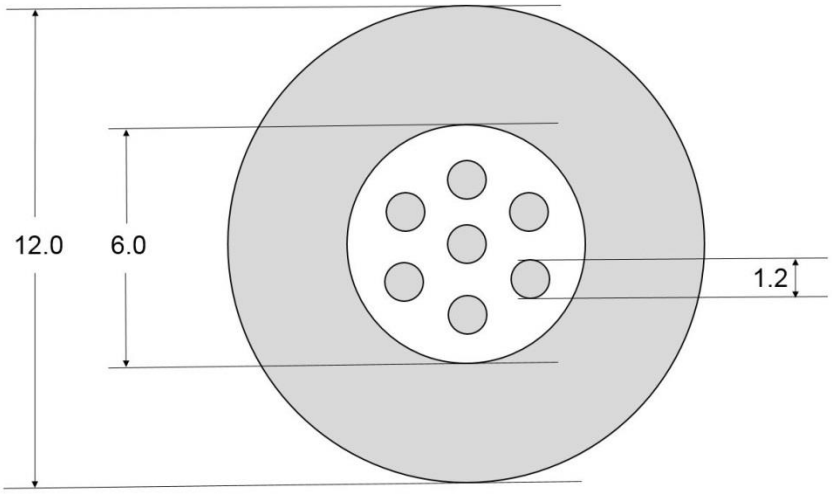

Figure 3.2: Indicative cross-section of PET tube with filaments system before drawing. Dimensions in mm.

1m lengths of tube and filaments were assembled and then die-drawn through a 30° conical die with an exit diameter of 7mm, following the same procedure as for the PET tube samples. This resulted in a final external diameter of 6.54mm for the samples, with internal fibres of average diameter 0.57mm. This corresponds to a draw ratio of 4.0 for the tubes and 4.4 for the internal fibres.

3.2.4. PET strips (commercially available)

The PET strip specimens were commercially available under the name 'shrink tite tape' and were obtained from Cytec (CYTEC, 2016). This is the same tape used by Jefferson et al. (2010) in previous studies. These strips are made from oriented PET but the manufacturing details are not available.

3.2.5. Summary

Table 3.1 shows a summary of the properties of all samples used during testing.

Table 3.1: Summary of properties of samples.

Designation	Material	Dimensions	Draw ratio	Draw rate (mm/min)
Strips	Oriented PET[1]	0.046mm thickness 32mm width	unknown	unknown
Solid filament	Die-drawn PET	0.95mm dia.	4.0	1000
Filament tube	Die-drawn PET	0.95mm dia.	4.0	1000
Tube	Die-drawn PET	6.61mm external dia. 2.56mm internal dia.	3.9	40 (initial)
Tube with filaments	Die-drawn PET	6.54mm dia.	4.0 4.4	40 (initial)

[1]Manufacturing details commercially sensitive

3.3. EQUIPMENT AND TEST SPECIMEN PREPARATION

3.3.1. Anchorage systems

As the samples received from Bradford University varied in cross-section, two anchorage systems were used to enable them to be active within an Instron environmental chamber. Both of these anchorage systems consisted of bolted plates as shown in Figure 3.3.

The *tube* and *tube with filaments* samples used anchorage 1, while the *solid filament* and *filament tube* used anchorage 2. In all cases, the sample was passed through the steel grips, before tightening the bolts and melting the protruding end using a soldering iron to form a plug. The inside face of the steel plates was sand-blasted to improve frictional grip.

In preliminary experiments, PET *tube* samples were clamped within anchorage 1 and subjected to tensile load until failure in an Avery-Denison tensile machine. Initially the plates were used without a central notch and the bolts were tightened to varying degrees of torque (2.5Nm, 3Nm and hand-tightened to maximum). The system with a central notch was tested at 3Nm torque, and a *tube* sample was also clamped directly into the tensile machine for comparison. The results can be seen in Table 3.2.

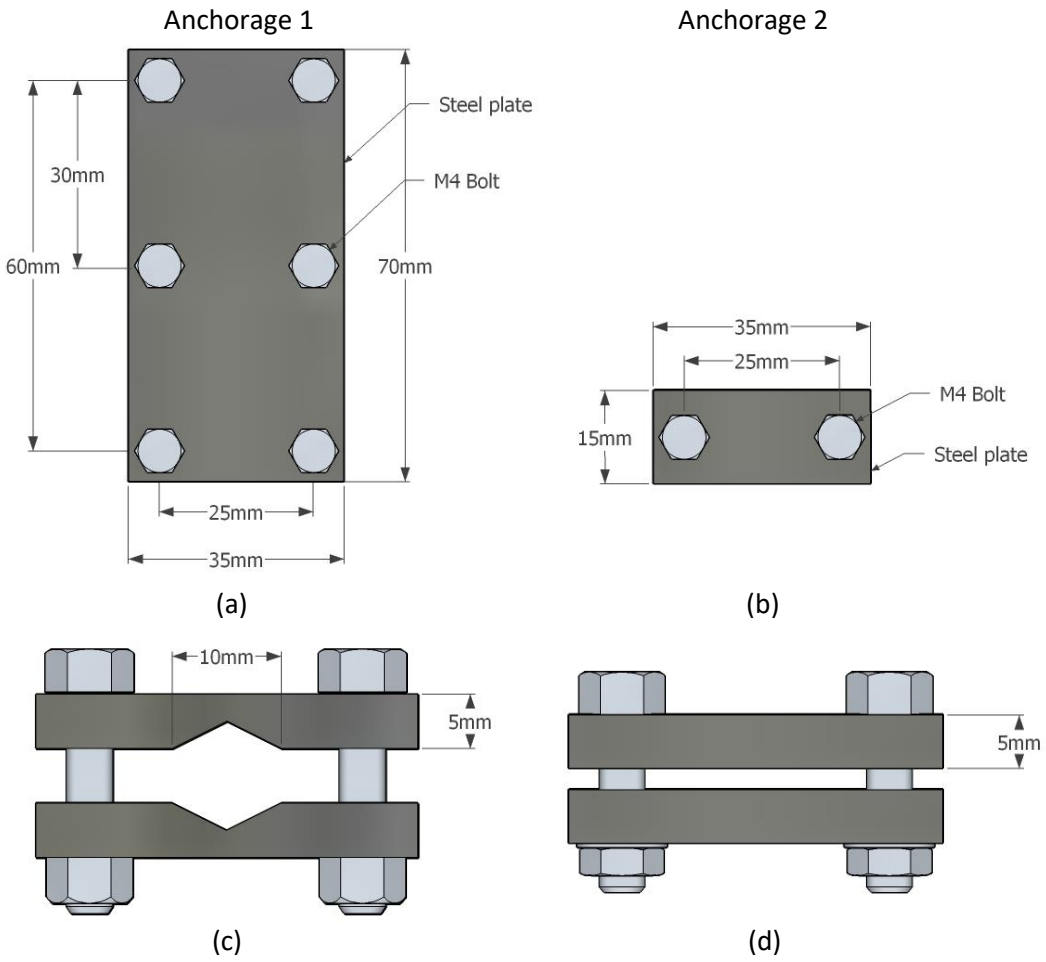

Figure 3.3: Schematic drawings of anchorage 1 (a) plan view and (c) end view; anchorage 2 (b) plan view and (d) end view.

Table 3.2: Preliminary anchorage experiment results.

Ref.	Type	Torque per bolt (Nm)	Peak load (kN)	Failure mechanism
1	Anchorage without notch	Hand tightened (high torque)	4.47	PET tensile failure
2	Anchorage without notch	2.5	5.00	Slippage within anchorage
3	Anchorage without notch	3	5.07	PET tensile failure
4	Anchorage with notch	3	5.93	PET tensile failure
5	PET *tube* alone in machine grips	n/a	6.62	PET tensile failure

As shown, all the anchored samples failed at a lower peak load than the sample within the tensile machine grips. This may be due to damage to the samples caused by the compressive force of the grips, as the poorest performance was seen from the un-notched anchorage tightened to a maximum torque. As the environmental chamber used to heat the samples could not fit around

the Avery-Denison machine, the samples could not be clamped directly into the machine for testing. Even in the worst-performance anchorage, however, a load of 4.47kN was reached. To produce this force, the restrained shrinkage stress of *tube* samples would need to reach 133MPa. This is far in excess of the largest stresses observed by unmodified drawn SMP within the literature (Meng and Hu, 2009, Xie, 2011).

A 2.5Nm torque was found to result in slippage of the sample within the anchorage. The best performance was seen from the 'anchorage with notch' at 3Nm torque, reaching a peak load of 5.93kN. It was therefore decided to use this anchorage system to test the PET *tube* and *tube with filaments* samples.

These experiments were not repeated for the *filament* and *filament tube* samples in anchorage 2. However, the restrained shrinkage test results (discussed in Section 3.5.1) produced similar profiles to those within anchorage 1; slippage would have been apparent from stress drops during heating, which were not observed. Similarly, no slippage relative to the grips was observed visually in any of the samples during testing.

3.3.2. Environmental chamber rig

The PET *strips* were clamped between two steel plates and screwed directly into the environmental chamber, using the same grips as Hazelwood et al. (2014). To accommodate anchorages 1 and 2, a steel cradle was manufactured which then screwed into the environmental chamber. This resulted in the set-up shown in Figure 3.4. The *strip* samples were therefore 430mm in length compared to 305mm for all other samples. It was found previously by Dunn (2010) that specimen length for the *strip* samples has a negligible effect on the polymer's stress development, making the results comparable.

The rigs were connected to a 5kN load cell and three thermocouples were placed on the samples, denoted T1, T2 and T3 on Figure 3.4. Load and temperature were recorded at a rate of 1Hz.

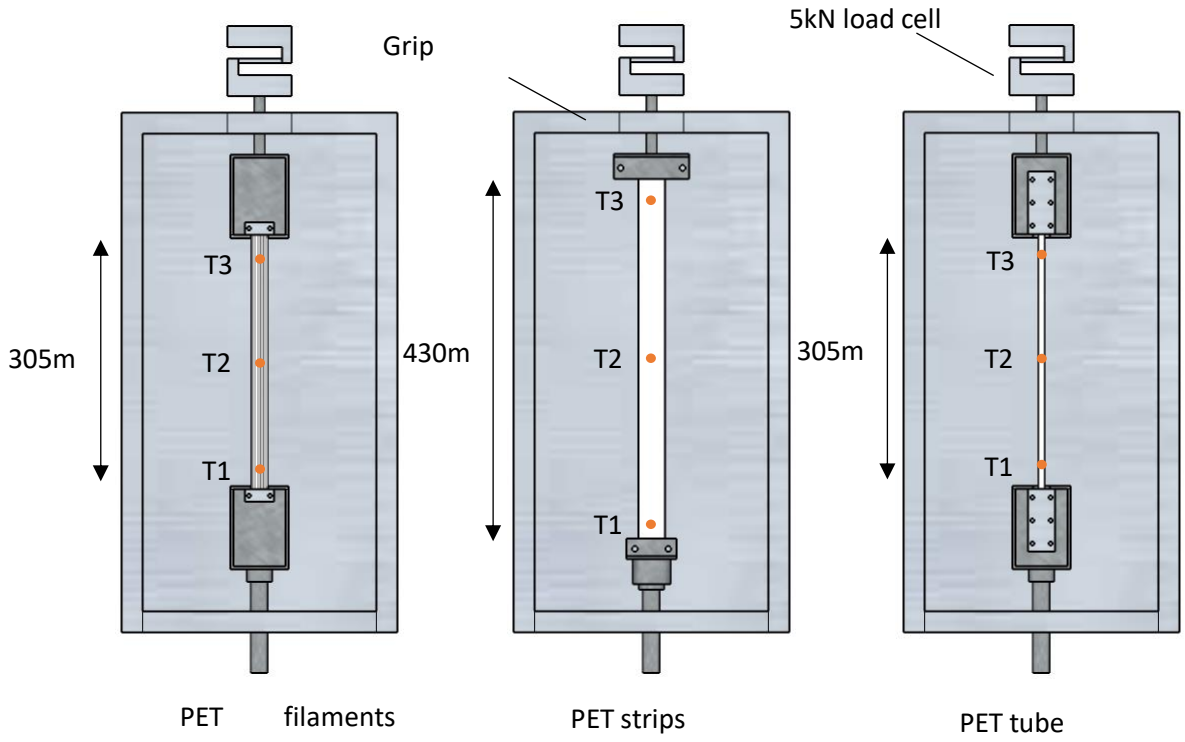

Figure 3.4: Environmental chamber rig setup for each sample type.

3.3.3. Pre-stress

To ensure that there was no slack within the samples, each was placed under an initial pre-stress prior to heating. A preliminary experiment with ten layered PET strips was carried out to determine a suitable initial pre-stress value. This consisted of varying the pre-stress and subjecting the strips to 90°C temperature for 1 hour, followed by cooling to 30°C and recording the resultant shrinkage stress. Pre-stress was varied by adjusting the vertical distance between the grips, using the same sample length. Pre-stress values used were 0MPa, 2MPa, 8MPA, 20MPa and 40MPa. In two samples, the grips were adjusted so that the distance between them was shorter than the sample length, producing a slack in the specimens. This slack was measured, using a ruler and string, as the horizontal distance between the vertical centre-line

of the grips and the mid-point of the PET when pushed out to full extension. This definition, along with the results of the experiment, can be seen in Figure 3.5.

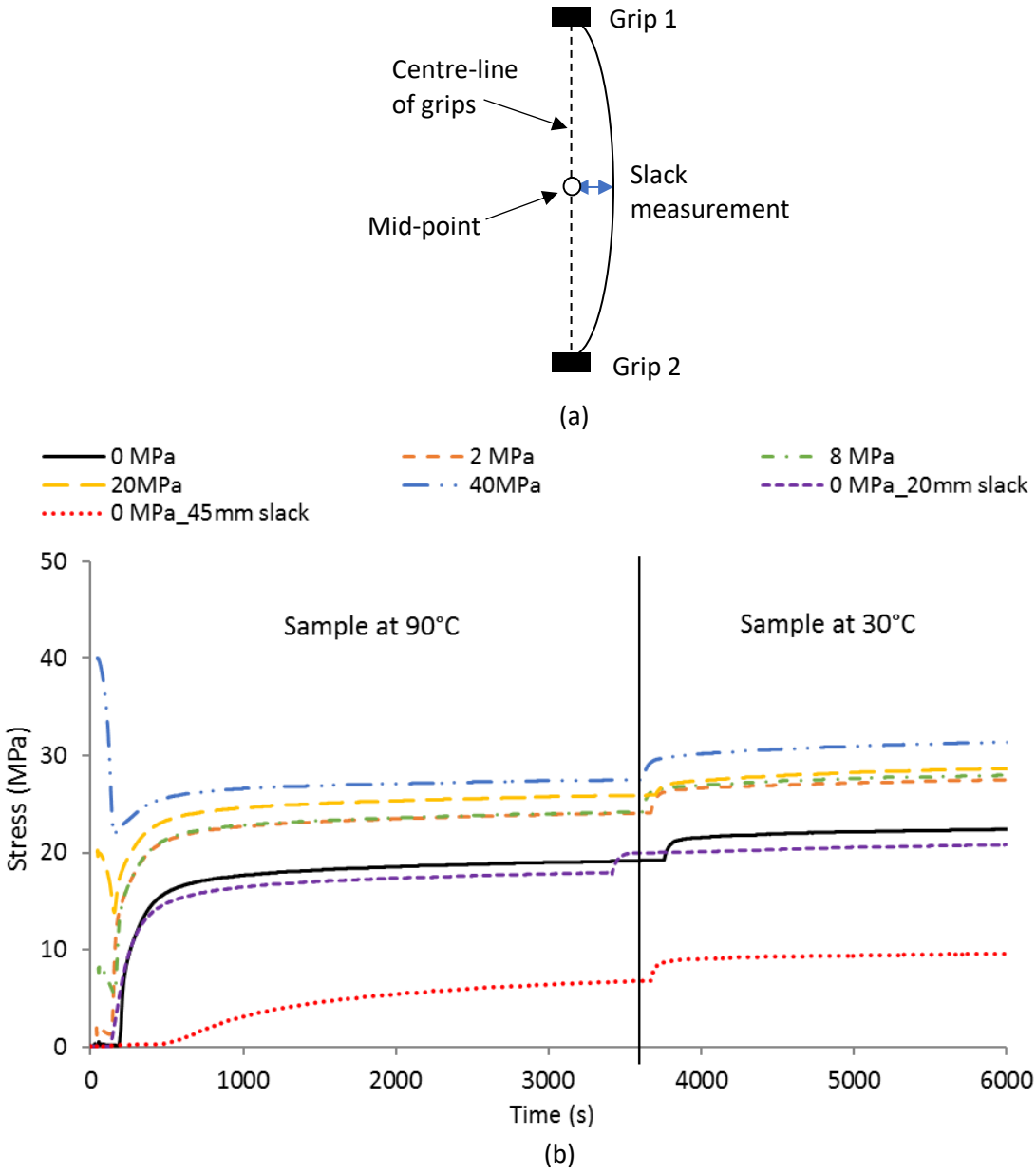

Figure 3.5: (a) Measurement of slack in PET samples; (b) Pre-stress influence on restrained shrinkage stress of PET strips.

It can be seen that 45mm of slack in the PET specimen significantly affects the final level of stress, while there is only a small difference between 20mm of slack and the strips being held taut (0MPa pre-stress). There is, however, a considerable increase in restrained shrinkage stress between a pre-stress of 0 and 2MPa. Further increases in pre-stress result in only moderate

increases in shrinkage stress. This suggests that a small level of pre-stress is sufficient to ensure a near-maximum restrained shrinkage stress when the PET strips are heated.

It is possible that at 0MPa some of the 10 strips tested were not fully taut, causing a lower final stress result. At 2MPa, all strips are taut resulting in a much higher final stress. Further increases in pre-stress beyond 2MPa do not therefore not have the same effect. Given this physical explanation, it was expected that the same effect would be observed for all samples. A pre-stress value of 2MPa was therefore chosen for future testing of all polymer samples.

From the graph it can also be seen that upon cooling there is a rapid rise in stress followed by a more gradual rise and eventually a plateau. This is due to the cooling effect of the metal grips used to hold the samples. This was an effect observed in all tests using the environmental chamber and is discussed alongside the experimental results in section 3.5.

3.4. TEST PROCEDURES

PET has a glass transition temperature in the range 60–80°C (Alves et al., 2002). Previous work undertaken at Cardiff University suggested that the peak uniaxial shrinkage stress for drawn PET tape is achieved at 120°C (Dunn et al., 2011);however, to ensure the system can be activated within concrete without causing structural damage, an activation temperature of 90°C was chosen for the restrained shrinkage stress experiments. These requirements are explained in more detail in section 2.3.3.

Once the samples were placed within the environmental chamber in the rig setup, and the 2MPa pre-stress had been applied, the samples were subjected to various testing procedures as described in the following section. Table 3.3 shows the number of repetitions and samples used in each test.

Table 3.3: Repetitions and number of samples per test.

Sample type	Tests and repetitions		Samples per test
Strips	TS1	3	10
	TS2	1	10
	TS3	10	1
	TS4	3	1
	TS5	3	4*
Solid filament	TS1	3	10
	TS2	1	10
	TS3	10	1
	TS4	3	1
	TS5	3	1
Filament tube	TS1	1	10
	TS2	1	10
	TS3	10	1
	TS4	3	1
Tube	TS1	1	1
	TS2	1	1
	TS3	1	1
Tube with filaments	TS1	1	1
	TS2	1	1
	TS3	1	1

*To achieve a roughly equal cross-sectional area to a single filament

3.4.1. Shrinkage stress at 90°C (Test Series 1, TS1)

To test the restrained shrinkage stress at the chosen activation temperature of 90°C, the samples were heated to 90°C in the environmental chamber and left at a constant temperature for 1 hour, referred to as the soak time. The environmental chamber was then turned off and the sample allowed to cool back to room temperature. Load and temperature were measured at a sample rate of 1Hz.

3.4.2. Temperature-shrinkage profile (Test Series 2, TS2)

Although 90°C is the target activation temperature, it was decided to test the restrained shrinkage stress of the polymers across a wider temperature range to better understand their shrinkage behaviour with varying temperature.

The samples were heated to 60°C, just below the glass transition temperature, within an Instron environmental chamber and held for a soak time of 30 minutes. The temperature was then increased in 10°C increments, keeping the soak time at 30 minutes for each increment, up to 140°C. The environmental chamber was then turned off and the sample allowed to cool back to 30°C. Load and temperature were measured at a sample rate of 1Hz.

3.4.3. Free shrinkage (Test Series 3, TS3)

A polymer with low free shrinkage will produce a restrained shrinkage stress over a smaller change in length compared to one with higher free shrinkage. Free shrinkage therefore suggests how sensitive the polymer may be to changes in pre-stress and differential movement, particularly important when placed within concrete which is liable to shrink or expand in changing conditions.

Samples of original length 305mm were placed within the environmental chamber and heated to 90°C for 18 hours. They were then allowed to cool to room temperature and their final lengths recorded.

The test series TS1 to TS3 were used to select a form of PET for further investigation. *Solid filament* and *filament tube* samples, having exhibited the highest restrained shrinkage stress at 90°C of all samples, were then subjected to additional testing to determine their mechanical properties. The PET *strips* were also subjected to further testing for comparison, having been used in previous concrete crack closure tests.

3.4.4. Tensile strength tests (Test Series 4, TS4)

Individual PET *solid filament*, *filament tube* and *strip* samples were subjected to tensile loading in a Zwick Z100 tensile testing machine. Loading was displacement-controlled. For the PET *strips*, loading rates of 0.05mm/s, 0.1mm/s and 0.2mm/s were used to check the effect of loading rate.

For the *solid filament and filament tube* samples, a 0.1mm/s rate was used. Loading was continued until failure of the samples. PET *strip* samples, which had been activated (heated to 90°C for 1 hour), were also tested for comparison. Load and displacement were measured at a sample rate of 1Hz.

3.4.5. Effect of temperature on Young's modulus (Test Series 5, TS5)

Using a Dartec tensile testing machine and an Instron environmental chamber, PET *solid filament* and PET *strips* samples were held at a pre-load, equivalent to a stress of 10MPa, while the temperature was increased in increments of 10°C from 30°C to 110°C with a soak time of 5 minutes. At each temperature increment, a cyclic stress with amplitude 10MPa was applied to the sample (increasing the applied stress from the pre-load magnitude of 10MPa to 20MPa, then decreasing back to 10MPa). Three rates of stress were used: $3.4MPas^{-1}$, $0.34MPas^{-1}$ and $0.034MPas^{-1}$ (equivalent to $10Ns^{-1}$, $1Ns^{1}$ and $0.1Ns^{-1}$ in the filament samples). Load and displacement were measured at a sample rate of 10Hz and used to calculate the Young's modulus at each temperature.

3.5. RESULTS AND DISCUSSION

3.5.1. Peak shrinkage stress in TS1 samples

In all of the TS1 samples, the peak restrained shrinkage stress, during the heating phase, occurred when the environmental chamber temperature was 90^{o}C. In some cases, higher stresses were observed upon cooling, which is thought to be due to the thermal contraction of the steel rig. This issue is discussed below. The peak stress results are shown in Table 3.4.

As can be seen from the stress results, the highest average shrinkage stress was observed in the PET *filament tube* samples, with the lowest stress exhibited by the *tube with filaments* specimens. Both of the *filament* samples produced significantly higher stresses than either the

strips or the larger PET *tubes*. The trend in these results is supported by the fact that the degree of crystallisation reduces with the cross-sectional area of a sample, and that crystallisation of the polymer matrix reduces the shape recovery potential of shape memory polymers by increasing the material's resistance to shrinkage (Mody et al., 2001).

Table 3.4: Peak restrained shrinkage stress results.

	Restrained shrinkage stress for TS1 specimens at 90°C (MPa)			
Polymer sample	**Highest**	**Lowest**	**Average**	**CoV (%)**
Strips	24.9	23.0	24.0	4.0
Solid filament	41.5	37.0	38.6	6.6
Filament tube	43.3	38.7	40.9	5.7
Tube	23.1	-	23.1	-
Tube with filaments	17.0	-	17.0	-

In addition, since the shrinkage stress is correlated to the stored energy within the polymer, maximising the force used to draw the filaments -through the use of a high drawing rate (1m/min)- further contributed to the increased shrinkage stresses in the *filament* samples relative to those of the *tube* samples (40mm/min initial). The *tube with filament* samples exhibited similar shrinkage behaviour to the *tube* samples, indicating that the maximum stress seems to be limited by the external tube. The graphical results of the restrained shrinkage stress at 90°C for all samples can be seen in Figure 3.6. In all cases, heating to 90°C produced a rapid increase in stress followed by a plateau. Upon cooling, there was a subsequent increase of 2-3MPa. This increase in stress can be attributed to the contraction of the steel rig used to transfer the shrinkage stress of the PET to the load cell. This was later confirmed in separate tests in which samples were heated using a system of embedded wires. This system caused no appreciable change in temperature in the steel rig. In this case, there was no increase in the polymer stress during the cooling phase.

The graphs in Figure 3.6 are typical results; repetitions were completed for the *strips*, *solid filament* and *filament tube* samples, the results of which are included as Appendix A. The coefficient of variation (CoV) in peak stress, also shown in Table 3.4, show that all polymers produced fairly consistent results. The *solid filament* and *filament tube* samples had a CoV of 6.6

and 5.7 respectively. While this was higher than the 4.0 of the *strip* samples, the lowest peak stress observed in a filament sample test (37.0MPa for *solid filament*) is still a vast improvement over the highest peak stress of 24.9MPa produced by the *strip* samples.

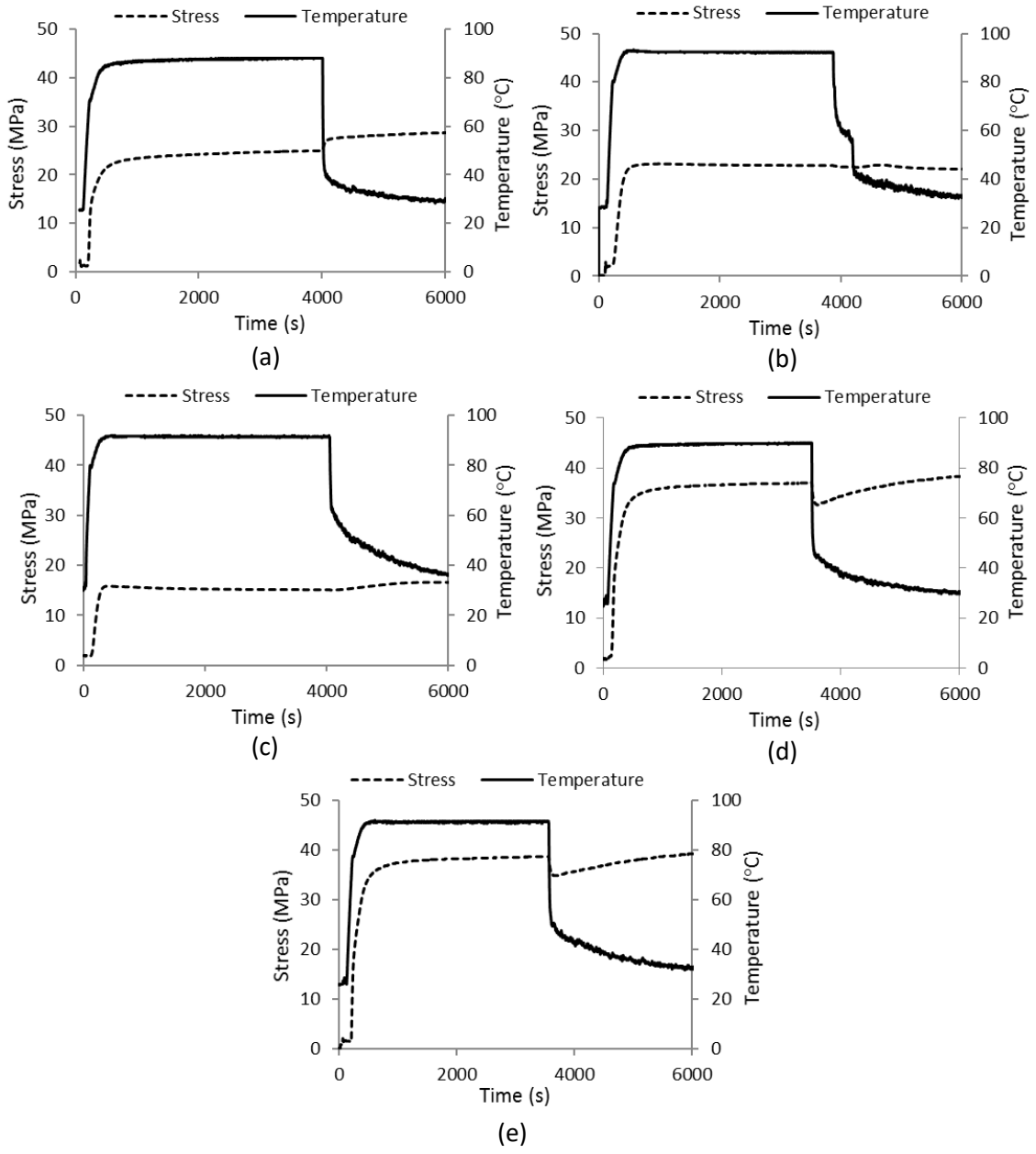

Figure 3.6: Restrained shrinkage stress at 90°C for (a) Strips; (b) Tube; (c) Tube with filaments; (d) Solid filaments & (e) Filament tube. Typical results graphs shown for samples with repetitions.

It is noted that the peak stress observed at 90°C in the PET *strip* samples is lower than the 30-35MPa found by Dunn et al. (2011). This variation may be due to manufacturing process changes since the original tests were undertaken and is discussed in more detail in section 3.5.5.

The *filament* (tube and solid) samples produced an initial drop in stress upon cooling, which was not observed in the other samples or in previous shrinkage experiments on PET *strip* samples. When the temperature exceeds T_g, shrinkage stress is entropic; the elastic modulus and therefore the stress (given constant strain) changes with absolute temperature (T), due to the decrease in the entropic state of the molecular chains that accompanies a reduction in T (Ward and Sweeney, 2013), i.e.

$$G=NkT \qquad (1)$$

in which *N* is the number of molecular chains per unit volume, *k* is Boltzmann's constant, *T* is the absolute temperature and *G* is the shear modulus. As *G* is proportional to stress (at constant strain), a stress drop is observed upon cooling.

However, this reduction in stress is counteracted by the thermal contraction of the material with decreasing temperature. The coefficient of thermal expansion (α) of PET in the direction of drawing has been found to decrease with increasing orientation (Pereira and Porter, 1984). It is therefore possible that for the *filament* samples, the increase in stress due to thermal contraction upon cooling is lower than in the *strip* samples, resulting in a drop in stress as the loss due to a reduction in entropy exceeds the thermal contraction effect. Conversely, in the *strip* samples it appears that thermal contraction was the dominant effect on stress change upon cooling. The potential to develop this theory as an addition to existing thermomechanical models, such as that presented by Hazelwood et al. (2014), is discussed further in section 7.2.

3.5.2. Temperature-shrinkage profiles in TS2 samples

The restrained shrinkage stresses recorded at each temperature interval have been plotted as temperature-shrinkage profiles in Figure 3.7.

It is observed for the PET *strip* samples that the shrinkage stress began to increase significantly when the temperature exceeded 70°C, reaching a peak of 28.7MPa at 130°C. Thereafter, the

stress began to fall as the temperature increased further, consistent with the findings from previous tests by Jefferson et al. (2010) and Dunn et al. (2011).

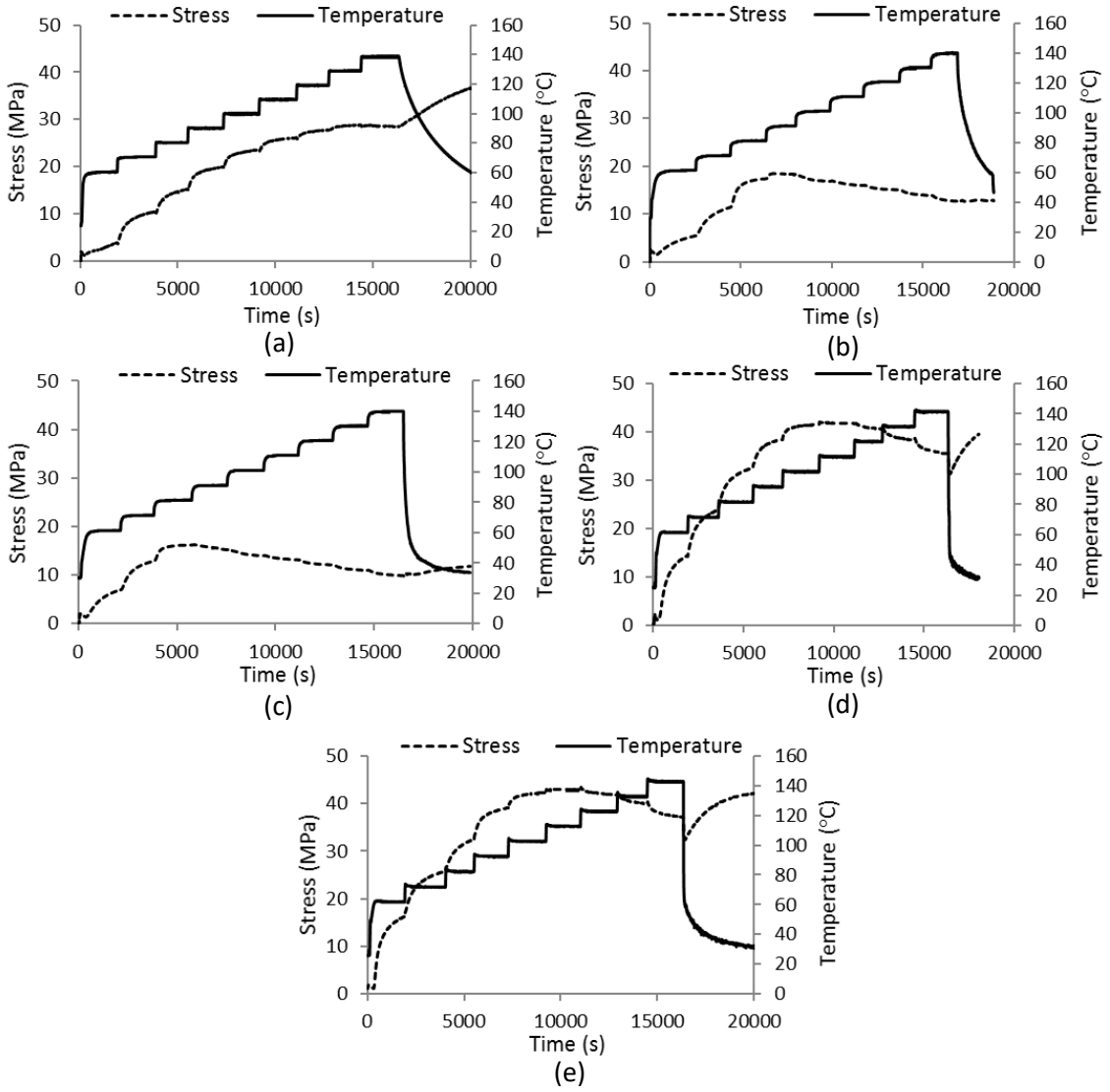

Figure 3.7: Temperature-shrinkage profiles for (a) Strips; (b) Tube; (c) Tube with filaments; (d) Solid filaments and (e) Filament tube.

The *solid filament* and *filament tube* samples exhibited stress peaks of 41.8MPa and 42.9MPa respectively, both at 110°C.

The *tube* and *tube with filaments* samples showed peak stresses of 18.3MPa and 16.2MPa respectively at the lower temperature of 90°. This could be related to the lower drawing temperature of 75°C in comparison to the 80°C of the *filament* samples. As discussed in section

2.4.3, the peak shrinkage stress of SMPs often occurs at or near the programming or drawing temperature, a phenomenon known as the temperature memory effect (TME) (Sun et al., 2011).

The low peak shrinkage stress measured in the *tube with filament* samples may be associated with a degree of relative slip between the external tube and the inner filaments, both along the length of the specimens and at the grips. Such slip behaviour would cause a reduction in the contribution of the filaments to the overall composite shrinkage force and therefore to the mean shrinkage stress. While the inner filaments were drawn inside the tube and should therefore be held by friction and compression, both surfaces were very smooth. The relatively weak bond between the two was indicated by the fact that the filaments could be pulled out of the tube by hand.

All samples show a drop in shrinkage stress beyond the peak activation temperature. This is believed to be caused by the reduction in yield stress that accompanies an increase in temperature, as predicted by Eyring's model (Ward and Sweeney, 2013), which becomes very significant beyond 140^{o}C.

3.5.3. Free shrinkage tests in TS3 samples

Results of the free shrinkage experiments, presented in Table 3.5, show that the shrinkage at 90°C observed for all manufactured samples exceeds that of the PET *strips*. This suggests that these samples would be less sensitive to differential movements and resultant changes in pre-stress than the *strip* samples.

The difference in draw rate between the *filament* samples and the *tube* samples does not seem to have altered the free shrinkage properties. The lower free shrinkage demonstrated by the *strips* could be a result of a lower draw ratio, with associated lower orientation (Lu and Hay, 2001). However, as discussed in section 2.4.3, the relationship between crystallinity, orientation and shrinkage in PET is complex and it is not possible to conclude the reasons for the lower free

shrinkage in the *strip* samples without knowledge of the parameters used in the drawing process.

Table 3.5: Free shrinkage at 90°C results.

Sample type	Number of repetitions	Draw ratio	Draw rate (mm/s)	Average shrinkage (% length)	CoV (%)
Strips	10	unknown	unknown	1.6	15.6%
Solid filament	10	4.0	1000	5.0	8.8%
Filament tube	10	4.0	1000	4.7	5.6%
Tube	1	3.9	40 (initial)	5.2	-
Tube with filaments	1	4.0 (tube) 4.4 (int. filaments)	40 (initial)	7.2	-

The *filament* samples also produce less variable free shrinkage results than the *strips*, with a CoV of 5.6% and 8.8% for the *filament tube* and *solid filament* samples respectively compared to 15.6% for the *strip* samples. Increased free shrinkage and reduced variability both indicate that the *filament* samples would be more suitable for use as a concrete crack closure system than the *strip* samples.

3.5.4. Tensile strength tests in TS4 samples

The results of the tensile strength tests are given in Table 3.6 and a typical stress-strain curve for the solid filaments and strips shown in Figure 3.8(a). The solid and tube filament samples exhibit significantly higher tensile strengths than the strips. A lower 'strain at failure' in the *filament* samples indicates an increased elastic stiffness. The strain at failure is also more consistent, with *strip* samples showing a higher CoV.

The rate of loading has little effect on the tensile stress of the samples at failure. Furthermore, the tensile strengths of the activated PET *strip* samples are similar to those of the non-activated *strips*. Figure 3.8(b) compares the stress-strain curves of the unheated and heated strip samples. The heated strip curves have been offset to account for the negative strain experienced by the samples during the heating process. The negative strain value used was -1.6%, the average free

shrinkage of the strip samples observed during testing, recorded in Table 3.5. The heated *strip* samples reach comparable stresses at failure but at lower strain, when taking into account the negative strain. This indicates that activating the polymers does not weaken the material in tension, which is beneficial in the context of their use in potentially providing tensile reinforcement to concrete.

Table 3.6: Tensile strength test results.

Sample	Type	Rate (mm/s)	Stress at failure (MPa)	Strain at failure (%)	Avg. stress at failure (MPa)	CoV (stress) (%)	Average strain at failure (%)	CoV (strain) (%)
1	Strip	0.1	186.5	14.6				
2	Strip	0.1	187.0	18.3	189.2	1.9	20.1	26.9
3	Strip	0.1	194.2	27.5				
4	Strip	0.2	188.7	15.0				
5	Strip	0.2	186.8	12.4	187.3	0.5	13.2	9.4
6	Strip	0.2	186.4	12.3				
7	Strip	0.05	177.6	9.7	179.7	1.2	10.8	10.2
8	Strip	0.05	181.9	11.9				
9	Strip - heated	0.1	188.9	11.4				
10	Strip - heated	0.1	178.8	7.7	185.0	2.4	10.5	19.5
11	Strip - heated	0.1	187.3	12.5				
12	Solid filament	0.1	305.2	6.7				
13	Solid filament	0.1	309.9	7.2	304.9	1.4	6.6	8.8
14	Solid filament	0.1	300.0	6.0				
15	Filament tube	0.1	317.8	7.8				
16	Filament tube	0.1	305.7	6.9	308.5	2.2	7.4	6.5
17	Filament tube	0.1	302.1	8.0				

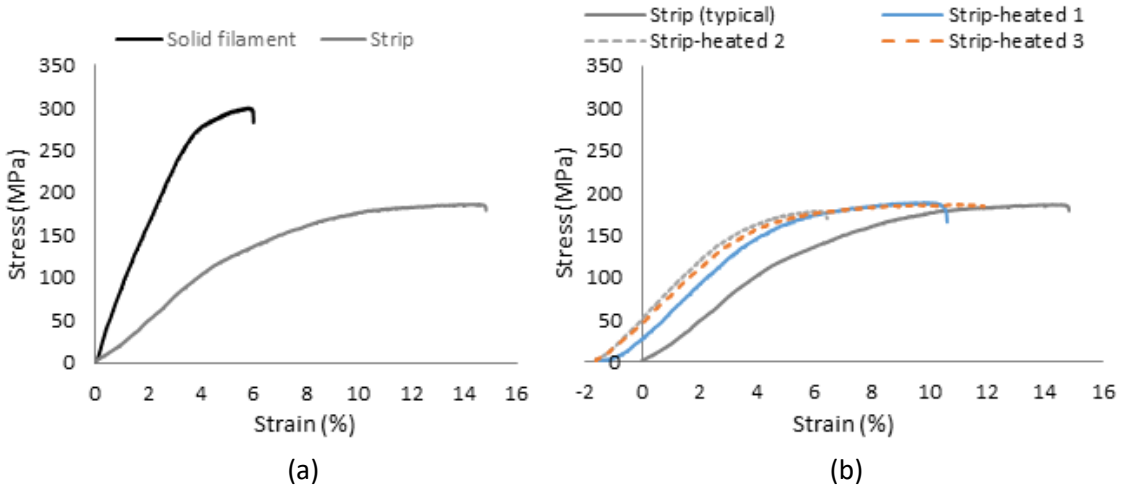

Figure 3.8: Stress-strain curves from tensile tests of (a) solid filament and unheated strip samples, typical graphs; and (b) unheated and heated strip samples.

The stress-strain curves of the heated *strip* samples in Figure 3.8(b) pass through the y-axis at between 28-51MPa. This gives an indication of the elastic energy released during the (unrestrained) heating process. Comparing this to the 29MPa peak observed for the restrained shrinkage of the *strip* samples during the temperature-shrinkage profile tests, it is probable that not all the elastic energy stored within the polymer was converted to restrained shrinkage stress during these tests. This concurs with Sun et al. (2011) who explains that the restrained shrinkage stress of shape memory polymers is only proportional to, not equal to, the stored elastic energy.

The stress-strain results suggest that the *strip* samples are probably drawn to a lower draw ratio than the filaments. This deduction is supported by the well-established trend that stiffness in drawn polymers increases with the draw ratio (Ward and Sweeney, 2013). The tensile test results also indicate that the two *filament* types, solid and tube, have very similar tensile strengths.

3.5.5. Effect of temperature on Young's modulus in TS5 samples

The results of the Young's modulus tests on the PET *solid filaments* and the PET *strips* are shown in Figure 3.9. As the PET solid filament and tube filament samples had exhibited almost identical shrinkage and tensile properties, having been subjected to identical methods of manufacture, modulus experiments were carried out only on the *solid filament* samples.

At each temperature, the average apparent Young's modulus (E_{ap}) was calculated from the loading and unloading portions of three 10MPa stress cycles. A comparison of measured E_{ap} values with increasing stress rate as shown in Figure 3.9, showed little variation and no clear relationship between the apparent E_{ap} value and increasing stress rate. The average E_{ap} over all three stress rates was then used to compare the *filaments* with the *strips*.

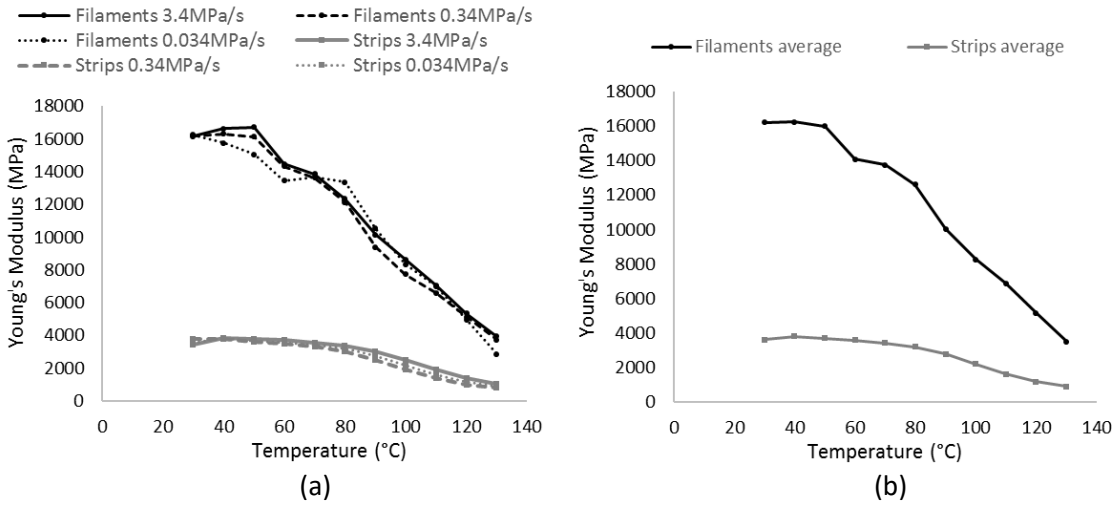

Figure 3.9: Young's Modulus with temperature for drawn PET solid filaments and PET strips (a) with 3.4 MPa s-1, 0.34 MPa s-1 and 0.034 MPa s-1 load cycles, and (b) as an average over all load cycles.

For both polymer forms, there is a clear reduction in E_{ap} with increasing temperature, a result of the polymer softening (Ward and Sweeney, 2013). The results show a clear drop in E_{ap} once the glass transition temperature of approximately 70°C has been reached, with continuing loss of stiffness to 130°C.

The *filament* samples produced significantly higher modulus results than the *strips*, which agrees with the findings from the tensile strength tests which show a much higher stiffness in the *filaments*. Dunn et al. (2011), however, observed higher E_{ap} results for the commercially available *strips*, around 6000MPa at 30°C compared to below the 4000MPa observed in the current samples. As discussed previously, there were also significant differences in the shrinkage stress results observed by Dunn et al. (2011) and those in the present study.

The supplier for the *strip* samples has changed ownership several times between 2009 and 2016, from Aerovac/Umeco (Dunn et al., 2011, Hazelwood et al., 2014, Umeco, 2012) to Cytec in 2012 (Today, 2012) then to Solvay in 2015 (Cytec, 2015). It is therefore very possible that changes in the source material or processing methods took place during that time. Upon contacting the supplier, no information could be given about these potential changes.

These results suggest that the commercially available strips were previously drawn to a higher draw ratio, leading to higher orientation and stiffness in the samples tested by Dunn et al. (2011) and Jefferson et al. (2010).

3.6. PET ALKALINITY RESISTANCE

One concern relating to the use of PET in concrete is its resistance to a highly alkaline environment. PET alkalinity resistance testing was therefore carried out on both commercially-available non shape memory PET, and the shape memory PET filaments used in the previous experiments.

Testing consisted of mixing an equivalent concrete pore solution (pH 13.4) from Calcium Hydroxide ($Ca(OH)_2$), Sodium Hydroxide (Na(OH)) and Potassium Hydroxide (K(OH)). Five commercially available PET rod specimens were submerged in this solution in a covered plastic bath, as shown in Figure 3.10, for 30 days at 60°C as per JSCE-E-538-1995 (JSCE, 1995). The mass and diameter of these rods were measured before and after submersion, and compared to control rods. Tensile strength tests were also carried out on all samples using an Avery-Dennison testing machine. The results of these tests can be seen in Table 3.7.

(a) (b)

Figure 3.10: (a) PET rods used in alkalinity tests, (b) concrete pore solution for alkalinity tests in covered plastic bath.

The results indicate that the alkaline solution caused an average reduction in overall mass of the PET rod samples of 1.28%. Similarly, the average tensile strength of the samples subjected to alkalinity testing was 80.9N/mm², a 1.3% reduction on the 82N/mm² observed in the control

samples. However, taking into account the variability of the strength results it is not conclusive that this strength reduction was caused by the alkalinity test. The submersion also had an effect on the surface of the PET samples, displaying a glossy surface prior to immersion and a dull surface after removal from the pore solution.

Table 3.7: Alkalinity testing of commercially available PET rod specimens.

		Initial condition		Final condition				
Specimen	Type	Mass	Dia.	Mass	Dia.	% mass loss	Peak tensile load (kN)	Tensile strength (N/mm²)
1	Test	38.24	10.39	37.74	10.24	1.31%	6.41	77.9
2	Test	38.71	10.40	38.23	10.29	1.24%	6.08	73.2
3	Test	38.17	10.33	37.72	10.21	1.18%	7.28	88.9
4	Test	38.56	10.37	38.04	10.26	1.35%	7.34	88.8
5	Test	38.41	10.34	37.91	10.23	1.30%	6.21	75.6
A	Control				10.43		5.98	70.0
B	Control				10.41		7.37	86.6
C	Control				10.37		6.51	77.0
D	Control				10.40		7.52	88.5
E	Control				10.42		7.49	87.9

The same experimental process was repeated using PET *solid filament* samples. 10 un-activated filaments, 300mm in length, and 10 activated filaments, 100mm in length, were placed into the equivalent pore solution at 60°C for 1 month. The activated samples were shorter due to the availability of activated material (previous samples having been discarded). As the measurement of degradation was percentage mass loss it was assumed this would have no effect on the results. The *filament* samples were not subjected to tensile testing as the 60°C temperature caused some deformation of the samples. The *filaments* before testing are shown in Figure 3.11.

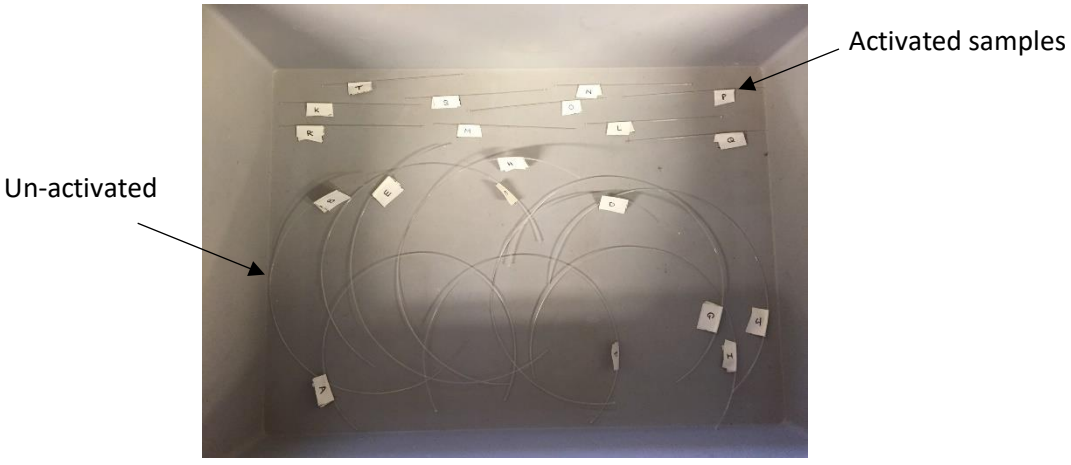

Figure 3.11: *Solid filament* samples prepared for alkalinity resistance testing.

During testing the labels separated from the samples. Results are therefore presented as the mean and CoV of the mass before and after submersion for the un-activated and activated samples, as shown in Table 3.8.

Table 3.8: Alkalinity test results for *solid filament* samples.

Sample set	Initial average mass (g)	Initial mass CoV (%)	Final average mass (g)	Final mass CoV (%)	% mass loss
Un-activated	0.24	2.1%	0.20	4.5%	15%
Activated	0.09	5.9%	0.07	6.4%	18%

The mass loss observed in the *filament* samples was much higher than for the PET rods, 15-18% compared to 1.2-1.4%. This may be due to the higher surface area of the samples in relation to their mass. The variation in final mass was slightly higher than that of the initial mass in the *filament* samples, indicating that the mass loss across all samples was not equal. The activated samples showed a slightly higher mass loss compared to the un-activated samples; this was not, however, significant enough to conclude any change in the material's resistance to alkalinity.

The results show that the PET samples were affected by the alkaline solution, particularly reflected as a loss of mass in the *filament* samples. This agrees with studies by Silva et al. (2005) and Pelisser et al. (2012) on alkaline hydrolysis of PET fibres in concrete. As the pH of concrete decreases over its lifespan, the conditions within this test are conservative in comparison to what would be experienced by PET samples embedded within concrete. Nevertheless, these tests, and those within the literature, indicate that the PET *filaments* should be protected against the external concrete environment to ensure significant mass loss and a resultant loss in performance does not occur. A more detailed study of the rate of deterioration over time within alkaline environments should also form part of a follow-on study, as discussed in section 7.2.

3.7. CONCLUSIONS FROM CHAPTER 3

- To improve upon the concrete crack closure system presented by Jefferson et al. (2010), Dunn et al. (2011) and Isaacs et al. (2013), a polymer capable of producing larger restrained shrinkage stresses than previously observed in commercially-available PET *strip* samples was required. A high tensile strength and free shrinkage were also desirable properties.

- The restrained shrinkage stress of PET samples of varying cross-section and processing histories has been tested, resulting in the development of a high shrinkage PET *filament* which produces approximately double the restrained shrinkage stress potential, and exhibits 1.7 times the tensile strength, of commercially available *strip* samples. It was concluded from the results that the restrained shrinkage stress potential in drawn PET samples improved with increasing draw rate (attributed to increased orientation) and decreasing specimen cross-section (attributed to a reduction in the degree of crystallinity).

- The *filaments* exhibited a stress drop upon cooling not previously observed for drawn polymer samples. This is believed to be due to the reduction in entropic elasticity with falling temperature (for T below T_g) being greater than the increase in stress from restrained thermal contraction. It is concluded that the balance between these mechanisms is different in the PET *filaments* from that in the other materials tested, which may be a result of a higher degree of orientation causing a reduction in the coefficient of thermal expansion in the direction of drawing.

- The *filament* samples demonstrated higher free shrinkage than the *strip* samples, suggesting a lower sensitivity to relative displacements when placed within concrete samples as the restrained shrinkage stress is produced over larger displacements.

- The apparent Young's Modulus (E_{ap}) of the *filament* samples was significantly higher than the *strip* samples (16207MPa compared to 3601MPa at 30°C), and reduced with increasing temperature above the glass transition temperature T_g (approximately 70°C). The higher E_{ap} is attributed to a higher degree of orientation of the *filaments*, and it is suggested that the *strip* samples tested by Jefferson et al. (2010) and Dunn et al. (2011) may have been drawn at a higher draw ratio than the samples tested in the current thesis.

- *Filament* samples placed within a high alkalinity equivalent concrete pore solution (pH 13.4) for 1 month at 60°C experienced a significant mass loss of 15-18%. This is attributed to alkaline hydrolysis, as discussed by Silva et al. (2005) and Pelisser et al. (2012). It is therefore necessary to protect the *filaments* when placed into concrete, a system for which is discussed in more detail in section 4.3.

In addition to their improved shrinkage and tensile properties over the *strips*, the *filament* samples potentially offer a more practical solution for their use in larger concrete specimens. Where the *strips* were layered forming a rectangular cross-section, the *filaments* can be bundled into 'tendons' in a similar manner to steel pre-stressing strands for concrete (Emcocables, 2016), resulting in a circular cross-section which may improve their ease of use alongside steel reinforcement in structural concrete.

As a result of this programme of work, the PET *solid filament* samples were taken forward to develop an improved crack closure system for concrete structural elements, described in Chapter 4.

Chapter 4. Shape Memory Polymer Concrete Crack Closure System

4.1. INTRODUCTION

This chapter details the work undertaken to incorporate shape memory polymers into concrete as a crack closure system, using the PET strips and solid filament investigated in Chapter 3. Section 4.2 first builds on the work of Jefferson et al. (2010), Dunn et al. (2011) and Isaacs et al. (2013) by introducing layered PET strips into concrete beams to investigate their effect on autogenous self-healing. Section 4.3 then describes the development of a shape memory PET filament tendon capable of being activated via an electric current. In section 4.4 these tendons are incorporated into both unreinforced and reinforced concrete beams as a crack closure system. The tendons developed and tested within this chapter were then introduced into a full-scale trial structure along with autonomous self-healing systems, the details for which are included in Chapter 5.

4.2. PET STRIPS IN CONCRETE: CRACK CLOSURE AND ENHANCED AUTOGENOUS HEALING

As discussed in section 2.3.3, previous experiments concerning the use of shape memory polymers in cementitious materials considered the placement of PET strips in mortar beams of size 25x25x150mm (Jefferson et al., 2010, Dunn et al., 2011, Isaacs et al., 2013). Whilst successful healing was observed in all tests, there remained the question over the efficacy of the crack closure technique at a larger scale. To investigate the ability of the PET strips tested in Chapter 3 to close cracks and enhance autogenous healing within larger concrete beams, an experimental series was undertaken.

4.2.1. Compressive stress calculation for beam samples

Prismatic beam specimens of dimensions 500x100x100mm were cast. Each test sample contained layered PET strips of 32mm width, nominal thickness 0.046mm. The cross-sectional layout of the test samples is shown in Figure 4.1.

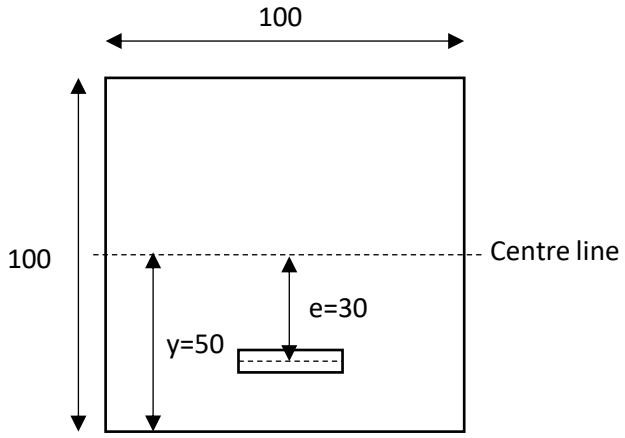

Figure 4.1: Cross-section of the PET strip test samples (dimensions in mm).

A compressive stress of 0.5MPa across a concrete crack face has been shown to improve strength recovery by autogenous healing (Heide and Schlangen, 2007). To account for uncertainty in upscaling the PET system, it was decided to multiply this requirement by a factor of two, therefore the required number of strips and their eccentricity (e) from the centreline to produce a stress of 1MPa on the bottom face of the beam upon activation was calculated. The compressive stress σ_c on the outer fibre of the compression face of a beam from statics can be expressed as shown in (2).

$$\boldsymbol{\sigma_c = \frac{F_P}{A_C} + \frac{F_P \cdot y \cdot e}{I_C}} \qquad (2)$$

Where F_p is the force provided by the activated polymer, A_C and I_C are the cross-sectional area and second moment of area of the concrete respectively, and y and e are as shown in Figure 4.1. The terms in (2) can be expressed as equations (3) to (5) as follows:

$$\boldsymbol{F_p = \sigma_p \cdot A_p} \qquad (3)$$

$$A_c = b \cdot h \quad (4)$$

$$I = \frac{b \cdot h^3}{12} \quad (5)$$

Where σ_p is the restrained shrinkage stress, A_p is the area of the polymer and b and h are as shown in Figure 4.1. Equation (2) can therefore be written as equation (6).

$$\sigma_c = \frac{\sigma_p \cdot A_p}{b \cdot h} + \frac{\sigma_p \cdot A_p \cdot y \cdot e}{\frac{b \cdot h^3}{12}} \quad (6)$$

The values for each of these parameters are shown in Table 4.1. Experiments in Chapter 3 on 10 layered strips produced an average restrained shrinkage stress of 24.02MPa. Preliminary restrained shrinkage tests were also carried out on 20 and 40 layered strips, with stresses of 24.22MPa and 24.18MPa produced respectively. It was therefore assumed that increasing the number of layered strips does not affect the restrained stress produced.

Table 4.1: Parameters used for PET strips in concrete beams to calculate applied stress.

h (mm)	b (mm)	y (mm)	e (mm)	σ_p (MPa)	A_p (mm²)
100	100	50	30	24.0[1]	147.2[2]

[1]From results of experiments in Chapter 3
[2]Nominal area from one hundred layered PET strips

The number of layered strips and the eccentricity were adjusted until the target theoretical compressive stress σ_c of 1MPa was achieved. One hundred PET strips were therefore placed at an eccentricity of 30mm in the beam.

4.2.2. Internal and external anchorage

To anchor the strips within the concrete beams, a bolted plate system was used (a larger version of 'anchorage 2' discussed in section 3.3.1), comprising two steel plates (50 x 25 x 5mm) with a 4mm bolt positioned either side of the PET strips as shown in Figure 4.2. The PET strips were fed through the plates, the bolts tightened and the strip ends melted to form a plug.

Figure 4.2: PET strip anchorage arrangement.

Two arrangements of PET strips were used within the test beams, shown in

Figure 4.3: internal, in which the strips and steel plates were entirely embedded within the concrete beam; and external in which the steel plates protruded out of the ends of the beam, and rested against the external face at both ends. Internal anchorage was recognised as the preferred option to avoid the polymer material extending beyond the dimensions of a beam. However, externally anchored strips were required to enable the strips to be removed prior to final loading, to isolate any load recovery due to autogenous crack healing in the beams.

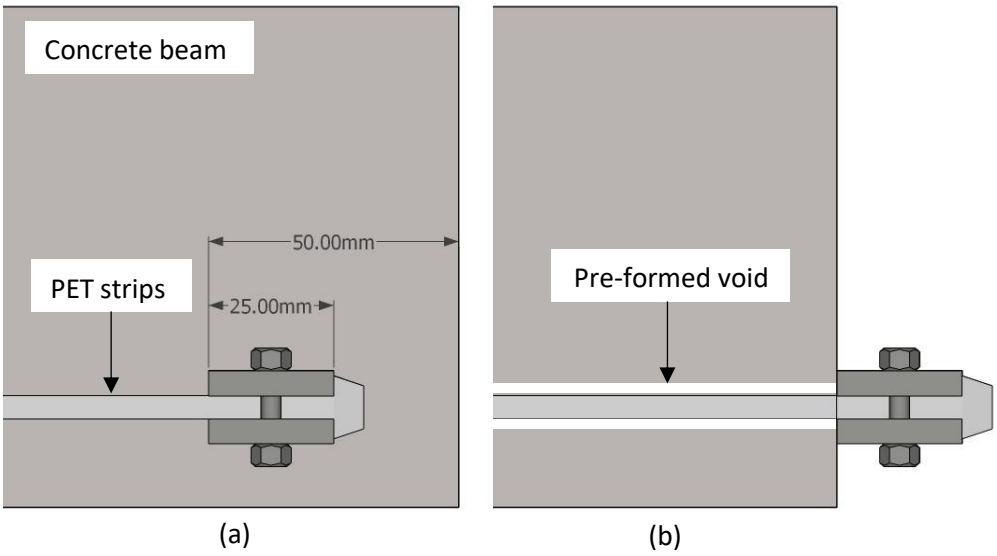

Figure 4.3 Arrangement of (a) Internally anchored PET strips and (b) Externally anchored PET strips in concrete beam samples. Both ends of the PET were anchored using the same method.

The externally anchored strips were placed through a pre-formed void in the concrete. The void was formed using polystyrene strips placed before casting. The polystyrene was dissolved using

acetone 1 day after casting, allowing the PET strips to be fed through and anchored at either end.

Experiments conducted by Jefferson et al. (2010) concluded that to function correctly as a crack closure system, the PET strips must be de-bonded over the length of the beam. This is to ensure there are no instances of excessive strain in the polymer caused by the strips forming a bridge over a crack. Consequently, in order to provide an internal anchor for the PET strips a de-bonding system was required.

Preliminary test beams were cast to trial two methods of de-bonding: cling film coated in mould releasing oil, and petroleum jelly applied directly to the polymer. Results showed that using the cling film worked well, allowing crack closure to take place upon activation and showing clear de-bonding of the strips upon fracture of the beam samples as shown in Figure 4.4. The petroleum jelly samples did not fully de-bond and resulted in no crack closure. The cling film and releasing oil was therefore used to internally de-bond the PET strips within beams.

(a)

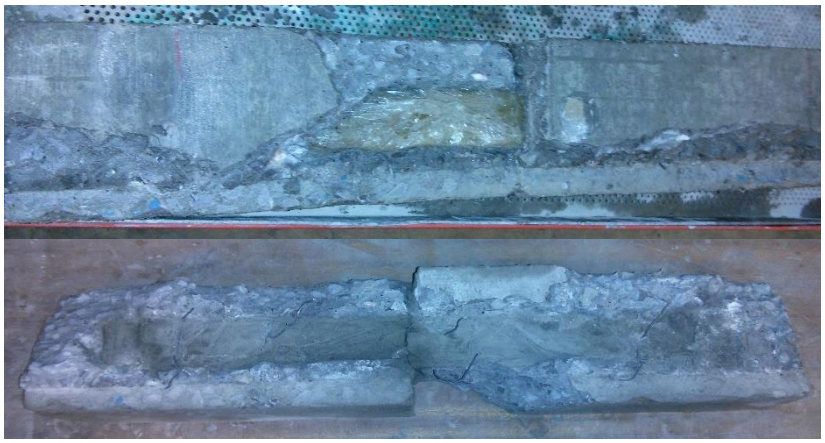

(b)

Figure 4.4: (a) PET strip sample wrapped in cling film and coated in releasing agent for de-bonding; (b) Successful de-bonding of PET sample as demonstrated upon fracture of concrete beam.

4.2.3. Experimental set-up

Each set of concrete beams consisted of three internally anchored PET test beams (PET), three externally anchored PET test beams (PETr) and three control samples (Control). The cross-sectional layouts of the beam samples can be seen in Figure 4.5.

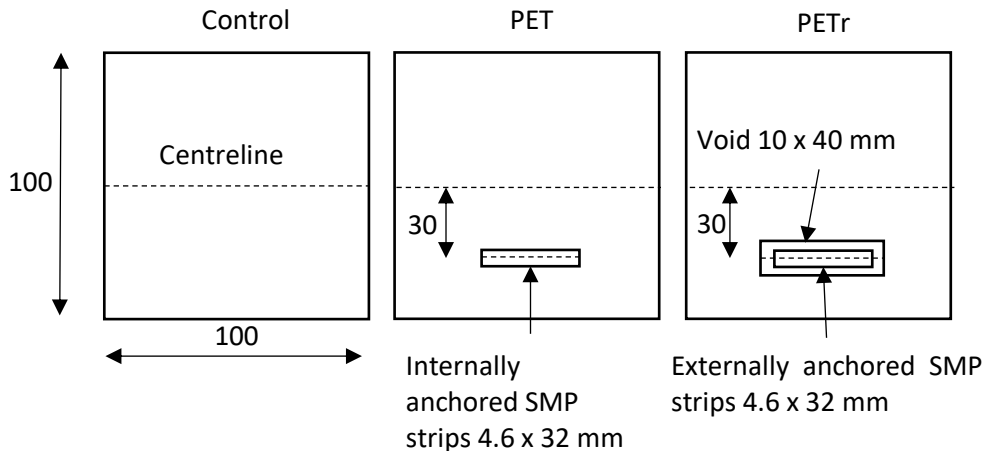

Figure 4.5: Cross-sections of the beam samples used within PET strip tests.

The internally anchored strips were layered and clamped at the ends before being placed within wooden beam moulds and de-bonded using cling film as previously described. Steel tie wire was tied around the steel plates, passed through a hole in the end of the beam mould and tightened against the end of the mould. This was repeated on both ends of the polymer to ensure there was no slack prior to casting.

For the externally anchored PET strips, the concrete beams were cast with a void as described previously. The strips were layered and clamped at one end using the steel plates. The loose end of the polymer was then fed through the void in the concrete. The strips were pulled taut by hand and clamped at the loose end using the steel plates. The set-up of the beam samples prior to casting can be seen in Figure 4.6.

Figure 4.6: (a) PET beam sample set-up (white tape was removed before casting); (b) PETr beam sample set-up (with polystyrene void-former).

4.2.4. Concrete mix design

The nominal concrete mix design used for all beam and cube samples is shown in Table 4.2. The mix was designed to achieve a consistency of class S3 (100-150 mm slump) to BS EN 206:2013 (BSI, 2013) and a target compressive strength of 53MPa at 28 days that corresponds to a C35/45 strength class (Fib, 2010). The actual quantities of aggregates, water and admixture used were adjusted for each cast based on the water absorption of the aggregates and the aggregate water content (tested before each cast) to maintain a water-cement ratio (w/c ratio) of 0.48. The range of actual mix proportions used within these experiments is shown in

Table 4.3.

Table 4.2: Nominal concrete mix design (saturated surface dry quantities).

Cement (kg/m^3)	w/c ratio	Coarse aggregate (kg/m^3)	Fine aggregate (kg/m^3)	Limestone dust (kg/m^3)	Water (kg/m^3)	Admixture (kg/m^3)
400	0.48	990	648	162	192[1]	1.75[2]

[1]Nominal SSD quantity, actual added water adjusted according to aggregate water content
[2]Plasticiser was added to reach the target slump range in amounts not exceeding 1.75kg/m^3

Table 4.3: Range of actual concrete mix proportions used.

Cement (kg/m^3)	w/c ratio	Coarse aggregate (kg/m^3)	Fine aggregate (kg/m^3)	Limestone dust (kg/m^3)	Water (kg/m^3)	Admixture (kg/m^3)
400	0.48	984.7-986.5	648.3-653.7	161.2-161.8	190.6-197.0	1.03-1.75

Coarse aggregate consisted of 4-10mm diameter limestone. Fine aggregate used was 0-4mm diameter natural sea-dredged sand from Swansea Wharf and 0-2mm diameter limestone dust sieved from 0-4mm diameter limestone aggregates. All of the limestone was sourced from Cornelly Drystone Quarry in Porthcawl, South Wales. The aggregate grading results from the supplier are included as Appendix B. The cement used was CEM II/B-V 32,5R with 21-35% Fly Ash content, consistent with BS EN 197-1 classifications. This was sourced from Lafarge Tarmac.

The concrete was mixed using a Belle Group Premier 200XT concrete mixer before being tested for consistency using a standard slump test. Adomast Adoflow Extra plasticiser was added to the mix after all other constituents to reach the target slump range, in amounts not exceeding 1.7 kg/m^3.

This mix was used for the current experimental series and in the PET filament tendon experiments described in section 4.4. The results of compressive strength and consistency tests are included in section 4.2.7 (for the PET strips tests) and section 4.4.4 (PET filament tendon tests).

4.2.5. Experimental methodology

Table 4.4 shows the sample designations and testing sequence used. Enhanced autogenous healing was investigated over one month (sample_35), three months (sample_91) and six months (sample_175). All PET/PETr beams were loaded on day 7 to a CMOD of 0.5mm, immediately followed by activation of the PET. Final loading then took place after the designated healing period in which the beams were submerged in water at 20°C. For each series, three control samples were loaded to failure at 7 days and three at the final loading stage. The beams in the Control_c35 series were also loaded to a CMOD of 0.5mm and submerged along with the PET/PETr beams, to later test for the occurrence of autogenous healing after 1 month.

Table 4.4: Enhanced autogenous healing samples.

Series	Sample notations	Total No. of beams	Initial loading - day 7 (number of samples)	Activation on day 7	Final loading or reloading (number of samples)
1-month healing	Control_c35	3	0.5 mm CMOD (3)	No	Reload to failure (3)
	Control_35	6	to failure (3)	No	Load to failure (3)
	PETr_35	3	0.5 mm CMOD (3)	Yes	Reload to failure (3)
	PET_35	3	0.5 mm CMOD (3)	Yes	Reload to 1mm CMOD (3)
3-month healing	Control_91	6	Load to failure (3)	No	Load to failure (3)
	PETr_91	3	0.5 mm CMOD (3)	Yes	Reload to failure (3)
	PET_91	3	0.5 mm CMOD (3)	Yes	Reload to 1mm CMOD (3)
6-month healing	Control_175	6	Load to failure (3)	No	Load to failure (3)
	PETr_175	3	0.5 mm CMOD (3)	Yes	Reload to failure (3)
	PET_175	3	0.5 mm CMOD (3)	Yes	Reload to 1mm CMOD (3)

All beam samples were cast using wooden moulds and compacted in three layers using a vibrating table. The moulds were removed 24 hrs after casting and the beams submerged in water at 20°C.

One day prior to initial loading, the beam specimens were removed from the water and a 5mm crack-inducing notch at mid-span was created. Knife edges were attached to the bottom of the beams either side of the notch to allow the crack mouth opening displacement (CMOD) to be measured using a clip gauge, as shown in Figure 4.7(a). An Avery-Denison testing rig was used to load the beams in 3-point bending, the set-up for which is shown in Figure 4.7(b) and Figure 4.8.

(a) (b)

Figure 4.7: (a) Notched beam specimens prior to testing; (b) Beam testing set-up in Avery Denison machine.

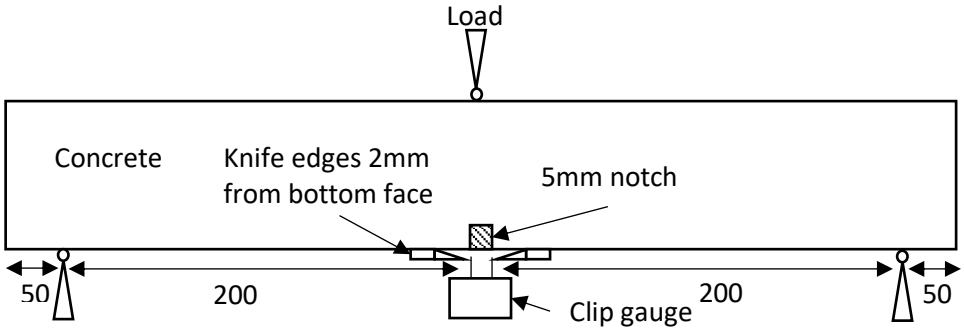

Figure 4.8: Three-point bend test set-up (dimensions in mm).

Initial loading consisted of a 3-point bend test, controlled by CMOD at a rate of 0.001mm/s. While Jefferson et al. (2010) performed the initial loading tests on mortar beams at an age of 4 days after casting, testing at 7 days reduces the effect of continued hydration on any observed load recovery. Later initial testing also reduces the effect of strength gain in the un-cracked concrete section during the healing period, an effect which has been commented upon by Davies (2014).

Activation of the PET strips in the PET and PETr specimens, after initial testing, was achieved by placing the beams in an oven at 90±5°C for 18 hours, following the process adopted by Jefferson et al. (2010). Experiments by Selvarajoo (2015) in which thermocouples were cast into beam samples, which were then placed into an oven set to 90±5°C showed that 90±5°C was achieved at the position of the polymer after only 4 hours, confirming that an 18-hour heating period was more than sufficient to activate the SMP strips. The effect of this heating period on the strength of the concrete was tested by heating cube samples, the results of which are discussed in section 4.2.7.

After activation, the beams were allowed to cool in air to room temperature before being placed back into curing tanks at 20°C. After the chosen healing time (1, 3 or 6 months), the beams were removed and reloaded to failure (in the case of PETr beams) or to 1mm CMOD (in the case of

PET beams). Control_c35 was also reloaded to provide a comparison against autogenous healing without PET. All other controls were tested as virgin samples (not previously loaded).

4.2.6. Measurements

Load recovery

During loading the CMOD (mm), and load (kN) were recorded at a rate of 1Hz. The data recorded during the initial and final loading stages were used to calculate the load recovery of the specimens and to measure autogenous healing efficiency. Figure 4.9 shows idealised loading curves from the three-point bending tests. Equation (7) was used to calculate load recovery for the Control and PETr specimens.

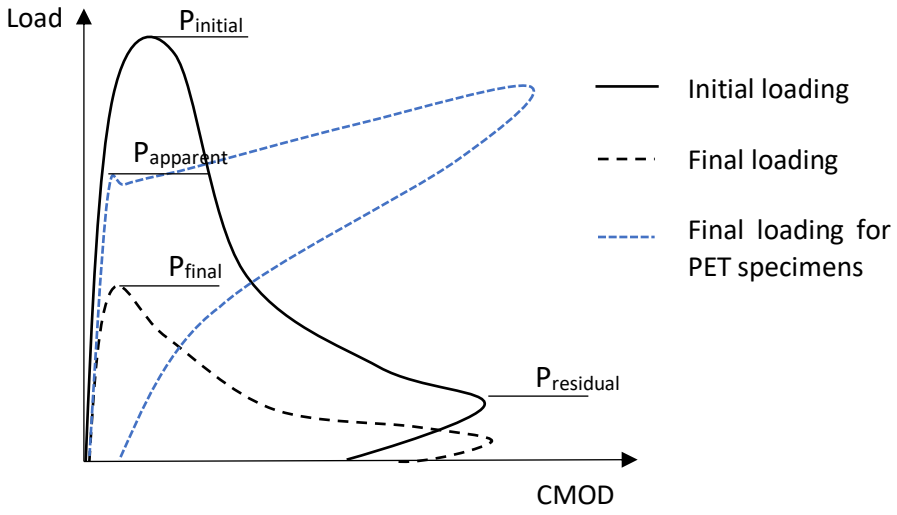

Figure 4.9 Idealised loading curve for load recovery calculation.

$$\boldsymbol{LR}\% = \frac{\boldsymbol{P_{final} - P_{residual}}}{\boldsymbol{P_{initial} - P_{residual}}} \text{ x } \mathbf{100} \qquad (7)$$

The load recovery for the PET specimens cannot be directly calculated as the activated SMP tendon acts as tensile reinforcement. An apparent load regain calculation has therefore been introduced, shown in equation (8). The $P_{apparent}$ is taken as the first load peak observed in the reloading cycle as shown in Figure 4.9.

$$LR_{apparent}\% = \frac{P_{apparent}}{P_{initial}} \text{ x } 100 \qquad (8)$$

Crack measurements

Images of the cracks were taken on both sides of the beams using a Veho Discovery VMS-001 USB microscope with a graduated scale. Three sets of images were captured for the PET, PETr and control_c35 samples: after initial loading, after activation (excluding the control) and immediately prior to final loading. From each image, three crack width measurements 0.75mm apart were made perpendicular to the crack face using ImageJ software (ImageJ, 2016), as illustrated in Figure 4.10. ImageJ allows the calibration of an image's scale based on a reference length within the image, provided in this case by the graduated scale. Distances within the same image can then be measured using the calibrated scale. The average result of crack measurements on both sides of the beam was used in crack reduction calculations.

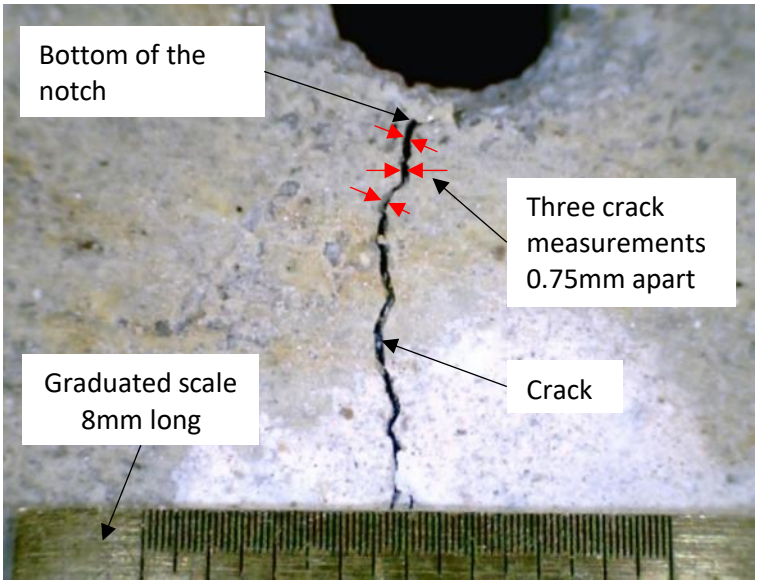

Figure 4.10 Crack measurement using microscope.

4.2.7. Results and discussion

Compressive strength and consistency class

Table 4.5 shows the concrete compressive strength results for all ages at which the beam specimens were tested, for two curing regimes. The 'Water' specimens were submerged at 20°C after demoulding until the age of testing. The 'Heated' specimens were also submerged after

demoulding, then heated for 18 hours at 90±5°C on day 7 after casting, before being allowed to cool to room temperature and returned to the water tank until the age of testing was reached. This was to replicate the heating regime used to activate the PET strips in the PET and PETr specimens.

Table 4.5: Concrete compressive strength results.

Curing regime	Age (days)	Compressive strength (MPa)	Coefficient of variation (%)
Water	7	38.82	5.5
	35	53.62	1.4
	91	58.87	3.5
	175	70.93	3.3
Heated	35	54.47	3.1
	91	54.57	2.3
	175	62.73	2.9

It can be seen from Table 4.5 that the compressive strength of the heated concrete is similar to that of the water-cured concrete samples at 35 days, but is lower by 4.3MPa and 8.2MPa for 91 and 175 days respectively. The relationship between age of concrete, temperature and compressive strength is complex, depending on the concrete mix constituents as well as the whole temperature history from casting until the time of testing (Neville and Brooks, 2010). As such, a detailed discussion is outside the scope of this thesis. These results do, however, provide evidence as to why a direct heating system for the polymers would be preferable, discussed further in section 7.2.

The measured slump of the mix ranged from 100-140mm throughout the samples cast, all falling into consistency class S3 (BSI, 2013).

Crack closure

Typical microscope images of the PET_35, PETr_35 and Control_c35 beams from the 1-month series are shown in Figure 4.11 to Figure 4.13. It can be seen that the cracks in the control samples in Figure 4.11, while appearing smaller, are still clearly visible after 28 days of healing.

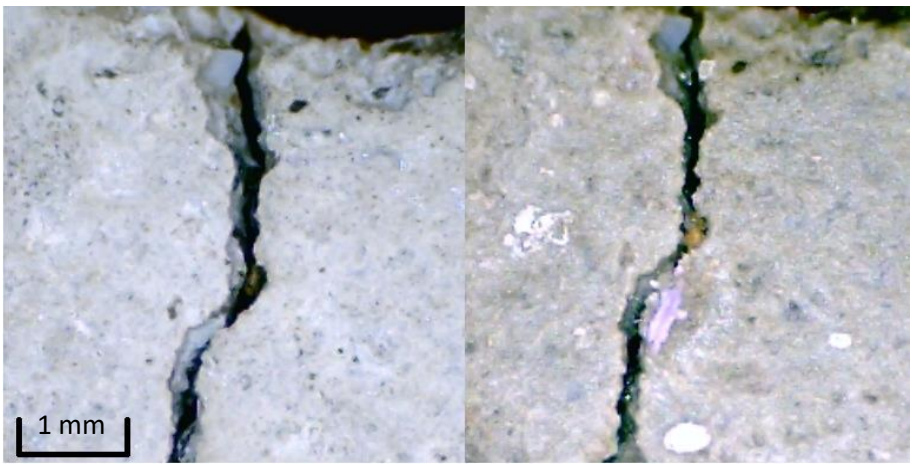

(a) (b)

Figure 4.11: Typical Control_c35 (1-month) specimen crack microscope image – (a) after initial loading; (b) before final loading.

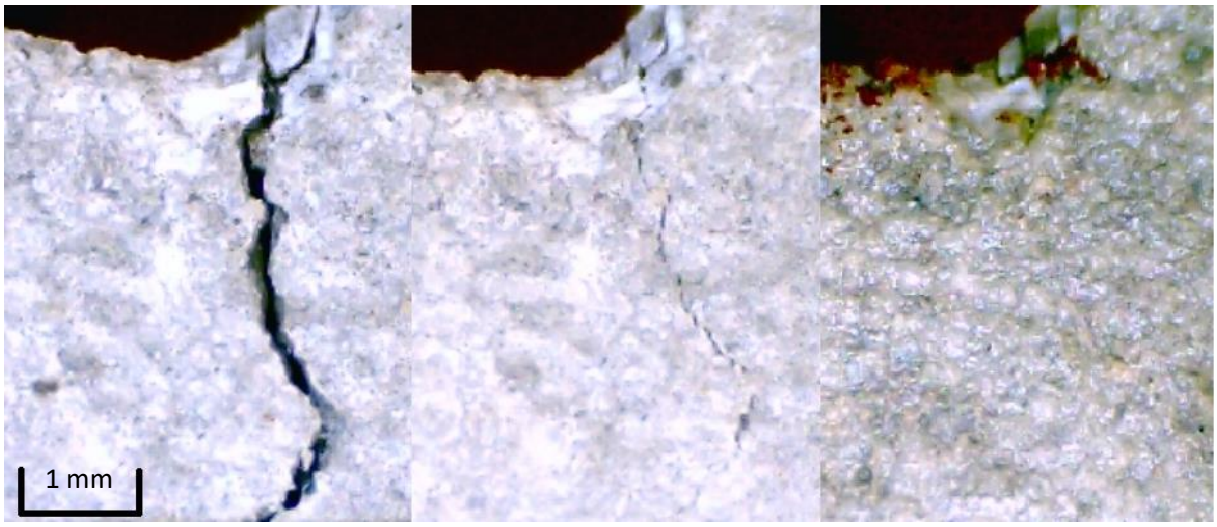

(a) (b) (c)

Figure 4.12 Typical PETr_35 (1-month) specimen crack microscope image – (a) after initial loading; (b) after activation; (c) before final loading.

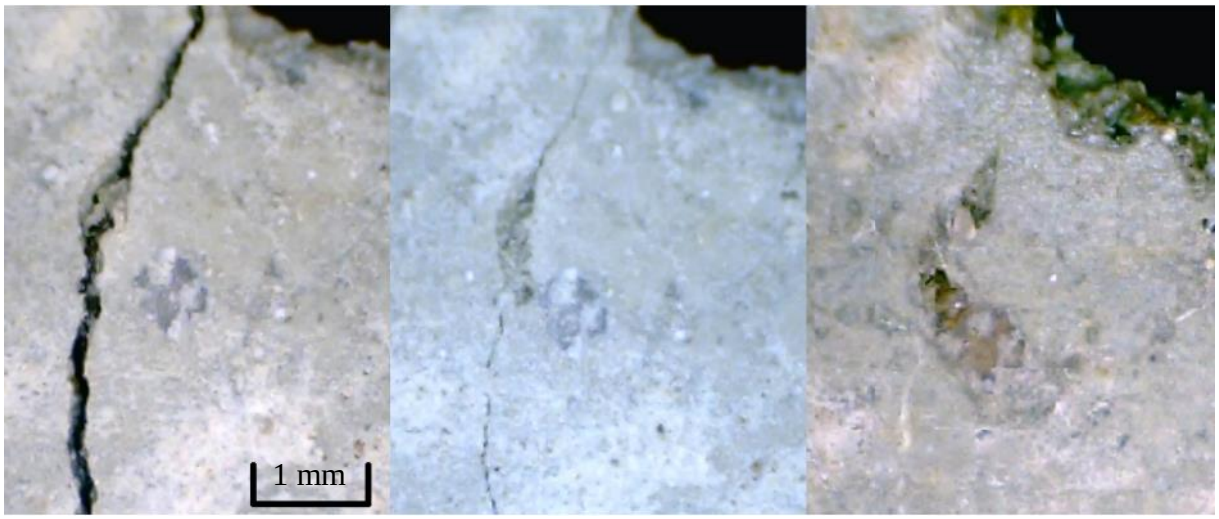

(a) (b) (c)

Figure 4.13 Typical PET_35 (1-month) specimen crack microscope image - a) after initial loading; b) after activation; c) before final loading.

Figure 4.12 and Figure 4.13 show a significant reduction in crack size for the PET and PETr samples after the SMP activation. This suggests that the SMP strips are performing as intended, providing a compressive stress on the concrete. A small residual crack can be seen in Figure 4.12(b) and Figure 4.13(b), which may be explained by the presence of debris in the crack plane during the initial loading process that is wedging the crack open, and a slight misalignment of the crack planes upon crack closure.

In most of the PET/PETr specimens, after the prescribed healing time the cracks were either fully closed and were not visible, as shown in Figure 4.12(c), or a white precipitate was visible in the location of the original crack, as shown in Figure 4.13(c). This suggests that after activation the width of the cracks is sufficiently small to allow autogenous healing to fill the crack surface.

Figure 4.14 and Figure 4.15 show the results of crack width measurements from microscope images on both sides of all beams for the 1-month healing series. The residual crack width after initial loading in the Control_c35 series (Figure 4.14) was in the range of 0.169 to 0.239mm, with an average width of 0.209mm. Experiments by Chen and Su (2013)found the characteristic crack opening (at which the cohesive stress/load bearing capacity of the concrete is 0) of different strength concrete mixes to vary from 0.165 to 0.240mm. This suggests that the Control_c35 samples were near to failure after initial loading. After 28 days of immersion in a water tank the measured crack widths had reduced to 0.098 to 0.205mm with an average width of 0.139mm.

The reduction in crack width suggests that some autogenous healing has taken place. While sources within the literature typically suggest a maximum crack width for full autogenous healing in cementitious samples as anywhere between 0.050-0.250 mm (Yang et al., 2011, Edvardsen, 1999, De Rooij et al., 2013), it is clear that in this case only partial healing has occurred. The majority of these sources, however, discuss experiments on mortar beam samples, as discussed in section 2.2. The inclusion of coarse aggregate in the current samples reduces the proportion of cement paste on the crack face compared to mortar beam samples, thereby reducing the potential for autogenous healing.

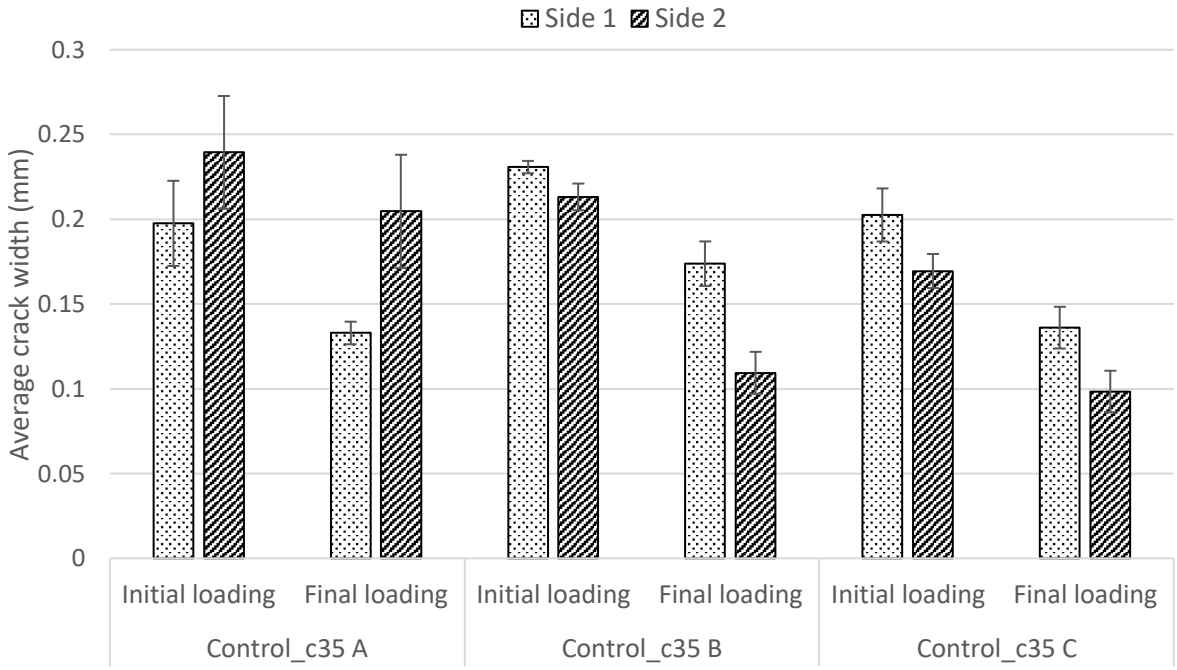

Figure 4.14 Crack width measurements for Control_c35 series beams.

The observed healing was not equal on both sides of the beam. This was in part due to the different width of the cracks, but may also be a result of the non-heterogeneous nature of concrete, particularly in the distribution of aggregates which may have an effect on healing potential.

Figure 4.15 shows the PET/PETr series crack width measurements for the one month healing samples after initial loading. The range of residual crack widths after initial loading for PET/PETr specimens was 0.036 to 0.221 mm with an average measurement of 0.164 mm, 21.5% lower than that of the control specimens. Similar results were observed in the 3 and 6 month healing series, with average crack widths of 0.135mm and 0.185mm respectively. This is due to the SMP strips present in PET/PETr specimens acting as tensile reinforcement during initial loading.

Generally, lower initial crack widths are observed in the PET compared to the PETr specimens. This is caused by the slightly higher reinforcing action provided by the embedded SMP strips in PET beams when compared to the externally anchored strips in the PETr beams. The embedded strips were tensioned using steel wire before casting the samples, whereas the externally

anchored strips were installed after the beam had been cast and, despite being pulled taut against the external faces, could experience small displacements relative to the beam.

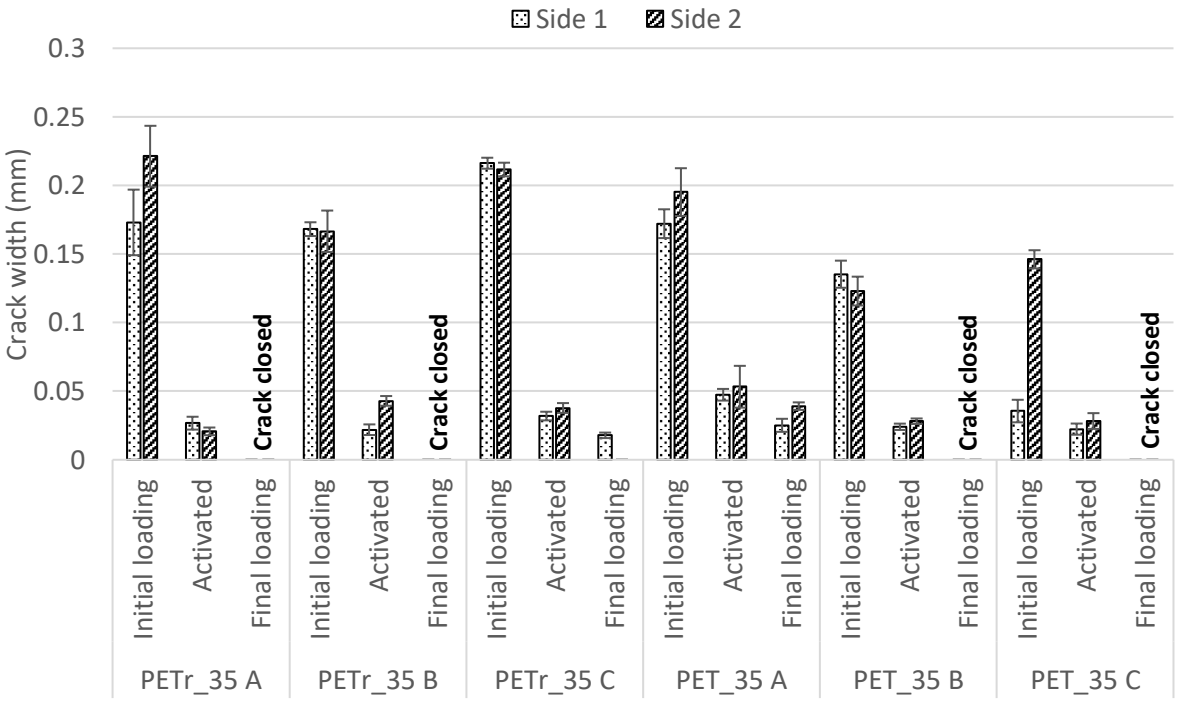

Figure 4.15 Crack width measurements for PET_35 and PETr_35 series beams.

Figure 4.15 shows that upon activation of the SMP tendons the cracks were reduced to an average width of 0.032mm, and that after 28-day healing in four of the six beams the cracks were fully closed, with an average crack width of 0.07mm measured over all beams.

There was a significant amount of variation in the residual crack widths produced by initial loading, assumed to be due to the non-heterogeneous nature of concrete and the difference in reinforcing action between the PET and PETr specimens, as discussed. Upon activation, however, the crack widths reduced to a similar level in all samples.

The crack width average measurements and crack width reductions have been summarised in Table 4.6. The crack width reduced by 33% in the control specimens compared to 96% in PET/PETr samples after one month of healing. The one, three and six month results of PET/PETr specimens show that the crack closure observed by microscope images is similar at all ages studied, giving an average of 78% crack width reduction upon activation and 95% crack width

reduction after healing. This suggests that for the studied crack range (after activation), autogenous healing fills the crack surface within the first 28 days.

Table 4.6: Average crack width measurements and reduction values.

Specimen series	Healing time	Average crack width (mm)			Crack reduction (%)	
		Initial	Activated	Final	Activated	Final
Control_c35	1 month	0.209	-	0.139	-	33
PET/PETr_35	1 month	0.164	0.032	0.007	77	96
PET/PETr_91	3 month	0.134	0.029	0.010	75	91
PET/PETr_175	6 month	0.185	0.029	0.009	83	96
PET/PETr average	All	0.161	0.030	0.009	78	95

From these results it can be concluded that the SMP system reduces the width of the initial crack, formed at 7 days, to a width at which autogenous healing mechanisms are capable of fully sealing the crack within 28 days, as observed by microscope measurements of the crack surface. This would potentially be beneficial in sealing early-age cracks in concrete structures. The following section examines the load recovery observed in the samples.

Load recovery

Figure 4.16 to Figure 4.18 show typical load versus CMOD plots for the three specimen series for 1 and 6 months of healing. Graphs of all load recovery results are included as Appendix C.

The Control_c35 specimens demonstrated minimal load recovery upon reloading after 1 month of healing. The peak load during final loading can be found at approximately 0.2mm CMOD as shown in Figure 4.16. In comparison, the PETr series show a prominent peak around 0.01 to 0.03mm CMOD, as shown by Figure 4.17, indicating a brittle failure response. This can be attributed to autogenous healing causing a bridging of the crack faces and a corresponding recovery in load capacity of the concrete in the latter specimens. Upon reloading of the control specimens, a brittle failure response is not observed, however there is a small increase in peak load compared to the residual load recorded during the initial loading stage. This suggests that

while substantial bridging of the crack did not occur on the bottom face of the beam, some autogenous healing may have taken place deeper within the crack, where the crack width is much smaller than at the location measured using the microscope.

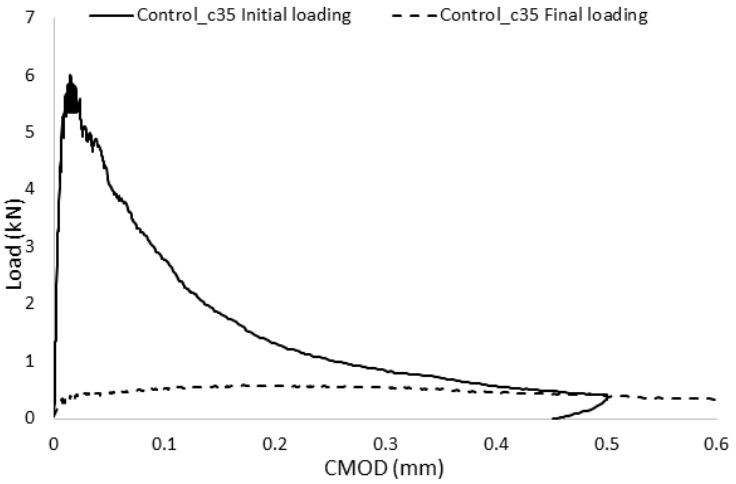

Figure 4.16 Typical Control specimen load vs CMOD plot – 1-month healing.

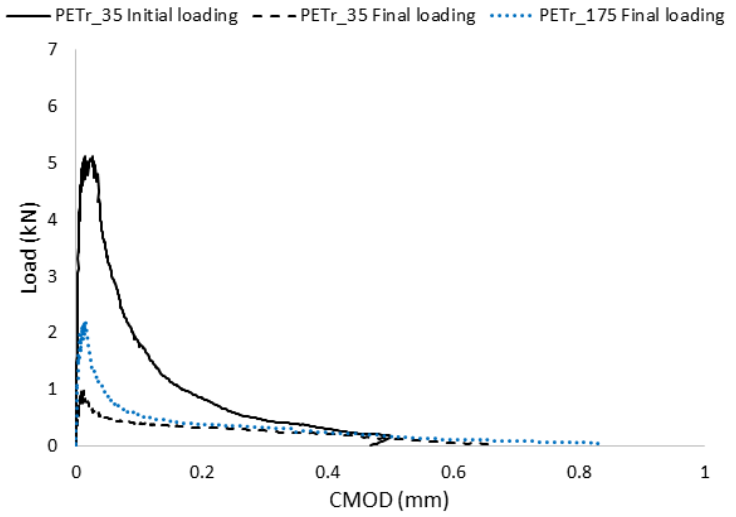

Figure 4.17 Typical PETr specimen load vs CMOD plot – 1 month (PETr_35) and 6 month (PETr_175) healing.

Figure 4.18 shows that the embedded SMP strips during initial loading provide some reinforcement to the beam as the load CMOD curve reaches a plateau after 0.4mm CMOD. Furthermore, upon unloading the residual crack is smaller than those observed in the control and PETr series beams. This was also confirmed by microscope image measurements.

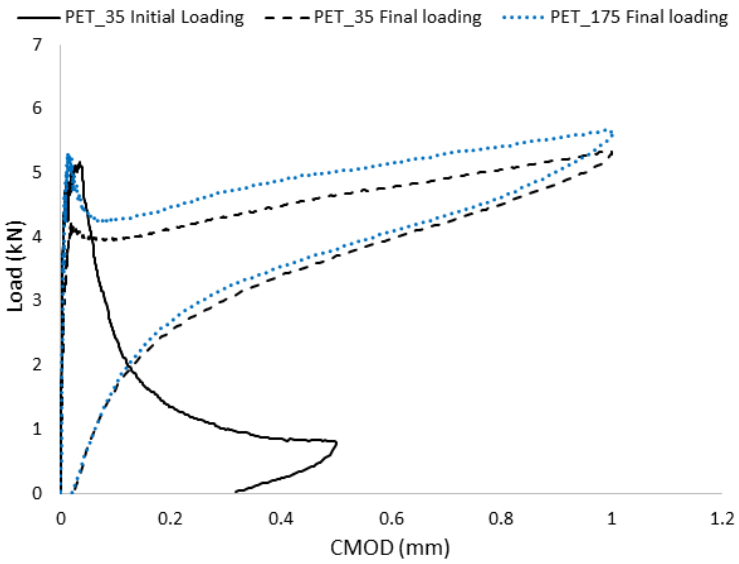

Figure 4.18 Typical PET specimen load vs CMOD plot – 1 month (PET_35) and 6 month (PET_175) healing.

During the final loading phase PET specimens exhibit an apparent peak in the 0.01mm to 0.03mm CMOD range followed by a change in the stiffness and linear elastic response until 1mm CMOD is reached. The load reached at the apparent peak for PET specimens is significantly higher than the peak loads observed in the PETr specimens. This suggests that there are two factors that simultaneously affect the apparent peak during final loading phase: strength recovery due to autogenous healing and the compressive force provided by the SMP strips that counteract the applied load. The brittle response demonstrated by the clear peak in the load-CMOD curves for both the PET and PETr samples indicates that load recovery has been achieved in the concrete. The contribution of the compressive stress applied by the strips in the PET beams is discussed in section 4.2.8. The residual crack after final unloading as measured by the CMOD in these specimens does not exceed 0.1mm, indicating that the PET strips are acting elastically during the final loading period and only a small amount of plastic deformation has occurred.

A clear increase in peak load can be seen in the PET and PETr samples between 1 and 6 months of healing. This corresponds to an average increase in load recovery from 14.1% after 1 month to 33.3% after 6 months in the PETr samples, and 65.9% after 1 month to 98.1% after 6 months in the apparent recovered load of the PET samples. This increase is seen despite the microscope

measurements showing a full closure after 1 month. This strength regain can therefore be attributed to further healing deeper within the crack, an increase in strength over time of the material bridging the crack faces, an increase in strength of the interface between the healed material and the original crack faces or a combination of these factors. This agrees with micromechanical observations of autogenous self-healing made by Davies (2014).

It can be seen that the initial loading peaks of PET/PETr series are lower than those of the control. The reduction in concrete cross-sectional area was 1.5% for the PET samples and 4% for the PETr samples, resulting in an average reduction in initial peak load of 8% and 9% respectively.

The average peak load, residual load and load recovery data for all specimen series have been summarised in Table 4.7. The Control_c35 series showed a 4.2% load recovery whereas the PETr_35 specimens healed for 1 month achieved 14.1% load recovery. The 9.9% higher load recovery for PETr_35 specimens demonstrates the effect of the SMP strips on enhancing autogenous healing by reducing the crack width (from 0.164mm average to 0.032mm average) and providing compressive stress on the crack plane during healing. The reduced crack width is well within the range at which full autogenous healing has been observed by numerous studies within the literature, discussed in more detail in section 2.2.3 (De Rooij et al., 2013, Edvardsen, 1999, Wiktor and Jonkers, 2011).

Table 4.7 Average peak load values and load recovery.

Specimen series	Initial loading peak (kN)	Residual load (kN)	Final loading peak (kN)	Load recovery (%)
Control_c35	6.03	0.37	0.60	4.2
Control_35	5.63	-	6.35	-
PETr_35	5.01	0.36	1.02	14.1
PET_35	5.04	0.67	3.32[a]	65.9[b]
Control_91	6.18	-	8.29	-
PETr_91	5.75	0.21	1.25	18.8
PET_91	5.97	0.58	4.93[a]	82.6[b]
Control_175	5.73	-	7.58	-
PETr_175	5.35	0.35	2.01	33.3
PET_175	5.25	0.60	5.15[a]	98.1[b]

[a] - apparent peak value as shown in Figure 4.9

[b] - apparent load recovery according to equation (8)

Isaacs et al. (2013) undertook experiments using shape memory PET strips with small mortar specimens cracked at 4 days and retested at 8 days. In their experiments, 79% load recovery was observed for PETr specimens and 127% for PET specimens activated in an oven before being submerged in water. The lower load recovery results for the current experiments could be attributed to several factors: later age of initial cracking; use of concrete instead of mortar resulting in a larger proportion of aggregate particles and possibly lower quantities of unhydrated cement on the crack face; larger initial crack sizes and the use of a load recovery formula which incorporates the residual strength left in the beams after initial cracking.

Images were taken of the crack planes after final loading of the specimens as shown in Figure 4.19. In the control_35 specimens, which were not previously cracked and were loaded until failure after a 35-day curing period, the crack face shows grey cement paste with inclusions of sand and coarse aggregate. In contrast, on the crack plane of the control_35c specimen, which was cracked on day 7 then submerged in water for 28 days, white precipitate around the edges exposed to water can be seen. This suggests calcite precipitation due to autogenous healing (De Rooij et al., 2013). However, this was insufficient to provide substantial load recovery and sealing of the crack. The crack face of the PETr_35 beam is fully covered in white precipitate with the exception of the exposed aggregate particles. These observations illustrate that the SMP strips have reduced the crack width to a size that enhances the autogenous healing of the concrete beams.

(a) (b) (c)

Figure 4.19 Crack plane images. (a) control_35c; (b) control_35; (c) PETr_35.

These results show that enhanced autogenous self-healing of concrete beams has been achieved using shape memory polymer strips to produce a compressive stress onto the crack faces. This healing has been measured as visual crack closure and mechanical load recovery that increases with longer healing periods. They also suggest that mortar beam experiments cannot be assumed to be representative of concrete mixes with larger aggregate particles when considering autogenous healing as the presence of these particles reduces the area of the crack face with the potential to self-heal.

Both the PET and PETr beams showed an increase in load recovery (or apparent load recovery) with increasing healing time from 1 to 6 months. This suggests that the PET strips did not lose significant restrained shrinkage stress over time, instead keeping the beams under compression and allowing autogenous healing to take place throughout the healing period.

4.2.8. Polymer restrained shrinkage stress within beam samples

The restrained shrinkage stress generated by the polymer strips inside the beams can be calculated from the load-CMOD reload curves of the PET and PETr beams after activation.

The final peak load values for the PET beams quoted in Table 4.7 can be divided into two parts: the applied load acting against the compressive stress generated by the PET strips, and the additional load capacity of the concrete beam due to autogenous healing. If it is assumed that the percentage load recovery due to autogenous healing in the PET beams is equal to the load recovery within the PETr beams of the same series, the assumed load recovery in kN can be calculated (as P_{final}) from equation (7) using the $P_{initial}$ and $P_{residual}$ values from Table 4.7. The remaining peak load (the final peak load from Table 4.7 less the assumed load recovery) can be used to calculate the compressive stress produced by the PET strips. This remaining peak load will be termed the polymer compressive load.

At the polymer compressive load, it is assumed that the applied stress at the extreme fibre is

directly counteracted by the compressive stress generated by the polymer tendon. This stress, calculated from the applied moment using equation (9), can therefore be used to calculate the force F_P provided by the activated polymer, and equation (3) used to calculate the restrained shrinkage stress σ_P of the polymer using the polymer area A_P. Table 4.8 shows the calculated restrained shrinkage stress values for the three PET samples using this method.

The applied moment M is calculated as $\mathrm{M} = \mathrm{P} \cdot \frac{\mathrm{L}}{4}$, where P is the polymer compressive load and L is the length between supports (400mm). It should be noted that the distance y between the neutral axis and the extreme fibre of the concrete beam was calculated from equivalent moments of area assuming a cracked linear elastic section.

$$\boldsymbol{\sigma = \frac{M \cdot y}{I_C}} \qquad (9)$$

Table 4.8: Calculated restrained shrinkage stress of PET strips within concrete beams.

Specimen series	Final peak load (kN)	Residual load (kN)	Assumed load recovery due to healing (kN)[1]	Polymer compressive load (kN)[2]	Calculated restrained shrinkage stress (MPa)[3]	CoV (%)
PET_35	3.32	0.67	1.29	2.03	16.48	27.8
PET_91	4.93	0.58	1.59	3.34	25.69	6.8
PET_175	5.15	0.60	2.15	3.00	24.37	3.1

[1]Calculated as 'P_{final}' from equation (7) using LR(%) from equivalent PETr series
[2]Calculated as final peak load less the assumed load recovery due to healing
[3]Average over three samples

Comparing these results to the restrained shrinkage test results from Table 3.4, the PET_91 and PET_75 series exhibited similar stresses within the beam samples, indicating that the full potential shrinkage stress was imparted onto the concrete beams. The PET_35 series showed a noticeably lower average restrained shrinkage stress and a high CoV of 27.8%. This was the result of two beams within this series demonstrating significantly reduced shrinkage stress (12.8MPa and 13.6MPa). The most probable cause of this is a difference in the pre-stress placed on the PET strips before casting. This pre-stress is difficult to control using the arrangement within these experiments and represents one of the limitations to this approach of using embedded

PET strips. The PET_35 beam samples were also the first to be cast out of the three series, human error in a lack of consistent placement of the PET within the beams was therefore more likely to play a part.

4.2.9. Conclusions

The SMP crack closure system developed by Jefferson et al. (2010) and Isaacs et al. (2013) using PET strips has been successfully scaled-up from use in 125x25x25mm mortar specimens to 500x100x100mm beams made of structural grade concrete.

The activation of the SMP strips in PET and PETr samples on average resulted in a 78% reduction in crack width immediately after activation, increasing to 95% after 28 days curing in water. The system reduces the cracks to a size at which they are able to autogenously heal, depositing cementitious products which bridge the two crack surfaces. This in turn results in load recovery of up to 33% after six months of immersion in water for specimens in which the SMP strips are removed prior to testing, and apparent load recovery of up to 98%, including the effects of a continued compressive load from the polymer, for specimens in which the SMP strips remain embedded.

While the PET strips produced a compressive stress in the concrete beam samples, the resultant stress varied due to the preload placed on the strips before casting. This preload level was challenging to control given that the strips were loose between the steel grips. The strips were also activated within an oven, which is not a practical method for in-situ concrete applications within industry, although it could be achieved for precast elements.

It is therefore desirable to develop a new tendon system which can be activated using a direct heating system and which is rigid prior to casting to improve its ease of application within concrete structures. The development of a new tendon system is the subject of the following section.

4.3. SHAPE MEMORY PET FILAMENT TENDONS: DEVELOPMENT

Tests carried out on shape memory PET solid & tube filaments, detailed in Chapter 3, demonstrate that the PET filaments produce larger restrained shrinkage stresses upon activation than the PET strips. In order to address the shortcomings identified with the use of PET strips in the previous section, a crack closure system was developed using PET solid filaments. These filaments are grouped into single specimens, which are hereafter referred to as tendons.

The experiments included within this section are developmental and commonly comprise single tests rather than triplicates. Given the relatively good consistency of results from the restrained shrinkage stress tests on the PET filaments in Chapter 3 (CoV of 6.6%), single tests were seen as sufficient in the development stage, before reverting to triplicates to test the final tendon arrangement in section 4.4.

4.3.1. PET filament tendon manufacturing and anchorage

The same pre-stress criterion used for the PET strips (discussed in section 4.2.1) was applied to the PET filament tendon, i.e. it can generate a 1MPa pre-stress across a concrete beam crack face. In order to satisfy this criterion, a tendon containing multiple filaments was required.

As the PET filaments are manufactured onto spools, they are naturally inclined to maintain their curvature when extended into tendons. To form the tendons, the filaments were wound around two pegs on a bespoke steel rig, shown in Figure 4.20. This rig allowed tendons of differing lengths to be made by altering the distance between pegs, before clamping the filaments together with the chosen anchorage system.

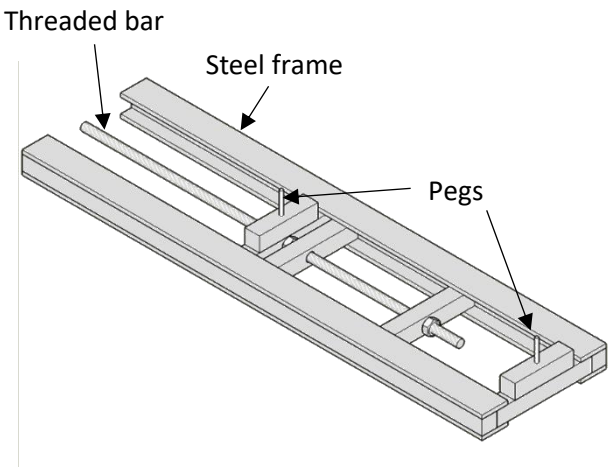

Figure 4.20: Schematic of bespoke steel rig for making filament tendons.

The bolted plate system used to anchor the filaments in Chapter 3 was no longer suitable as this had only been designed to hold the filaments in a single layer. Alternative anchorage methods were therefore investigated. The first consisted of jubilee clips fastened around each end of the tendons with the remaining length melted to form a plug, as shown in Figure 4.21(a). A tendon of 80 filaments was tested using the same experimental set up and methodology as in the restrained shrinkage experiments detailed in section 3.4.1. Heating to 90°C for 1 hour in the environmental chamber resulted in slippage of the filaments within the anchorage (observed visually upon removing the sample), with associated lower shrinkage stress results (maximum of 21.89MPa) compared to the bolted plate system (average of 38.58MPa). This result is shown in Figure 4.21(b).

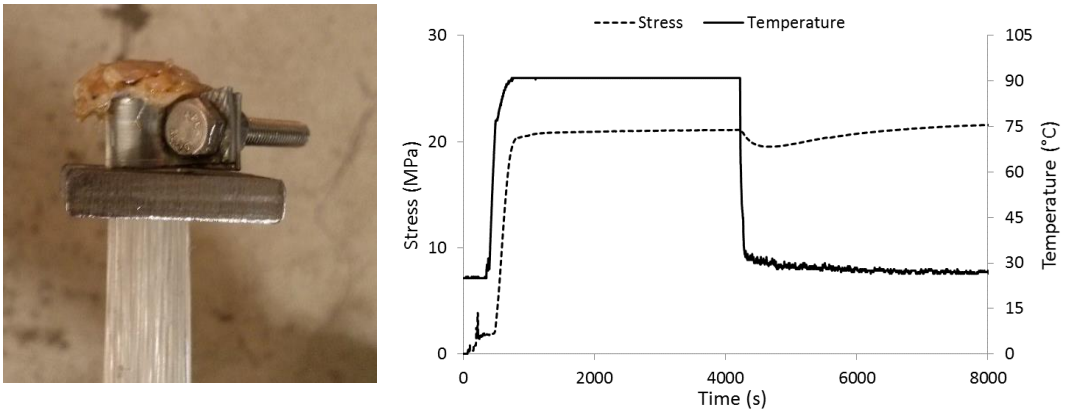

(a) (b)

Figure 4.21: (a) Jubilee clip anchorage (b) jubilee clip anchorage stress results from 80 filaments.

The same experimental set-up was used to test a second anchorage system consisting of stainless steel wire rope clips, shown in Figure 4.22. Various standard sizes between M4 (designed for 4mm diameter rope) to M10 (10mm diameter rope) according to BS EN 13411-5 (BSI, 2008a) were used depending on the number of filaments to be anchored. The clip was passed over the tendon and the nuts tightened with a spanner until no further rotation was possible. The ends of the filaments were again melted to from a plug. With 30 filaments, heating to 90°C for 1 hour resulted in a peak restrained shrinkage stress of 32.65MPa, 15.4% lower than the average from 10 filaments, as shown in Figure 4.23(a). With 70 filament tendons however, a lower peak of 28.35MPa was observed, shown in Figure 4.23(b). Unlike with the jubilee clips, no slippage was observed at the anchorages after testing.

(a) (b)

Figure 4.22: (a) Wire rope clips (Treasure, 2016); (b) Wire rope clip on PET filaments.

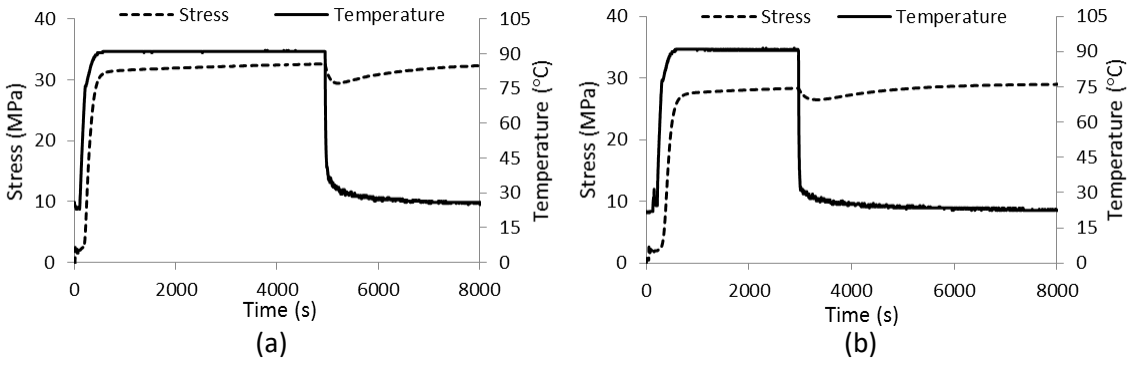

Figure 4.23: Restrained shrinkage stress results with wire rope clip anchorage with (a) 30 filaments; (b) 70 filaments.

The observed loss in restrained shrinkage stress with increasing number of filaments may be attributed to a misalignment of filaments within the tendon and subsequent variations in the level of pre-stress per filament, since some filaments may have been less taut than others within the tendon as a result of the tendon manufacturing technique. This would result in a lower restrained shrinkage stress being produced when considering the entire tendon, an effect which is more significant the higher the number of filaments.

Prior to each stress test, a line was drawn on the filaments along the inside edge of the anchorage. This was to monitor any slippage within the grips during testing, which would be shown as an apparent movement of the line relative to the grips. This movement was seen in the jubilee clip tests, but not with the wire rope clips. As the drop in stress in the wire rope clip samples did not appear to be due to any slipping of the filaments within the grip, the wire rope clips were chosen to anchor the final filament tendons.

4.3.2. Electrical activation system

Heating an entire concrete beam in an oven to activate the polymer tendons is both inefficient and time-consuming compared to directly heating the polymers. It is also extremely impractical for in-situ applications. An electrical activation system capable of achieving polymer activation was therefore designed and tested.

The system consisted of coils of PTFE-coated Nickel-Chrome (Nichrome) wire wrapped around the filaments, which were themselves coated in silicone grease to improve their thermal conductivity. This setup is shown in Figure 4.24. Nichrome wire was chosen due to its high resistance to electrical current (generating high temperatures at relatively low voltage) and low cost. Coated wire was used to reduce the risk of short circuits and to improve the safety of the system.

The wire generates heat depending on the magnitude of a supplied voltage. The heat supply to the polymer tendon could therefore be controlled by altering the supply voltage, and the resultant temperature measured using thermocouples.

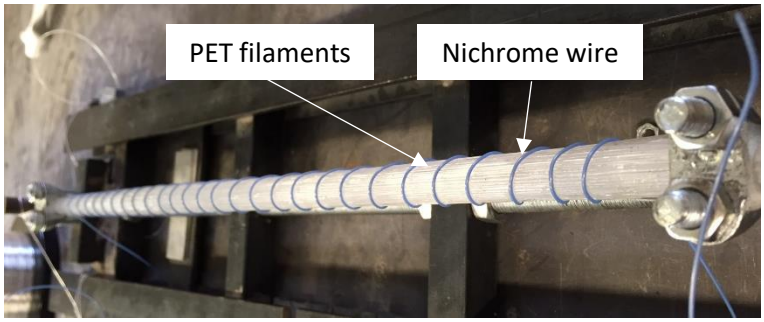

Figure 4.24: Nichrome wire wrapped around PET filaments.

To determine the most appropriate diameter of nichrome wire, three different diameters were tested. One metre lengths of wire of diameter 0.2mm, 0.315mm and 0.5mm were cut, and three thermocouples attached along their lengths. A current was then passed through each wire. The input voltage was increased in 5V increments using a variable transformer, with a 2 minute 'soak' time at each increment. The temperature was measured at a rate of 1Hz and used to plot the results shown in Figure 4.25.

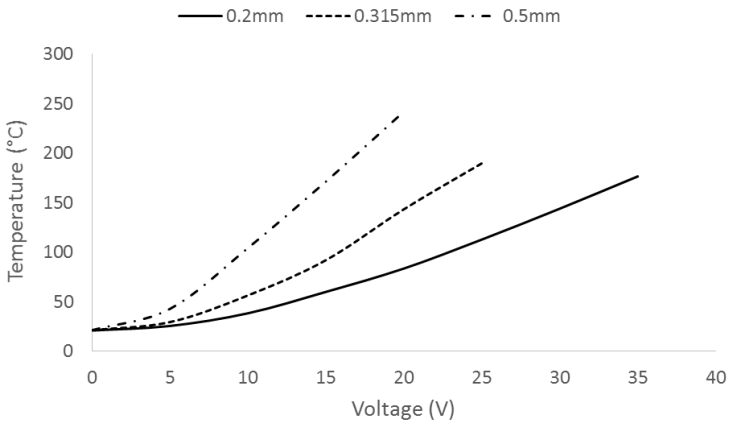

Figure 4.25: Temperature against voltage for three different diameters of Nickel-Chrome wire.

It is clear that the larger the diameter of wire, the lower the voltage required for the same temperature output. The 0.5mm diameter wire was therefore used, to reduce the input voltage required. Experimental work by Selvarajoo (2015) investigated the ability of the 0.5mm diameter

wire to heat a tendon of 75 PET filaments (the same as those used in the current work) to 90°C with varying coil spacing. The author concluded that, while the smaller the spacing the quicker the heating process, a spacing of 10mm between coils was sufficient to heat the entire tendon to 90°C within a 30min test period when the wire was held at a constant temperature of 90°C. A coil spacing of 10mm was therefore adopted for use in the current filament tendon tests.

Two thermocouples were incorporated into each tendon, as shown in Figure 4.26, to measure temperature during activation. The first, 'internal' thermocouple was placed near the centre of the filament bundle. The second 'external' thermocouple was placed on the surface of the filaments, between two heating coils.

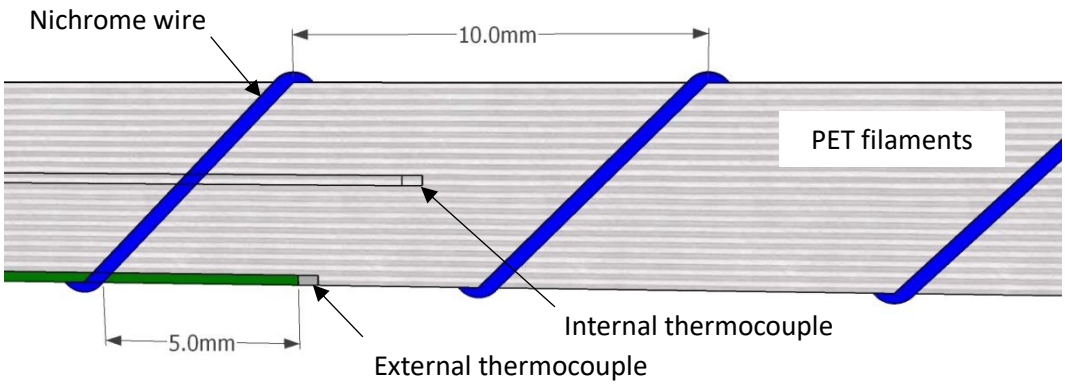

Figure 4.26: Position of thermocouples within PET filament tendon.

4.3.3. Protective sleeve

Keeping the tendon straight upon removal from the rig, especially when made from large numbers of filaments, was a challenge. In addition, a method of de-bonding the tendon from the concrete in a similar manner to the PET strips, and protecting the filaments from the alkaline environment, was required. All of these challenges were addressed by developing a protective sleeve for the filaments.

Various prototypes for the sleeves were designed and made from poly-lactic acid (PLA) on an Ultimaker 3D printer. The sleeves were required to be rigid enough to restrict the force of the filaments attempting to revert to their manufactured shape until testing, but also not restrict

the shrinkage of the polymer upon activation. PLA was used as it has a glass transition temperature of 55°C (Hagen, 2009) which signifies that it will experience a loss of stiffness during the activation period of the PET, prior to the shrinkage of the PET itself. The sleeves were made from two halves, which allowed them to be placed around the tendon while on the rig and connected together using cable ties, holes for which were placed every 50mm along the sleeve length. The 3D printed sleeves are shown in Figure 4.27.

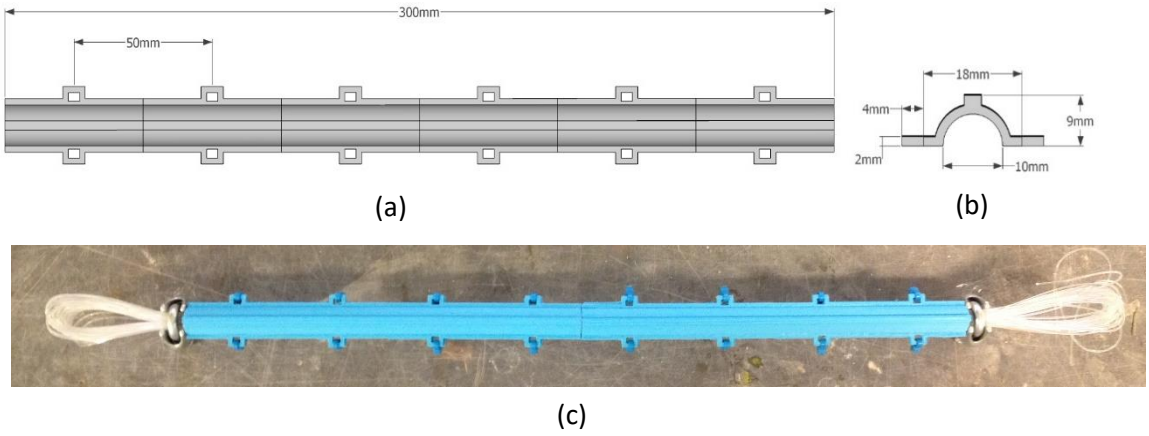

Figure 4.27: 3D printed sleeve for filament tendons (a) plan view; (b) end view; (c) applied to PET tendon.

To test the wire activation and sleeve system, two tendons, each containing 75 filaments and encased in a PLA sleeve, were heated to 90°C. One was heated in the environmental chamber, the second using the electrical wire system. The temperature of each tendon was measured using the internal and external thermocouples. The results are shown in Figure 4.28.

As can be seen from Figure 4.28(b), the wire-activated tendon reached a temperature of approximately 100°C, which resulted in a peak shrinkage stress of 31.78MPa, compared to 30.14MPa from the oven-activated tendon in Figure 4.28(a). Both peaks are followed by the characteristic drop in shrinkage stress observed in Chapter 3 and discussed in section 3.5.1. The wire-activated tendon then reaches a final stress plateau, while the oven-activated tendon begins to show an increase in stress due to the retraction of the steel grips upon cooling. This is not observed in Figure 4.28(b) as the grips were not heated, confirming that this is the cause of the stress rise observed in previous oven-activated tests.

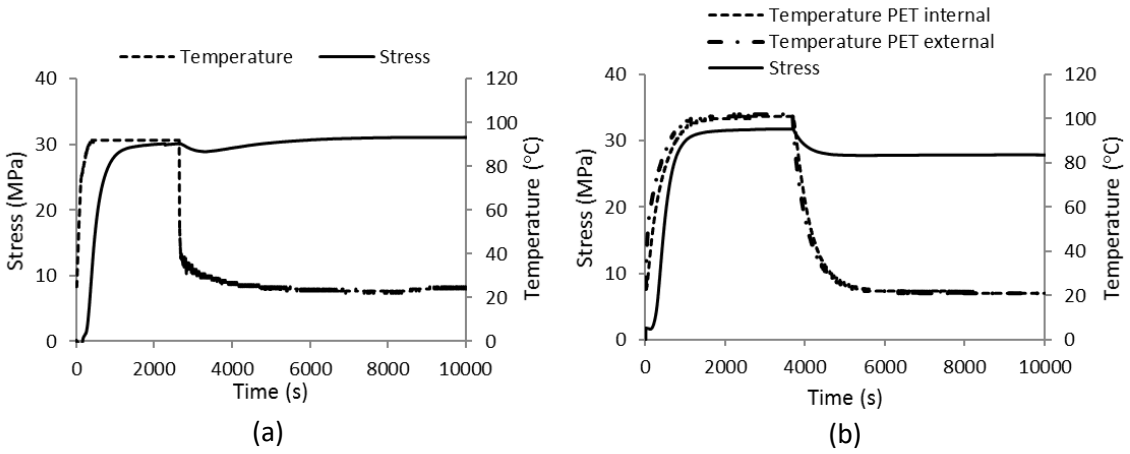

Figure 4.28: Comparison of activation methods on a tendon with 75 filaments (a) heated in environmental chamber; (b) heated using electrical wire system.

4.3.4. Final PET tendon system

The final tendon system is shown in Figure 4.29. A steel plate was added between the wire rope grip anchorage and the protective sleeve as shown in Figure 4.29(b) to provide an even surface for the transfer of compressive force from the filaments to the concrete.

The final sleeves were injection moulded from PLA material to enable mass production for the site trials. The final number of filaments per tendon was 200. This quantity was chosen to maximise the force produced by each tendon while keeping its outer diameter (including the sleeve) limited to 20mm. This was primarily to suit the arrangement of tendons used for the site trial, discussed in section 5.3.2.

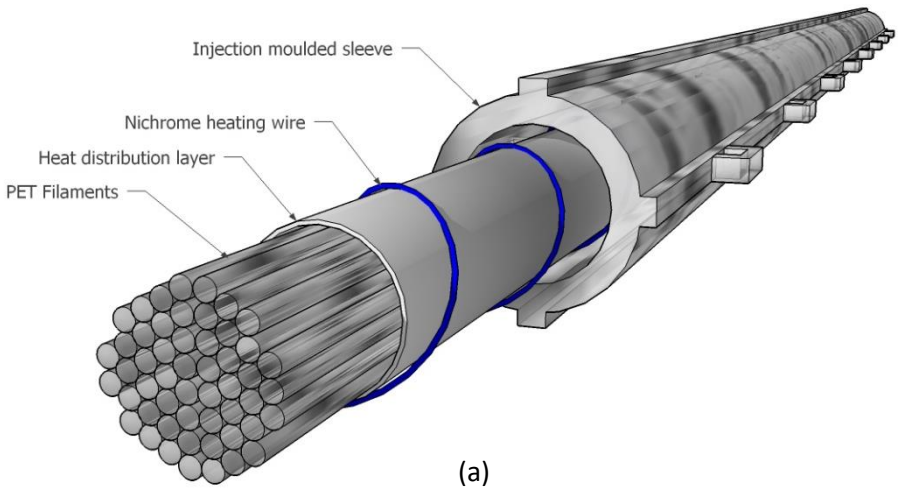

(a)

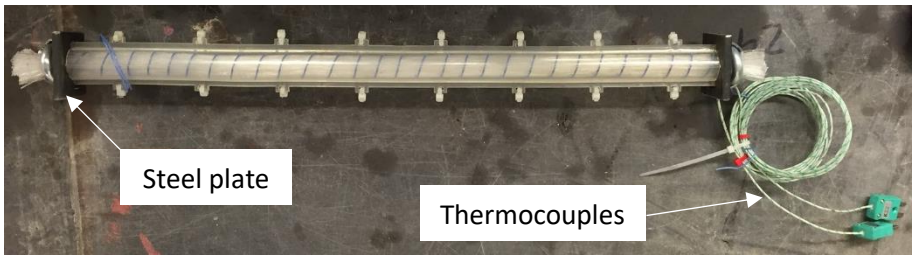

(b)

Figure 4.29: Shape memory PET tendon concrete crack closure system (a) schematic (b) photo.

4.4. SHAPE MEMORY PET FILAMENT TENDONS: CRACK CLOSURE EXPERIMENTS

The tendons were first tested outside of concrete beams to determine their restrained shrinkage stress, in a similar arrangement to that described in section 3.4.1. Tendons were then placed into unreinforced and reinforced concrete beams and activated using the electrical system to test their ability to close cracks.

4.4.1. Experiment set-up

Restrained shrinkage test

To test their restrained shrinkage stress, tendons of length 400mm containing 200 filaments were placed within a steel grip arrangement as shown in Figure 4.30. The grips were connected to a 5kN full bridge strain gauge to measure load. Before testing, the tendons were loaded to a pre-stress of 2MPa using the steel rig. Each end of the nichrome heating wire was connected to

a length of low-resistance copper wire, which was in turn attached to an Ashley-Edison AE-130-LB variable transformer connected to a 230V mains supply, allowing the input voltage to be manually varied.

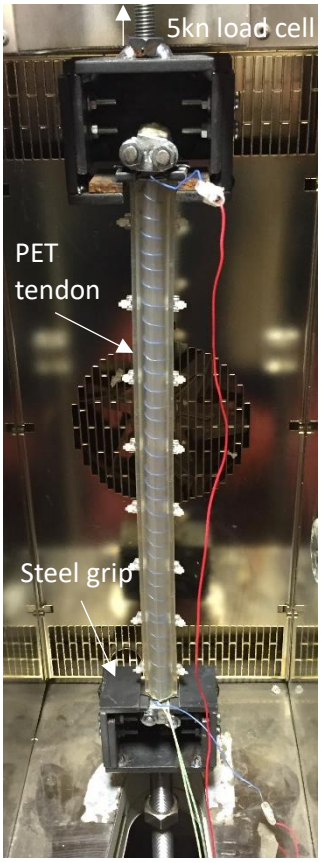

Figure 4.30: Shape memory PET tendon testing rig arrangement.

Concrete crack closure tests

The concrete beam samples measured 500x100x100mm and were cast using steel moulds. Each of the test beams contained one PET tendon of length 400mm, containing 200 filaments. The reinforced samples also contained two 6 mm diameter high tensile ribbed steel bars. The set-up of the reinforced samples prior to casting is shown in Figure 4.31 and the cross-sections of unreinforced and reinforced beam samples are shown in Figure 4.32.

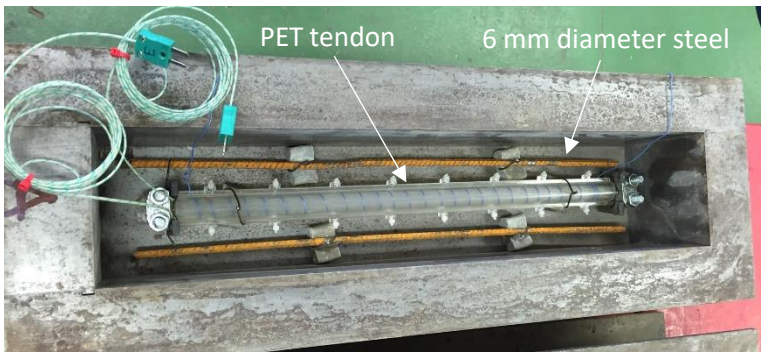

Figure 4.31: Reinforced test sample set-up prior to casting.

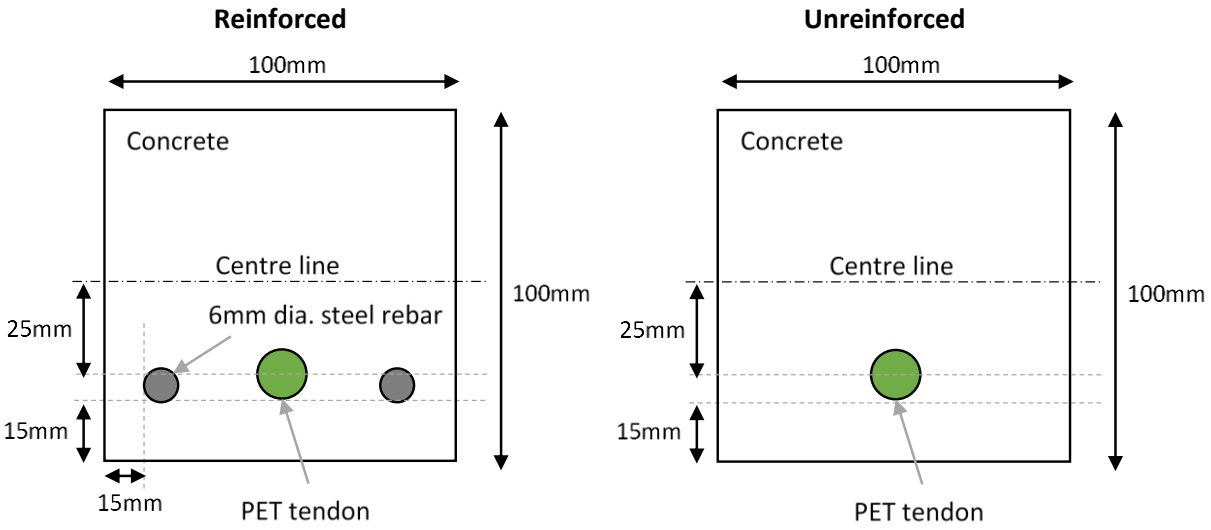

Figure 4.32: Cross-section of reinforced and unreinforced test beams.

The concrete mix design described in section 4.2.4 was mixed using a Belle Premier 200XT mixer and compacted in three layers on a vibrating table. After air-curing for 24 hours, the specimens were submerged in water at 20°C until 24 hours before testing. A 5mm deep notch was then cut as a crack-inducer at mid-span and knife edges attached to measure CMOD. The beam sample references and descriptions are given in Table 4.9.

Table 4.9: Specimen descriptions.

Sample	Series	Description
PET A	Unreinforced	500x100x100mm concrete beam containing 1 PET tendon
PET B	Unreinforced	500x100x100mm concrete beam containing 1 PET tendon
PET C	Unreinforced	500x100x100mm concrete beam containing 1 PET tendon
Control (x3)	Unreinforced	500x100x100mm concrete beam
PET A-r	Reinforced	500x100x100mm concrete beam containing 1 PET tendon and 2 no. 6mm diameter high tensile steel bars
PET B-r	Reinforced	500x100x100mm concrete beam containing 1 PET tendon and 2 no. 6mm diameter high tensile steel bars

PET C-r	Reinforced	500x100x100mm concrete beam containing 1 PET tendon and 2 no. 6mm diameter high tensile steel bars
CONT A-r	Reinforced	500x100x100mm concrete beam containing 2 no. 6mm diameter high tensile steel bars
CONT B-r	Reinforced	500x100x100mm concrete beam containing 2 no. 6mm diameter high tensile steel bars
CONT C-r	Reinforced	500x100x100mm concrete beam containing 2 no. 6mm diameter high tensile steel bars
Cubes (x6)	Unreinforced & reinforced	100x100x100mm cube samples for compression tests

4.4.2. Experimental methodology

Restrained shrinkage test

The input voltage was raised until 90°C was recorded on the internal thermocouple. The temperature was then regulated by manually switching the system on and off to keep the reading within 5°C of this target temperature for 15mins. This caused the temperature measured by the external thermocouple to fluctuate between 80-90°C due to a higher rate of heat loss on the external face of the tendon. The electricity supply was then turned off, allowing the tendon to cool to room temperature. The load and temperature were measured at a rate of 2Hz using the load cell and thermocouples respectively. This test was repeated with three tendons.

Concrete crack closure tests

Table 4.10 describes the testing methodology for the PET tendon in unreinforced and reinforced beam samples. Cube samples were also tested at 7 and 28 days for compressive strength. The three-point bending set-up used was identical to previous tests using PET strips, shown in Figure 4.8.

Table 4.10: Testing methodology for PET tendons in unreinforced and reinforced beam samples.

Day from casting	Action	Description
0	Casting of all beams	Beams cast and left to cure in air
1	Submersion	Beams removed from steel moulds and submerged in water at 20°C
6	Preparation for testing	Removal from water, given 5mm notch and knife edges
7	Initial 3-point bend testing of all beams	**Unreinforced beams (PET A-C and controls)** Loaded to 0.5mm CMOD at a rate of 0.001mm/sec (CMOD controlled). At 0.5mm the CMOD was held constant while microscope images were taken of both sides of the beam (at crack location). The beams were then unloaded and additional microscope images taken. **Reinforced beams (PET A-r, B-r, C-r and CONT A-r, B-r, C-r)** Loaded to 15kN at a rate of 0.001mm/sec (CMOD controlled). At 15kN the CMOD was held constant while microscope images were taken of both sides of the beam (at crack location). The beams were then unloaded and additional microscope images taken.
7	Activation of PET tendons	Immediately after initial testing, the tendons were activated by passing a current through the nichrome wire. The voltage was increased until either a temperature plateau of 90°C was reached on the internal thermocouple, or the wire temperature reached 150°C. This voltage was then kept constant for 1 hour[1] before turning off the electricity supply and allowing the tendon to cool to room temperature. Cont B-r was also left for an hour as a control to test the effect of the reinforcing steel on the gradual crack closure over this time period.
7	Retesting of beams in 3-point bending	**Unreinforced beams (PET A-C)** Reloaded to 1mm CMOD at a rate of 0.001mm/sec, additional microscope images taken, then unloaded. **Reinforced beams (PET A-r, B-r, C-r and CONT A-r, B-r, C-r)** Reloaded to 15kN at a rate of 0.001mm/sec, additional microscope images taken, then unloaded. For PET A-r, PET C-r and Cont B-r two additional reloads were completed to investigate the cyclic loading effect. Cont A-r was also reloaded a second time before a machine error caused the failure of the beam. Cont C-r was only reloaded once.

[1]The temperature was not regulated as the thermocouple readings reached a plateau using voltage control alone.

4.4.3. Crack width and strain measurements

Images of the cracks were taken on both sides of the beam samples using a Veho Discovery VMS-001 USB microscope along with a graduated scale. The crack width was measured from these images using the method described in section 4.2.6.

Images were taken at peak load and after unloading on both the initial and reload cycles. Additional images were taken immediately after activation of the tendon. Average crack width measurements from both sides of the beam were used for comparison.

Displacement and strain were also measured using a Digital Image Correlation (DIC) system. DIC works through the comparison of multiple digital photographs of a patterned surface, analysing displacements of discrete subsets (blocks of pixels) of that surface (LaVision, 2016). By tracking the subsets, the system can build up 2D and 3D deformation vector fields and strain maps. To achieve this, the subsets must be random and unique, with a range of contrast and intensity levels (McCormick and Lord, 2010). DIC systems have been used previously to analyse cracking in concrete beams, for example to evaluate fatigue behaviour (Mahal et al., 2015), flexural cracking (Hamrat et al., 2016) or shear capacity (De Wilder et al., 2015).

The DIC system used consisted of two LaVision Imager X-lite 8M CCD cameras and DaVis analysis software. A speckle pattern (to create unique subsets) was painted on to the side of all beams containing PET tendons and one control beam from both the unreinforced and reinforced beam series. A typical example of this pattern is shown in Figure 4.33. Images were taken every 30 seconds during loading, activation and reloading using the DIC system. These images were then post-processed in the DaVis software to track movement over time, generating 2D strain images to visualise crack closure.

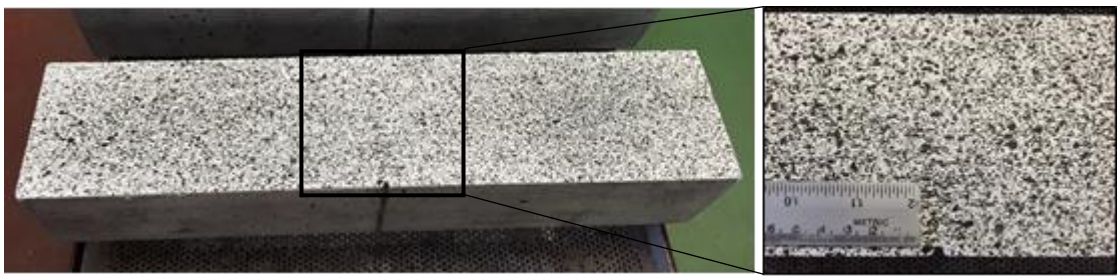

Figure 4.33: Applied speckle pattern for DIC system.

4.4.4. Results and discussion

Polymer tendon shrinkage stress

Figure 4.34 shows the graph of stress and temperature against time from the restrained shrinkage stress test 1 on the PET tendons. This is typical of all of the tests undertaken. Table 4.11 shows the peak and final restrained shrinkage stress values for all three tendons. The final stress is defined as the stress at 30°C after cooling.

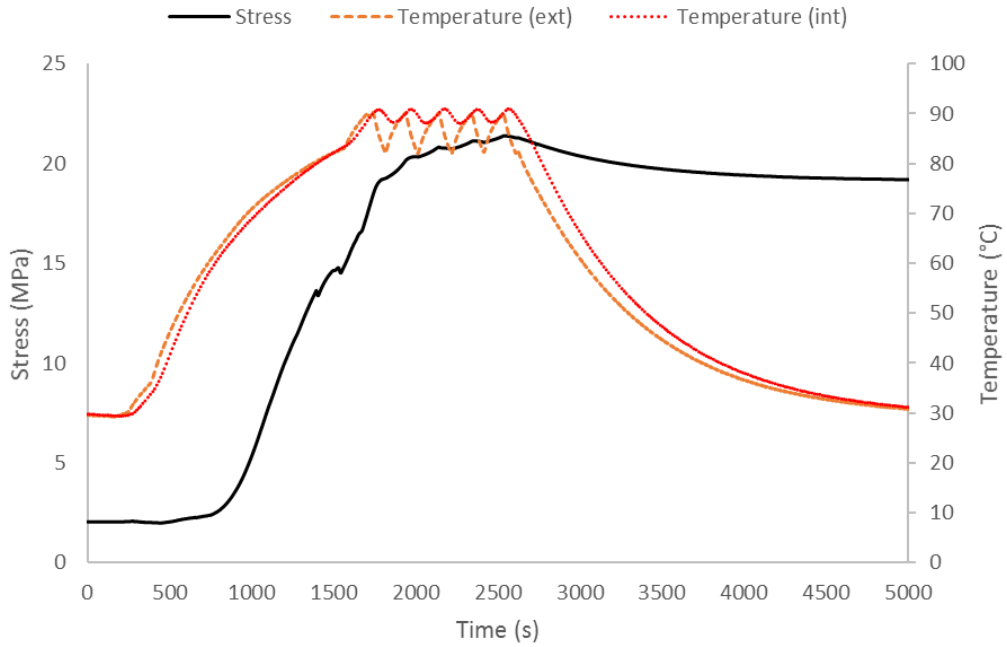

Figure 4.34: Restrained shrinkage stress test on PET tendon – test 1.

In all three tests, as the temperature was raised above T_g (60-80°C) the restrained shrinkage stress rapidly increased, up to a maximum of 19.93 to 21.39MPa after 15 minutes at 90°C. This was significantly lower than the 38.58MPa observed during earlier tests on 10 filaments described in 3.5.1. As discussed in section 4.3, preliminary tests on bundles of 30 and 70 filaments also showed decreasing shrinkage stress with increasing number of filaments per tendon. This effect may be due to two factors: some filaments within the tendon being more 'slack' than others, and incomplete activation of all filament.

Table 4.11: Peak and final restrained shrinkage stress results from PET tendon tests.

Test	Peak stress (MPa)	Final stress (MPa)	CoV peak (%)	CoV final (%)
1	21.39	19.19		
2	19.93	17.83	3.2	3.6
3	20.11	17.76		

Misalignment of filaments within the tendon becomes more probable with higher numbers of filaments. In addition, as more filaments were wound onto the tendon rig (shown in Figure 4.20), the tension within these filaments may have caused slight inward displacements (contraction) in the rig itself, causing the filaments wound first to be looser than those wound last. Both of these factors result in some filaments remaining slack within the tendon. Given the impact of slack on the restrained shrinkage stress of the PET strips discussed in section 3.3.3, it is possible that this resulted in the significant reduction in stress observed within the filament tendons compared to earlier tests.

Heat conductive silicone grease was used within the tendons to improve their thermal conductivity, shown in preliminary experiments and by Selvarajoo (2015) to be effective in tendons containing 75 filaments. However, despite the internal and external thermocouples measuring 90°C within the tendon, it is possible that some of the 200 filaments within these tendons did not reach this temperature. As shown by the results of temperature-shrinkage profile experiments in section 3.5.2, this would result in lower restrained shrinkage stresses being observed. Potential methods for improving the heating and temperature measurement system are discussed in section 7.2.

Upon cooling, there was a gradual drop in shrinkage stress, an effect previously observed and explained in section 3.4.1, resulting in a final stress plateau at between 17.76 and 19.19MPa.

A separate test conducted on 10 filaments showed a continued drop in final stress after activation, resulting in a plateau after 14 days with a final stress loss of 4% compared to the stress observed immediately after cooling. This is similar to results from a study conducted by Hazelwood et al. (2014) on the long-term relaxation of thermally activated PET strips, in which

a 2-3% loss was observed over 6 months. Assuming a loss of 4%, the average final stress produced by the polymer tendons would reduce to 17.5MPa.

The coefficient of variation for both the peak and final stress, shown in Table 4.11, was 3.2% and 3.6% respectively, lower than the 6.6% observed in tests on 10 filaments. This indicates that while a significant amount of potential shrinkage stress has been lost, the stress produced by each tendon appears to be consistent. The method of manufacture, although not ideal in terms of stress generation upon activation, does produce repeatable peak and final stresses in the manufactured tendons.

Compressive strength and consistency class

Table 4.12 shows the compressive strength results from the cube samples. All of the strength results were above the target characteristic compressive strength (from cube samples) of 45N/mm², with a mean value exceeding 49N/mm². The mix therefore conforms to the strength class C35/45 based on EN 206:2013 in terms of both strength and variability. The measured slump of the mix was 150mm, falling into consistency class S3 (BSI, 2013).

Table 4.12: Compressive strength results from cube samples (average of 3 cubes).

Age (days)	Compressive strength (N/mm²)	CoV (%)
7	36.96	2.35
28	51.17	0.55

Unreinforced beams

Figure 4.35 shows typical load-CMOD curves for the unreinforced test and control samples, and Figure 4.36 the stress block diagrams at various stages of the experiment. Comparing the initial loading peaks (point 1) gives an average reduction in peak load of 6.2% for the PET samples (4.78kN compared to 5.10kN for the controls). This is similar to the 7-8% reduction in peak observed for the PET strip samples as discussed in section 4.2.7. This is to be expected as the area of concrete replaced by the PET filament tendons was 1.8%, compared to 1.5% and 4% for the internally and externally anchored PET strip samples respectively.

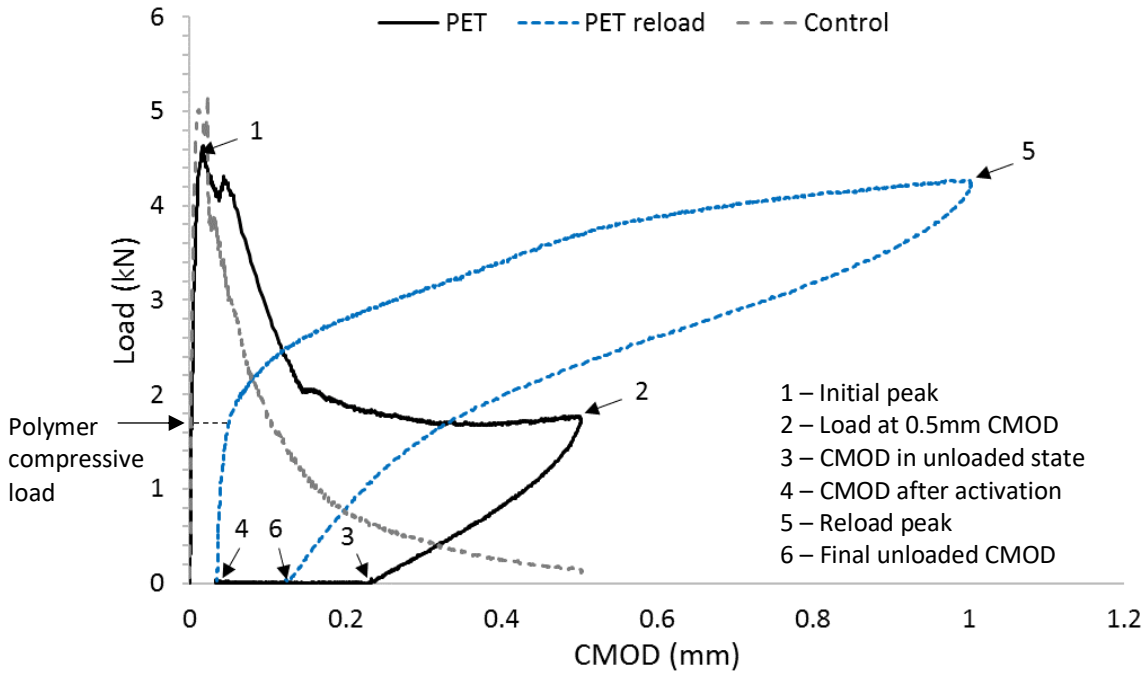

Figure 4.35: Load-CMOD curves for unreinforced test and control beams - typical graph.

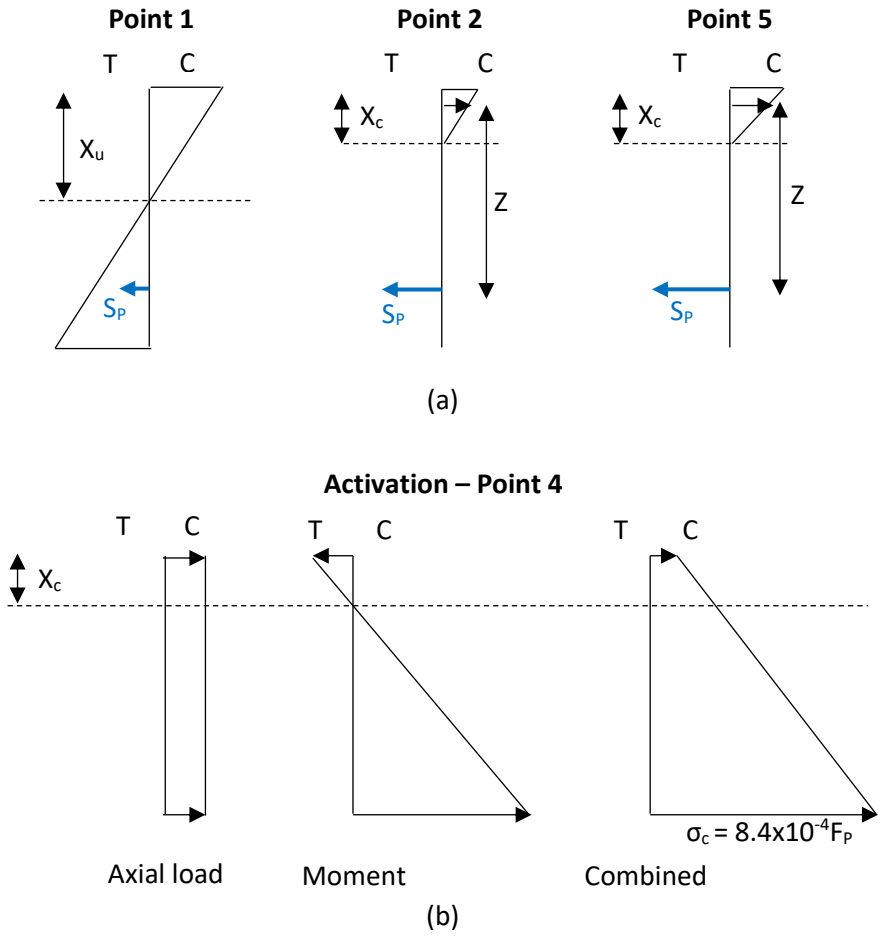

Figure 4.36: Stress block diagrams for (a) Points 1, 2 and 5 on Figure 4.35; (b) Activation of the polymer tendon (Point 4 on Figure 4.35). T=tension, C=compression, S_P=Stress applied to polymer tendon, X_u=depth of neutral axis (uncracked section), X_c=depth of neutral axis (cracked section), F_P= shrinkage force applied by the polymer.

As illustrated by Figure 4.36, at point 1 the concrete is contributing in both compression and tension (uncracked state). The polymer tendon is therefore subject to a stress, denoted as S_P, equal to the stress in the surrounding concrete multiplied by the factor n (ratio of the Young's Modulus of the polymer to the concrete). This results in a stress of 0.5N/mm^2 in the polymer for the typical sample shown in Figure 4.35.

Upon cracking, the depth of the neutral axis reduced and all tensile load was taken by the PET tendon, resulting in a drop in applied load. Loading continued to a CMOD of 0.5mm at point 2. The un-activated polymer tendon clearly supplied some tensile reinforcement to the PET beam samples, indicated by the much higher load observed at 0.5mm CMOD compared to the control specimen. At this stage the stress in the polymer S_P can be calculated using equation 10.

$$S_P = \frac{M}{Z \cdot A_P} \qquad (10)$$

Where M is the applied moment, Z is the lever arm and A_P is the area of the polymer. With an applied load of 1.77kN (for the typical graph shown), S_P is 21.6N/mm^2. This is well within the polymer's elastic zone on the stress-strain curve, included as Figure 3.8 in section 3.5.4.

Upon unloading (point 3), a residual CMOD of 0.195mm to 0.231mm was recorded. Although this suggests plastic deformation, it is improbable that yielding of the polymer had occurred during the initial loading stage given the low stress in the polymer. The residual CMOD of the PET beam is clearly lower than that of the control sample in Figure 4.35. It is apparent therefore that the polymer began to contribute to the beam's resistance to loading once a CMOD of approximately 0.2mm was reached, at which point elastic behaviour of the beam was observed as a distinct change in the gradient of the loading curve. This delay can be attributed to some initial slack in the polymer filaments. This resulted in curvature of the beam occurring before the filaments became taut and began to resist loading.

Upon activation (point 3 to point 4), the compressive stress produced by the tendon caused a

reduction in CMOD, as the crack faces were drawn back together. Figure 4.36(b) shows the stress profile of the beam at this stage, made up of the axial and moment stresses applied by the polymer.

Table 4.13 shows the percentage crack closure of each of the test samples. This closure was measured both by the change in CMOD readings and from microscope measurements of the induced crack before and after the activation process. The recorded CMOD values were larger than the microscope measurements due to the position of the gauge, approximately 4mm below the bottom surface of the beam. The difference between the two measurements was 0.035mm-0.063mm before activation, reducing to 0-0.007mm after activation as the crack faces were pulled back together. The variation in measurements between beams is caused by differing crack width, variations in actual notch depth and variation in the exact position of microscope measurements relative to the CMOD gauge.

The reduction in difference between measurements upon activation is due to a decrease in beam curvature caused by the compressive force. It is therefore to be expected that the crack closure measured by change in CMOD will be slightly higher than those measured by microscope images.

Table 4.13: Crack closure of unreinforced beams by PET tendon activation.

Sample	CMOD before (mm)	CMOD after (mm)	CMOD closure (%)	Microscope before (mm)	Microscope after (mm)	Microscope closure (%)
PET A	0.231	0.035	**85**	0.169	0.028	**83**
PET B	0.195	0.045	**77**	0.132	0.045	**66**
PET C	0.2	0.060	**70**	0.165	[1]	

[1]Measurement not taken due to equipment error

Activation of the polymer tendon significantly increased the stiffness of the beams. This is shown by the reload curve (point 4 to point 5) in Figure 4.35, which exhibited two distinct behaviours: an initial increase in load without corresponding displacement followed by a linear elastic response to further loading. The initial lack of displacement is attributed to the stress generated by the applied load acting against the compressive stress produced by the tendon. The

subsequent linear elastic response begins once the tendon's restrained shrinkage stress has been exceeded and the polymer is acting as tension reinforcement. Within this region, the polymer appeared to provide higher tensile restraint than before activation. This apparent increase in tensile strength of the tendon is ascribed to all the filaments being taut after activation, whereas previously it is possible that a proportion remained slack despite the stress applied to the beam sample.

At point 5, the stress applied to the polymer S_P can again be calculated from equation 10, as at point 2, the difference between the two being an increase in magnitude of the applied moment and therefore an increase in stress in both the concrete and the polymer. With an applied load of 4.27kN, S_P is equal to 52.1N/mm^2. This is still well within the elastic zone of the polymer, so it can be assumed that yielding has not occurred.

Upon unloading (point 6), the CMOD did not return to its value after activation (point 4). The residual CMOD after reloading was, however, smaller than the residual CMOD before activation (point 3), despite having been loaded to a CMOD of 1mm upon reloading compared to 0.5mm initially. This demonstrates that even after significant displacement, the activated tendon was still capable of supplying a force to close the crack. The fact that the CMOD did not return to the post-activation value indicates that some relaxation of the polymer restrained shrinkage stress may have occurred during the loading process. This should be investigated further in future studies for the purpose of assessing long-term performance.

The results indicate that the compressive stress produced by the tendons was sufficient to close the induced crack width by up to 85%. This crack closure is also shown by the strain images in Figure 4.37 produced by the DIC camera system.

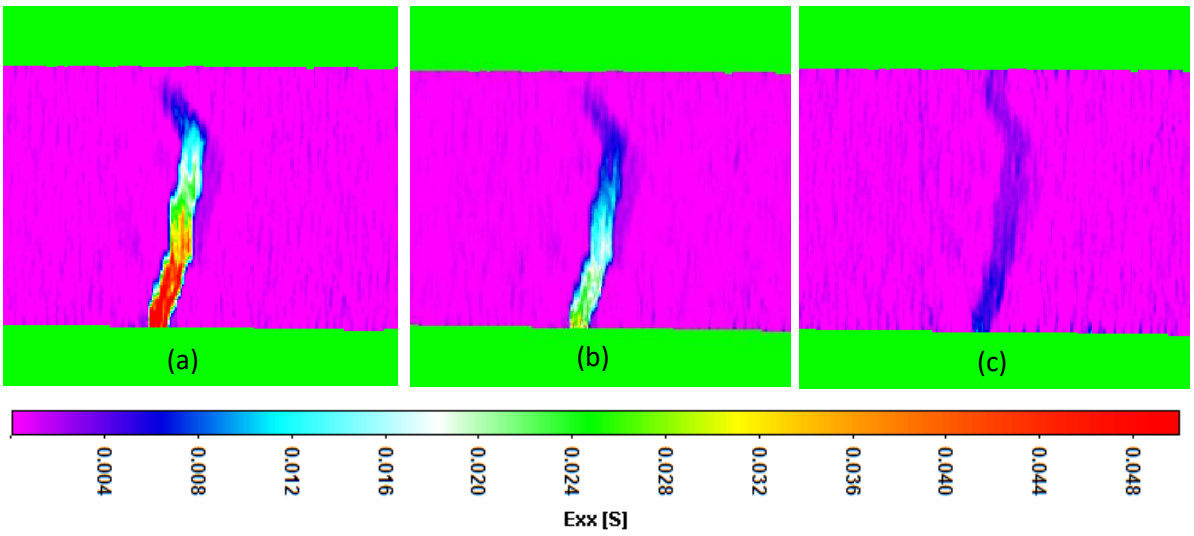

Figure 4.37: Digital Image Correlation (DIC) camera snapshots showing closure of concrete crack using PET tendons. Axis indicates strain. (a) Loaded to 0.5mm CMOD; (b) Unloaded; (c) Post-activation.

The restrained shrinkage stress generated by the polymer tendons inside the beams was calculated from the reload curves (point 4 to point 5 on Figure 4.35) of the PET beams after activation.

The load at which the load-CMOD reload curve changed from near-vertical to an elastic response is denoted as the polymer compressive load in Figure 4.35. At this load it is assumed that, as displacement is negligible, the applied stress at the extreme fibre is counteracted by the compressive stress generated by the polymer tendon. The stress at the extreme fibre generated by the polymer, as indicated in Figure 4.36(b), is calculated from equation (2) as $8.4 \times 10^{-4} F_P$, where F_P is the shrinkage force applied by the polymer. The polymer compressive load was used to calculate the shrinkage force F_P, and therefore the restrained shrinkage stress, as per the method described in section 4.2.8. Table 4.14 shows the calculated restrained shrinkage stress values for the three PET samples using this method.

Table 4.14: Restrained shrinkage stress of polymer tendons within beams - calculated values.

Sample	Polymer compressive load (kN)	Calculated polymer restrained shrinkage stress (MPa)	CoV (%)
PET A	1.7	19.71	11.5
PET B	1.3	15.1	
PET C	1.4	16.23	

The calculated values are similar to the final stress values observed in the tendon experiments

undertaken outside of concrete beams, given in Table 4.11. PET B and C exhibited lower shrinkage stress results than PET A, which agrees with the lower percentage of crack closure observed in Table 4.13. The CoV of 11.5% within the beam samples compared to 3.6% outside indicates increased variability of results when activating the tendons inside concrete. The concrete beam arrangements add several new variables, including the eccentricity of the tendons and any expansion and contraction of the concrete, which affect the final shrinkage stress observed from the tendons.

These results indicate that crack closure of unreinforced concrete beams has been achieved through the use of shape memory polymer filament tendons activated using an electrical wire system.

Reinforced beams

Figure 4.38 shows the load-CMOD curve for the PET A-r test beam compared to CONT B-r. This control sample was used for comparison as it was left for an hour following loading to investigate the effect of the steel reinforcement in closing the crack over time.

The inclusion of the un-activated PET tendon had no noticeable impact on the load at which concrete cracking took place (point 1). However, there is an apparent increase in overall stiffness of the PET beam prior to activation as shown by a reduced CMOD reading at the maximum load of 15kN (point 2). On average, the CMOD of the PET beams at 15kN before activation was 10.6% lower than the control beams (0.202mm compared to 0.226mm).

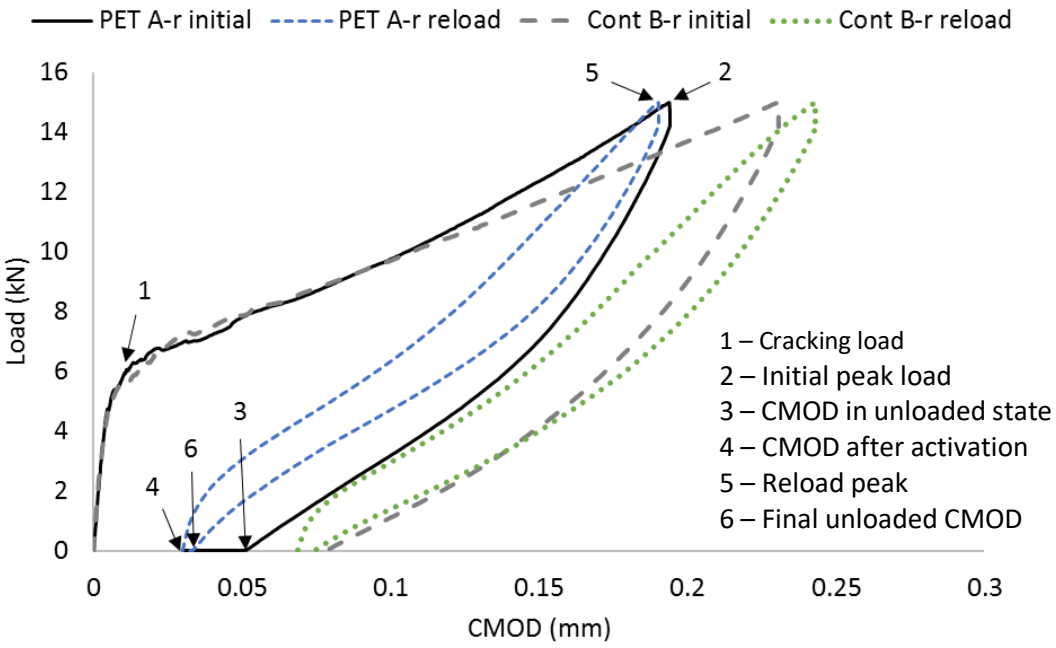

Figure 4.38: Load-CMOD curves for PET A-r and CONT B-r samples.

Upon activation (point 3 to point 4), the CMOD reduced by between 26-39% for the PET beams, compared to an 11% reduction due to the action of the steel in CONT B-r when left for an hour after loading. The microscope and measurements show very similar results, with 25-39% closure in PET A-r and PET B-r samples compared to 13% in CONT B-r. Table 4.15 shows the crack closure upon activation for all beams based on the CMOD and microscope measurements. A notable exception is PET C-r which shows only 10% closure based on microscope measurements compared to 26% based on CMOD. The reason for this discrepancy in unclear, although the residual crack width measured from microscope images in this sample were the smallest of all samples, making changes in crack width more difficult to measure.

The target internal thermocouple temperature of 90°C was not achieved in any of the samples, even when the temperature on the heating wire was raised to 150°C. The wire temperature was not increased beyond this point to avoid locally melting the PET filament. The maximum recorded temperatures are shown in Table 4.16.

Table 4.15: Crack displacements and closure from CMOD and microscope measurements (in mm) – microscope measurements are an average over both sides of the beam samples.

	PET A-r		PET B-r		PET C-r		CONT A-r		CONT B-r		CONT C-r	
	CMOD	Micro.	CMOD	Micro.	CMOD	Micro.	CMOD	Micro.	CMOD	Micro.	CMOD	Micro.
Peak load	0.194	0.120	0.217	0.126	0.196	0.120	0.246	0.168	0.231	0.132	0.201	0.126
Unloaded	0.050	0.023	0.064	0.028	0.063	0.021	0.080	0.043	0.077	0.032	0.059	0.024
Activated	0.030	0.014	0.048	0.021	0.047	0.019	-	-	0.069[1]	0.028	-	-
Crack closure	0.019	0.009	0.017	0.007	0.016	0.002	-	-	0.008	0.004	-	-
Crack closure (%)	**39%**	**39%**	**26%**	**25%**	**26%**	**10%**	**-**	**-**	**11%**	**13%**	**-**	**-**

[1]CONT B-r left for an hour following unloading, closure due to elastic effect of steel reinforcement

Table 4.16: Maximum recorded temperatures during activation.

	PET A-r			PET B-r			PET C-r		
Thermocouple	External	Internal	Wire	External	Internal	Wire	External	Internal	Wire
Temperature (°C)	82.7	84.6	135.8	60.8	74.2	147.0	59.2	68.1	150.0

PET A-r, in which the highest external and internal thermocouple readings were observed, also demonstrated the most successful crack closure (39%). The thermocouples positioned within PET C-r did not reach higher than 68.1°C, below the glass transition temperature (approximately 70°C) at which polymer shrinkage is expected. However, the recorded wire temperature in both PET B-r and C-r was between 140-150°C. It is possible therefore that partial activation has taken place in these tendons as the temperature of the filaments between the location of the nichrome wire and the thermocouples may have exceeded 70°C. This is supported by the crack closure results, which show an improvement over the control sample for PET B-r and C-r despite the low thermocouple readings.

It should also be noted that, at temperatures exceeding 110°C, the restrained shrinkage stress of the tendons may decrease, as observed in section 3.5.2. It is therefore possible that some over-activation has occurred in one or more of the samples due to the high wire temperature observed during activation.

It is currently unclear why the tendons within the reinforced beams did not reach the desired temperature, while those within the unreinforced beams did. It is possible that the electrical activation system was inducing a current in the reinforcing bars, resulting in lower heat output

from the nichrome wire. Alternatively, the bars may have been acting as a heat sink, drawing the heat away from the tendon. This is discussed further in section 7.2.

The reload curve following activation of PET A-r (point 4 to point 5 in Figure 4.38) again shows an apparent increase in stiffness, as the CMOD at 15kN load reduced from 0.194mm to 0.190mm. In contrast, the CMOD of CONT B-r at 15kN was 0.243mm upon reloading, an increase from 0.231mm on initial loading.

A comparison of three successive reload cycles of PET A-r and CONT B-r is shown in Figure 4.39. The CMOD and microscope measurements at peak load and after unloading for all samples are displayed in Table 4.17.

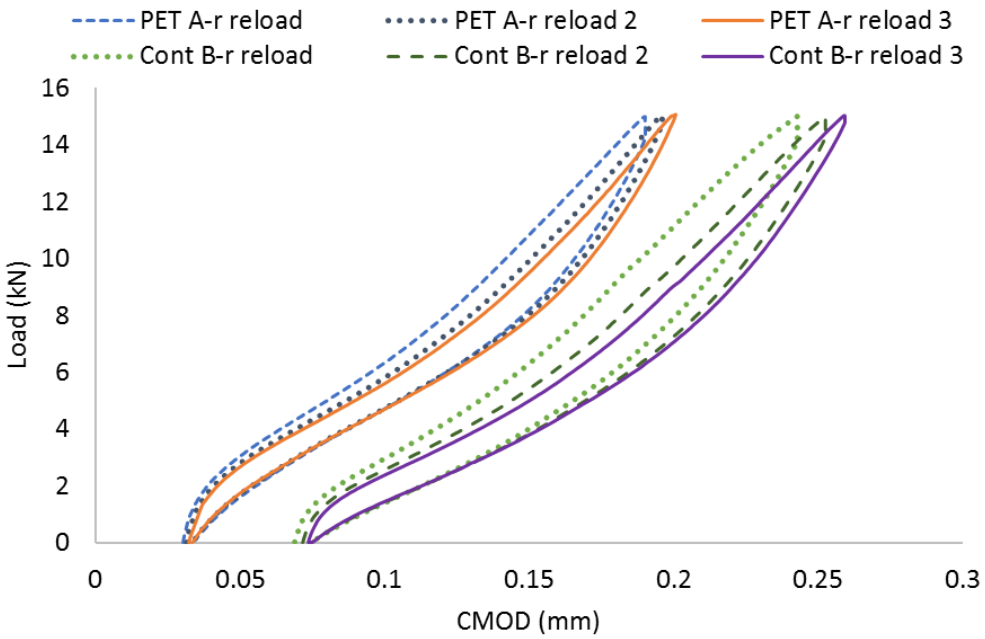

Figure 4.39: Load-CMOD reload curves for PET A-r and CONT B-r.

While all samples experienced increasing displacement at peak load with repeated loading, this effect was reduced in the PET samples. On average, the peak load displacement increased by 4.8% over three reload cycles for the PET beams, compared to 6.6% for CONT B-r. Moreover, the average final, unloaded CMOD reading after all load cycles for the PET beams was 0.045mm, 39% smaller than the 0.074mm measured on CONT B-r. Considering only PET A-r, which experienced the most successful polymer activation, this reduction in final CMOD reading

increases to 54%. This suggests that the compressive stress produced by the polymer tendon can reduce gradual displacement over time due to cyclic loading and that the compressive force generated by the PET was not lost during reload cycles.

Table 4.17: CMOD and microscope crack measurements on reload cycles for all samples (mm unless stated).

	PET A-r		PET B-r		PET C-r		CONT A-r		CONT B-r		CONT C-r	
	CMOD	Micro.	CMOD	Micro.	CMOD	Micro.	CMOD	Micro.	CMOD	Micro.	CMOD	Micro.
R1 peak	0.190	0.108	0.223	0.118	0.204	0.114	0.263	0.173	0.243	0.168	0.215	0.140
R1 unload	0.032	0.012	0.052	0.024	0.050	0.018	0.079	0.047	0.074	0.038	0.061	0.035
R2 peak	0.196		0.229		0.213		0.274		0.252			
R2 unload	0.033		0.052		0.050		0.080		0.074			
R3 peak	0.199		0.232		0.216				0.259			
R3 unload	0.034		0.052		0.050				0.074			
Increase over 3 cycles	4.7%		4.0%		5.9%				6.6%			

These results are similar to those produced by Yachuan and Jinping (2008) using shape memory alloy (SMA) wires in their super-elastic form in concrete beams, in which deflections were recovered over repeated load cycles. However, the SMA in this form can only recover displacements, not produce a compressive stress on the crack faces required to enhance autogenous healing. An autonomic healing response was instead introduced using brittle, adhesive-filled fibres.

Figure 4.40 shows DIC images of the test on sample PET A-r. It can be seen that three separate cracks are created by the loading process in both the PET and control beams due to the presence of the reinforcement. The cracks are still present in the sample following activation, although the crack closure is not as clear from the DIC strain images as in the unreinforced samples.

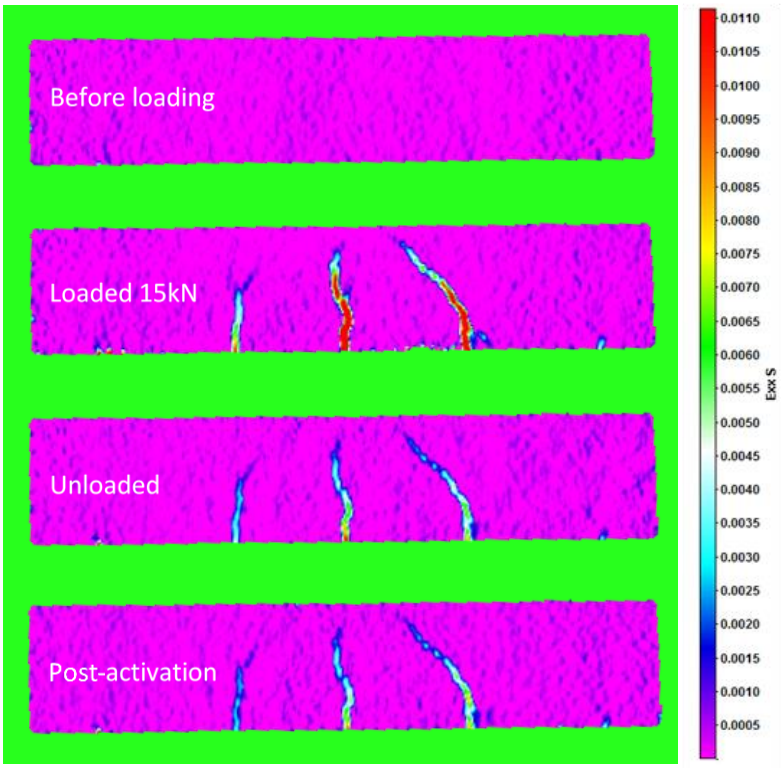

(a)

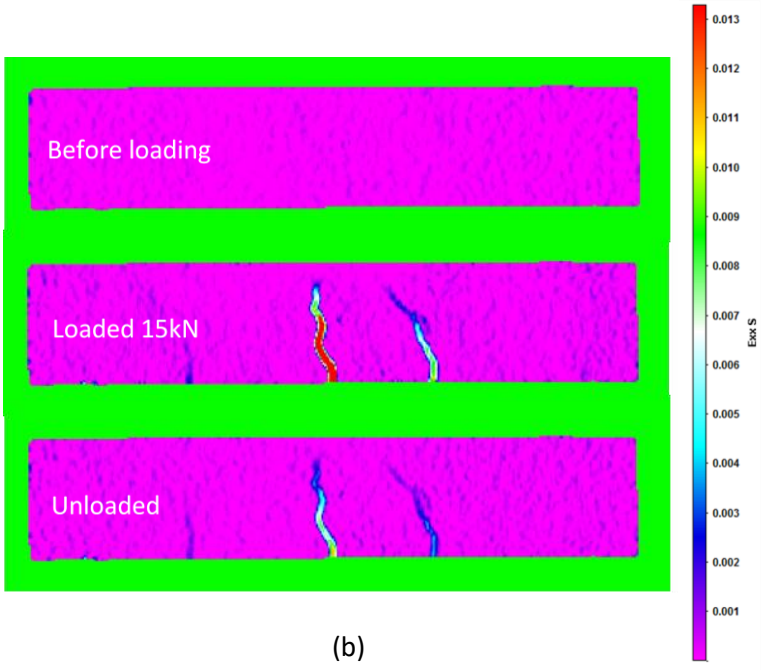

(b)

Figure 4.40: Digital Image Correlation (DIC) snapshots (a) activation of tendon in PET A-r (b) loading of CONT A-r. Axis indicates strain.

Due to the steel reinforcement, the induced cracks are much smaller in the reinforced PET samples upon unloading (average of 0.059mm CMOD compared to 0.209mm CMOD in unreinforced samples). In addition to the challenges of activation, such as achieving 90°C across

all of the filaments, the polymer tendon is also working against the misalignment of the crack faces and any debris wedged in the crack following initial loading to achieve any crack closure. In the unreinforced samples the residual cracks from initial loading were large enough to allow some crack closure to occur before effects of misalignment or debris could become significant.

The apparent increase in stiffness shown in both the initial and reload curves can be explained by the appearance of multiple cracks. As the CMOD measurement spanned only the central crack, the cracks which opened at higher loads were not recorded as additional displacements. This is demonstrated in Figure 4.41, which shows the reload curve as load plotted against displacement using a virtual strain gauge spanning the length of the beam derived from the DIC data, compared to displacement from the CMOD gauge. The DIC reload curve shows a more linear stiffness response as the displacement of the additional cracks is taken into account, thereby showing the 'actual' stiffness of the beam.

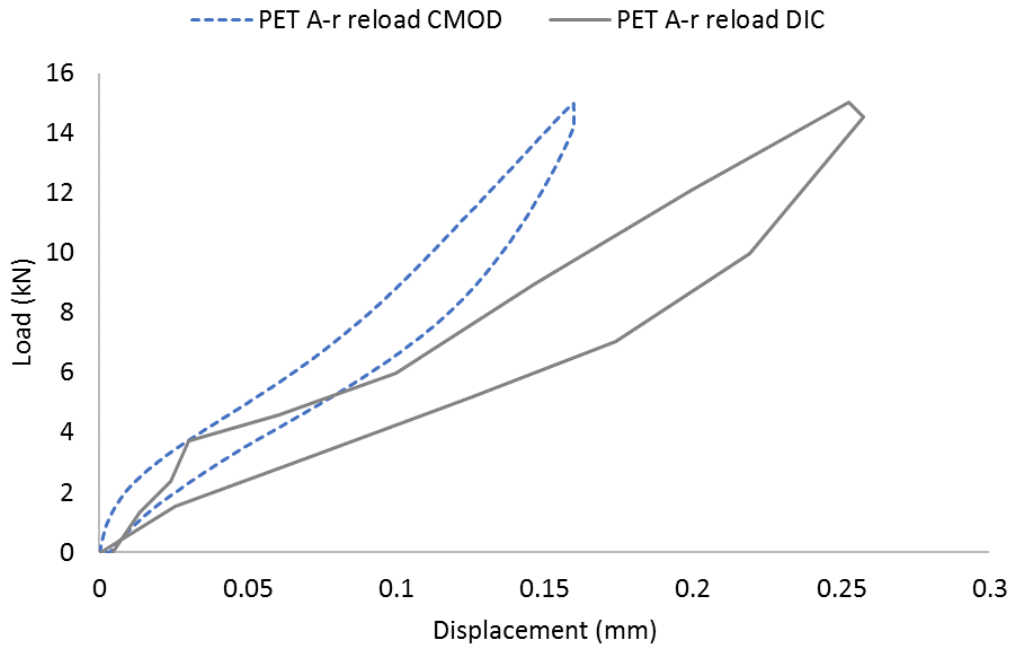

Figure 4.41: Comparison of load-displacement reload curves using CMOD and DIC displacement measurements.

The second and third cracks in the PET A-r sample were larger than those in CONT A-r, as shown by the DIC images in Figure 4.40, which would result in an apparent higher stiffness when measuring displacement across the central crack alone. It cannot therefore be concluded from

the CMOD measurements alone that inclusion and activation of the PET tendons results in an increase in stiffness of the beam samples.

4.4.5. Conclusions

A shape memory PET filament tendon has been developed which can be activated via an electrical wire system to close cracks in concrete beam samples. Restrained shrinkage stress experiments performed on the polymer tendons alone produced stresses of 17.79-19.19MPa upon activation and cooling.

Tendons embedded within unreinforced and reinforced concrete beams were cracked in three-point bending before activating the polymer using the electrical wire system. The stress produced in unreinforced beams resulted in crack closure of up to 85% and a significant increase in beam stiffness on reloading. In reinforced beams, despite challenges in achieving full activation of the polymer tendons, the measured crack closure was 26-39% based on CMOD measurements across the largest crack. Incremental increases in CMOD during repeated loading cycles on the reinforced beams were also reduced by the polymers.

4.5. CONCLUSIONS FROM CHAPTER 4

- Shape memory PET strips have been incorporated into 500x100x100 mm unreinforced concrete beam samples to enhance autogenous self-healing. Activation of the polymer resulted in a 78% reduction in surface crack width, increasing to 95% after 28 days curing in water. Load recovery of up to 33% was observed after six months' immersion in water for specimens in which the SMP strips were removed prior to testing, and an apparent load recovery of up to 98%, including the effects of a continued compressive load from the polymer, for specimens in which the SMP strips were embedded in the beams.

- A tendon made from 200 shape memory PET filaments has been developed following the higher shrinkage stress observed from these samples compared to PET strips in Chapter 3. The tendons are rigid prior to activation and can be activated via an electrical current, making them more practical for addition into concrete structures than the PET strips.

- The developed filament tendons have been tested without being embedded in the concrete beams, resulting in a restrained shrinkage stress of 17.79-19.19MPa upon activation and cooling. Their incorporation into unreinforced concrete beams resulted in a reduction in surface crack width of up to 85% and a significant increase in beam stiffness on reloading. In reinforced beams the reduction in crack width was 26-39% based on CMOD measurements due to the restraint to closure provided by the steel reinforcement and challenges in reaching the desired activation temperature within the polymer tendons.
- The restrained shrinkage stress produced at 90°C by the PET filament tendons containing 200 filaments (17.79-19.19MPa) was significantly lower than that produced by 10 filaments (36.98-41.50MPa) in Chapter 3. However, the stress produced by the tendons was consistent across the tests, demonstrating that while the manufacturing procedure could be improved to maximise the shrinkage stress of the tendons, it was sufficient to produce repeatable shape memory tendons capable of concrete crack closure in beam samples.
- The PET filament tendons have been manufactured into rigid elements with the addition of an injection-moulded PLA sleeve. This both retains the polymer's shape prior to installation within a concrete structure and protects the polymer and activation system from the concrete surroundings. This system would be far more practical to install than the previously-used PET strips, as they do not require pre-stressing against a mould and could be tied directly to steel reinforcement if required.

- The PET filament tendons developed and tested in this chapter were taken forward for implementation on full-scale site trials, described in Chapter 5. This required the development of an activation and temperature monitoring system capable of activating multiple tendons simultaneously. The site trials also involved the combination of PET tendons with flow networks, investigated as part of the Materials for Life project.

Chapter 5. On-Site Application of Self-Healing Concrete

5.1. INTRODUCTION

A key objective of the Materials for Life research project was the implementation of site trials on a live construction project. The aim of these trials was twofold. Firstly, to address the challenges associated with the implementation of self-healing concrete techniques at something akin to full-scale and secondly, to assess their feasibility and effectiveness in the field. This was achieved thanks to the support of the project's leading sponsor, Costain.

A trial structure was designed, constructed and tested containing the shape memory polymer tendons described in section 4.3.4. A healing system using microcapsules, developed at Cambridge University (Giannaros et al., 2016) and a bacterial healing system developed at Bath University (Sharma et al., 2015) were also tested, along with a 2D flow network system (Davies et al., 2015). These techniques are explained in more detail in section 5.3.

Within this chapter, a focus is given to the performance of the shape memory polymer tendons, with results from the other techniques included where these are relevant for comparison and where measurements have been taken by the author.

5.2. SITE TRIAL LOCATION AND STRUCTURAL DESIGN

The trial took place on the A465 Heads of the Valleys (HoV) section 2 project in South Wales, UK. This was a £200M contract to upgrade an 8.1km section of the A465 road between Gilwern and Brynmawr from single to dual carriageway. Costain Group Plc were the lead contractor for the project, the location of which is shown in Figure 5.1.

Figure 5.1: A465 Heads of the Valleys section 2 project location.

An area within the project site compound was used as the location for the trial structure. In this way, the structure was not interfering with the works taking place in the area but would be exposed to the same environmental conditions as concrete structures being built on the project. The research team aimed to replicate a conventional structure being constructed as part of the project. As the A465 HoV project includes long lengths of retaining wall structures of varying heights and designs, a retaining wall form was chosen.

Multiple sections of mock retaining walls, referred to as panels, were designed to contain different combinations of the self-healing techniques. Two panels that didn't contain any self-healing mechanisms were also constructed to act as controls. The overall structure included a reaction wall for loading the trial panels as well as a base slab to prevent overturning of the walls during loading. The base slab also provided a rigid datum from which the panels were monitored during testing. A concept model of the structure is shown in Figure 5.2.

For all elements of this structure the detailed structural design was completed according to the provisions of BS EN 1992. Although this model shows six panels, the central panel wasn't cast along with the others, but was retained as a reserve in case of unforeseen problems during construction. The panels were designed to crack at 500mm above the base slab by including 16mm diameter starter bars at 200mm centres on the front face up to this point, before changing to an A393 mesh (10mm diameter bars at 200mm centres) to create a weak section in

the panel at this location. This position is referred to as the change of section location (CoS) and is indicated in Figure 5.2.

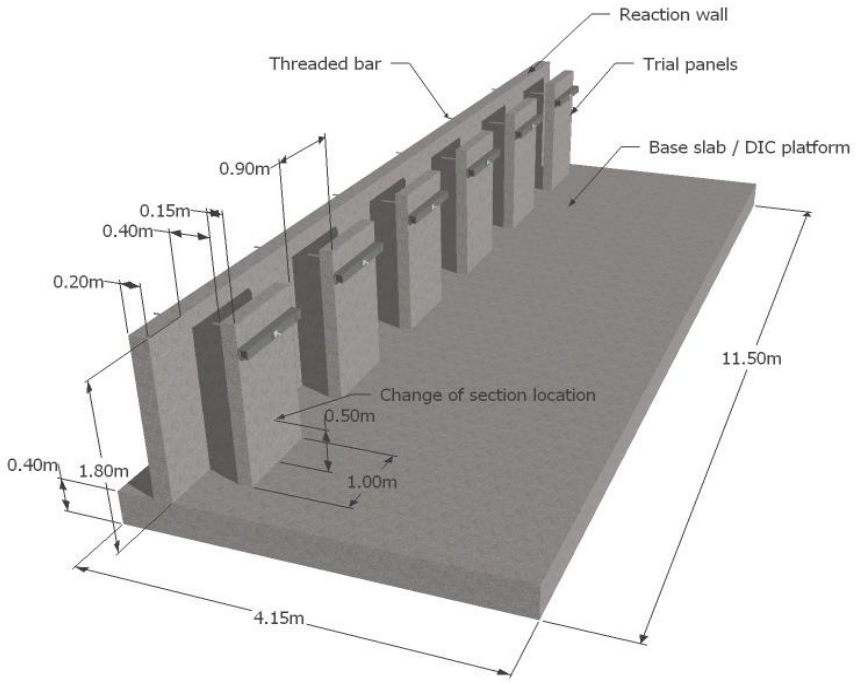

Figure 5.2: Concept model of trial structure.

A C40/50 structural concrete mix was specified, referred to as the control mix. This mix design is detailed in Table 5.1. This mix was used to cast the trial panels, with self-healing techniques added dependent on the panel as described in section 5.3. The control mix was designed to have a consistency of class S3. The measured slump when casting the trial panels was 100mm. To ensure the quality and robustness of the mix throughout the casting procedure a retarder was also added.

The concrete used for the base slab was a C40/50 strength, S3 consistency mix using CEM IIIA+SR (50% GGBS) with a minimum cement content of 380kg/m³ and maximum water-cement ratio of 0.4. The reaction wall was cast using a C40/50 mix with 70% GGBS cement replacement at the request of the permanent works project team who wished to trial this mix for use elsewhere on the site. As this mix was still intended to achieve its design strength after 28 days this change was not considered to be significant.

Table 5.1: Control mix design.

Material	SSD Quantity (kg/m³ unless noted otherwise)
Cement (CEM I)	415
10mm Limestone aggregates	944
Limestone fines (0-2mm)	396
Marine sand	393
Water	179
Admix: VS100 (SIKA) plasticiser	0.35 l/100kg cement
Admix: SIKATARD R retarder	0.1 l/100kg cement

The trial structure was constructed over an 8-week period. The base slab was initially cast and allowed to cure for a minimum of 28 days before casting the reaction wall and finally the trial panels. The trial structure as constructed is shown in Figure 5.3.

Figure 5.3: Trial structure.

5.3. TRIAL PANEL CONTENTS

The self-healing techniques incorporated into each panel are detailed in Table 5.2. The trial panels and their contents are shown schematically in Figure 5.4. Panels B, D and E were cast using the control mix directly from the mixing truck. For panel A, the concrete was transferred to a 120l Belle mixer prior to casting to add the microcapsules. Panel C included a section of bacteria concrete, containing CEM II cement and a lightweight aggregate of bacteria infused perlite particles. This was also mixed on-site using the 120l Belle mixer.

Table 5.2: Trial panel and embedded self-healing mechanisms.

Panel	Research Institution	Materials
A	University of Cambridge	C40/50 Reinforced concrete with microcapsules containing sodium silicate solution
B	Cardiff University	C40/50 Reinforced concrete with shape memory polymers and flow networks
C	University of Bath	C40/50 Reinforced concrete with bacteria-infused pearlite and flow networks
D	All	C40/50 Reinforced Concrete (control)
E	All	C40/50 Reinforced Concrete (control) with flow networks

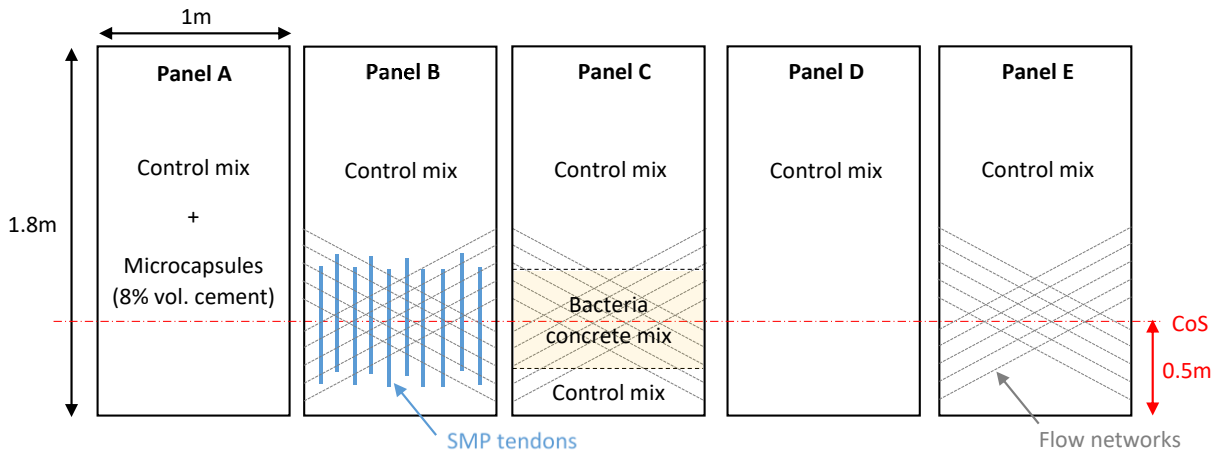

Figure 5.4: Self-healing panels arrangement.

5.3.1. Panel A: Microencapsulated sodium silicate in concrete

Spherical, polymeric microcapsules, carrying liquid sodium silicate, were used in panel A. Sodium silicate was selected as the healing compound as it can form products of a similar nature to the host cementitious matrix. The potential of sodium silicate solution as a healing agent for cement-based composites had previously been investigated both in terms of crack closure and durability by Kanellopoulos et al. (2015) and found to be the most suitable healing material for this type of encapsulation. The microcapsules had a polymeric shell made of cross-linked gelatin and acacia gum. Their cargo was a solution of mineral oil and liquid sodium silicate (40% weight in H_2O). The microcapsules average size was 290μm, with a density of approximately 0.98gr/cm^3. Figure 5.5 shows an optical microscope image of the microcapsules.

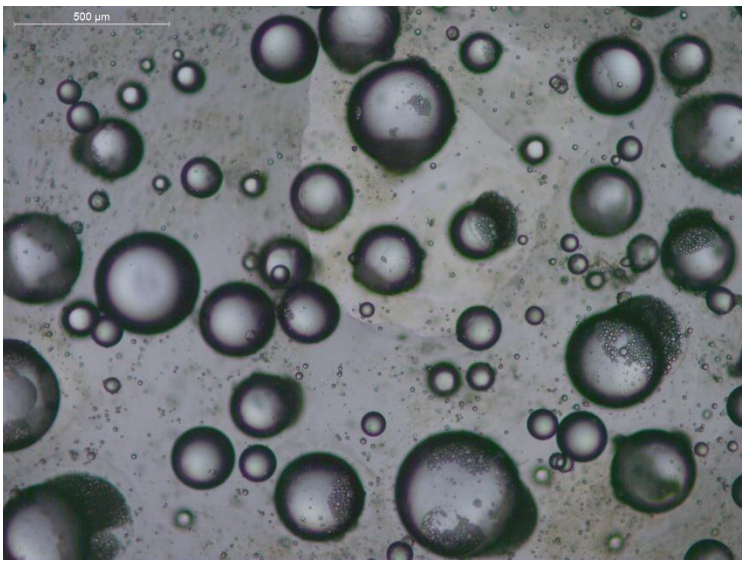

Figure 5.5: Microscope image of the microcapsules used in this study (Kanellopolous et al., 2016b).

A total of 8% by volume of cement of microcapsules were mixed into the concrete using the onsite mixer. A small quantity of water was used to disperse the microcapsules within the concrete mix. This increased the water-cement ratio of the mix from 0.43 to 0.45 for panel A. It also resulted in an increase in the slump value to 120mm, compared to 100mm for the control mix. It was anticipated that this would result in a small decrease in compressive strength, but that the mix would still fall within the C40/50 strength class. Figure 5.6 shows the microcapsules prior to and during their addition to the mix.

(a) (b)

Figure 5.6: (a) Microcapsules in dispersion prior to mixing and (b) addition of microcapsules into the mix.

5.3.2. Panel B: Shape memory polymer tendons and flow networks

Panel B contained the control mix, with polymer tendons and flow networks already set up within the formwork prior to the pour. The tendons described in section 4.3.4 were manufactured to a length of 750mm and tied to the reinforcement within the trial structure using steel tie wire. At a selected time after casting, the tendons were activated via an electrical current.

The required number of tendons within the panel to generate a minimum stress of 0.5MPa across the cracked external face was calculated, based on the stress needed to enhance autogenous healing (Heide and Schlangen, 2007). While a minimum stress of 1MPa was used for concrete beam samples in the laboratory experiments in section 4.4, for the trial panel this was found to result in a congested cross section, which would have made compaction of the concrete difficult.

The theoretical applied stress due to the shrinkage of the tendons was calculated using the same method as for the concrete beam samples in section 4.2.1. The concrete panel parameters (h=150 mm, b=1000 mm, y=75 mm, e=40 mm) were substituted into equation (6) along with an estimated restrained shrinkage stress for the polymer filaments.

Due to the project timescales, the set-up of the tendons within the site trial panel took place prior to the experiments detailed in section 4.4. The restrained shrinkage stress σ_P was therefore taken as 30MPa, as a conservative estimate based on the results detailed in section 3.5.1. Based on these calculations, ten tendons were placed within panel B, to generate a stress of 0.59MPa across the cracked external face upon activation.

If the restrained shrinkage stress is instead taken as the average stress calculated from the results of the tendons within unreinforced beam samples from section 4.4.4 (17MPa), the theoretical stress generated on the external face falls to 0.34MPa.

The layout of the tendons in panel B can be seen in Figure 5.7 and Figure 5.8. The tendons were staggered within the panel as shown. This was to reduce the risk of a crack being induced at either end of the row of tendons upon loading because of the alignment of the tendon anchorages.

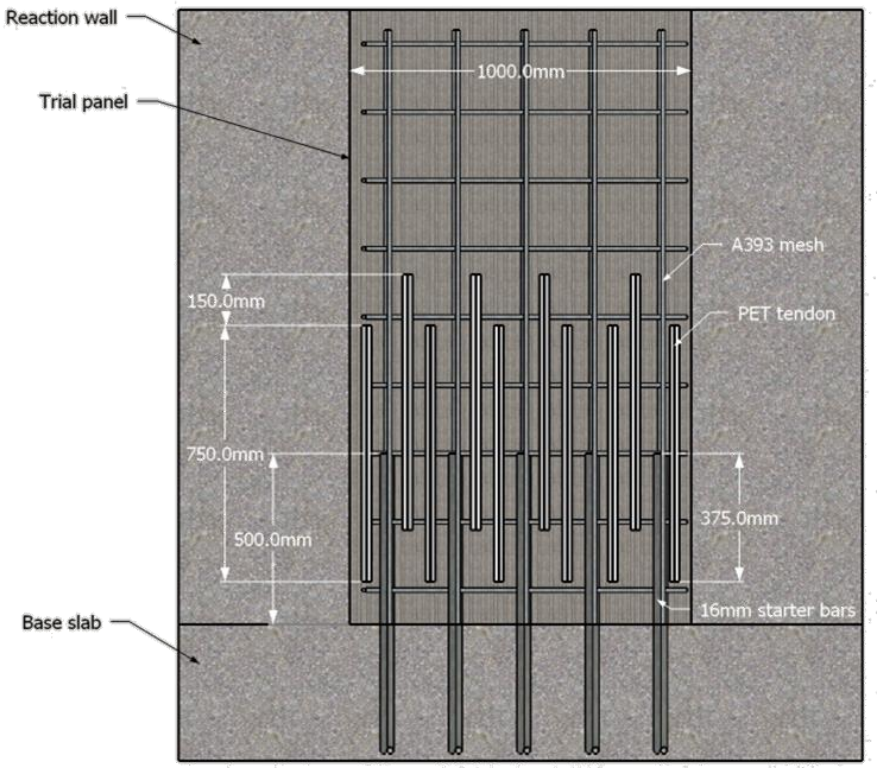

Figure 5.7: Position of PET tendons within trial panel B.

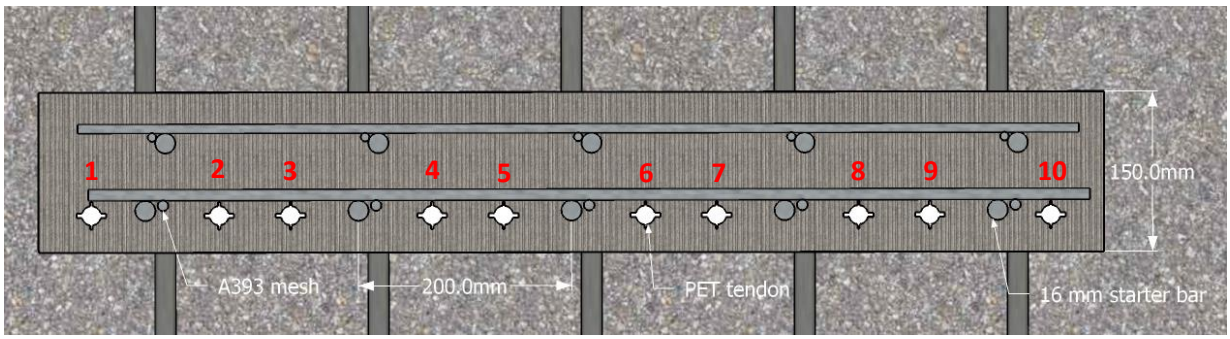

Figure 5.8: Cross-section of panel B layout with PET tendons.

To allow the activation of the polymer tendons and the measurement of temperature within them, the activation wires and thermocouples were passed through the back of the wooden

formwork through drilled holes. The activation system is described in detail in section 5.6. The holes were then plugged with silicone around the wires. This set-up is shown in Figure 5.9.

Figure 5.9: Set-up of polymer activation wires within formwork.

Flow networks were included in panels B, C and E. For panels B and E this was to allow the injection of sodium silicate solution into the panel as a healing agent. For panel C the networks were included to provide a mechanism for feeding the bacteria.

A 2D network of 4mm diameter channels was created using polyurethane tubes, which were removed from the concrete after a minimum of 24 hours curing. The channels were connected by 3D printed joints made from polylactic acid (PLA), shown in Figure 5.10, which were tied to the outermost reinforcement. The tubes were fastened against the side of the formwork using crocodile clips, before being pulled tight and fastened at the opposing end. The tubes were then coated in petroleum jelly to ensure a low friction surface, to aid their removal. This arrangement, in panel E, is shown in Figure 5.11.

In panel B, the networks were placed in front of the polymer tendons, shown in Figure 5.12. Holes were drilled into the sides of the panel and the flow networks were terminated with a lockable steel injection packer. This allowed each channel to be sealed individually to load and pressurise the network.

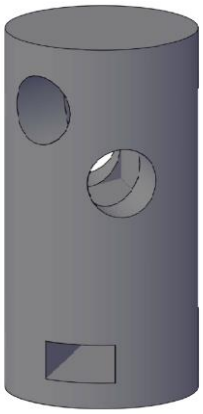

Figure 5.10: 3D-printed joint for flow networks.

(a) (b)

Figure 5.11: Panel E flow network set-up: (a) front view, (b) side view of formwork

Figure 5.12: Layout of SMP tendons and flow networks in panel B.

5.3.3. Panel C: Bacteria concrete and flow networks

The bacteria concrete mix developed by the University of Bath for use within the site trial contained spores of *Bacillus pseudofirmus* DSM 8715, infused into lightweight perlite aggregate

particles. An organic mineral precursor, which included yeast extract and calcium acetate, was also included in separate aggregate particles as a food source for the bacteria.

Due to the challenge of producing sufficient quantities of bacteria to fill an entire panel, it was decided that panel C would contain three lifts; the first a 250mm layer of structural concrete using the control mix, the second a 500mm layer of bacteria concrete in the zone in which the panels had been designed to crack, and a third layer of the control mix to complete the panel. Panel C also contained flow networks as a potential feeding system for the bacteria in the later stages of testing. These networks were formed in the same way as in panel B.

5.3.4. Panels D and E: Controls

Panels D and E were cast as controls. Panel D was cast using the control mix without any additions, while Panel E contained the control mix together with flow networks as in Panels B and C.

5.4. CONSTRUCTION

Construction of the base slab and reaction wall began on 10th August 2015. The structure was situated in a former public car park which had an existing flexible pavement surface. An excavator was used to remove the asphalt surface (using a hydraulic breaker attachment) and to excavate down to 500mm below the existing surface level.

A 50mm blinding concrete layer was cast to provide a level surface for the base slab reinforcement. The reinforcement cage, shown in Figure 5.13, was tied and placed as per the design drawings in Appendix D. The cage consisted of 12mm diameter high tensile steel bars in both directions, top and bottom with a nominal 30mm cover and at 200mm centres. 16mm diameter starter bars were also placed at 200mm centres for both the reaction wall and trial panels as per the design.

Figure 5.13: Base slab reinforcement.

The base slab concrete was poured to a depth of 425mm. The concrete was poured from 6m³ concrete wagons using an excavator, and compacted using vibrating pokers before being given a tamp finish. This process is shown in Figure 5.14.

(a) (b) (c)

Figure 5.14: Base slab concrete pour: (a) placement. (b) compaction, (c) finishing.

The reaction wall vertical steel reinforcement on the back face (to be loaded in tension) consisted of 16mm diameter high tensile steel running throughout the entire height at 200mm centres. Horizontal reinforcement comprised 12mm diameter high tensile steel bars placed at 200mm centres. On the front compression face A393 steel mesh (10mm diameter both ways at 200mm centres) was used for anti-cracking reinforcement. The steel was tied on to the starter bars as shown in Figure 5.15(a).

(a) (b)

Figure 5.15: Reaction wall (a) reinforcement and (b) formwork arrangement.

Formwork for the reaction wall consisted of the PERI TRIO system: steel faced modular panels 1.8m in height and 2.4m wide which were clamped together to run the length of the wall. The set-up prior to the concrete pour is shown in Figure 5.15(b). The reaction wall was poured using a 'tremie' skip attached to an excavator, compacted using vibrating pokers and given a float finish on top. This process can be seen in Figure 5.16.

Figure 5.16: Reaction wall concrete pour.

The reaction wall was left to cure for 48 hours before the formwork was removed. The structure at this stage is shown in Figure 5.17.

Figure 5.17: Reaction wall and base slab.

The steel reinforcement for all trial panels consisted of an A393 steel mesh (10mm diameter both ways, 200mm centres) on the front (tensile) face, and an A142 steel mesh (6mm diameter both ways, 200mm centres) on the back (compression) face. The cover to the front face was 30mm (nominal), and 20mm (nominal) on the back face. Formwork for the panels was made up from plywood sheets and timber. The final arrangement of the formwork prior to the concrete pour can be seen in Figure 5.18.

The trial panels were poured 7 weeks after the base slab. A delivery of 2m³ of the control mix (described in Table 5.1) was made. As the concrete for panels A and C required on-site mixing, a 120l Belle mixer was hired from Speedy hire and placed alongside the panels. The pour sequence for all of the panels is described in Table 5.3, and the mixing set up shown in Figure 5.19.

Figure 5.18: Trial panel formwork prior to concrete pour.

Table 5.3: On-site mixing and pouring sequence for trial panels.

Sequence step	Action
1	Pour first layer of control mix into panel C (250mm nominal depth) and compact
2	Mix bacteria concrete in mixer (while sequence step 3 carried out)
3	Pour control mix into control panels D and E and compact
4	Pour bacteria concrete layer into panel C (500mm nominal depth) and compact
5	Clean out mixer using water and aggregates (while sequence step 6 carried out)
6	Pour control mix into panel B and compact
7	Mix control mix with microcapsules in mixer
8	Pour microcapsule concrete into panel A and compact

Figure 5.19: On-site concrete mixing set-up.

All of the panels were compacted in three roughly equal layers using a 25mm diameter vibrating poker, with the exception of panel C in which the layer depths were determined by the quantity of bacteria concrete. Twelve concrete cubes (100x100x100mm) were taken for compressive strength tests.

The panels were left to cure for two days before the formwork was removed. For panels B, C and E the flow network tubes were then removed by pulling on one end of each tube until the entire tube slid out of the panel. The panels were then left to cure for a minimum of 28 days to ensure the full design strength of the concrete was achieved.

5.5. LOADING CONFIGURATION

To monitor crack healing, it was necessary to damage the panels through controlled loading. To apply this loading, a threaded bar and hydraulic jack system was used. The arrangement of this system is shown in Figure 5.20.

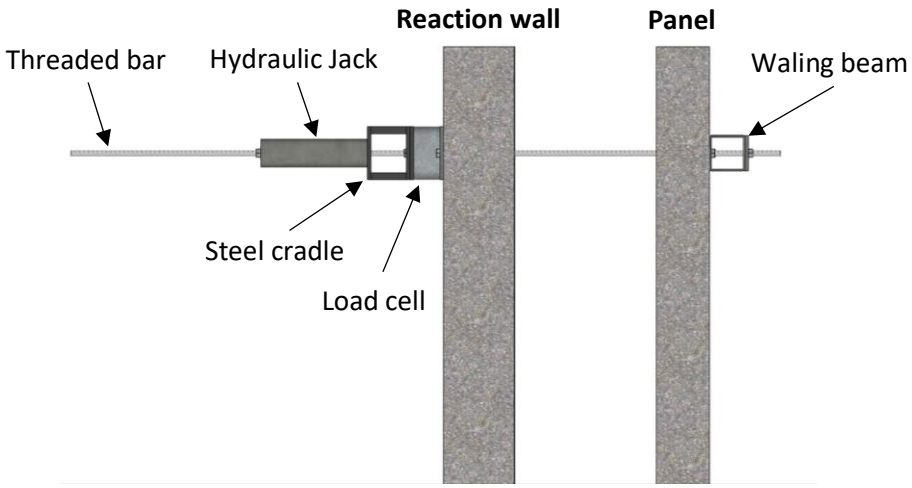

Figure 5.20: Loading arrangement through reaction wall and trial panel.

To accommodate the threaded bars, holes were cast at a height of 1.5m above the base slab into each panel and into the reaction wall. The bar was then passed through the structure and bolted on to a 100x100x10mm rectangular hollow steel waling beam, which in turn was attached to the panel's front surface with anchor bolts. This waling beam was used to distribute the load across the width of the panel to a contact point at either side, minimising uneven load distribution. On the back face of the reaction wall, the threaded bar was passed through a 200kN load cell and steel cradle to allow 'locking off' of the applied load using a nut. Images of this loading system on site are shown in Figure 5.21.

When loading the panels, the hydraulic jack was placed onto the threaded bar and rested against the steel cradle, in turn resting against the load cell. The load applied by the jack was controlled via a hand pump. Once the specified maximum load had been applied, a nut was tightened within the cradle to avoid the load gradually dropping while measurements were taken.

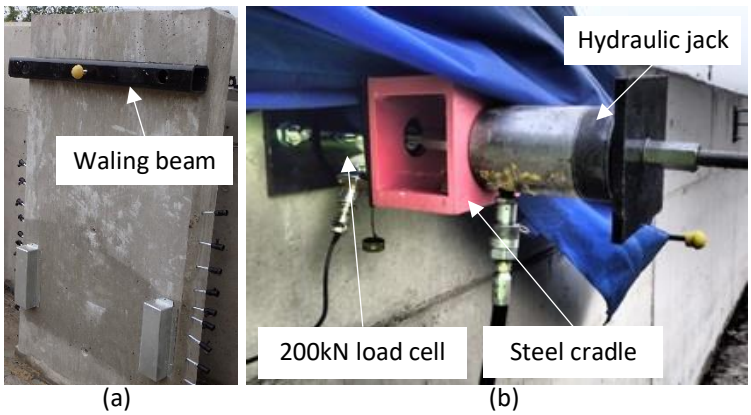

Figure 5.21: Loading arrangement (a) front face of panel; (b) back of reaction wall.

On the front face of each panel, the threaded bar passed through the mid-span of the waling beam. At the two anchor points of the waling beam to the trial panel, steel washers were used to provide a contact point. This is shown in Figure 5.22.

Figure 5.22: Waling beam mounting arrangement on face of trial panel.

5.6. SMP ACTIVATION SYSTEM

The wire heating system described in section 4.3.2 was incorporated into the polymer tendons manufactured for use on site. This consisted of a length of 0.5mm diameter nickel-chrome wire wrapped around each tendon with an approximate coil spacing of 10mm. As it was convenient

for activation on site for both ends of the wire to terminate at the same end of the tendon, one end of the heating wire was spliced onto a length of stranded copper wire using solder and heat shrink tubing, then run down the outside length of the tendon sleeve within a 6mm diameter plastic tube.

It was planned to activate all of the PET tendons within the concrete structure simultaneously. To achieve this, a circuit board was built which allowed ten channels, wired in parallel, to be powered from a single source and turned on and off using relays. The board and its constituent parts are shown in Figure 5.23. A LabView model was then built which could monitor the internal and external temperature of each individual tendon through the embedded thermocouples, sending signals to the relays to turn each channel on and off, maintaining a set temperature. This model also had a built-in manual override button to switch each channel off if necessary.

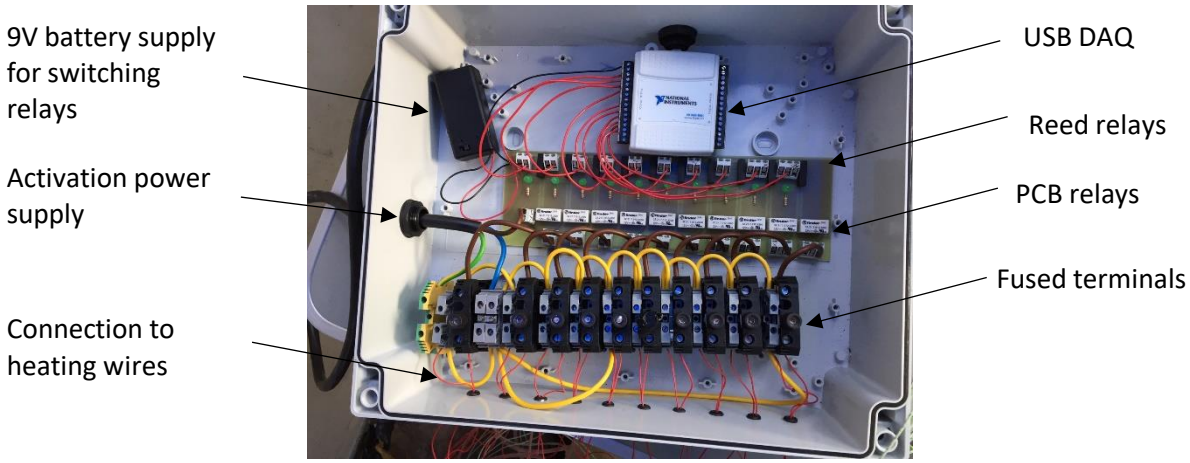

Figure 5.23: Activation circuit board.

Each channel was turned on and off using a National Instruments USB data acquisition (DAQ) device with digital input and output ports. A simplified wiring diagram for the circuit is shown in Figure 5.24. Each channel on the activation circuit was wired into a single output port on the DAQ device, which were then controlled by the LabView model on the laptop. When turned on, the DAQ sent a 5V signal to the reed relays, which in turn allowed the 9V signal to be sent through to the PCB relays, tuning the channel on and allowing the activation power supply to pass through to the heating wires.

Once a target temperature had been reached for a single channel, the LabView model commanded the DAQ to stop sending the signal, turning the power supply off for that heating wire. Once the temperature had dropped back below the target temperature the reverse occurred and the channel was turned back on. Each channel was also connected to an LED to indicate which channels were on at any one point.

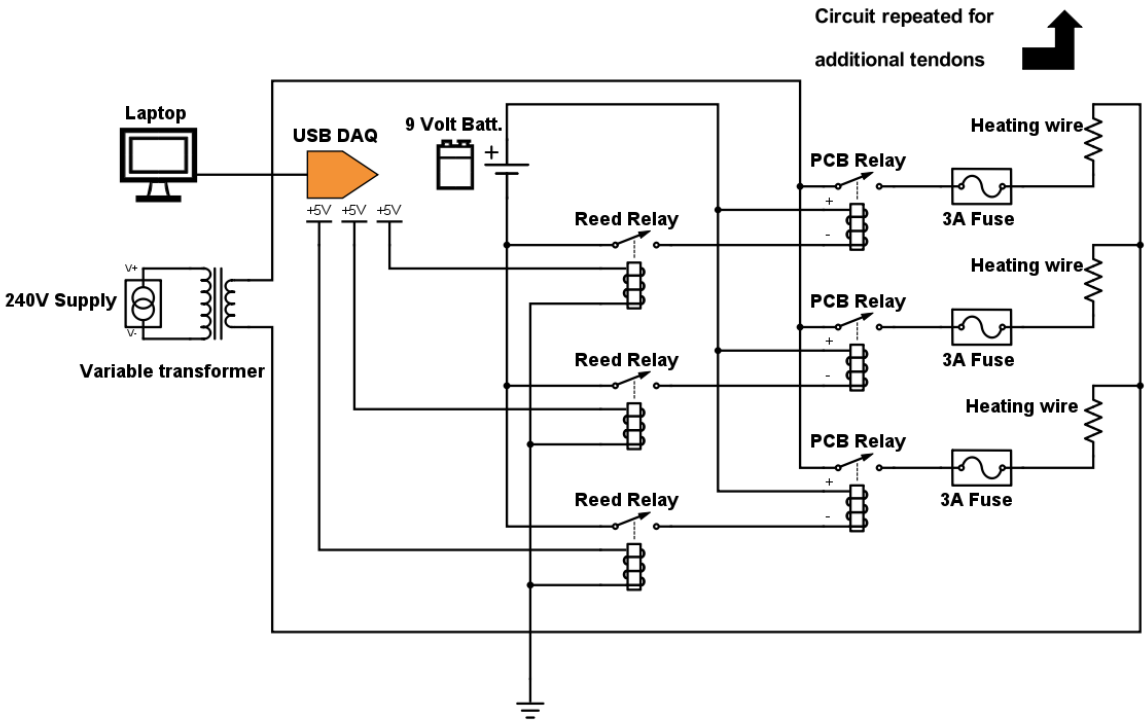

Figure 5.24: Activation system wiring diagram showing three channels.

As all channels were wired in parallel to avoid excessive voltage, the main risk was that the Nichrome wires within the polymer tendons would draw too much current. The nominal resistance of the Nichrome wire was 5.5ohms/metre (Company, 2016). The estimated required voltage for the 4m length of wire incorporated into each tendon to reach the desired 90°C was 35V based on experiments detailed in section 4.3.2. This resulted in an estimated drawn current of 1.59A per tendon. Ten tendons activated simultaneously therefore gives an estimated total current load of 15.9A on the system.

To manage this estimated current, each part of the activation system was designed to withstand a current of 30A. An Ashley-Edison variable transformer with a maximum constant current load

of 30A was used, to be connected to a 32A generator. The activation circuit was directly plugged into this variable transformer to then distribute the current across the ten activation channels. Each channel contained a 3A fuse to ensure that if a single channel began drawing excessive current this would not cause damage to the rest of the system.

A laboratory test was carried out to simulate the activation on site. Ten 4m lengths of the 0.5mm Nichrome wire were cut and each connected to its own activation channel. One of the wires (wire no. 9) was left deliberately short, at 2.95m rather than 4m, as there was a concern that if any of the heating wires in the tendons on site were shorter than the others these would draw more current and overheat. This setup would test whether the regulation of the activation circuit was sufficient to prevent this from occurring.

As this test was carried out in the lab, the power was supplied from a standard 230V, 13A connection. A fixed transformer was therefore used to reduce the supply to a safer 110V and the voltage on the variable transformer was limited to 20V (corresponding to an estimated 9A total current across all wires) to ensure the fuses were not blown. An ammeter was also wired into the circuit to check these assumptions. This set-up is shown in Figure 5.25.

Figure 5.25: Activation system lab test setup.

The heating wires were coiled to simplify testing. A K-type thermocouple was inserted into each coil of heating wire and fixed in place using electrical tape. These thermocouples were

connected to a National Instruments SCXI-1000 chassis containing an SCXI-1102 thermocouple amplifier, in turn connected via an SCXI-1600 USB data acquisition module to a laptop running the LabView software. The target temperature on the LabView model was set to 90°C. A multimeter was used to check the voltage across the channels during testing.

The voltage was set to 20V on the variable transformer, and the power supply was turned on. All channels were left on for a period of three minutes, before being turned off and the wires allowed to cool back to room temperature for a further six minutes. The results of this experiment can be seen in Figure 5.26.

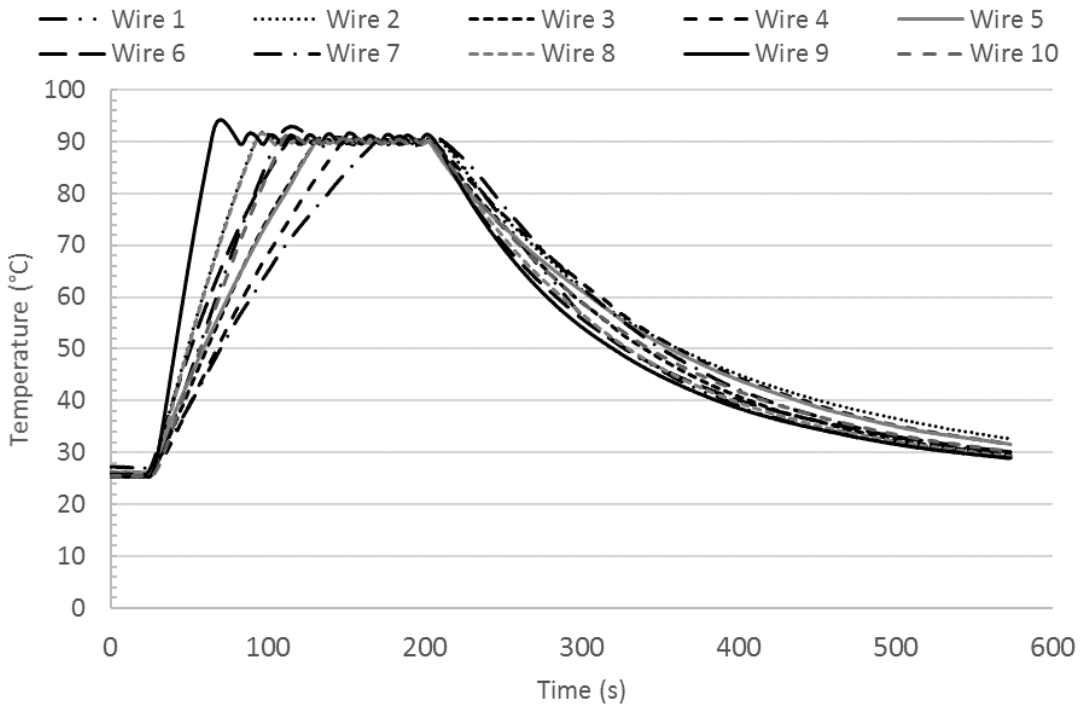

Figure 5.26: Activation system lab test results.

The activation system successfully heated all of the wires to the 90°C target temperature with just a 20V supply, suggesting that this lower value may be sufficient when activating the polymer tendons on site. The current recorded by the ammeter with all channels activated was 8.2A, lower than the expected 9A. This suggests an actual wire resistance of 5.94ohms/metre.

As expected, wire 9 (the shortened length) heated up to 90°C much faster than the other lengths of wire. This resulted in a small overheating of this wire upon reaching the target temperature

by 4-5°C. For all other heating wires, the temperature was regulated to within 3°C of the target temperature through the use of the LabView model and data acquisition system. Given that the polymer shrinkage stress continues to rise with temperatures up to 110°C, this level of control was deemed sufficient for the system's use on site.

5.7. MONITORING EQUIPMENT AND METHODOLOGY

Throughout the site trial the crack widths, deflections, strains and applied load on the panels were all monitored. This was achieved using a combination of a demountable mechanical (DEMEC) strain gauge, optical microscope, linear variable displacement transducers (LVDT), load cells and a Digital Image Correlation (DIC) system. A summary of the monitoring equipment used within the site trial is detailed in Table 5.4.

Table 5.4: Monitoring equipment specifications.

Equipment	Description	Measurement	Accuracy
NI SCXI-1000	SCXI Chassis	None-chassis only	-
NI SCXI-1600	USB data acquisition module	None-connection to laptop	-
NI SCXI-1102	32 channel Thermocouple amplifier	Temperature (°C) through thermocouples	-
NI SCXI-1520	8 channel strain gauge input module	Load (N) through load cell	-
NI SCXI-1540	8 channel LVDT input module	Displacement (mm) through LVDTs	-
Thermocouples	K-type thermocouple	Temperature (-60°C – 350°C)	±1.5°C (tolerance class 1 to IEC 584)
Load cell	200kN annular compression load cell	Load (N) up to 200kN	±0.2% of max load
LVDTs	Unguided model ACT1000 LVDT	Displacement (mm) ±25mm	linearity error <±0.5% of full range output
DIC camera system	LaVision Imager X-lite 8M CCD camera with DaVis software	Strain (S), displacement (mm)	Varies with field of view – 5.5x5.5µm pixel size, CCD resolution 3312x2488 pixel
Microscope	Veho vms-004 20-400x digital USB microscope at 20x magnification	Microscope images	-

A National Instruments (NI) SCXI chassis containing modules for strain, temperature and displacement measurements was used to collect and combine the monitoring results. The

modules allowed all measurements to be received simultaneously through a USB connection to a laptop. A programme in LabView 2013 was created to record these inputs and, in the case of panel B, to turn the activation system on and off as described in section 5.6.

Strains across the face of each panel were also monitored using the LaVision DIC camera system described in section 4.4.3. This allowed strain images of the panels during the loading, activation and monitoring period to be generated.

The speckle pattern was created on the faces of the trial panels using standard paint by first painting the surface white, then applying a black pattern using a paint roller with a studded cover, which resulted in a relatively uniform arrangement of black spots. This pattern was then supplemented using a wooden block with a patterned surface to create an uneven arrangement of spots across the whole surface of the panel. It was necessary to use both techniques to ensure that the pattern was random, as the DIC system needs to be able to split the surface into distinct groups of spots which are distinguishable from adjacent groups. This process is shown in Figure 5.27.

(a) (b) (c)

Figure 5.27: Application of DIC speckle pattern to trial panels (a) uniform spots; (b) uneven application using wooden block; (c) final pattern.

For panels A, C and D the pattern was only applied to half of the width of the panel as the team from Cambridge planned to take permeability measurements on both the painted and

unpainted surfaces of these panels. The surfaces of panels B and E were completely covered in the speckled pattern as it was necessary to monitor the strain developments over the whole of the panel to determine the performance of the SMP tendons.

5.7.1. Crack width and displacement measurements

Six LVDTs were used to monitor each panel. The locations of these are shown in Figure 5.28. The two LVDTs on the front face (LVDTs 0 and 1) were used to monitor the cracks generated by the test loads and their variation over the monitoring period. LVDTs 2-5, shown in Figure 5.29, were used to monitor the displacement of the panel and reaction wall. These LVDTs were attached to an angle section steel beam, in turn attached to a square hollow section steel column bolted to the base slab using chemical anchor bolts. This was to ensure that the support system was independent of the panel and reaction wall. Using four LVDTs in this arrangement allowed any 'twist' in the panel to be recorded, as well as monitoring overall displacement during loading and monitoring. All LVDTs were covered with aluminium sheet boxes to protect them from the weather.

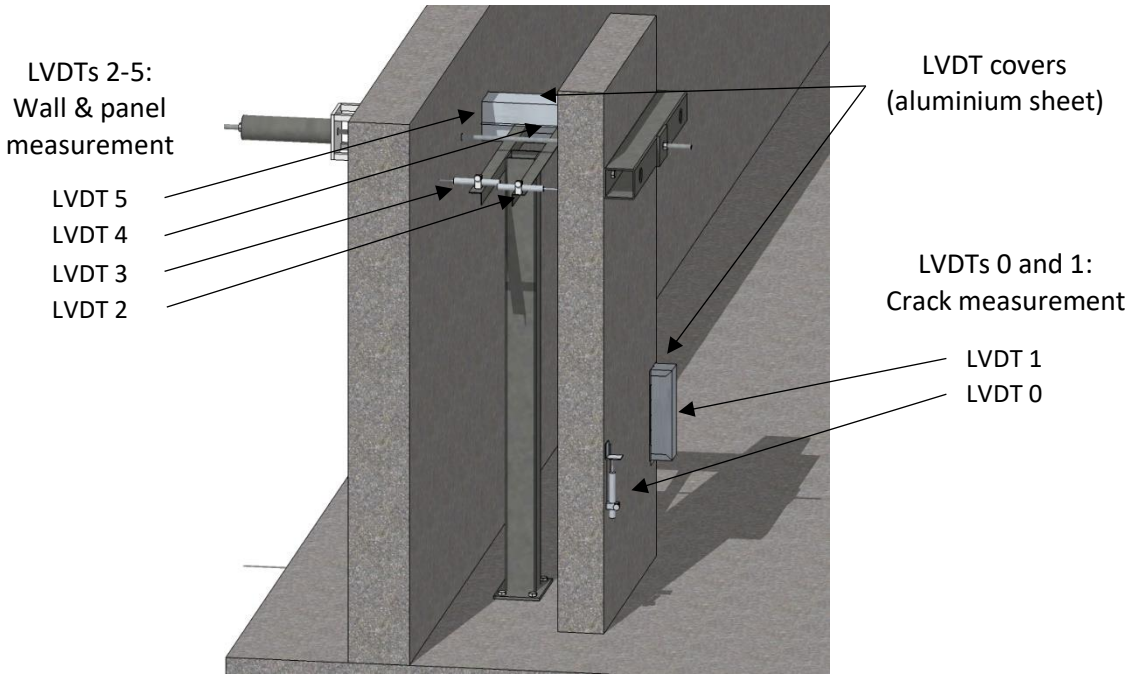

Figure 5.28: Locations of LVDTs on trial panels.

Figure 5.29: LVDTs 2-5, positioned to measure displacements of the trial panel and reaction wall.

In addition to the LVDTs, to monitor displacement across the cracks, DEMEC pips were placed on the front face of each panel as shown in Figure 5.30(b). Three sets of pips, 1A-1B, 2A-2B and 3A-3B, each with a gauge length of 100mm, were placed on both the left and right hand sides of every panel spanning the Change of Section (CoS). A staggered arrangement was used to ensure that any cracks would be picked up by at least one set of pips, as shown by the crack example shown in Figure 5.30(b), which appeared at approximately 35mm below the CoS location.

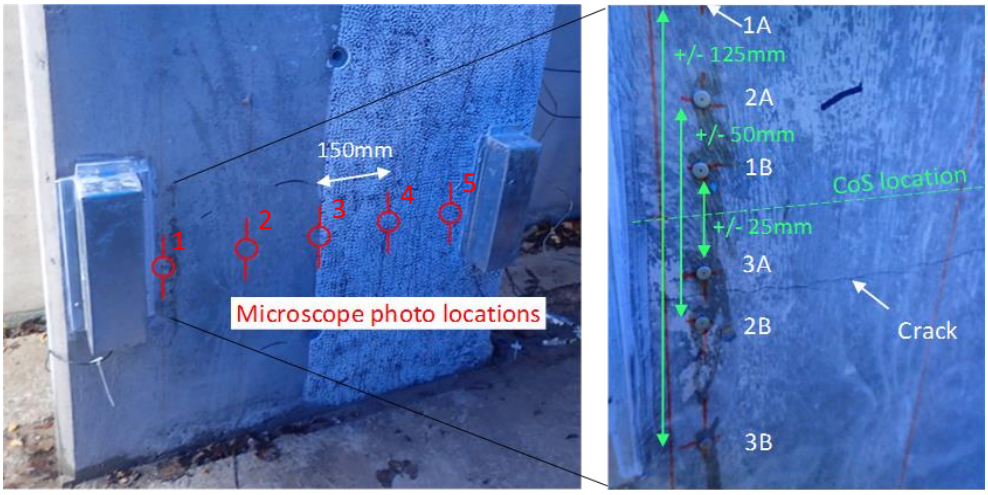

(a) (b)

Figure 5.30: Location of (a) microscope photos, (b) DEMEC pips for crack width measurements.

Figure 5.30(a) shows the five locations across the width of each panel at which crack width measurements were made from photographs taken through a microscope. A notched gauge was used as a scale for each image and the crack width was measured perpendicular to the crack direction using ImageJ software (ImageJ, 2016). Three measurements were made from each

image, at approximately equal spacing across the field of view and then averaged to give a single crack width value for that location.

5.8. LOADING AND DISPLACEMENT MONITORING PROCEDURE

The testing and monitoring schedule is shown in Table 5.5. Each panel was loaded at a rate of approximately 200 N/s until cracking occurred at the CoS location. This moment was clearly identifiable by a significant drop in load and the appearance of a visible crack at approximately 500mm above the base slab. An approximate measurement of the crack width was then obtained using the front face LVDT measurements, and, if necessary, the panel was loaded further until this crack width was at least 0.5mm to ensure a sufficiently large residual crack remained when the load was removed. Panels B and E were loaded to 20kN post-cracking to ensure repeatability following activation of the polymer tendons.

Table 5.5: Site trial testing and monitoring schedule.

Process	Panels	Days after casting
Initial loading and unloading	All Panel E load 'locked off' at 20kN	35 ±2
Second loading and unloading	Panels B and E - loading to 20kN and unloading to remove autogenous healing effect. Panel E first unloaded from locked off state	58
Activation of polymers and post-activation loading	Panel B	58
1-month measurements	All	63 ±2 (28 days after initial loading)
2-month measurements	All	91 ±2
3-month measurements	All	119 ±2
4-month measurements	All	147 ±2
Loading of flow networks with sodium silicate	Panels B and E	147
Flushing of flow networks with water	Panels B and E	149
5-month measurements	All	175 ±2
Loading of flow networks with sodium silicate	Panels B and E	175 ±2
6-month measurements	All	203 ±2
Final loading and unloading	Panels A, B, D and E	203 ±2

The peak load on the panels was held constant by tightening the locking nut on the loading arrangement, while microscope and DEMEC measurements were taken. This arrangement was

used to avoid a reduction in pressure from the hand pump causing a drop in load. The load was then reduced to zero. To achieve this, a small additional load above the peak load was applied using the pump to allow the locking nut to be loosened safely, before reducing the load applied by slowly releasing the hydraulic pressure using a valve on the pump itself. Panel E was immediately reloaded and the applied load 'locked off' at 20kN using the nut arrangement to monitor creep of the panel.

At zero load, the crack widths were measured again as before. Throughout the loading, sustained load and unloading cycles the DIC camera system was used to take sequential images for post-processing. This was controlled manually to coincide approximately with every 1kN of load and then at one image per minute while measurements were taken.

Measurements from all of the LVDTs were taken continuously at a sample rate of 4 Hz during the loading, unloading and activation stages. At 28 day intervals following the initial loading/unloading stage, LVDT displacements, optical microscope crack widths and DEMEC measurements were taken. The initial loading to the 6-month measurement stage is referred to as the monitoring period.

Activation of the tendons within panel B using the electrical activation system was undertaken twenty-three days after initial cracking. Before activation, the panel was reloaded up to 20kN and unloaded back to zero, to remove the effect of any autogenous self-healing during the interval between initial cracking and activation. The activation system was used to heat the polymer tendons up to a target temperature of 90°C (+-10°C) for a target period of 10 minutes. The tendons were then allowed to cool before microscope and DEMEC measurements were taken. After activation the panel was again subjected to a 20kN load-unload cycle with measurements taken at the peak and zero load. The loading cycles before and after activation for panel B are referred to as the pre-activation and post-activation loading respectively.

At the 4-month measurement stage (147 days after casting), sodium silicate solution was pumped through the networks in panels B and E using a foot pump and packer arrangement.

Testing of this arrangement in the laboratory is shown in Figure 5.31. To ensure all air was expelled from the networks, the packers were first set to an open position and the solution was pumped through the network slowly. As each packer began to expel liquid, it was closed off. This continued until the entire network was filled.

Figure 5.31: Flow network pump and packer arrangement during laboratory testing.

Due to the cracks induced in the panel, a sustained pressure on the solution within the networks could not be achieved. Instead, pumping was continued until the solution was observed exiting from the cracks on the front face of the panel.

Two days after the pumping of sodium silicate solution, water was used to flush the networks to allow them to be re-used. This was achieved by pouring water into a funnel connected to the topmost packer, allowing the water to flow by gravity alone through the network. Each of the packers were set to open one at a time to ensure the flow of water had reached all parts of the network.

At the 5-month monitoring stage, the networks were again filled with sodium silicate solution using the same procedure as at the 4-month stage. This time the networks were not flushed with water.

At the 6-month monitoring stage, panels A, B, D and E were reloaded for a final time following the same procedure as in the initial loading stage. Panels B and E were loaded to 20kN, while

panels A and D were loaded back to their initial peak load. The panels were then unloaded and final measurements taken at both the peak load and unloaded state. Panel C was left for loading at a later date to allow warmer weather to aid any bacterial healing. The results from the final loading of panel C are not included in this thesis.

5.9. RESULTS AND DISCUSSION

5.9.1. Compressive strength

The compressive strength of the three mixes used (control, microcapsules and bacteria) was assessed by taking 100x100x100mm cube samples and testing them in accordance with BS EN 12390-2. Table 5.6 shows the results of these tests. The target strength class for all mixes was C40/50, requiring an associated mean compressive strength from cube samples of 58MPa at 28 days (Fib, 2010). The mean strength of the control mix was 59.3MPa.

Table 5.6: Compressive strength results.

Mix	7-day compressive strength, MPa (average over 3 tests)	CoV (%)	28-day compressive strength, MPa (average over 3 tests)	CoV (%)
Control mix	50.25	1.14	59.30	0.83
Microcapsule concrete	28.15[2]	34.79	42.20[2]	12.55
Bacteria concrete	29.10[1,2]	-	35.10[1,2]	-

[1]single test only
[2]test carried out by team members at Bath/Cambridge University

The bacteria concrete was found to have a compressive strength 41% lower than the control mix; however, the addition of the perlite had a significantly adverse effect on the workability of the mix making it extremely difficult to manufacture reproducible cube specimens. Likewise, although previous work (Kanellopolous et al., 2016a, Giannaros et al., 2016) had indicated that the addition of microcapsules would not significantly affect the strength of the concrete, the 28 day results obtained from the site trials were very inconsistent and suggested strength reductions of 23-36% compared to the control mix.

Based on these results, the microcapsule and bacteria mixes would fall into the strength classes C25/30 and C20/25 respectively (Fib, 2010). However, given the small sample size and the challenges associated with compaction, further testing of these mixes should be undertaken to reach a well-founded conclusion.

5.9.2. Initial loading: load-displacement

Displacement of the panels during loading was recorded from LVDTs 2 and 4 positioned at the level of the loading bar (see Figure 5.28) between the panel and the mounting column on the left and right hand sides respectively. To check whether any uneven loading of the panels took place, the maximum difference in displacements between these two LVDTs during the initial loading stage was used to calculate the maximum angle of rotation of the panel using equation (11). The definitions of the variables are illustrated in Figure 5.32 and the results are shown in Table 5.7.

$$\theta = \tan^{-1}\frac{\delta}{0.5 \cdot L} \qquad (11)$$

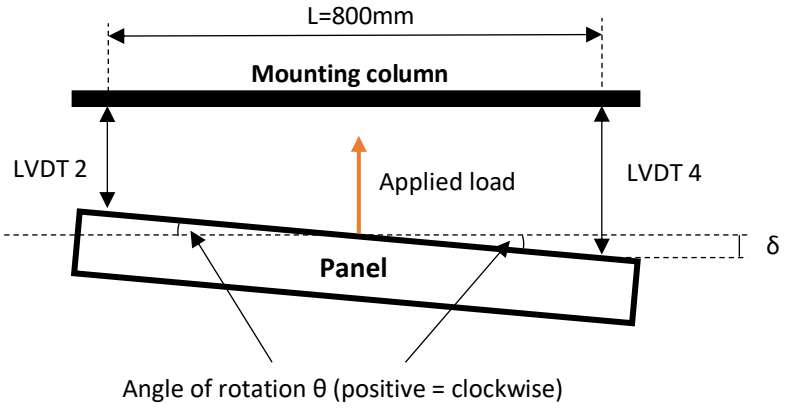

Figure 5.32: Calculation of the angle of rotation of the panels during loading (plan view).

Table 5.7: Calculated maximum angle of rotation for panels during initial loading.

Panel	A	B	C	D	E
Maximum δ (mm)	0.43	-	0.06	0.32	-0.20
Calculated angle of rotation θ (rad.)	π/3000	-	77π/1800000	π/4000	-29π/180000

LVDT 4 on panel B was found to be giving erroneous results so was excluded from the analysis. Given the small angles of rotation on all other panels, it was decided that the average displacement over LVDTs 2 and 4 was an appropriate measurement of overall displacement.

This average value (and LVDT 2 only for panel B) was therefore used to plot load against displacement curves for all panels during the initial loading stage, presented in Figure 5.33. This comparison was undertaken to explore any differences in the stiffness and flexural strength of the panels.

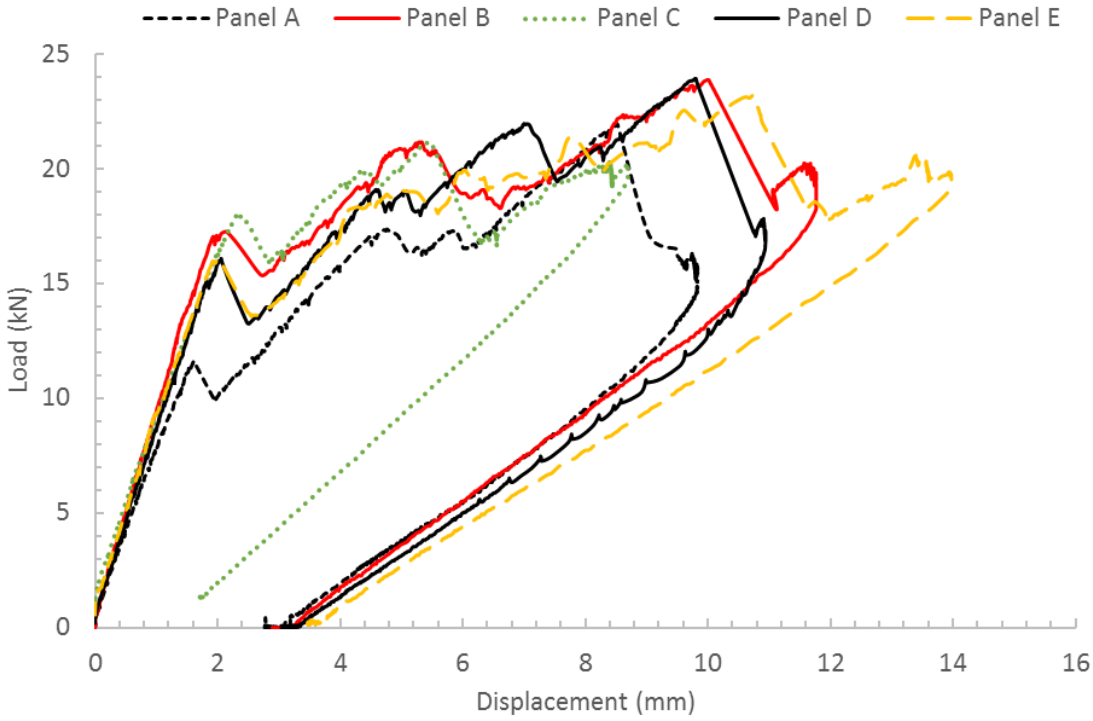

Figure 5.33: Load-displacement curves for all panels during initial loading stage.

In panels B, C, D and E, initial small reductions in load can be observed at between 16-18kN and correspond to the first cracks at the base of the wall. Further fluctuations in load are observed beyond this point, with a second significant reduction in load at approximately 21-22kN corresponding to a second crack 200-300mm above the base. Further load was then applied until a crack formed at the CoS location. This occurred together with a significant drop in load on panels B, D and E at between 22-24kN. Panel C, containing the bacterial concrete layer, experienced cracking at the CoS location at 21.2kN load. Panel A, containing microcapsules,

experienced initial cracking at the much lower load of 11.6kN with slightly higher displacements occurring (relative to the applied load) compared to all other panels until a crack formed at the CoS at 21.9kN.

The gradient of the initial loading curve for panel B is slightly greater than that of all the other panels. This indicates that this panel has an increased stiffness, probably due to the contribution of the PET tendons. The loading curve of Panel A has the smallest gradient, indicating that this panel has the lowest stiffness, which could be a result of the inclusion of the polymeric capsules or the slightly higher water-cement ratio of this concrete compared to the control mix.

Figure 5.34 displays the DIC snapshot images of the front face of Panel B with increasing load. From these images, the order of the cracks as they appeared during loading is confirmed. The first was a crack at the base of the panel at the interface with the kicker, followed by a crack between the base and the CoS location and finally a larger crack at the CoS location itself. The DIC images show the situation immediately following the formation of each crack, with the load that is displayed indicative of the cracking load. The scale below the images indicates the strain measurement across each of the cracks.

The final DIC image shows the panel following unloading. There is a clear reduction in crack size based on the strain measurements obtained, although the residual cracks are still significant. This reduction is due to the steel reinforcement acting elastically to close the induced crack.

Figure 5.35 shows DIC images of all five panels immediately following cracking at the CoS. The loads displayed are indicative of the peak load immediately before the formation of the cracks, as in Figure 5.34.

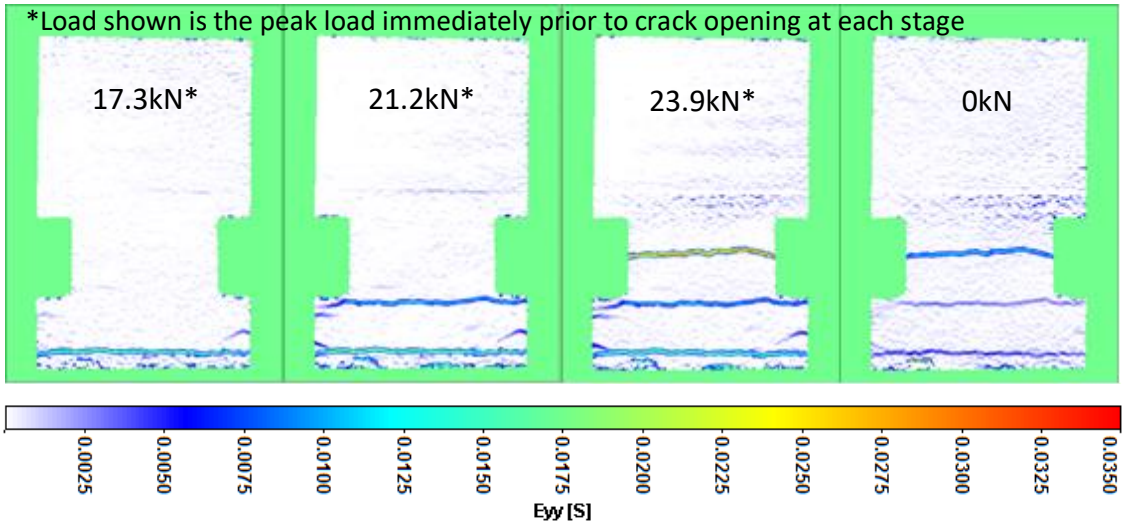

Figure 5.34: DIC crack images during initial loading of panel B.

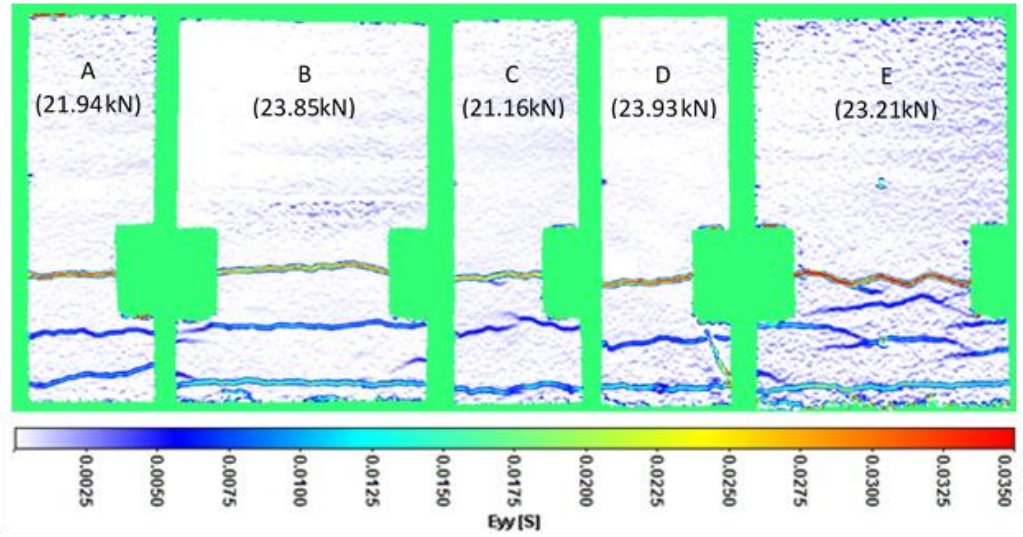

Figure 5.35: DIC images of all panels at peak load during initial loading.

With the exception of Panel A, all of the panels cracked in a similar fashion to Panel B, with the initial crack occurring at the base of the panel. In Panel A, this initial crack occurred at approximately 250mm (+/-20mm with local crack propagation) above the base, which was the location of the second crack for all other panels. As mentioned, this panel also experienced initial cracking at a much lower load than all the others. This may be a result of the decreased strength of the concrete containing microcapsules compared to the control mix used in the other panels, as suggested by the compressive strength results.

The load at which the crack at the CoS forms for all panels can be seen from Figure 5.36, which compares load against crack displacement (defined as the average of LVDTs 0 and 1) throughout the loading and unloading. During testing, this displacement reading was taken as an approximation of the crack width, ignoring any other micro-cracks within the length of the LVDTs, and each panel was loaded until this displacement had reached 0.5 mm. For this reason, Panel C was loaded up to 20kN following the initial appearance of the crack at this location before being unloaded, as the initial displacement after cracking was only 0.3mm.

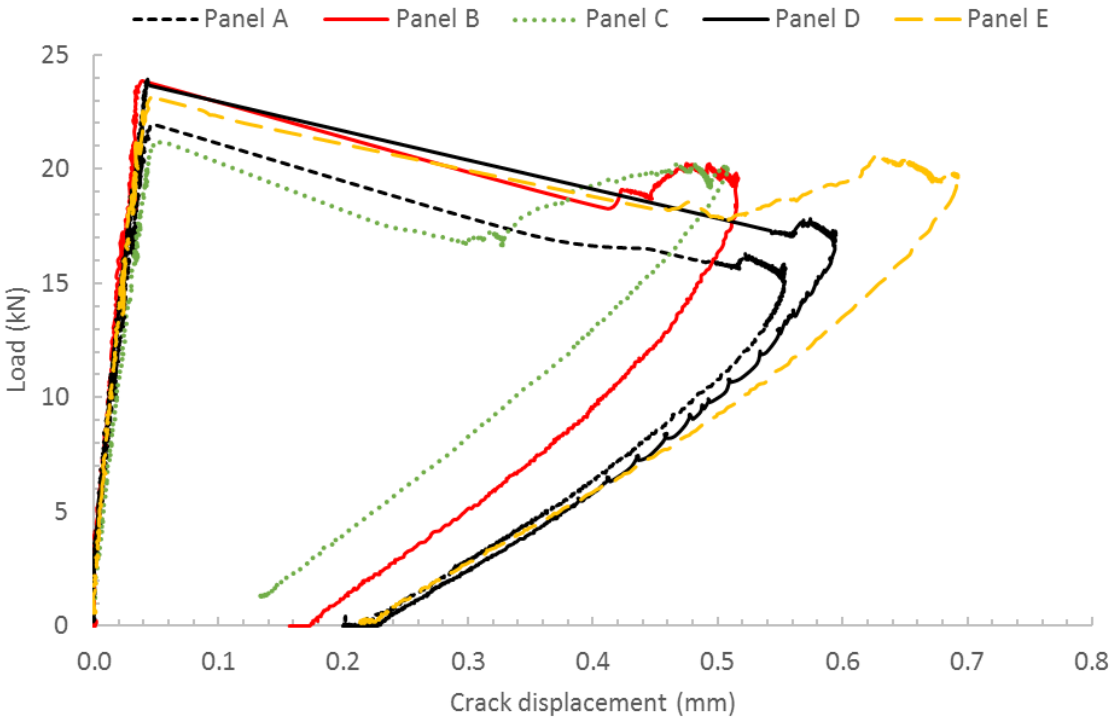

Figure 5.36: Load against crack displacement for all panels during initial loading.

5.9.3. Initial loading crack width measurements

A summary of the peak and residual crack width values as measured using the optical microscope are shown in Table 5.8. The residual crack measurements show that following unloading of the panels a significant residual crack remained in each panel.

Table 5.8: Peak and residual crack widths from microscope measurements during initial loading.

Panel	Position on panel 1	2	3	4	5	Average (mm)
A - peak	0.29*	0.26	0.40*	0.43	0.39	0.35
A - residual	0.06*	0.08	0.14*	0.15	0.11	0.11
B - peak	0.27	0.40	0.39	0.37*	0.43	0.37
B - residual	0.03	0.11	0.11	0.09*	0.12	0.09
C - peak	0.28*	0.36*	0.30*	0.34	0.39	0.33
C - residual	0.07*	0.08*	0.05*	0.06	0.06	0.06
D – peak	0.44	-	0.35	0.44	0.42	0.41
D – residual	0.17	0.16	0.18	0.15	0.15	0.16
E – peak	0.51	0.53	0.40	0.37	0.31	0.43
E – residual	0.15	0.13	0.09	0.11	0.03	0.10

*multiple cracks - measurement is a sum of crack widths

Figure 5.37 shows a comparison between the crack measurements taken from LVDT, microscope images and DEMEC measurements. As expected, the LVDT displacements show larger values as these span a larger distance across the face of the panel, and therefore include any micro-cracks within this range. The measurements taken from the microscope photos and from the DEMEC pips spanning the crack at the CoS location are very similar, giving confidence in the reliability of the measurements of crack width that have been obtained.

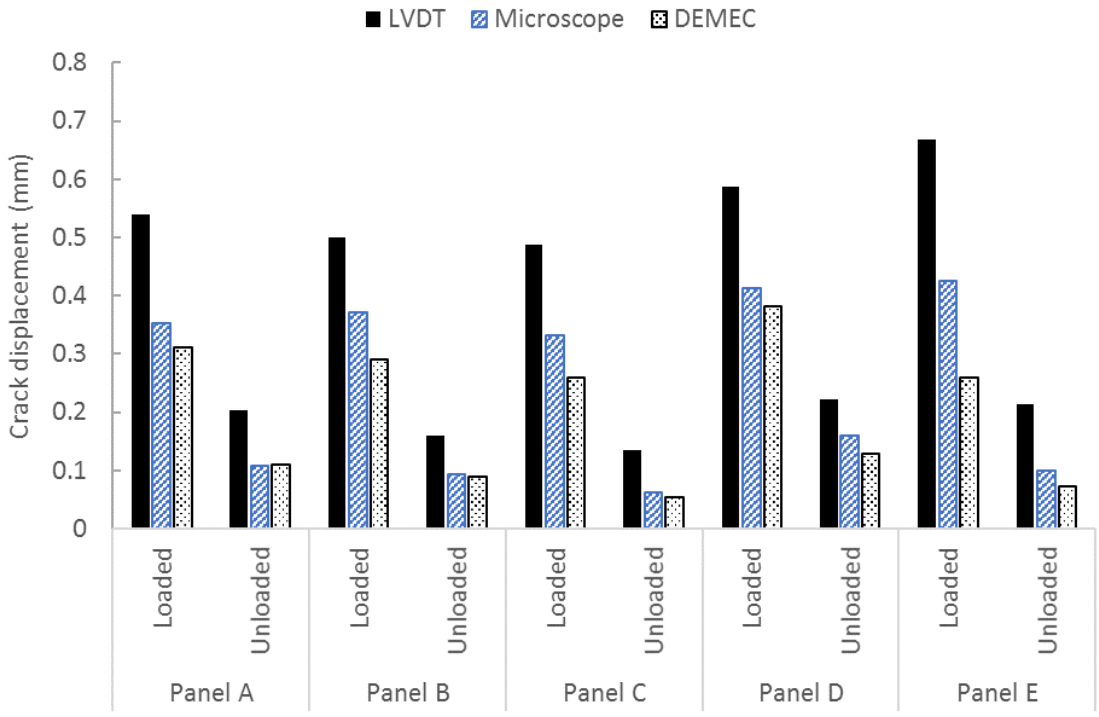

Figure 5.37: Crack width measurements after initial loading from LVDT, microscope images and DEMEC measurements.

All of the measurements show a large reduction in crack width upon unloading, which can be attributed to the steel reinforcement acting in an elastic manner. The existence of fairly significant residual crack widths, however, suggests that some unrecoverable strain was experienced by the panels and it is possible that some plastic deformation of the steel also occurred. There may also have been some movement of fragments within the crack during loading and unloading which stopped the cracks from closing completely.

Although the intention had been to produce very similar crack widths in all panels, the nature of the cracking process resulted in some significant differences. In particular, the residual cracks within panel C are much smaller than the other panels, while those in panel D were much larger. The fact that there were multiple cracks at the CoS for panels A and C also resulted in smaller individual cracks which could have an effect on any healing.

5.9.4. Activation of polymer tendons in panel B

It was originally planned to activate all of the tendons simultaneously. However, after initial turning on of the activation system on site it was clear that the tendons would require more power than anticipated to reach the desired temperature, possibly due to the additional length of non-heating wire in the circuits increasing the circuit resistance.

To avoid overloading the system, it was decided to activate the tendons in two 'batches' of five. Batch 1 consisted of the odd-number tendons and batch 2 of the even-number tendons. The selected channels were switched on and the input voltage raised using the variable transformer until 90°C was recorded on the thermocouples. The 'target temperature' set for both the internal and external thermocouples was 90°C.

Figure 5.38 shows the temperature of the polymer tendons over time. Activation of the polymers occurred as the glass transition temperature of the polymer (between 60-80°C) was passed.

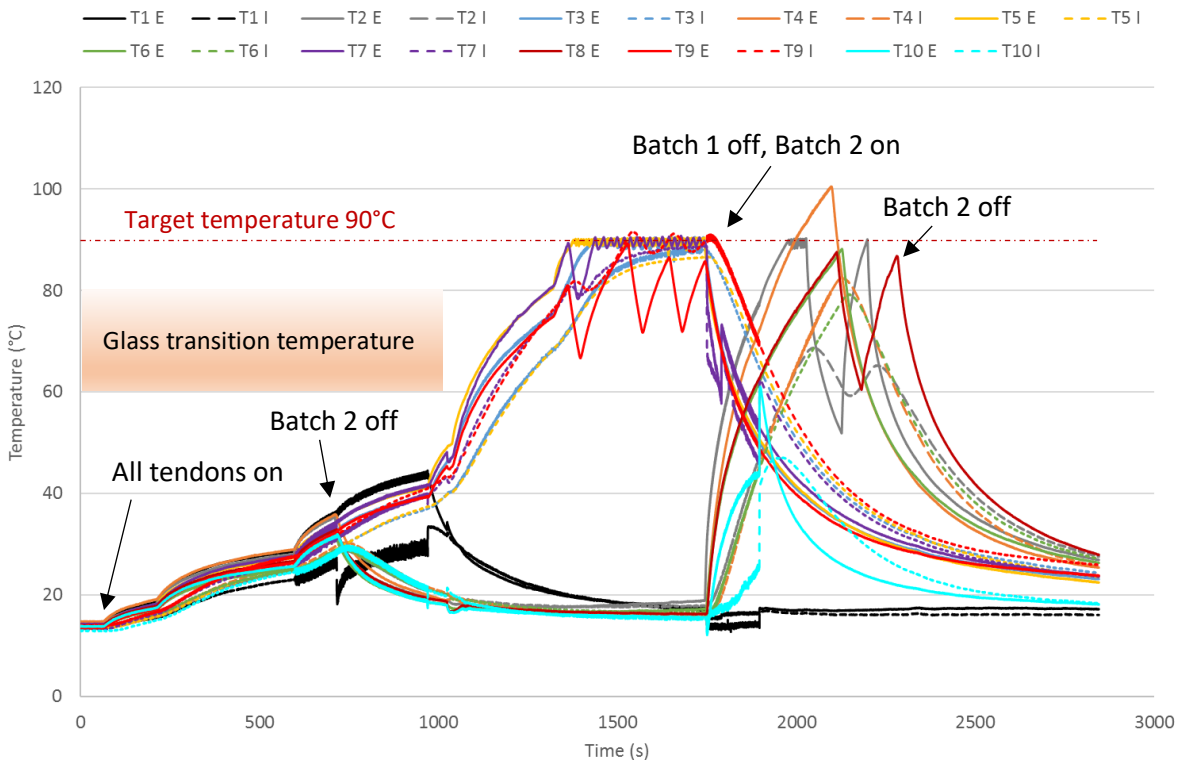

Figure 5.38: Tendon temperatures upon activation.

As shown, not all of the tendons reached the desired temperature of 90°C on the internal (I) and external (E) thermocouples. In particular, tendons 1 and 10 began heating up but quickly dropped in temperature, indicating a failure of the channel. It was later found that the 3 amp fuses in these circuits had blown. This could have been caused by ingress of water into the tendons, which subsequently came into contact with an uninsulated section of wire, causing a low resistance path, which would then have caused a large current to be drawn through a single channel. However, this cannot be confirmed without demolishing the panels and extracting the tendons.

In batch 1 all of the tendons, with the exception of tendon 1, reached the desired temperature on both the external and internal thermocouples. The temperature within the tendons was then successfully regulated at the target temperature as within the laboratory testing of the activation system (section 5.6). One noticeable variation is T9 E, which shows large peaks and troughs in temperature. This can be explained by the fact that the internal thermocouple had reached 90°C before the external thermocouple, thereby turning off the circuit and causing rapid

cooling on the external face. In all other tendons within batch 1, the external temperature target was reached first. Tendon 9 clearly reached the desired temperature however, so can be considered as fully activated.

The second batch was more variable, with large differences between internal and external temperature measurements. An example is tendon 2, which clearly reached 90°C based on the external thermocouple measurement, but measured a maximum of only 69°C on the internal thermocouple. For this case it can be said that the polymer was partially activated, as the laboratory experiments in Chapter 3 have shown that stresses are produced by the polymers upon heating above 60°C. For tendon 8 there was no internal measurement as the thermocouple had failed (presumably becoming damaged at some point during construction). Although the external measurement reached 90°C for a short period of time, it cannot be assumed that the internal temperature reached this value so this tendon must also be assumed to have been partially activated.

Some of the variability between internal and external measurements can be accounted for by differing placement of the thermocouple end within the polymer tendons, as this was very difficult to keep consistent during manufacture. As an example, the external thermocouple was placed between two coils on the external face, as described in section 4.3.4. In the case that the thermocouple end was accidentally moved so that it was in contact with or close to the heating wire, this would result in a much more rapid temperature rise, causing the circuit to turn off before the internal temperature had reached the target of 90°C. This is one potential explanation for the results of tendon 2, resulting in a quicker temperature rise on T2 E than the other tendons in batch 2 and a low maximum temperature recorded on T2 I.

A noticeable temperature overshoot can be observed in T4 E, with external temperature reaching just over 100°C. This was due to a wiring failure causing the direction of the reading being reversed (increases in temperature were measured as reductions), meaning the automatic on/off system for the circuit did not function on this channel. However, based on the polymer

experiments in the laboratory showing no drop in polymer stress until well above 100°C and taking into account the maximum internal temperature measurement of 82°C this tendon can be taken as fully activated.

Based on these results, assumptions as to the degree of activation of the tendons were made, as shown in Table 5.9.

Table 5.9: Activation temperatures of polymer tendons in panel B.

Tendon	Max external temperature (°C)	Max internal temperature (°C)	Activation
1	44.5	33.5	None
2	90.3	68.8	Partial
3	90.6	88.6	Full
4	100.5	82.4	Full
5	90.6	86.7	Full
6	88.2	79.3	Full
7	90.8	88.8	Full
8	87.6	Not available	Partial
9	89.3	91.6	Full
10	61.0	47.1	None

Figure 5.39 shows the crack displacement from LVDTs 0 and 1 during activation of the polymers. Two of the tendon temperatures (T2 E and T7 E) have also been plotted to show the times at which the two batches of tendons were activated. LVDT B1, spanning the crack on the right hand side (RHS) of the front face of the panel, shows a displacement of approximately 0.01mm upon activation of the first batch, increasing to almost 0.03mm after activation of all polymers. This indicates a small amount of crack closure on the panel. However, this displacement is not replicated in LVDT B0 on the left hand side (LHS) of the panel.

Table 5.10 shows the crack width measurements before and after activation from the microscope images. These measurements agree with the LVDT results, showing a closure of approximately 0.03mm on the RHS of the panel (location 5) compared to a slight increase in crack width on the LHS (location 1). This could be due to the tendons towards the RHS of the panel producing a higher shrinkage force than on the LHS. Tendon 1, on the far LHS of the panel,

was not successfully activated, while the next tendon along (tendon 2) was only partially activated, which supports this conclusion.

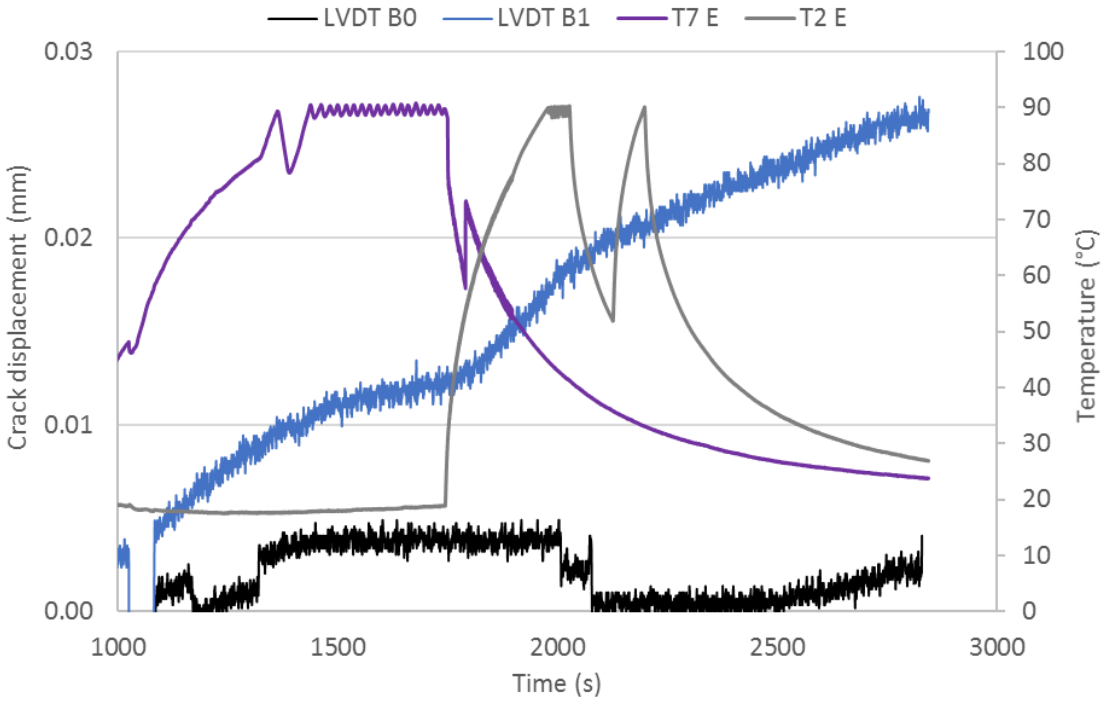

Figure 5.39: LVDT crack displacements during tendon activation.

Table 5.10: Crack width measurement on panel B before and after activation from microscope images (mm).

	Measurement location (see Figure 5.30)				
	1	**2**	**3**	**4**	**5**
Pre-activation	0.08	0.12	0.10	0.08	0.10
Post-activation	0.09	0.10	0.09	0.07	0.06

The average crack closure observed upon activation was 10% based on LVDT measurements, 12% from DEMEC measurements and 16% from microscope measurements. This is significantly smaller than the 26-39% observed in the reinforced beams tests described and discussed in section 4.4.4. As the target activation temperature for all polymer tendons was not met, the applied compressive stress on the panel will have been significantly lower than that calculated before activation.

Assuming the two 'partially' activated tendons (2 and 8) produced 50% of their estimated shrinkage stress, it is estimated that probably only around 70% of the total stress that was

anticipated from all ten tendons was actually applied to the panel. Taking a potential restrained shrinkage stress of 17MPa for each tendon and using the same calculation as in section 5.3.2, this suggests that the compressive stress that was applied across the crack surface upon activation was only 0.24MPa.

In this case, the compressive stress produced by the polymers, while resulting in a small reduction in crack width, was insufficient to fully close the induced crack.

5.9.5. Post-activation loading of panel B

Following activation of the polymer tendons, panel B was reloaded back up to 20kN. Figure 5.40 shows the load against crack displacement readings for the initial, pre-activation loading and post-activation loading for panel B.

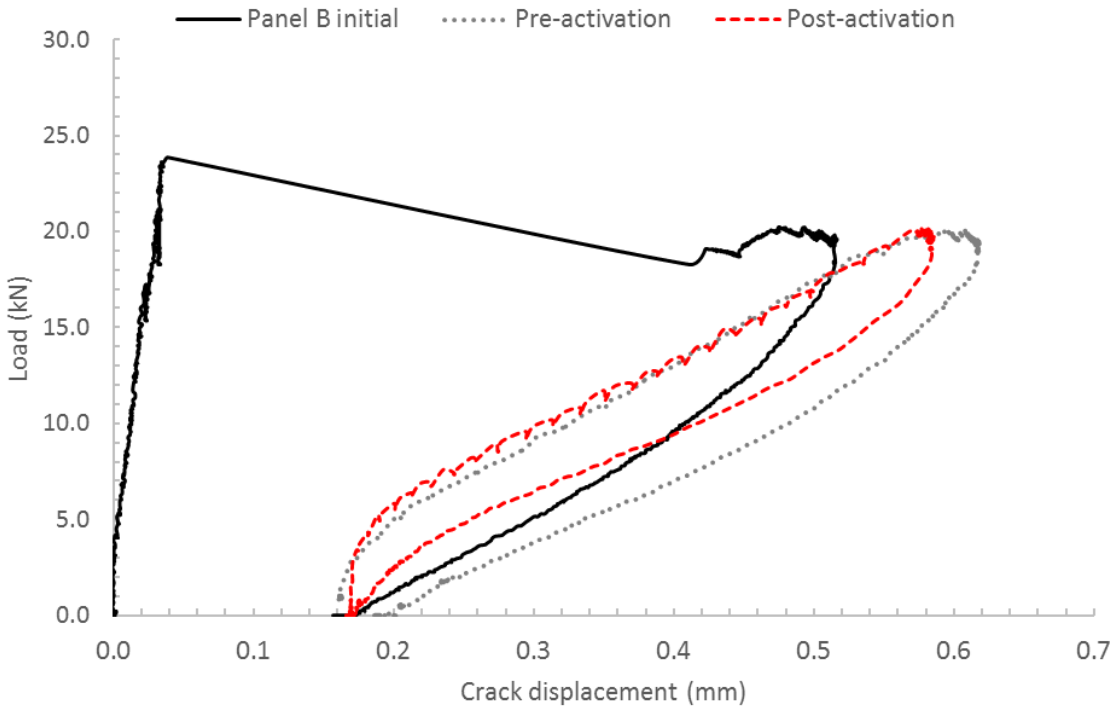

Figure 5.40: Load against crack displacement for initial, pre-activation and post-activation loading of panel B.

The post-activation reloading curve shows a reduction of 0.03mm in crack displacement at peak load. An increase in initial stiffness of the panel is indicated by the vertical portion of the post-activation reload curve, caused by the compressive force applied by the PET tendons. Once this

force has been overcome by the applied load the elastic portion of the reload curve shows no increase in stiffness compared to the pre-activation curve. The residual crack returned to its original post-activation displacement upon unloading, suggesting that no additional plastic deformation had occurred.

Figure 5.41 shows the crack displacement results from the two front-face LVDTs at the initial loading, second loading, activation and post-activation loading stages. Comparing the unloaded post-activation crack displacement to the unloaded pre-activation value shows an average crack reduction of 0.021mm, or 10.9%. This crack closure is higher on the RHS of the panel (15.7%) than the LHS (6.1%), in agreement with the displacement results during activation itself.

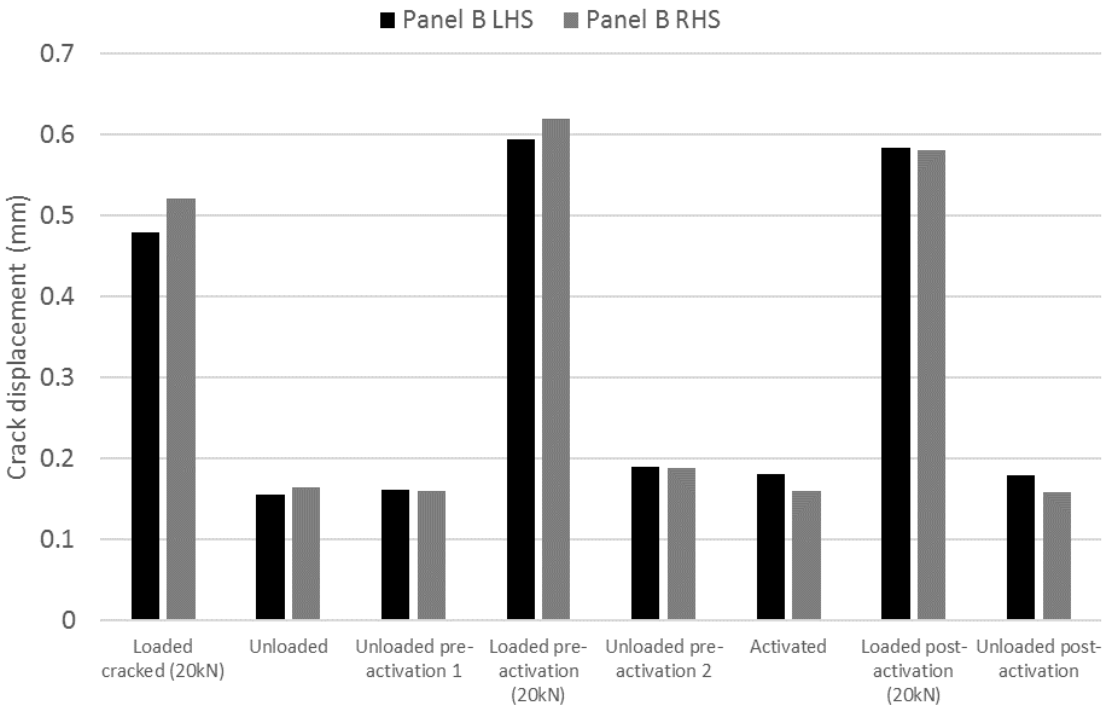

Figure 5.41: LVDT crack displacements on panel B throughout initial and second loading.

5.9.6. Crack monitoring over six months

Figure 5.42 displays the measurements from the microscope images, DEMEC and LVDTs for panel B, from the unloaded stage post-activation to 6 months after initial loading.

The LVDT results indicate a clear reduction in crack displacement over time. The measured displacement reduced by 77.3% from 0.169mm after activation to 0.038mm at 6-months after initial loading. However, this magnitude of crack closure was not replicated in the microscope and DEMEC measurements, showing only 16% and 5% closure respectively over the same period.

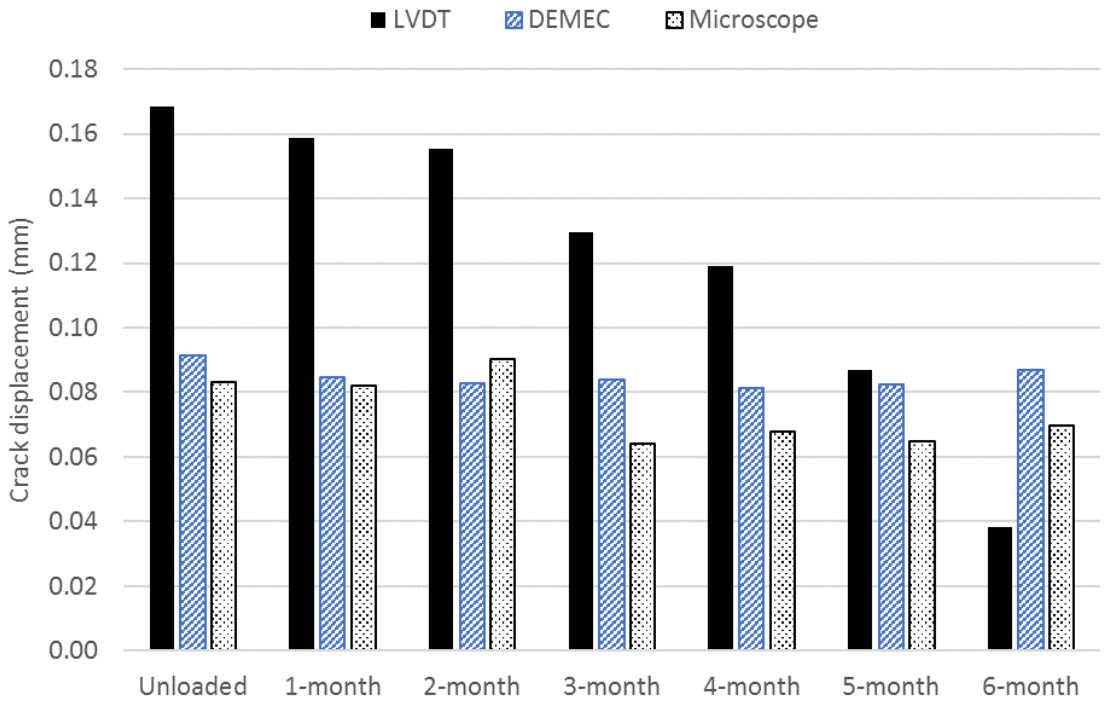

Figure 5.42: Panel B crack displacement results over 6-month monitoring period.

The three measurement methods span different lengths, with LVDTs spanning 150mm, DEMEC measurements 100mm and microscope photos covering only the crack at the CoS location. One explanation therefore is that the difference between the displacement results is caused by a closure of micro-cracks spanned only by the LVDTs. However, DIC strain images indicate that there are no cracks spanned by the LVDTs other than the crack at the CoS location. If, therefore, the reduction in displacement shown by the LVDTs had occurred, this would be clearly visible as a closure of this crack in the microscope photos, and as a change in displacement in the DEMEC measurements. Figure 5.43 shows the microscope photos at the start and end of the monitoring period.

Figure 5.43(d)-(f) show a clear residual crack in the panel. It therefore seems improbable that the LVDT results are reliable. It is unclear why the LVDT results show such a significant reduction in crack width, particularly as both LVDTs B0 and B1 show the same trend which is not replicated in any other panels. However, considering the contradictory DEMEC and microscope measurements the LVDT results must be disregarded.

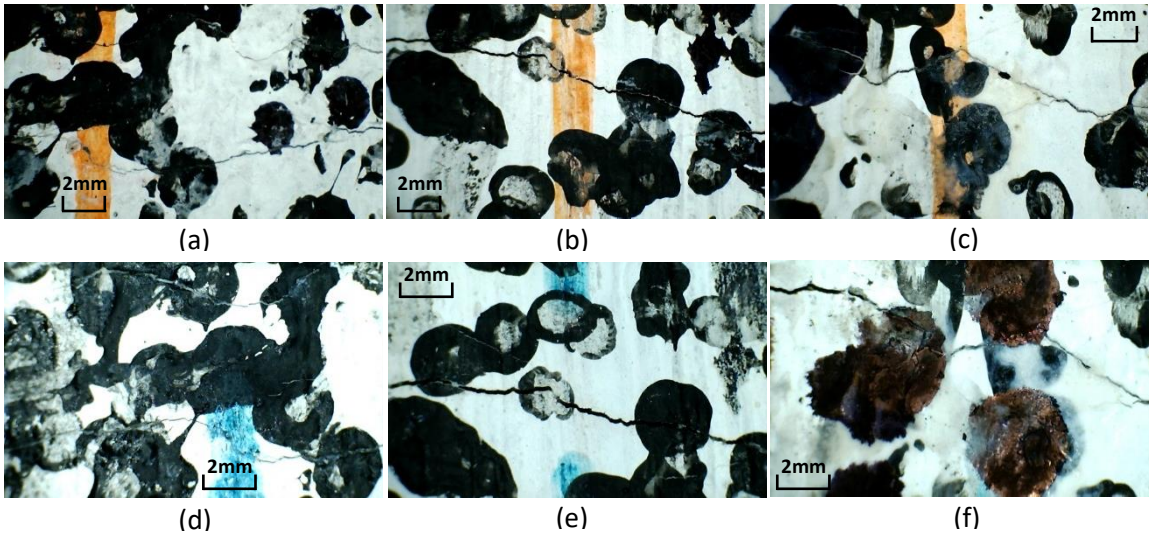

Figure 5.43: Microscope photos of the crack at CoS location on panel B: (a), (b) and (c) positions 1, 3 and 5 respectively at the start of the monitoring period; (d), (e) and (f) positions 1, 3 and 5 respectively 6-months after initial loading. See Figure 5.30 for positions of microscope photos.

Figure 5.44 shows the DEMEC and microscope measurements for all panels, excluding panel E for clarity due to its larger crack widths, over the monitoring period. Table 5.11 summarises the DEMEC and microscope measurements at the start and end of the monitoring period for all panels.

DEMEC readings show very little change in crack displacement, while the microscope measurements show a reduction for all panels with the exception of panel C. A reduction in microscope measurement without corresponding reduction in DEMEC measurement suggests that the reduction is caused by a build-up of material within the crack rather than any structural movement. This result would be expected if crack healing had taken place.

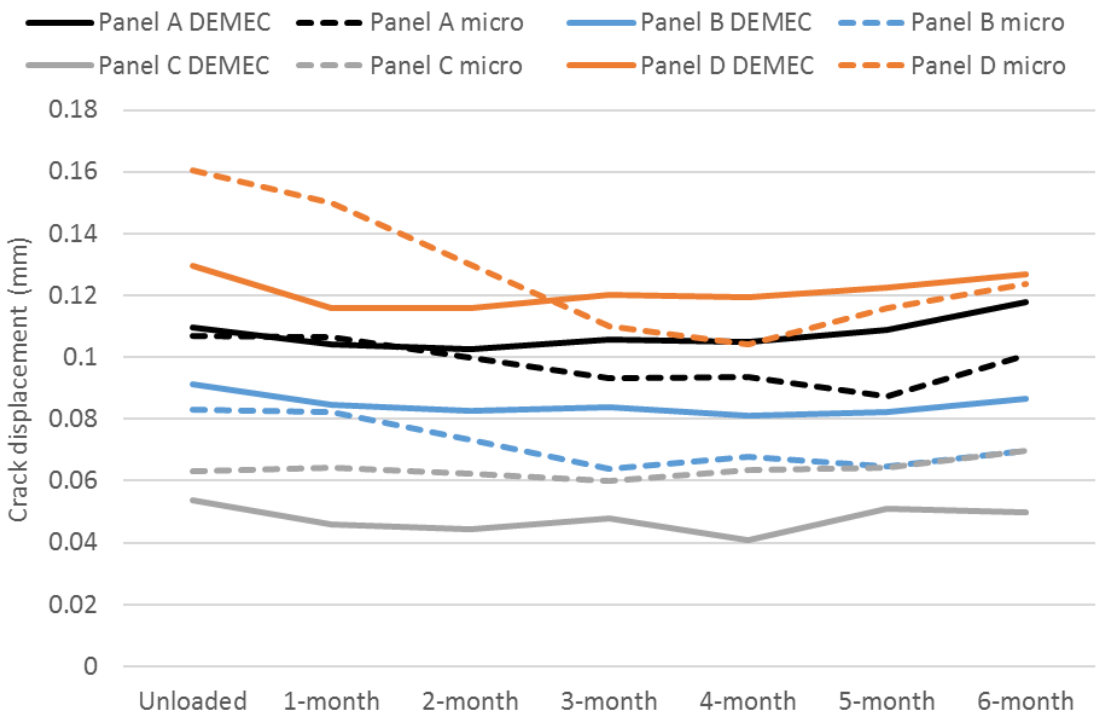

Figure 5.44: DEMEC and microscope measurements for all panels (excluding panel E) over the monitoring period.

Table 5.11: DEMEC and microscope measurements at start and end of the monitoring period for all panels.

		Panel A	Panel B	Panel C	Panel D	Panel E[1]
DEMEC	Start	0.11	0.09	0.05	0.13	0.16
	End	0.12	0.09	0.05	0.13	0.13
Microscope	Start	0.11	0.08	0.06	0.16	0.25
	End	0.10	0.07	0.07	0.12	0.23

[1]DEMEC result from one side only as DEMEC pip fell off of panel

These results show that the largest reduction in crack width based on microscope images is in control panel D. This suggests that none of the trialled techniques has resulted in a noticeable improvement in self-healing compared to the controls. However, it must be acknowledged that the measurement of crack healing through microscope images is only indicative, and does not take into account any healing within the depth of the crack or any impact it may have had on concrete properties such as permeability.

5.9.7. Use of sodium silicate solution in the flow networks

At the 4-month monitoring stage, when loading the flow networks with sodium silicate solution, this solution was observed leaking from the cracks on the front face of the panels, as shown in Figure 5.45. This occurred in both panels B and E. This confirmed that the crack had passed through the networks and that the applied pressure was sufficient to push the solution into the crack. Upon flushing with water, the water exited from all of the packers, confirming that the networks had not been blocked by the sodium silicate solution and could be re-used. While it is possible that some of the sodium silicate solution was also flushed out during this process, the high viscosity of the liquid exiting the packers suggested that this was minimal (as the sodium silicate solution was of significantly lower viscosity).

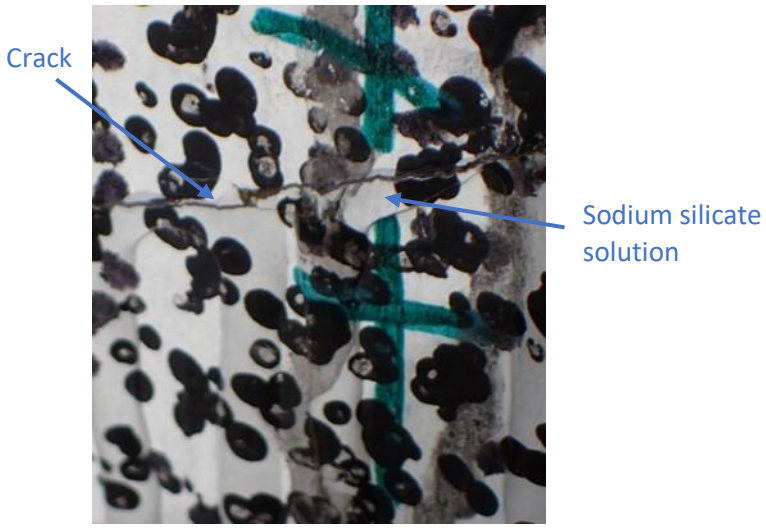

Figure 5.45: Sodium silicate solution exiting from the crack during pumping of flow networks.

At the 5-month monitoring stage, no clear crack sealing was observed from the microscope images, so the networks were again filled with sodium silicate solution using the same procedure as at the 4-month stage. This time the networks were not flushed with water.

The expected build-up of C-S-H material on the crack faces was not evident in either of the panels, based on the microscope images at the 6-month monitoring stage. This could be the result of insufficient availability of calcium hydroxide within the crack at the 4 and 5-month monitoring stages when the solution was introduced. A detailed discussion of the reactants

required for C-S-H deposition with sodium silicate solution are outside the scope of this thesis. From the observations made within this trial, the flow networks were successfully filled, flushed with water and re-used, using a sodium silicate solution as a healing agent. However, healing of the crack does not appear to have been successful.

5.9.8. Weather data

Weather data were obtained from the Met Office (WeatherAnalytics, 2016). These data included daily minimum and maximum air temperatures and relative humidity as well as daily rainfall quantities covering the period 1st June 2015 – 31st May 2016. The two weather stations closest to the trial site were used, situated at Tredegar and Usk. Their locations are shown in Figure 5.46.

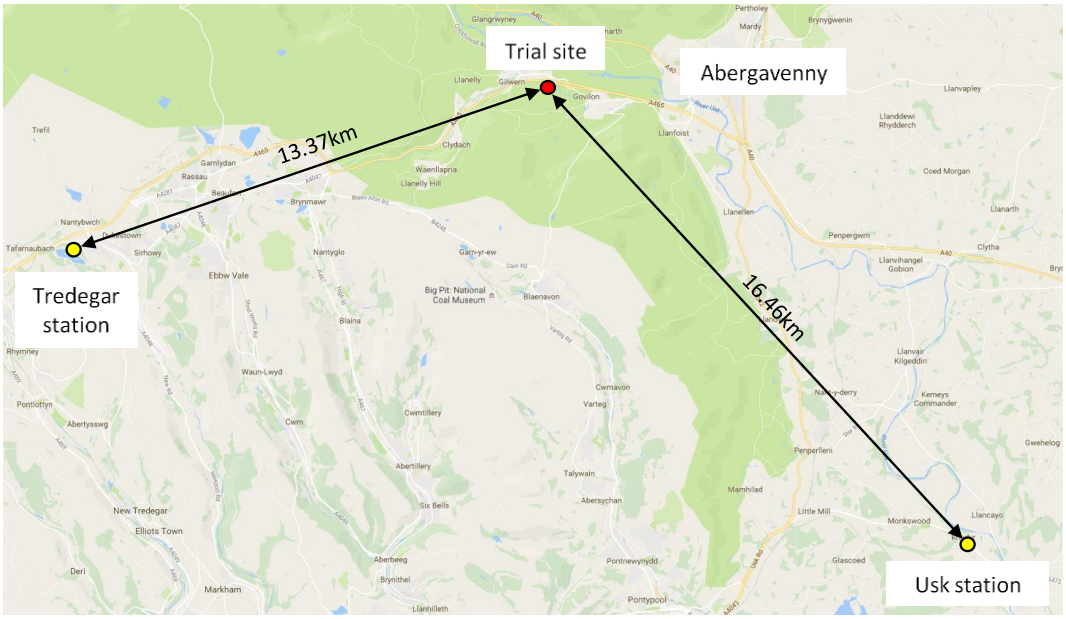

Figure 5.46: Location of weather stations.

Figure 5.47 shows the data obtained from the two stations. For reference, the dates for the initial loading, activation and monitoring stages are shown in Table 5.12.

There was a significant difference in total rainfall measured between the two stations. Over the monitoring period (183 days), the total rainfall recorded at the Tredegar station was 1374mm,

with 149 days in which at least some rainfall was observed. At Usk the total rainfall was 887mm over 124 days in which rain was recorded. While it is unclear which of these stations would be most representative of the site itself, both indicate that a substantial amount of rainfall occurred.

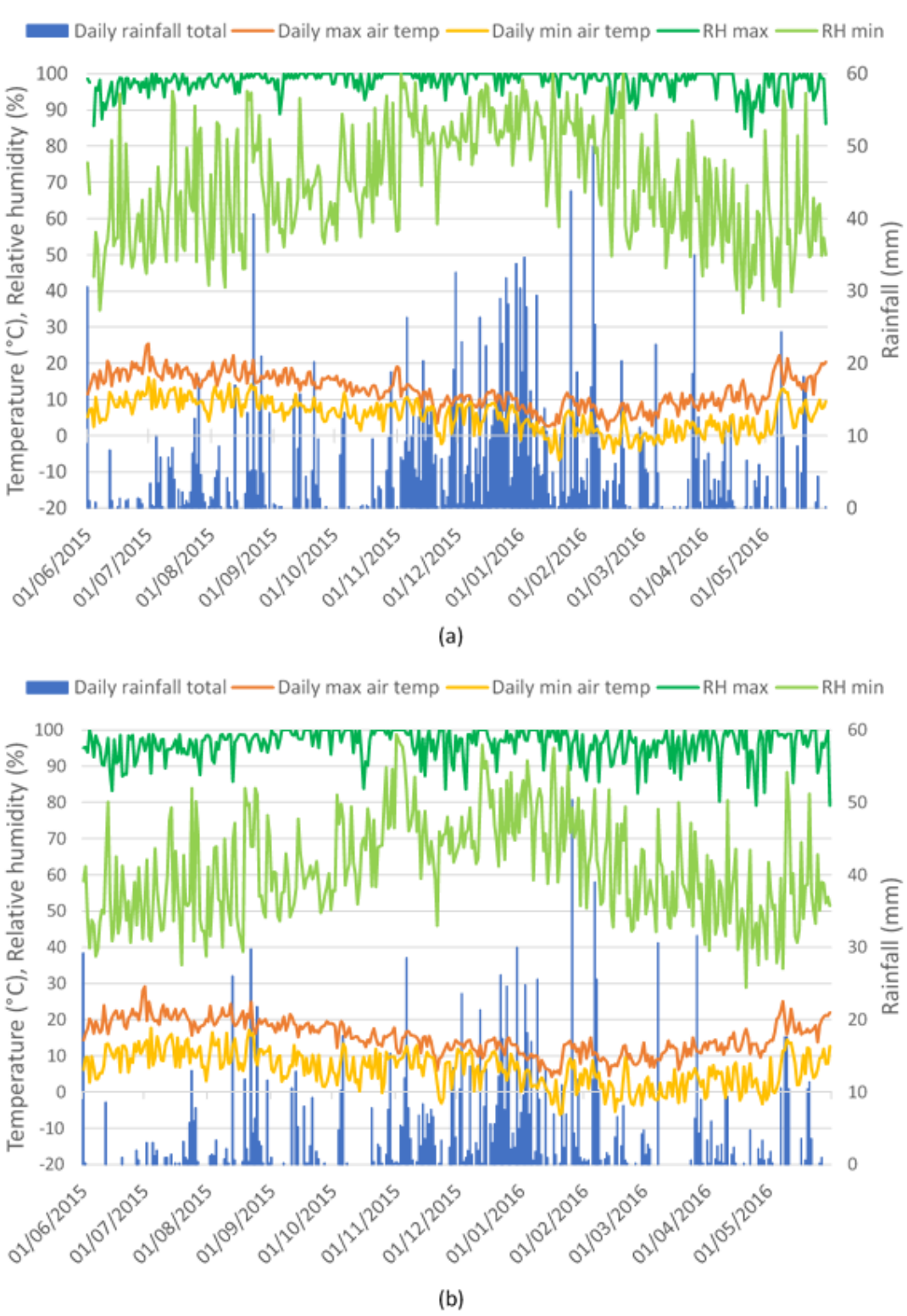

Figure 5.47: Weather data from (a) Tredegar and (b) Usk weather stations.

Table 5.12: Initial loading, activation and monitoring stage dates.

Stage	Start date	End date
Initial loading	09/11/2015	12/11/2015
SMP activation	04/12/2015	04/12/2015
Monitoring period	09/11/2015	09/05/2016

The presence of water is essential for both autogenous healing and the autonomous systems used. As discussed in section 0 and 5.9.7 however, 100% crack healing does not seem to have occurred within any of the panels based on microscope measurements. In experiments in the laboratory (Chapter 4), the samples were fully submerged. It is possible that during the trial, while the surfaces of the panels were exposed to the rain, the water did not then permeate into the crack faces and cause healing. Although the relative humidity was also high, as shown by Figure 5.47, this has been found previously to be insufficient for autogenous healing to take place without the direct presence of water (De Rooij et al., 2013).

Temperature is important for the bacterial healing method in panel C. The *Bacillus pseudofirmus* strain used has been found to grow well at temperatures between 25-35°C (Sharma et al., 2015). The temperature throughout the monitoring period ranged from -6.8°C to 25.1°C. For this reason, as mentioned in section 5.8, panel C was left for a longer period of time than the other panels before final loading, and as such the final loading results for panel C are not included in this thesis.

5.9.9. Final loading

At the end of the six-month monitoring period, panels A, B, D and E were loaded for a final time. Figure 5.48 shows the final load-crack displacement curve for panel B compared to pre and post activation. The starting displacements have been zeroed for this comparison.

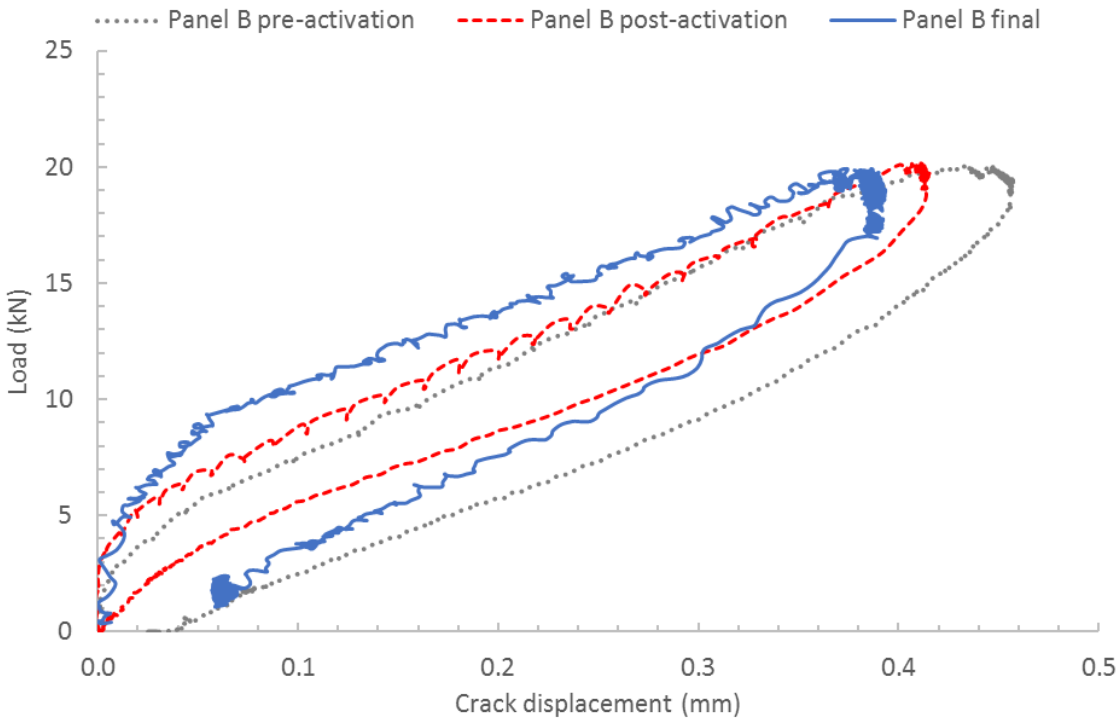

Figure 5.48: Panel B load-crack displacement curves: pre-activation, post-activation and final loading stages.

The final loading curve exhibits a higher initial gradient and a decrease in final crack displacement at the peak load of 20kN compared to the pre and post-activation loading cycles. A similar response was observed for panel E (Figure 5.49) compared to the reload cycle at 1-month after initial loading. This could be the result of autogenous healing within the crack, autonomous healing from the sodium silicate solution pumped through the flow networks, an increase in strength via continued hydration of the un-cracked portion of the concrete panel, or a combination of these factors.

Due to an equipment error, the final loading curve for panel D was not recorded. Figure 5.50 shows the final loading curves of panels A, B and E. This shows that panel A did not experience the same increase in load at small crack displacements as the other two panels. This suggests that the sodium silicate solution introduced through the flow networks in panels B and E may have contributed to this effect, rather than autogenous healing or ongoing hydration of the un-cracked portion of the panel. However, the concrete within panel A was shown to be weaker at the initial loading stage. It is therefore unclear from these results which factor had the most significant role in the improvement in load-crack displacement response in panels B and E.

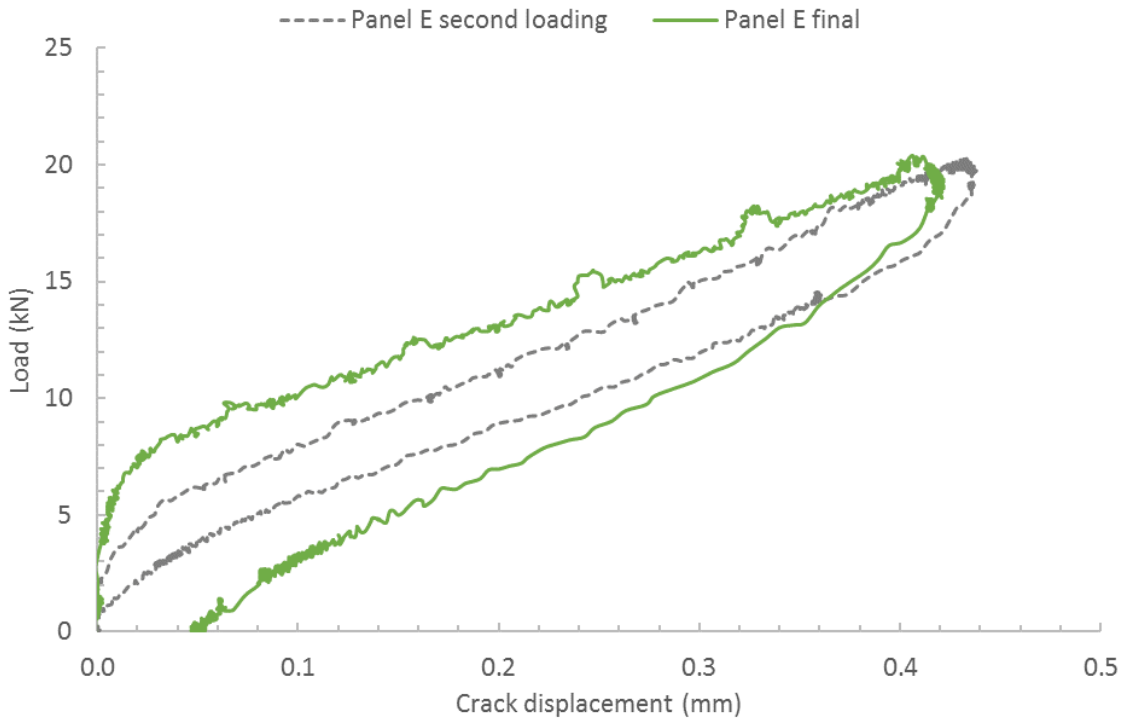

Figure 5.49: Panel E load-crack displacement curves for second and final loading stages.

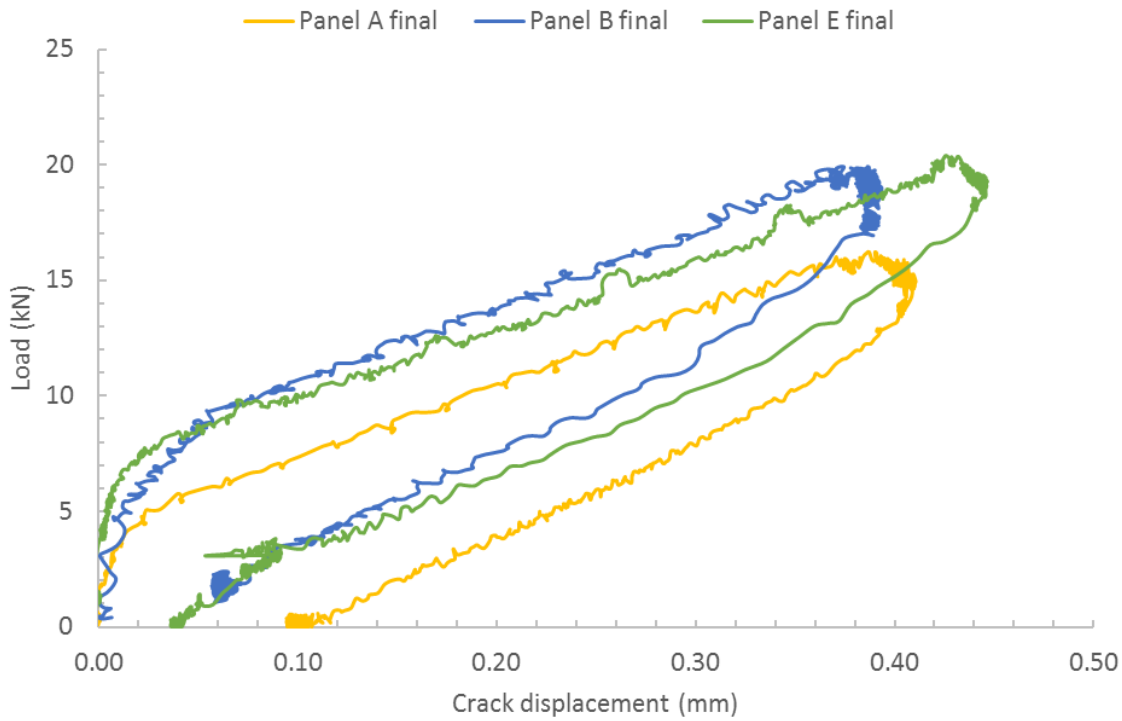

Figure 5.50: Panels A, B and E load-crack displacement curves for the final loading stage.

From the results of the site application of these techniques, it has not been possible to conclude that the microcapsules containing sodium silicate solution, the bacteria concrete mix or the sodium silicate solution introduced within flow networks have been successful in improving self-

healing within the concrete panels. It is clear that additional investigations are required to bridge the gap between laboratory testing and full scale application, discussed further in Chapter 7.

Were these site application tests to be repeated, it would be beneficial to use a more controlled loading process with a larger number of samples. A focus on a particular cause of degradation, for example chloride transport, may also make it easier to draw conclusions, although this would introduce additional challenges associated with taking reliable measurements.

5.10. CONCLUSIONS FROM CHAPTER 5

- The inclusion of the PET filament tendons resulted in an increase in stiffness of panel B compared to control panels D and E, as observed during the initial loading phase.
- The use of microcapsules within the concrete mix, in the proportions used, had a negative effect on the compressive strength, tensile strength and stiffness of panel A.
- Activation of the tendons in panel B, despite challenges in reaching the 90°C activation temperature on all tendons, resulted in an average crack closure of 10-16% on panel B. The tendons applied an estimated compressive stress of 0.24MPa across the crack faces. A reduction in crack displacement at peak load was observed upon reloading the panel immediately after activation.
- The flow networks included in panels B and E were successfully filled with sodium silicate solution, flushed with water and filled a second time with the solution. In each filling, the sodium silicate solution was observed exiting from the crack on the front faces of the panel, demonstrating that the flow network system could deliver a healing agent into the cracks as planned.
- Monitoring of the panels over a 6-month period showed some reduction in crack width in all panels except panel C, based on microscope images, suggesting that some crack healing had occurred. However, no clear increase in this healing was observed within

the test panels A-C compared to control panels D and E. In addition, a residual crack was observed on all panels following 6 months of monitoring.

- Differences in healing results between laboratory tests and observations from the site trial are attributed in part to a lack of available water within the crack plane. While there was a significant amount of rainfall during the monitoring period, this may not have permeated into the crack faces, whereas the laboratory samples were submerged during the curing period.
- The age of first cracking may also have had an effect on the amount of healing, with a reduction in the availability of unhydrated cement for the panels, loaded after 28 days, compared to the laboratory samples tested in section 4.2, loaded after 7 days.
- Results from the final loading stage showed an improved load-crack displacement response for panels B and E, into which sodium silicate solution was introduced through flow networks, compared to panel A which contained microcapsules. However, panel A was found to be weaker during the initial loading stage and it is therefore unclear whether the use of the sodium silicate solution caused the improved response.

Chapter 6. Life Cycle Cost Assessment of Self-Healing Concrete in Highways Bridge Decks

6.1. INTRODUCTION AND LITERATURE REVIEW

This chapter introduces a life cycle cost assessment of self-healing concrete in highway bridge decks. One of the key justifications for the development of self-healing materials is a potential reduction in repair and maintenance costs of structures (Van Breugel, 2007) and therefore a reduction in life cycle costs.

This section includes a literature review on life cycle costing, including its definition, aspects of a life cycle cost analysis, managing uncertainty and relevant previous studies. Section 6.2 then provides details of a preliminary study undertaken using historical data sourced from Highways England (HA, 2014).

Section 6.3 introduces an existing asset management planning toolkit along with adaptations made for the purposes of the current study. A case study using a concrete bridge built as part of the A465 Heads of the Valley project is described in Section 6.4, in which the adapted model is used to compare life cycle costs of the structure with and without a theoretical self-healing concrete bridge deck. The results of this study are presented in Section 6.5, followed by a sensitivity analysis of the key model variables in Section 6.6.

6.1.1. Definition of life cycle cost

Life Cycle Cost (LCC) and Whole Life Cost (WLC) are terms which are often confused. This is partly due to changing terminology over the years. The basic principles of life cycle costing have been developed for more than a century, although systematic implementation did not begin until around 35-40 years ago (Boussabaine and Kirkham, 2004). Pre-1970s, most capital investment decisions in the building procurement sector were based solely on capital cost. In the early

1970s, professionals with an interest in the concept of increasing capital expenditure to save on overall costs, an area known as 'terotechnology', began including operational and maintenance costs in these decisions. These costs were referred to as 'cost-in-use' (Boussabaine and Kirkham, 2004, Salem et al., 2003).

However, the inclusion of cost-in-use did not consider the need for accurate future cost forecasting. In the mid to late 1970s, the idea of a single 'Life Cycle Costing' process emerged as a solution, with the aim of encompassing all perceivable costs from construction through to disposal. LCC became more widely recognised in the years which followed, until it was written into a British Standard within BS 3843 1992 'Guide to Terotechnology (the economic management of assets)', and in 2000 incorporated into ISO 156868 Part 1 –Service Life Planning (Boussabaine and Kirkham, 2004, BSI, 1992).

In the late 1990s, the new terminology of 'whole life costing' and 'whole life-cycle costing' (WLCC) emerged. These two terms are recognised by Boussabaine and Kirkham (2004) as interchangeable, but as an evolution from the earlier LCC in that WLC attempts to quantify risk and uncertainty to a greater extent.

In the same discussion, the authors attempt to demonstrate the lack of agreement over whether WLC and LCC are different terms. Following an online survey sent to academics and practitioners in the field of LCC/WLC, it was concluded that "not one of the respondents in the survey defined WLCC in similar terms; some though pointed out that LCC and WLCC were two of the same thing" and that it therefore remains a subjective opinion (Boussabaine and Kirkham, 2004).

(Flanagan and Jewell, 2005) presented the opinion that the change from LCC to WLC was little more than terminology, one which was repeating itself with the emergence of the term Whole Life Appraisal (WLA). WLA is so termed as it includes both cost and performance, thereby embodying through-life costs.

This confusion of terms no doubt influenced the release of BS ISO 15686-5:2008, which focusses on LCC and sets out clearer definitions to distinguish LCC from WLC. In this standard WLCs are defined as "all significant and relevant initial and future costs and benefits of an asset, throughout its life cycle, while fulfilling the performance requirements", while LCCs are defined as the "cost of an asset or its parts throughout its life cycle, while fulfilling the performance requirements". By this definition, a WLC assessment will contain within it a LCC analysis, as well as additional items such as non-construction costs, income and externalities. This difference is highlighted in Figure 6.1 (BSI, 2008b). For the purpose of this thesis, the BS ISO 15686-5:2008 definitions of LCC and WLC will be used.

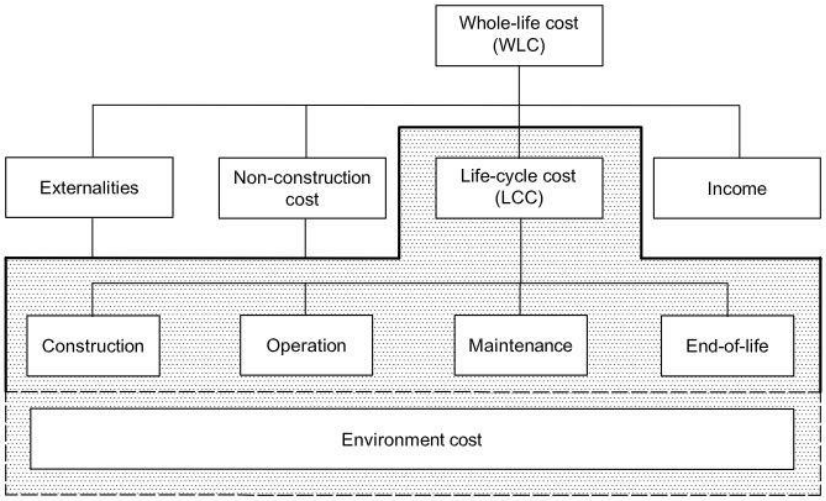

Figure 6.1: Elements of whole life cost and life cycle cost (from BS ISO 15686-5:2008 (BSI, 2008b)).

6.1.2. Aspects of a life cycle cost assessment

The purpose of a LCC assessment is to compare the economics of two or more potential solutions, taking into account current and future costs over a specific study period. The standard criterion for comparing LCCs is by expressing them in terms of Net Present Value (NPV), defined as the equivalent value in present monetary terms for all future costs (Ryall, 2010, BSI, 2008b). The NPV takes into account the time value of money by discounting all present and future costs and revenues associated with each option. Discounting is required as cash available now has a

greater value than the same quantity of money in the future. It is based on the principle, known as 'time preference', that people generally prefer to receive goods or payment now rather than later (Treasury, 2011). The amounts calculated in the analysis are therefore not a prediction of actual future costs (Churcher, 2008, Horner, 2005).

The NPV of a future cost is calculated using the following formula:

$$NPV = Cost\ X\ \frac{1}{(1+r)^n} \qquad (12)$$

Where r is the discount rate and n is the time of occurrence, usually expressed in years (Churcher, 2008). The discount rate used will depend on how far in the future the money is exchanged. Normal practice is to apply a discount rate per year, with all payments in the same year having the same rate applied (Churcher, 2008). Higher discount rates put more emphasis on short-term costs and revenues; with the opposite effect for lower rates. The 'correct' discount rate is therefore very important in a LCC analysis.

The discount rate, including inflation effects, recommended by the Treasury for public sector projects up to 30 years in length is 3.5% per annum. For longer term projects, it is recommended to use a declining discount rate as per Table 6.1. This includes a rate of 3% between 31-75 years and 2.5% between 76-125 years (Churcher, 2008, Treasury, 2011). This fall in discount rate with project length reflects the added uncertainty for such long time periods.

Table 6.1: Declining long term discount rate (Treasury, 2011).

Period of years	0-30	31-75	76-125	126-200	201-300	301+
Discount rate	3.5%	3.0%	2.5%	2.0%	1.5%	1.0%

The time frame over which a LCC analysis takes place is known as the study period. This is often taken as the assumed life of an asset, but can theoretically be any length of time. LCCs are often highly sensitive to the study period, so any assumptions relating to it must be well justified (Churcher, 2008, Horner, 2005).

It is very important that the costs to be included in a LCC analysis are clearly defined, as well as those costs which are excluded, along with justifications or comments on how such exclusions could affect the results of the assessment (BSI, 2008c). According to (BSI, 2008b), an LCC analysis should “cover a defined list of costs over the physical, technical, economic or functional life of a constructed asset, over a defined period of analysis”.

In order to predict future costs, an asset’s function must be defined in terms of performance, degradation mechanisms and the costs of maintenance or intervention (Horner, 2005). This can be achieved using a cost model to build up compound costs. LCC cost models are typically lists of activities within a study period, along with associated costs or benefits. The complexity of the model depends on the amount of activities and the depth of detail in each (Churcher, 2008).

There are two common approaches to building up a LCC model for complete assets: historical or predictive. Historical data are generally taken from similar facility or project data and are useful for broad estimates, though lack accuracy. The predictive approach considers each element or component of the asset and its maintenance requirements. Costs and timescales are attached to these requirements based on condition surveys of similar assets or cost plans for the proposed asset itself. This is a more detailed approach which allows the optimisation of costs (Horner, 2005).

6.1.3. Uncertainty in life cycle cost modelling

LCC models, as with any modelling, are an approximation and will never be entirely accurate. As Churcher (2008) states, life cycle costing is about being “approximately right rather than precisely wrong”. For this reason, it is important that the uncertainties and risks within the model can be assessed.

Uncertainty due to cost variability is a key aspect to take into account in LCC (BSI, 2008c). The uncertainty of the future value of an asset or the future cost of materials and labour increases

the complexity of life cycle costing, especially over long time frames. Predicted future costs can be made as accurate as possible through the use of known costs, historical data, expected performance models and 'best guesses' (BSI, 2008b). However, within the construction industry in particular, reliable data tends to be an issue and future cost assessments are often formed in a large part from subjective evaluation (Wang, 2011).

Undertaking a sensitivity analysis is a common technique used to indicate the range of uncertainty and risk associated with a LCC model (BSI, 2008b). In this analysis, the model is assessed against its vulnerability to future uncertainty in each key variable (Treasury, 2011). By changing individual inputs, such as the discount rate, and comparing the results for each option, the sensitivity of the model to that range of data can be determined. If a major change in an input has little or no effect on the overall outcome of the analysis, then the variability of this input can be ignored. If, however, there is a clear change in the results following the alteration of an input, the assumptions behind that variable should be closely scrutinised (Churcher, 2008).

A sensitivity analysis can therefore be important in assessing the most significant assumptions which have been made within the model (BSI, 2008b). As all the results of the model are approximations, options which are close in terms of final LCC are often considered equal. According to (Churcher, 2008), some analysts like to use a rule of thumb, such as any LCCs with a difference of 10% or less can be taken as equal.

A more detailed analysis of model sensitivity can be undertaken using a Monte Carlo analysis. This allows the assessment of the consequences of simultaneous uncertainty and can take into account correlations between these inputs. This method is particularly useful when there are many variables with significant uncertainties (Treasury, 2011, BSI, 2008b). A Monte Carlo analysis will not be included as part of this thesis but is discussed in more detail in section 7.2.

6.1.4. Life cycle cost modelling of bridge structures

A procedure for evaluating tenders for the construction of concrete bridges in the UK using WLC rather than just capital costs was suggested by Arya and Vassie (2004). This approach was based on chloride damage in concrete and took into account coatings, impregnation materials, modifications to the concrete mix, cathodic protection, the type of reinforcement and any modified design details. However, this method was very sensitive to some of the input parameters such as cover and initial chloride concentration around the reinforcement, making it difficult to apply to general bridge structures in which these parameters may not be known (Arya and Vassie, 2004).

Ugwu et al. (2005) proposed an object-oriented framework for bridges to compare the durability of design options in terms of LCC. The inputs for their framework include design and economic assessment parameters such as materials, discount rate and environment type. These are entered into a database model, the outputs of which are an economic comparison of the given options. In this model, the design, construction and recurrent costs are estimated for each component within the structure to build up a LCC for the whole structure. This framework successfully combined a bottom-up engineering approach to cost estimation with environmental effects, however this model was developed to assess bridges in Hong Kong so may not be directly applicable to standards within the UK (Ugwu et al., 2005).

Guidance for the LCC of structural assets, including bridges, in the UK was set out in the Code of Practice on Transport Infrastructure Assets (CIPFA, 2010). This identified the information required to carry out a LCC assessment including inventory data, condition data at time 0, defined programmes of work, identified maintenance needs and intervention levels, deterioration rates for elements and materials and the calculated costs for carrying out (or not carrying out) works. The stages of a life cycle planning process for structures were summarised into a high level flow diagram, shown in Figure 6.2 (CIPFA, 2010).

This process was developed upon by Atkins (2011) to produce guidance for local highway authorities. This introduced a simplified methodology for carrying out a WLC assessment of maintenance options, based around comparing strategies for 'do nothing', 'do minimum', or 'do something'. From 2010 onwards, a cost model incorporating all of the aspects recommended to assess the LCC of highways structures was developed by Atkins and the UK bridges board, supported by the UK Department for Transport (DfT) and the Chartered Institute of Public Finance and Accountancy (CIPFA) (Atkins, 2015b, CIPFA, 2016, CIPFA, 2010). This model was named the Structures Asset Management Planning Toolkit (SAMPT) (Atkins, 2015a).

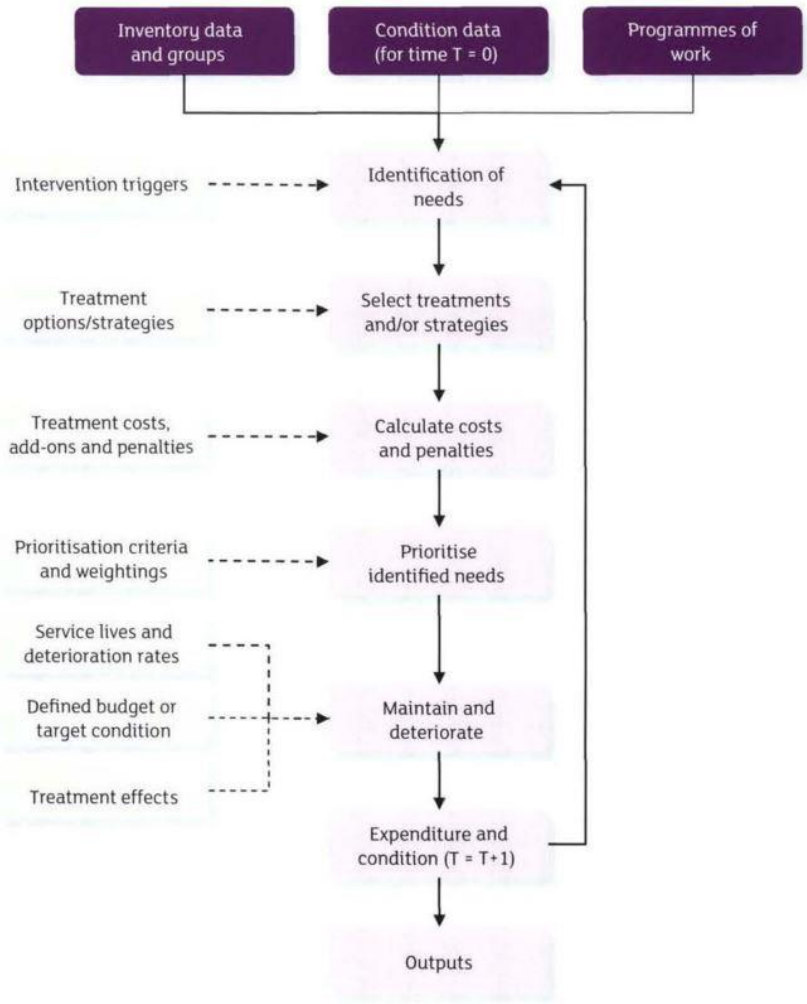

Figure 6.2: Stages of a life cycle planning process for structures, from the Code of Practice on Transport Infrastructure Assets (CIPFA, 2010).

The SAMPT has been developed for use by local authorities, using the data gathered by regular visual inspections. The functional elements of the SAMPT model are described in Section 6.3,

along with adaptations made to incorporate self-healing concrete for the purposes of this thesis. It was chosen to use this model as a foundation for a LCC assessment of self-healing concrete due to its relevance to UK standards, its element-based approach allowing the alteration of the properties of individual elements within the model and its use of defined material deterioration curves, explained in detail in Section 6.3.1.

6.1.5. Cost studies on self-healing materials

In his book, *Self Healing Materials*, Van der Zwaag (2007) defines the concept of 'Damage Management' in relation to self-healing materials, over the conventional 'Damage Prevention'. The key difference is that the damage level for a given conventional material will always be either constant or increasing, whereas in self-healing materials this damage level can decrease over time, increasing the lifespan of the material and theoretically enabling materials with infinite life (Van der Zwaag, 2007).

Van der Zwaag (2007) also defined the properties of 'ideal' and 'minimal' self-healing materials, as shown in Table 6.2. An ideal self-healing material would therefore be able to heal any and all levels of damage completely, many times over its lifespan.

Table 6.2: Properties of an "ideal" and a "minimal" self-healing material, from Van der Zwaag (2007).

An "Ideal" Self-Healing Material	A "Minimal" Self-Healing Material
Can heal the damage many times	Can heal the damage only once
Can heal the damage completely	Can heal the damage partially
Can heal defects of any size	Can heal small defects only
Performs the healing autonomously	Needs external assistance to heal
Has equal or superior properties to current materials	Has inferior properties to current materials
Is cheaper than current materials	Is terribly expensive

(Van Breugel, 2007) attempted to graphically represent the costs over time of a conceptual self-healing cement-based material compared to conventional and high quality reinforced concrete. This followed a similar principle of damage management to Van der Zwaag (2007), relating damage level to performance and therefore cost. The author concluded that, while a self-healing

concrete would be expected to incur higher initial costs, these should be outweighed by reduced repair and maintenance costs and an extended service life of the structure. This conceptual model is shown in Figure 6.3, but no figures were given or detailed analysis was undertaken to prove this benefit.

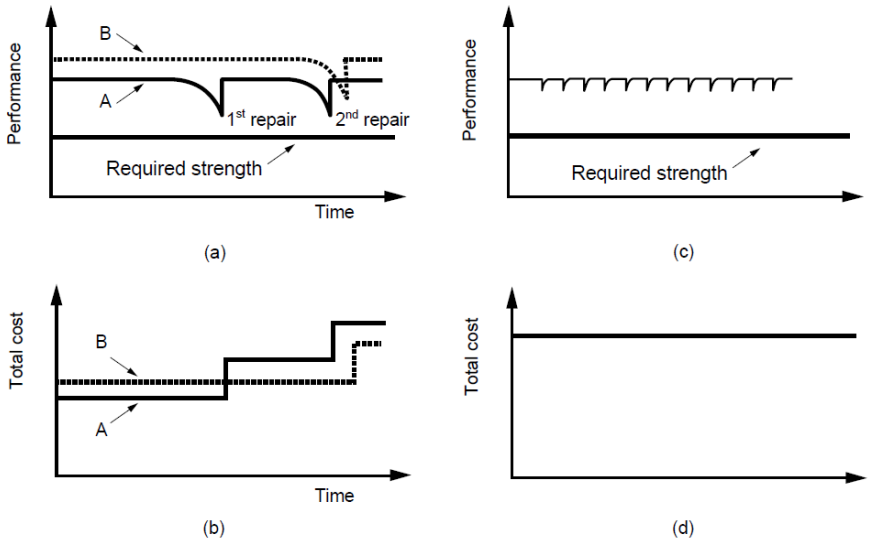

Figure 6.3: (a) and (b): Conceptual model of performance and cost against time for a standard quality concrete A and high quality concrete B. (c) and (d): The performance and cost against time for a self-healing concrete alternative. Original model from Van Breugel (2007), diagram from Li and Herbert (2012).

Li and Herbert (2012) undertook a simple cost analysis of self-healing concrete bridge decks based on this principle. Their study using the Life-365 model (Life-365, 2016) concluded that, for Engineered Cementitious Composites (ECC) in particular, despite the initial material costs being over twice as high, a self-healing concrete would result in a lower LCC per square metre than conventional reinforced concrete. This was based on a reduction in chloride diffusion and a subsequent delay to the onset of reinforcement corrosion.

The authors (Li and Herbert, 2012) developed this further by proposing six criteria to determine the 'robustness' of a self-healing material: shelf life, pervasiveness, quality, reliability, versatility and repeatability. They assessed five categories of self-healing technique against these criteria: chemical encapsulation (all approaches using self-healing chemical agents contained in microcapsules dispersed uniformly), bacterial encapsulation, mineral admixtures, chemicals in glass tubing and 'intrinsic healing' (enhanced autogenous healing) with controlled crack widths.

Of these, chemical encapsulation, mineral admixtures and intrinsic healing techniques were found to have the potential to score highly across all of the criteria; however, all techniques were found to be lacking sufficient data to complete a reliability assessment at the time of the study (Li and Herbert, 2012).

Within this thesis, a preliminary historical data study is described (Section 6.2) in which the highway bridge elements which typically require the most regular and costly repairs were identified. The SAMPT model (Atkins, 2015a) was adapted to include a theoretical self-healing concrete in the life cycle cost assessment. Self-healing concrete capable of varying number of healing cycles was modelled to represent the performance of 'minimal' to 'ideal' self-healing materials. This adapted model was then used in a case study to compare the LCC of a concrete bridge structure with a deck made from self-healing concrete with that of one made with conventional reinforced concrete.

6.2. PRELIMINARY STUDY: HISTORICAL DATA

An initial study was carried out to determine which elements within a bridge structure require the most regular and costly repairs. This would then highlight elements which would most benefit from improved resilience. To this end, data were gathered from the Transport Research Laboratory (TRL) on a number of highways bridges within the UK. All of the bridges were made primarily of reinforced concrete but could, for instance, contain steel beams as part of the support structure. Post-tensioned structures were excluded for the purpose of simplicity. This resulted in a data set comprising 30 structures.

These data were taken from the Highways England (HE) structures database known as the Structures Management Information System (SMIS) (HA, 2014). This initial list of thirty structures was then used to carry out a search for more detailed repair information from the HE

project cost team, some of which was available for more recent repairs (typically 2012 onwards). These two sources of information were brought together to carry out the preliminary study.

The repair and maintenance histories of all these structures were mapped out by working through the available information and putting any known activities and associated costs in chronological order. It was soon noticed that for the majority of the structures, there was little reliable information available for costs incurred before 2010, making any detailed analysis very difficult. It was then decided to take those structures with the most reliable information forward and use these to identify the most common repair costs. This resulted in ten structures being used in an element-based study of historical costs. The aim of the element-based study was to attribute the known costs that were incurred within the existing lifespan of the bridges to the various bridge elements, and then to identify those areas with the largest repair costs as those which could most benefit from replacement with self-healing concrete.

The locations of the ten structures used in the element-based study are shown in Figure 6.4, with their basic characteristics shown in Table 6.3. As can be seen, these are distributed widely across England and include bridges of a variety of sizes.

The element categories and definitions used to split down the recorded costs are shown in Table 6.4. These have been taken from Highways England (HA, 2007) to correspond with industry standards, with the adaptation that the category ‘superstructure’ has been expanded into ‘slab’ and ‘beam’, and the category ‘substructure’ expanded into ‘abutment’ and ‘piers/columns’ for clarity. In some cases, the bridges had undergone strengthening works to bring them up to required standards. These works were not deemed as ‘repairs’ and were therefore excluded from the analysis.

Figure 6.4: Locations of structures used within preliminary study.

Table 6.3: Basic characteristics of structures used within preliminary study.

Ref	Road	Spans	Piers	Length (m)	Width (m)	Date of construction
1	M1	1	0	6.50	40.70	1959
2	M62	4	3	58.53	35.53	1968
3	M3	4	3	41.20	24.32	1969
4	M6	4	3	76.00	12.06	1964
5	M6	3	2	71.60	12.60	1970
6	M18	2	1	50.68	11.35	1966
7	M62	3	2	86.46	12.80	1972
8	M62	3	2	86.60	12.80	1972
9	A38(M)	7	6	132.50	9.90	1971
10	A34	3	2	70.20	19.50	1969

As each of the bridges were constructed in different years their repair and maintenance costs could not be compared directly. Instead the costs were compared using an Equivalent Annual Cost (EAC) process using the NPV repair and maintenance costs. To achieve this, the costs incurred for each year were converted into 2014 costs using the output price index for repair and maintenance to take into account inflation. Where available, from 2010 onwards, the infrastructure specific value for this index was used. Before 2010 the public non-housing value was used.

Table 6.4: Bridge element group categories, adapted from the Inspection Manual for Highway Structures (HA, 2007).

Category	Definitions
Inspection	Principal, general or special inspections; assessments
Slab	Works to the load-bearing slab
Beam	Works to beams making up the bridge superstructure
Abutment	Works to abutments
Piers / columns	Works to supporting piers or columns including crossheads
Durability elements	Works to Drainage; waterproofing; expansion joints or surface finishes. Also bearings
Safety elements	Works to Handrails; parapets; safety fences; walkways or access gantries.
Ancillary elements	Works to Invert; aprons; wing walls; embankments; lighting; carriageway or footway/verge.

Once converted, the NPV cost of each repair was calculated using equation (12) (Section 6.1.2). For simplicity, a constant discount rate r of 3% was used rather than a declining rate.

The NPV costs were summed for each of the element categories and used to calculate an equivalent annual cost (EAC) using equation (13). Using EACs is the only accepted method for comparing two net present value costs which use different study periods (Churcher, 2008).

$$\boldsymbol{EAC = NPV \times \frac{r}{1-(1+r)^n}} \qquad (13)$$

This method enabled EACs to be calculated for each of the element categories across all of the structures studied.

A study period of 50 years was chosen over which to compare the structure costs, to avoid extrapolating the cost data over too large a number of years. The NPV costs for each bridge over a 50-year study period were calculated by multiplying the EAC values by 50. The results from this analysis are shown in Figure 6.5.

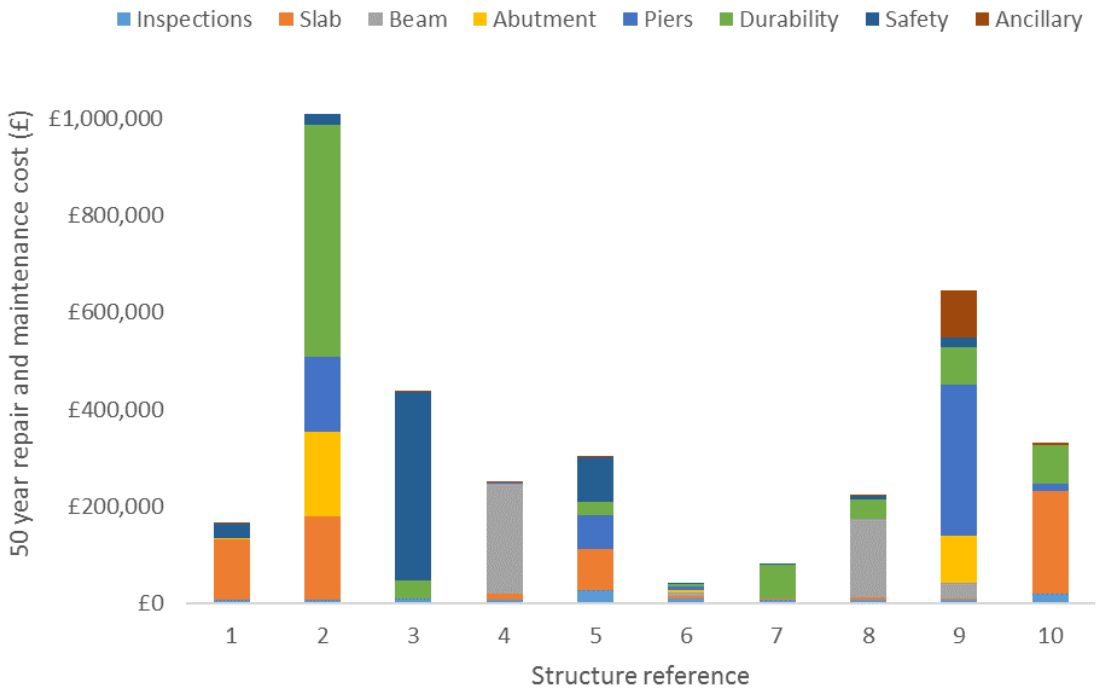

Figure 6.5: Repair and maintenance costs over 50 years, calculated from equivalent annual costs.

One immediate observation is the high cost of some of the elements in the 'durability' category. This category includes waterproofing works and surface refurbishments, and as such can include major repair or renovations. Figure 6.6 has excluded this category for clarity. As can be seen, there is a large amount of variance within the results. This is in part to be expected due to the different locations and therefore exposure conditions of the bridges. However, even with these selected bridges the historical data available on repair and maintenance was sparse, meaning a single large repair for a bridge, such as the 'durability element' repair for structure 2, completely alters the final EAC for that structure. For some repairs it was also difficult to separate repairs due to degradation over time from upgrade works or emergency repairs, as this information was not available.

Of the categories included, slab, piers, beams and abutments are those which are of interest in relation to replacement with self-healing concrete. For all of the structures, with the exception of bridge 4, at least some costs can be attributed to concrete slab repairs. Pier repairs were also common, with six out of the eleven structures requiring some repair work to concrete piers. Repairs of abutments and beams were less common overall.

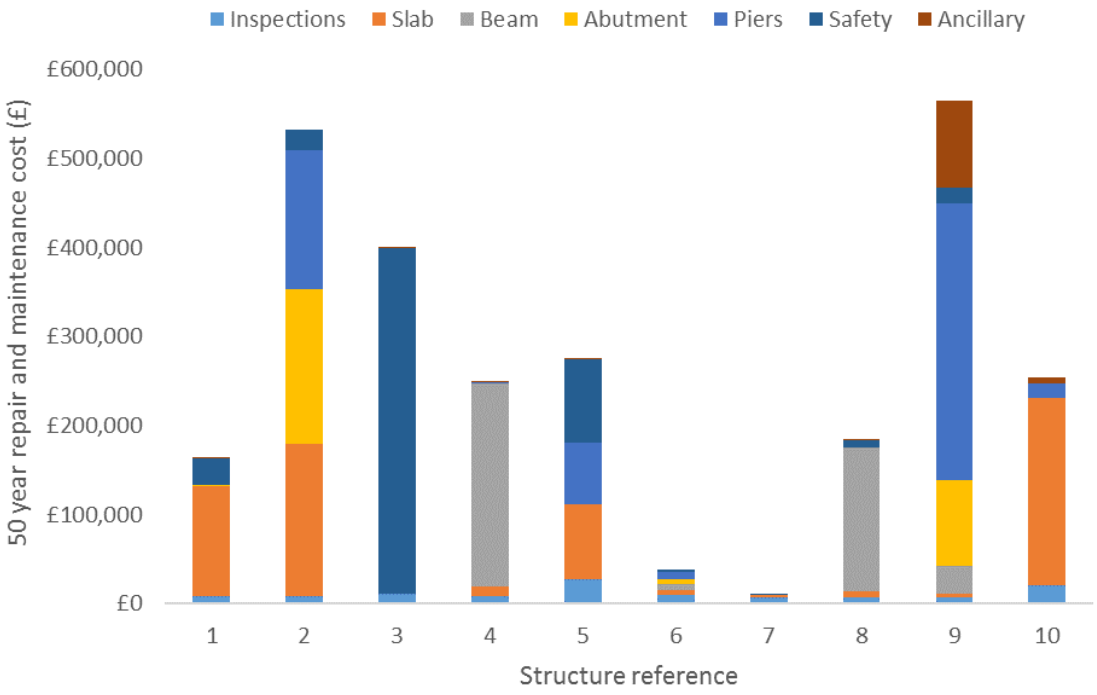

Figure 6.6: Repair and maintenance costs over 50 years excluding 'durability' category elements, calculated from equivalent annual costs.

However, the results of this analysis are based on incomplete historical data and as such are highly sensitive to individual records of repairs being included or excluded from the analysis. There is also no guarantee that other major repairs, particularly early on in the life of the structure, took place but have not been recorded within the SMIS database. It was therefore decided that the data was too sparse and unreliable to be used in the formation of a predictive cost model, particularly to then model the potential cost implications of changing material properties. This agrees with comments by Horner (2005) who stated that historical data models "can lack robustness and are unlikely to be suitable as a cost optimisation tool".

It should also be recognised that significant changes to construction practice have occurred since the construction of these structures (1959-1972). These include new cement blends, increases in the cover specified to the reinforcement and the preferential use of integral bridges and composite deck systems, which all have an effect on the deterioration rates of structures.

It was therefore decided to use an existing theoretical model and, based on the outcomes of this preliminary study, focus on the cost implications of the replacement of traditional concrete with a self-healing concrete in bridge decks.

6.3. STRUCTURES ASSET MANAGEMENT PLANNING TOOLKIT

The Structures Asset Management Planning Toolkit (SAMPT), has been developed by members of Atkins and the UK bridges board for the Department for Transport, to help local authorities manage their structural assets in a cost-efficient manner (Atkins, 2015c). It enables current structure condition information to be used as an input, and then makes use of material deterioration curves and estimated repair costs, based on historical information and industry experience, to estimate the future costs of maintaining those structures.

The deterioration curves in the SAMPT model the degradation of structural elements over time using severity and extent codes, as per the Inspection Manual for Highway Structures (HA, 2007). These codes are made up from a number between 1 and 5 to indicate severity and a letter from A-E to indicate extent of damage. The codes are defined in Table 6.5.

Table 6.5: Condition codes for extent and severity of defects in structures, from the Inspection Manual for Highway Structures (HA, 2007).

Extent	
Code	**Description**
A	No significant defect
B	Slight, no more than 5% of surface area/length/number
C	Moderate, 5-20% of area/length/number
D	Wide, 20-50% of area/length/number
E	Extensive, more than 50% of area/length/number
Severity	
Code	**Description**
1	As new or defect has no significant effect on the element (visual or functional)
2	Early signs of deterioration, minor defect/damage, no reduction in functionality
3	Moderate defect/damage, some loss of functionality could be expected
4	Severe defect/damage, significant loss of functionality and/or element is close to failure/ collapse
5	The element is non-functional / failed

The time taken for each material or element to deteriorate and therefore move up a level in extent and severity of damage is mapped out as a deterioration curve within the toolkit. The curves are calculated as a proportion of the mean time to failure, which can take into account routine maintenance or allow for accelerated deterioration in the case that no routine maintenance is carried out. The mean time to failure and the time proportions which define the deterioration curve are dependent on the exposure condition of the structure and whether any protective coating has been applied.

Three exposure conditions are used; mild, moderate and severe. All primary materials within the model have a defining deterioration curve for each exposure condition, allowing faster deterioration to take place with more severe exposure. An exception is any waterproofing layer, which deteriorates at the same rate regardless of exposure condition.

Different maintenance strategies, which define at which level of deterioration a repair is undertaken, can also be modelled. These strategies can also vary with each element or material. The four maintenance strategies that can be used within the model are: planned preventive, planned targeted, planned do minimum and unplanned reactive. Maintenance strategies can be set on an element basis. For the life cycle cost comparison reported in this thesis, the maintenance strategy 'planned do minimum' was used, as this was deemed the most common strategy to be adopted in practice.

The standard model can be run for a period of 30 years to assess the condition of each element within the structure and the costs required for repair over this period. For the purposes of modelling the costs of a bridge structure, it was recognised that a longer study period than 30 years would be required. The purpose of a self-healing concrete is to extend the service life of a structure, with the ultimate aim of requiring no structural repairs over its entire design life. For concrete bridge structures, this design life is typically 120 years. For this study, therefore, the assumptions and deterioration curves from this model were extended to cover this design life.

Deterioration curves were then modified to model a theoretical self-healing system, as explained in Section 6.3.1.

A declining discount rate was used to calculate the NPV costs for estimated future repairs, following the suggested rates in Table 6.1.

6.3.1. Deterioration curves

The deterioration curves for in-situ reinforced concrete (RC) at the three exposure conditions are given in Figure 6.7. All deterioration profiles used within the model are included as Appendix E.

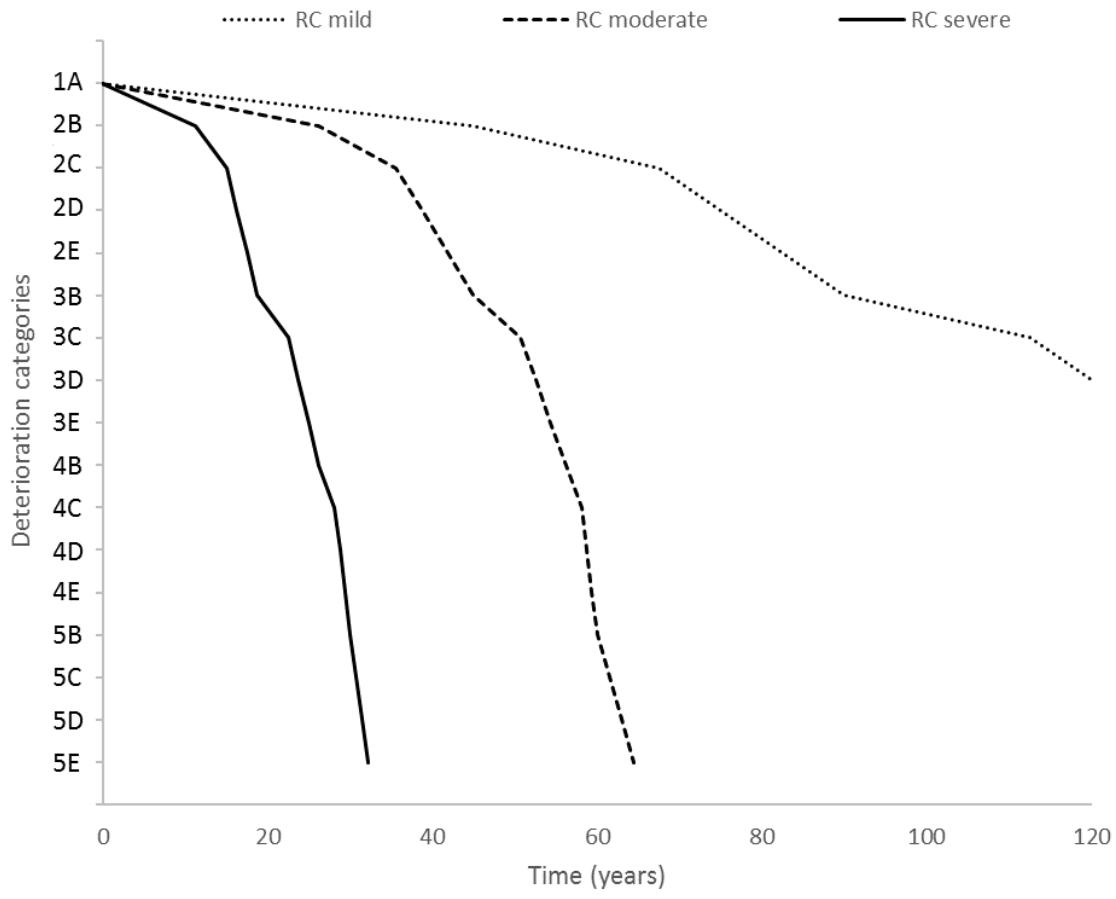

Figure 6.7: Assumed deterioration curves for reinforced concrete with exposure class. Data from (Atkins, 2015).

A repair is 'triggered' once the concrete reaches a given deterioration category. For the 'planned do minimum' regime, the SAMPT model uses a deterioration category of 4D as an

intervention level for RC. Upon reaching this level, the concrete is repaired, returning to a 2B category. The model assumes that repair does not result in an 'as-new' element (deterioration category 1A) as this is not what tends to be found in practice, where often structures need to be repaired on multiple occasions.

It was decided to model a theoretical self-healing concrete (SHC) as one which, in a single healing cycle, repairs an element back to 'as-new' condition after low-level damage or deterioration has occurred. Multiple cycles were then used to model repeated healing. A self-healing concrete capable of a number of healing cycles was then used to represent the 'ideal' self-healing material proposed by Van Breugel (2007) and Van der Zwaag (2007).

Separate deterioration curves for SHC subject to different exposure conditions were needed. It was assumed that a SHC would deteriorate at the same rate as conventional RC; deterioration curves within the SAMPT model for in-situ RC were therefore used as a basis and adapted based on the principle of repeated healing cycles. It was also assumed that, for a SHC with finite healing cycles, the concrete is repaired in the same manner as RC once the healing cycles are complete. This resulted in the deterioration curves shown in Figure 6.8. These curves relate to an element subject to 'severe' exposure conditions.

Each healing cycle begins when the element deteriorates from condition 1A to 2B. It is then assumed that the element fully heals within one year, returning to condition 1A and beginning the deterioration process again. One, two, three and indefinite healing cycles were modelled. It was assumed that these healing cycles require no human input and therefore have no associated cost. Using these deterioration curves, a total life cycle cost comparison can be made between a structure with conventional RC elements and one in which elements have been replaced with a SHC.

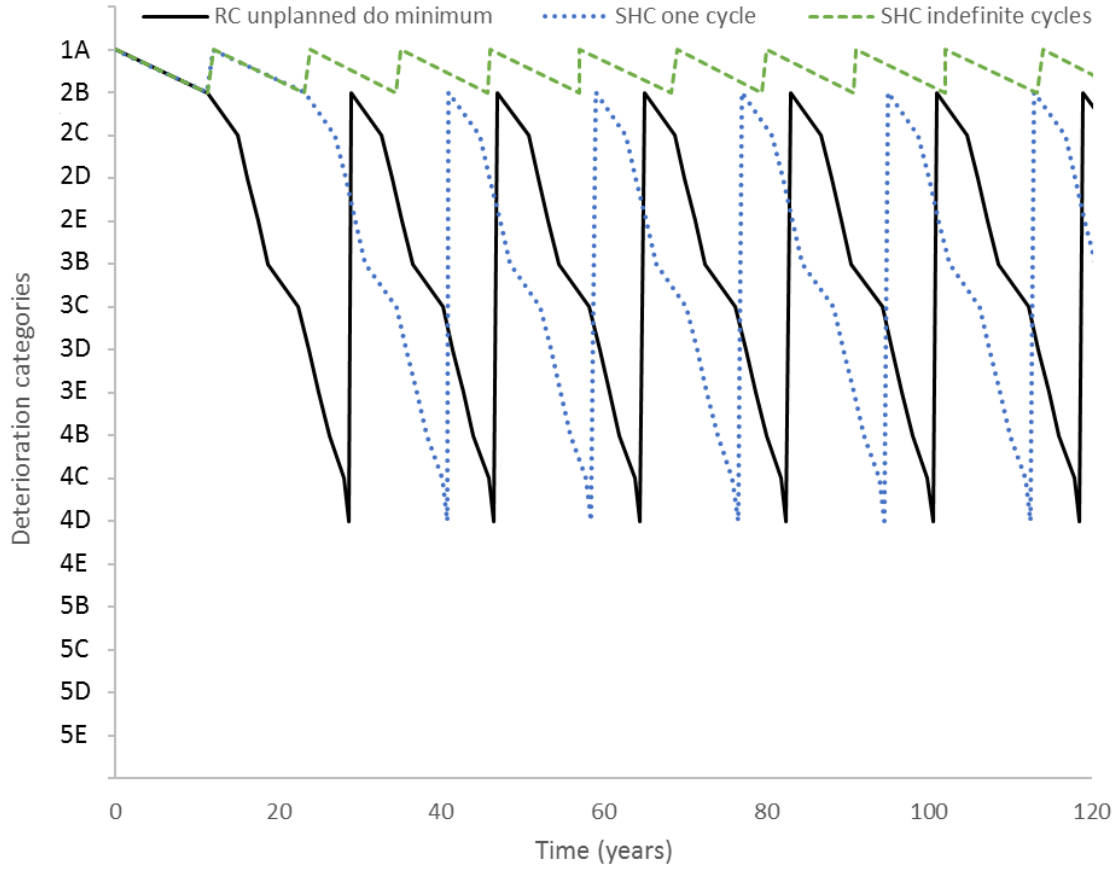

Figure 6.8: Healing cycles and repair regime deterioration curves for severe exposure conditions.

6.3.2. Model assumptions and inclusions

As with all theoretical models, a number of assumptions were made, as detailed in Table 6.6. A list of costs included and excluded from the LCC assessment, and justifications for these decisions, are included as Table 6.7.

It was decided to exclude end-of-life costs, which would usually form part of a LCC assessment (BSI, 2008b), as the impact of the wide variety of potential self-healing techniques on these costs is unclear. For the purposes of this assessment, any end-of-life costs are assumed to be equal. However, future cost assessments investigating individual self-healing techniques would need to take these costs into account.

Table 6.6: Key assumptions followed within the life cycle cost assessment.

Number	Assumption
1	Deterioration profiles and repair cost formulae recommended within the SAMPT are reliable as an approximation for predicting life cycle costs over the chosen study period.
2	No routine maintenance is carried out on the structure being modelled. This is taken into account using an acceleration rate of 0.25 (decreasing the mean time to failure), as suggested by the SAMPT guidance (Atkins, 2015c).
3	A self-healing cycle would result in full repair of an element (to condition 1A).
4	The cost of repair does not change over time other than with inflation, taken into account through net present value calculations.
5	Concrete deck slab repairs are undertaken from below the structure, so do not include removal and replacement of surfacing.
6	A waterproofing layer, while intact, prevents deterioration of the concrete deck slab underneath. This assumption is also adopted by the SAMPT model.
7	Elements are repaired once a 'condition at intervention' state has been reached, defined in Table 6.10.
8	Condition after treatment is 2B unless element replacement takes place, in which case the condition is set at 1A.
9	Only daytime working is applicable for undertaking repairs.

Table 6.7: Items included or excluded from life cycle cost model.

Cost	Description	Included / Excluded	Justification
Design costs	Cost of the initial design of the structure and assessment of options.	Excluded.[1]	Assumed this cost does not change across model cases.
Construction costs	All construction costs including labour, material and plant.	Included.	Cost changes across model cases.
Repair costs	Repair costs over study period, including direct works cost, traffic management, preliminary costs and design cost (see Section 6.4.2).	Included.	Main focus of comparison is the impact of self-healing on repair costs.
Routine maintenance costs	Cost for routine maintenance of the structure over the study period.	Excluded.	Assumed no routine maintenance is carried out (assumption 2, Table 6.6).
End-of-life costs	Cost of demolition or decommissioning of structure.	Excluded.	Impact of self-healing materials unclear.

[1]Design costs excluded with the exception of those associated with repairs, included in equation (14).

The construction and repair costs for all bridge elements were included, despite only the bridge deck slab material being altered. This was to enable a percentage cost-saving comparison against the life cycle costs of the whole structure.

6.4. CASE STUDY: A465 HEADS OF THE VALLEYS BRIDGE STRUCTURE

A structure on the A465 Heads of the Valleys section two improvement project was selected as a case study to explore the variation in life cycle cost if self-healing materials had been used. This approach was chosen to ensure that the cost assessment was relevant to a contemporary design, and to allow accurate construction costs to be included in the analysis. The structure was constructed in Spring 2016.

6.4.1. Structural details

The bridge structure chosen for the analysis was a single span, integral bridge with a composite deck consisting of steel girder beams, steel transverse beams and an in-situ reinforced concrete slab deck. The bridge carries a dual carriageway with two lanes in each direction over a roundabout. Plan and elevation drawings for the structure are shown in Figure 6.9.

The length of the structure was taken as 24m, with an average width of 22.7m. The life cycle cost comparison focused on the potential use of self-healing concrete for the concrete deck slab. This slab was 250mm thick, made from a C40/50 structural concrete mix and high tensile reinforcement. While the focus was on the deck slab, all other bridge elements were also modelled to enable the calculation of percentage cost savings against the construction and repair costs for the entire structure. The abutments and wing walls were made from reinforced concrete, with the latter having pre-cast concrete block facing panels.

For the purpose of the analysis, the deterioration curve for reinforced concrete recommended by the SAMPT was used to model the deterioration of the slab and all other reinforced concrete elements on the structure. Parameters related to the structure used for the analysis to calculate repair costs are shown in Table 6.8.

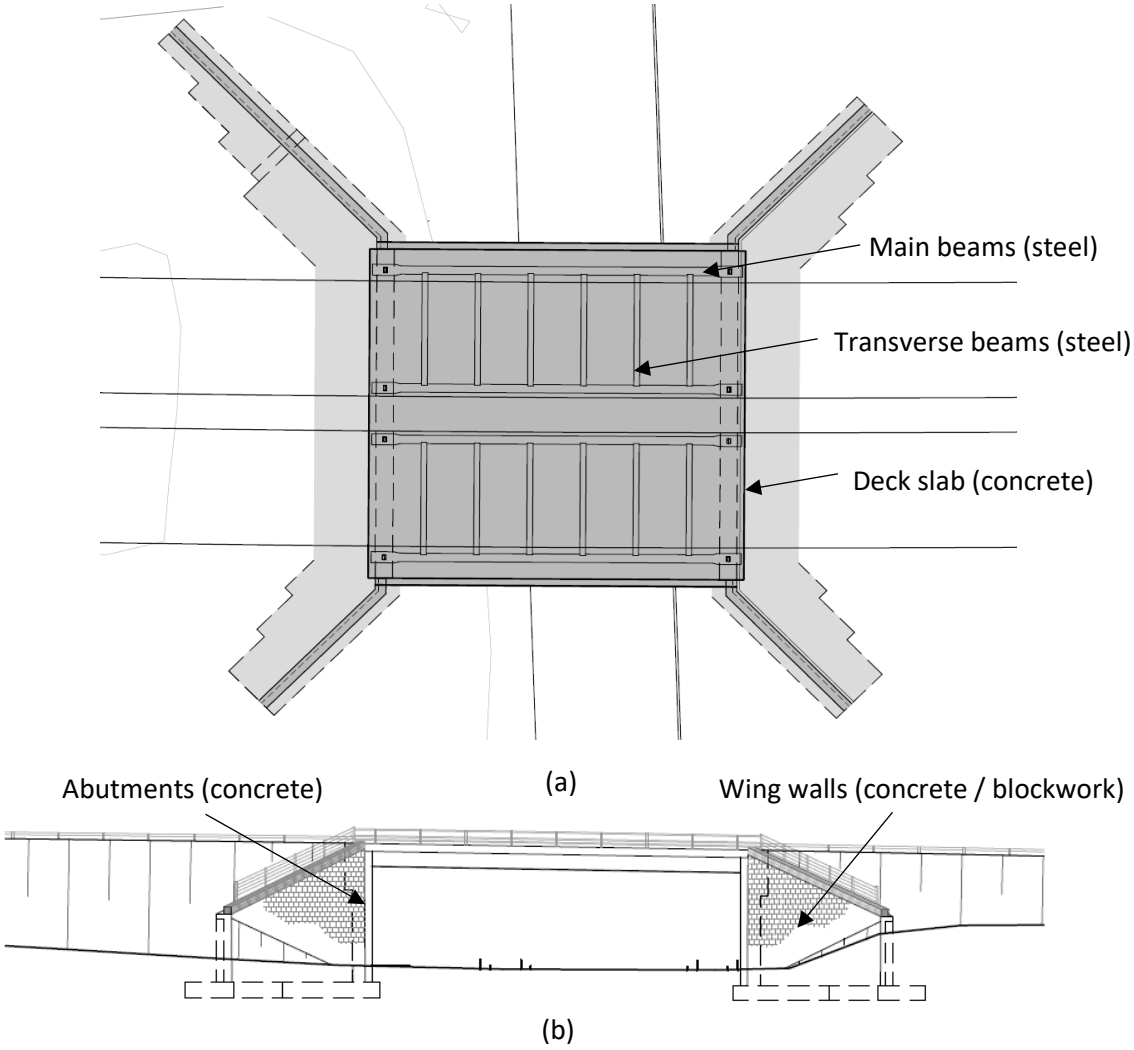

Figure 6.9: (a) plan and (b) front elevation design drawings of case study structure.

Table 6.8: Parameters relating to the case study structure used to calculate repair costs.

Parameter	Value
Length (m)	24
Average width (m)	22.7
Average critical headroom (m)	5.3
Spans	1
Location	Rural
Route supported	Motorway
Traffic quantity	High (definition from (Atkins, 2015c))
Obstacle crossed	Local road – A class
Additional rates	Environmentally sensitive area

6.4.2. Model cases and costs

Seven model cases, detailed in Table 6.9, were used to explore the life cycle costs of the structure. In the actual structure, a spray waterproofing layer is included between the top of the concrete slab and the underside of the pavement layers. An assumption within the existing

SAMPT model is that while a waterproofing layer remains intact, the concrete slab beneath it will not begin to deteriorate. This made it necessary to include a waterproofing layer as one of the model variables.

Table 6.9: Model case definitions.

Model case	Waterproofing installed	Waterproofing maintained	Concrete slab maintained	Healing cycles
Base case 1 (BC1)	Yes	Yes	-	-
Base case 2 (BC2)	Yes	No	Yes	-
Base case 3 (BC3)	No	-	Yes	-
Self-healing 1 (SH1)	No	-	Yes	1
Self-healing 2 (SH2)	No	-	Yes	2
Self-healing 3 (SH3)	No	-	Yes	3
Self-healing 4 (SH4)	No	-	-	indefinite

Three base cases were therefore used: BC1 was identified as the most probable actual scenario, in which the waterproofing is installed and also maintained. BC2 modelled the same case but without any maintenance taking place on the waterproofing, allowing the reinforced concrete slab to then deteriorate and be subject to repair. BC3 modelled the structure without a waterproofing layer.

The construction costs for the structure used within the model were taken from the actual scheme budget provided by principal contractor Costain. Repair costs for the various elements were calculated using equation (14) (Atkins, 2015c). The cost elements included within this equation were calculated from the formulae suggested by the SAMPT model, included as Appendix E. For each of the bridge elements, the relevant deterioration profile was used to calculate intervals between subsequent repairs.

$$SC=WC+TMC+PC+DC+OC \quad (14)$$

Where SC is scheme cost (repair cost), WC is works cost, TMC is traffic management cost, PC is preliminary cost, DC is design cost and OC is other costs.

Based on the model cases, the repair costs were split into variable (deck slab and waterproofing), and non-variable (all other elements). The non-variable costs were included in the analysis to

show savings for each model case relative to all repair costs for the bridge structure. The calculated repair costs for all elements using equation (14) are shown in Table 6.10.

Table 6.10: Bridge elements, deterioration profiles and calculated repair costs used within the model (excluding self-healing concrete, described in section 6.3.1).

Type	Element	Deterioration profile	Condition at intervention	Scheme cost (cost per repair)
Variable costs	Concrete deck slab	In-situ concrete severe	4D	£446,606
	Sprayed waterproofing	Spray systems	5B	£452,367
Non-variable costs	Main steel beams	Fabricated steel severe	4D	£711,508
	Transverse steel beams	Fabricated steel severe	4D	£210,717
	Concrete parapet beam	In-situ concrete severe	4D	£36,825
	Concrete abutments	In-situ concrete severe	4D	£195,145
	Superstructure drainage	Internal drainage moderate	5B	£9,918
	Substructure drainage	Internal drainage moderate	5B	£2,190
	Aluminium safety barriers	Aluminium mild	5B	£69,424[1]
	Handrail	Handrail (other) severe	5B	£69,424[1]
	Concrete wing walls	In-situ concrete mild	4D	£91,904
	Blockwork facing of wing walls	Blockwork moderate	4D	£104,929

[1]Cost is for replacement rather than repair, as per SAMPT model (Atkins, 2015c).

To model the self-healing concrete slab, the modified deterioration curves discussed in Section 6.3.1 were used. One, two, three and indefinite healing cycles were modelled. The construction costs for all self-healing model cases included the standard cost for reinforced concrete, with no addition for self-healing techniques. This was to allow the output of the model to be an assessment of the allowable increase in the cost of the concrete to incorporate the modelled levels of healing, based on differences in life cycle costs. Waterproofing was not included in the self-healing model cases as it was clear this would result in no change to the model outputs compared to the base cases.

6.5. RESULTS AND DISCUSSION

Figure 6.10 shows the calculated non-variable costs for the structure over the study period, while Figure 6.11 shows the variable costs for each model case. Table 6.11 shows the total life cycle cost for all of the cases over a 120-year lifespan along with the calculated savings over BC1.

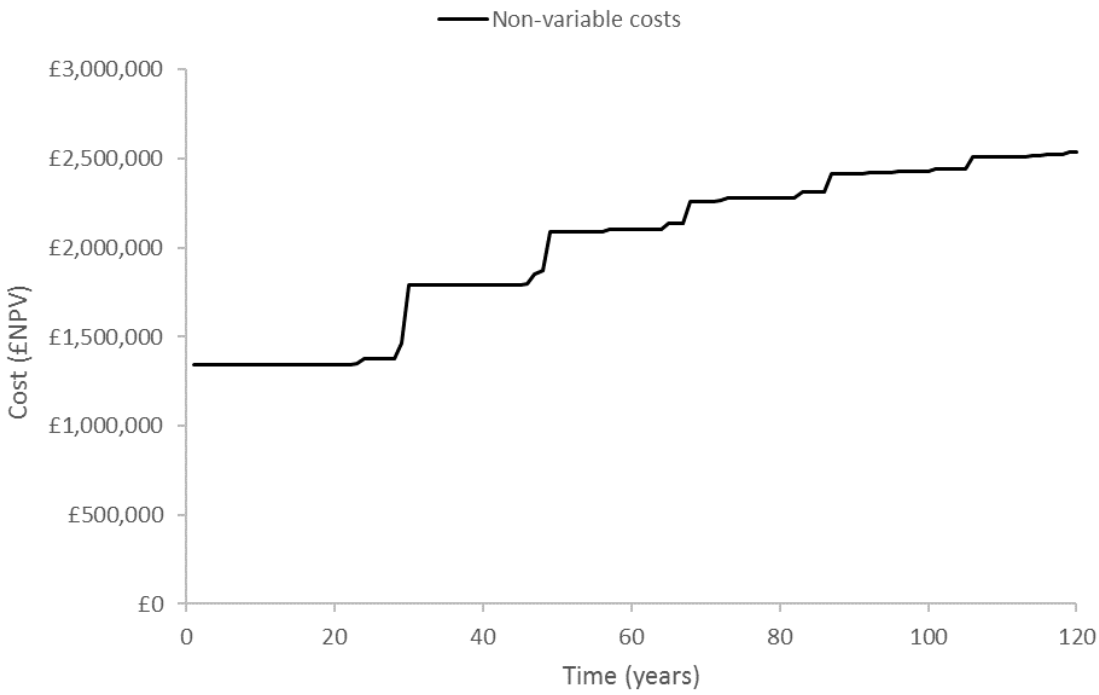

Figure 6.10: Non-variable costs over the life of the structure.

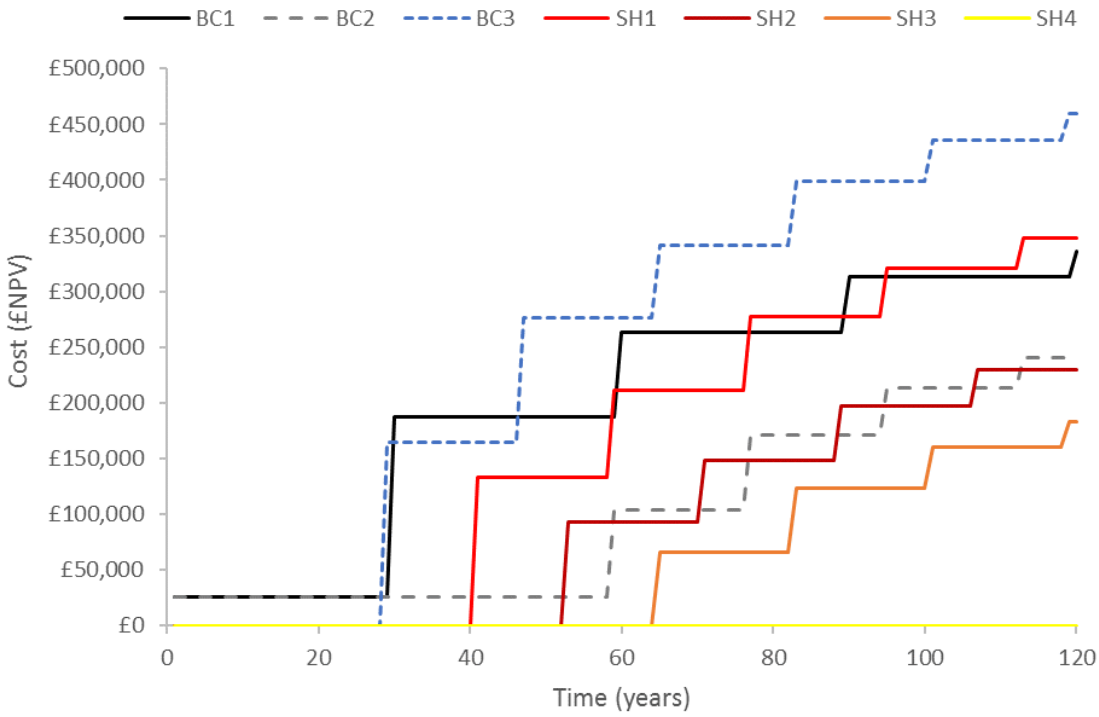

Figure 6.11: Variable costs for each model case over the life of the structure.

These results show that there are significant savings possible by increasing the durability of the concrete deck slab. Compared to the most probable scenario of BC1, all of the self-healing options, with the exception of SH1, have reduced estimated life cycle costs when considering a

120-year lifespan. It is clear that the estimated cost savings only become attractive with repeated healing cycles. A single healing cycle, modelled in SH1, results in a cost increase of £11,790 over the whole life. However, as this is just 0.4% of the total life cycle costs for BC1 over a 120-year period, this difference is considered to be negligible.

Table 6.11: Total life cycle costs for all model cases over 120 years.

	Model cases						
	BC1	**BC2**	**BC3**	**SH1**	**SH2**	**SH3**	**SH4**
Construction costs	£1,369,568	£1,369,568	£1,343,788	£1,343,788[1]	£1,343,788[1]	£1,343,788[1]	£1,343,788[1]
R&M costs (£NPV)	£1,505,533	£1,410,181	£1,654,645	£1,543,103	£1,424,594	£1,378,639	£1,195,198
TOTAL	**£2,875,101**	**£2,779,749**	**£2,998,433**	**£2,886,891**	**£2,768,383**	**£2,722,428**	**£2,538,986**
Savings over BC1	£0	£95,352 (3.3%)	-£123,332 (-4.3%)	-£11,790 (-0.4%)	£106,718 (3.7%)	£152,673 (5.3%)	£336,115 (11.7%)

[1]Not including any additional cost for self-healing techniques, as explained in Section 6.4.2.

Life cycle cost savings of £106,718 (3.7%) are estimated for two healing cycles, £152,673 (5.3%) for three cycles, and £336,115 (11.7%) for indefinite healing cycles.

It should be noted that, although the percentage savings seem relatively low, these are the result of replacing a comparatively low-cost element of the structure. Extracting the construction cost of the concrete deck slab (material and labour), taking the unit rate of £113.22/m³ used within the scheme budget, gives a value of £15,421, just 1.1% of the total construction cost. If this slab was replaced with a material capable of the healing cycles modelled in SH4, for example, the cost of this concrete could be increased by up to 2180% and still result in a lower life cycle cost for the structure. This concept is demonstrated in Table 6.12. Allowable cost is defined as the maximum cost for the concrete at which the life cycle cost for the structure, over the 120-year study period, would not be increased.

Table 6.12: Allowable increase in concrete cost for self-healing slabs.

	BC1	**SH2**	**SH3**	**SH4**
Savings over 120 years (£NPV)	-	£106,718	£152,673	£336,115
Allowable concrete slab cost	£15,420.56	£122,138.87	£168,093.92	£351,535.78
Allowable concrete cost (£/m³)	£113.22	£896.76	£1,234.17	£2,581.03
Percentage increase (%)		692%	990%	2180%

This suggests that a self-healing concrete deck slab capable of multiple healing cycles could justify a significant increase in material cost compared to conventional reinforced concrete, based on savings in repair costs over the life cycle of the structure. This generally agrees with the conclusions of research by Li and Herbert (2012) on Engineered Cementitious Composites, in which cost savings are predicted over the life of a structure despite increases in material cost of over 100%, based on its self-healing capacity.

Due to the large cost of concrete repairs over the life of the structure, any delay in the deterioration of the concrete over this life will inevitably result in significantly reduced costs, even when discounting these costs over time. However, it must be recognised that these figures relate to a 120-year period and, due to the nature of life cycle cost modelling, are subject to significant uncertainty.

It is also apparent from Table 6.11 that BC2 resulted in lower life cycle costs than BC1, SH1 and SH2. It appears that the estimated cost of repairing the waterproofing layer over the 120-year period in BC1 outweighed the cost of repairing the concrete slab in BC2, as the deterioration of the slab in BC2 had been delayed by the initial presence of the waterproofing layer. This delayed deterioration was actually more beneficial in terms of life cycle cost than using self-healing concrete with up to two healing cycles. The sensitivity of these results to the estimated cost of the waterproofing and concrete repair was therefore investigated as part of the sensitivity analysis in section 6.6.

As expected, BC3 resulted in higher life cycle costs compared to all other options, as deterioration of the concrete slab occurred rapidly without a protective waterproofing layer, resulting in large repair costs.

6.6. SENSITIVITY ANALYSIS

To investigate the significance of key variables within the model and in accordance with guidance from BS ISO 15686-5:2008 (BSI, 2008b), a sensitivity analysis was undertaken. The variables assessed and their range of values is detailed in Table 6.13.

Table 6.13: Variables subject to sensitivity analysis.

Variable	Standard value	Range
Study period	120	50-120 years, intervals of 10
Discount rate	3.5-2.5%[1]	1.0-7.0%, intervals of 0.5%
Exposure class	severe	mild, moderate, severe
Concrete deck repair cost	£446,606	±5,10,15,20 and 50%
Waterproofing repair cost	£452,367	±5,10,15,20 and 50%

[1]Declining rate from 3.5-2.5% used within the model. Fixed rates used within the sensitivity analysis for simplicity.

6.6.1. Study period

As life cycle cost analyses are very dependent on the study period used, the model outcomes were assessed throughout the range of 50-120 years. The results of this analysis are shown in Figure 6.12.

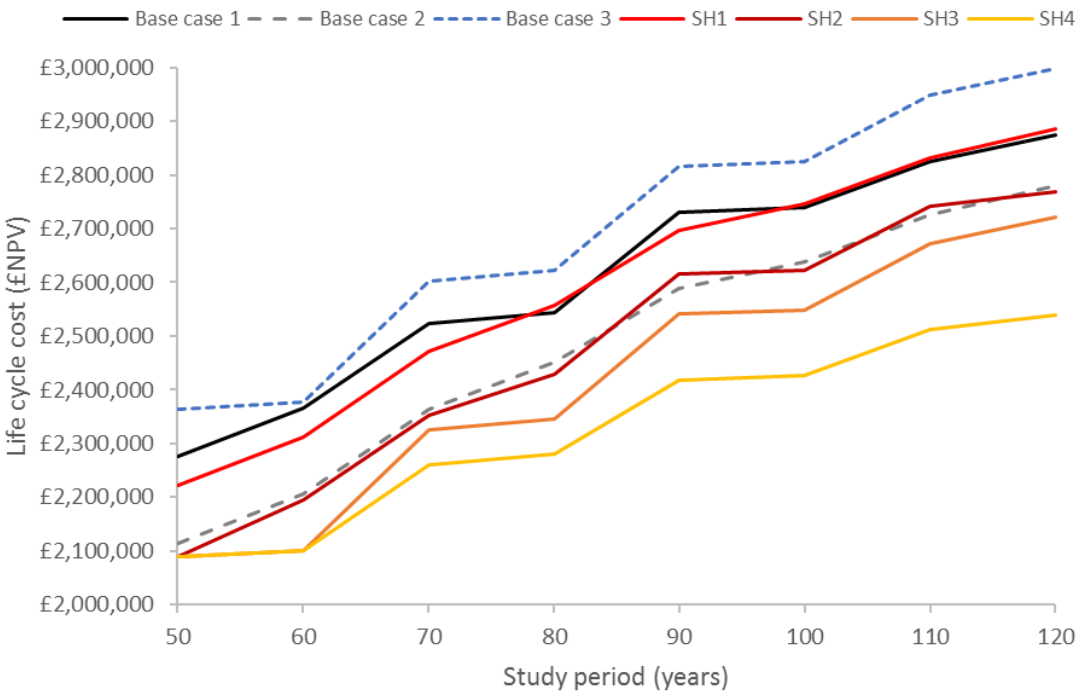

Figure 6.12: Sensitivity of life cycle cost assessment results to changing study period.

As expected, longer study periods result in significantly higher life cycle costs for all model cases. The cost savings for repeated healing cycles, particularly SH4, become more significant with increasing study period. For all other cases there is not much change in the ranking of results with changing study period. It can therefore be concluded that the outcomes of the model in terms of demonstrating the cost-saving potential of a self-healing concrete bridge deck, are not very sensitive to changes in the study period in the range 50-120 years.

6.6.2. Discount rate

A declining discount rate of 3.5% to 2.5% over the 120 year period was used within the model, following the guidance for long term and large value public sector projects (Treasury, 2011). Different rates may be used, however, based on the client, project, degree of risk and levels of future inflation (Horner, 2005). Figure 6.13 shows the change in life cycle cost as the discount rate is varied from 0% to 7% for all model cases.

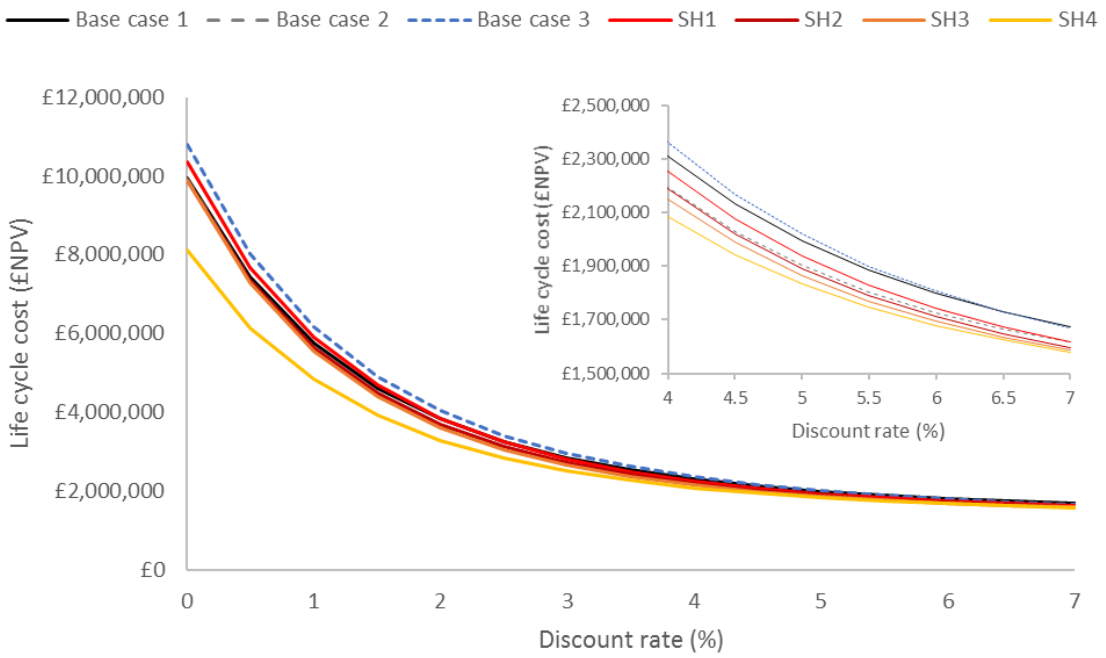

Figure 6.13: Sensitivity of life cycle cost results to changing discount rate; inset: change in ranking with higher discount rate.

It can be seen immediately that the main effect of increasing the discount rate is to cause both a reduction in the life cycle cost and for the results to converge, reducing the difference between them. Lower discount rates enhance the perceived benefit of a self-healing concrete bridge deck because higher rates reduce the value of costs incurred later in the life of the structure, such as repairs. As the benefit of a self-healing concrete is to avoid these types of repair, it is logical that using a higher discount rate will make such a material seem less cost-effective.

However, increasing the discount rate actually causes BC1 to become less favourable, moving from the 5th lowest WLC with a 0% rate to the most expensive option with a 7% rate. This is due to the increased importance of construction costs with high discount rates, making BC1 less favourable because of the additional cost of installing a waterproofing layer.

At a discount rate of 7%, the LCC saving for SH4 over BC1 is only £94,173 (or 5.6%) compared to £1,835,249 (18.5%) using a rate of 0%. Even with a rate of 7%, however, the calculated savings for SH4 would allow an increase in material cost of up to 611% (from £113 to £805/m^3) compared to conventional RC.

It can be concluded that the discount rate significantly affects the final life cycle cost and the calculated benefit of a self-healing concrete deck slab, and has some impact on the model case rankings. Across the range studied (0-7%), a concrete deck slab capable of multiple healing cycles still shows significant LCC benefit when considering a study period of 120 years.

6.6.3. Exposure condition

A severe exposure condition was used within the model to estimate the deterioration of the bridge structure. This assumption was based on the high probability of the structure's exposure to road salts, temperature fluctuations and cyclic loading from road traffic. To assess the sensitivity of the model to this variable, the comparison was re-run with mild and moderate exposure conditions.

As shown in Figure 6.14, the exposure class used within the analysis significantly changes both the value of the results and the difference between each model case. This is particularly evident in BC1, which is less cost-effective in moderate and mild exposure conditions. This is due to the assumption within the model that the exposure condition does not affect the rate of deterioration of the waterproofing layer, suggesting that maintaining and repairing a waterproofing layer is not cost-effective when the structure is not exposed to severe environmental conditions.

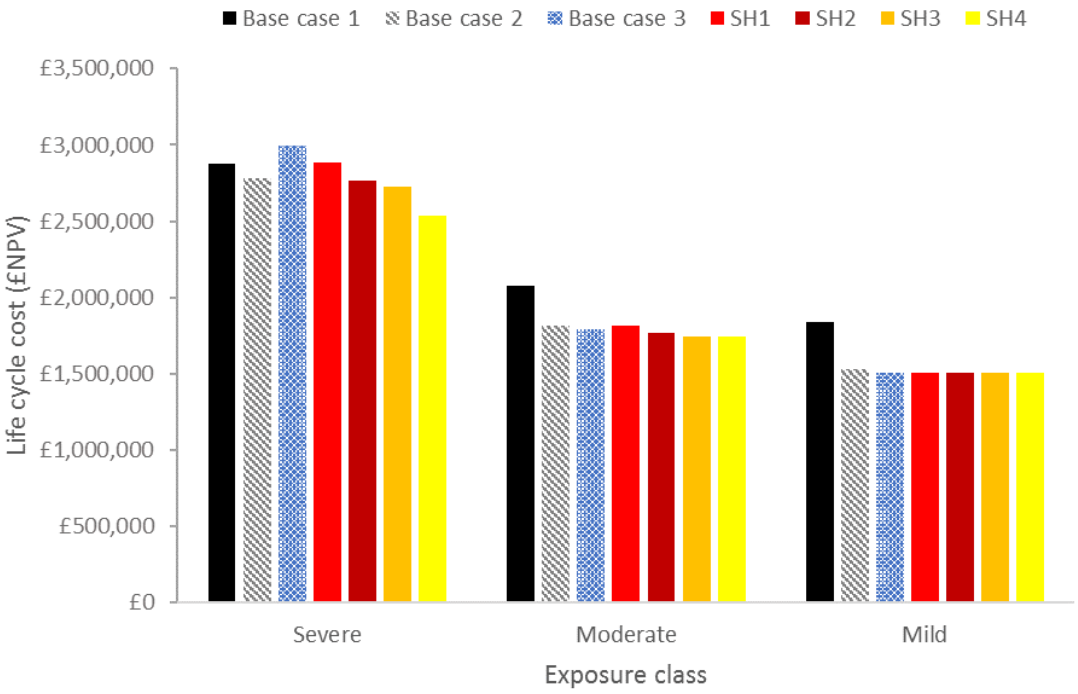

Figure 6.14: Sensitivity of life cycle cost to changing exposure class.

A second conclusion relating to exposure condition is that the estimated cost benefit of incorporating a self-healing concrete slab is greatly reduced with moderate exposure, and non-existent for mild exposure. For mild exposure in particular, the model predicts that no concrete repairs are required over the 120-year lifespan, suggesting that a SHC would not bring any benefit to the structure. For mild exposure there is no difference in LCC between the model cases, with the exception of BC1 and 2. It is therefore apparent that the life cycle cost model is very sensitive to changes in exposure class.

6.6.4. Concrete deck repair cost

The cost of repair for the concrete deck slab was calculated based on the equations used within the SAMPT model, included as Appendix E. Figure 6.15 shows the changing life cycle cost for all model cases when the concrete deck slab repair cost is varied from -50% to +50% of the estimate.

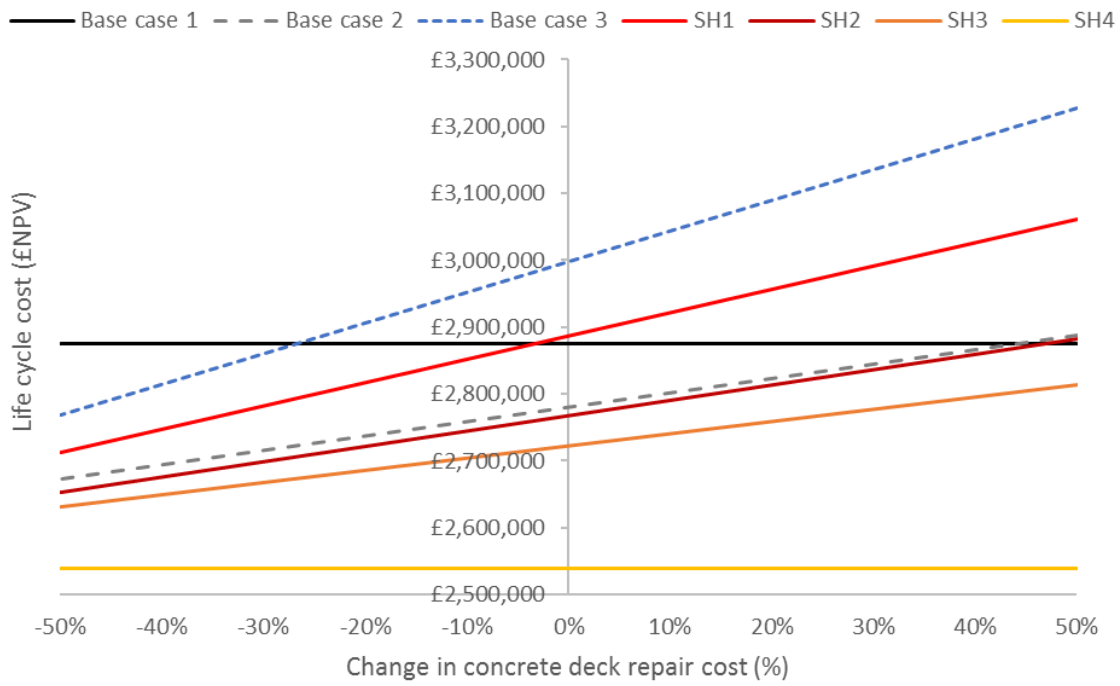

Figure 6.15: Sensitivity of life cycle cost to changing concrete deck repair cost.

In all cases (with the exception of BC1 and SH4 in which concrete repairs are not carried out), increasing repair cost causes a significant increase in the LCC of the structure. SH4 and SH3 remain the most cost-effective options throughout the range modelled. It can therefore be stated that the model is sensitive to this variable, but it does not change the overall conclusion that repeated self-healing is the most cost-effective option.

6.6.5. Waterproofing repair cost

The cost of waterproofing repair was varied in the same manner as the concrete deck slab repair cost, over a range of -50% to +50%. The results are shown in Figure 6.16.

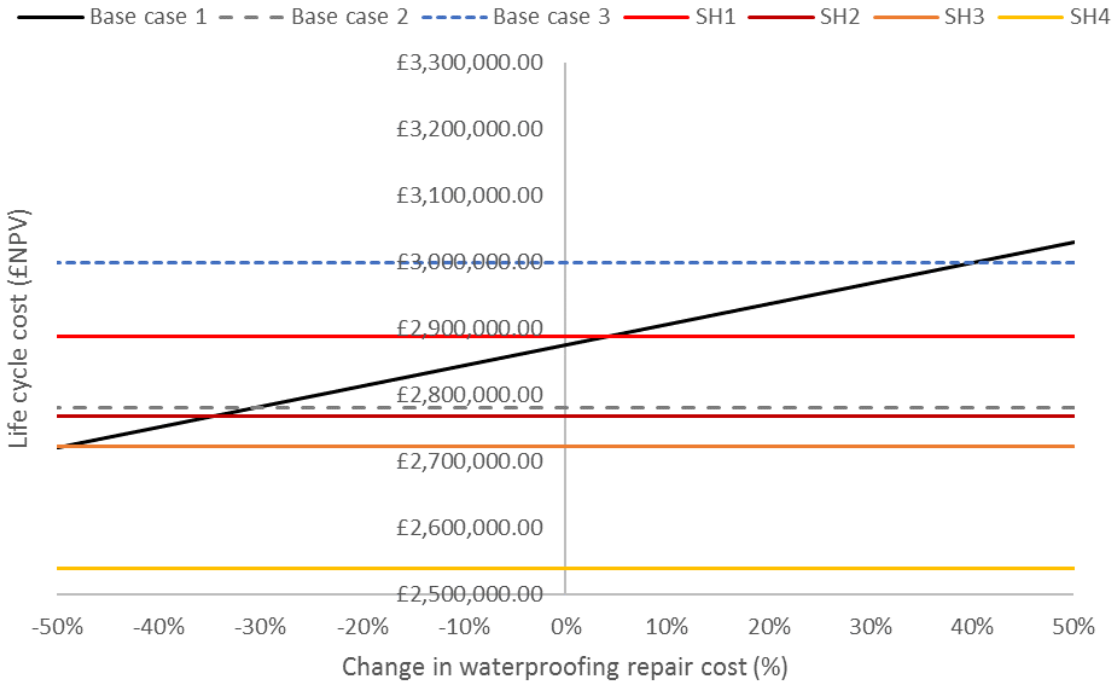

Figure 6.16: Sensitivity of life cycle cost to changing waterproofing repair cost.

BC1 is the only model case which is affected by this variation, being the only case in which the waterproofing is repaired over the life of the structure. However, this is significant as BC1 is the most probable real-life situation, and is the most logical case to use for comparison to the self-healing model cases. Within the identified range, even with repair costs 50% below the estimated cost, BC1 is still less cost-effective than SH4 and has approximately the same LCC as SH3. With increased waterproofing repair cost, BC1 becomes less and less cost effective in comparison to the other model cases, eventually becoming the most expensive option with a 50% increase.

6.6.6. Conclusions from sensitivity analysis

From the sensitivity analysis it can be concluded that, while the resultant costs from the LCC assessment change significantly with variations in study period and discount rate, the ranking of each model case does not fundamentally change making the overall conclusion the same; i.e.

that a self-healing concrete deck slab capable of repeated healing cycles would result in lower life cycle costs.

The same cannot be said of the exposure class used within the analysis. With moderate rather than severe exposure, the cost benefit of a self-healing deck slab is significantly reduced, while with a mild exposure class it is apparently non-existent. This suggests that a self-healing concrete in this application is only beneficial when the structure is exposed to severe conditions, based on the definitions within the SAMPT model.

Variations in the cost of both concrete deck repair and waterproofing repair also affect the outcomes of the model. With higher concrete repair costs, a self-healing alternative is predictably more beneficial. With changing waterproofing repair costs, the base case used for comparison (BC1) becomes more or less desirable, but within the range analysed never becomes more cost effective than a self-healing concrete capable of indefinite healing cycles.

6.7. CONCLUSIONS FROM CHAPTER 6

- A preliminary study using historical costs of ten existing concrete bridges around England has concluded that concrete deck slabs are often subject to significant repair costs over the life of the structure. However, insufficient historical data was available to form a predictive model using this method.

- Adaptations were made to deterioration curves in the Structures Asset Management Planning Toolkit (SAMPT) to allow self-healing concrete deck slabs to be modelled with varying number of self-healing cycles.

- The adapted model was used to carry out a life cycle cost assessment, using a bridge constructed as part of the A465 Heads of the Valleys road improvement project as a

case study. The LCC of the structure was modelled, comparing the costs associated with a conventional RC deck slab against a SHC deck slab capable of one, two, three and indefinite healing cycles.

- The results of this assessment have shown that a concrete deck slab capable of a single healing cycle would not reduce the LCC of the structure. However, with multiple healing cycles the LCC is reduced significantly, saving up to 11.7% of the structure's construction and repair costs. Given the relatively low material cost of the concrete deck slab compared to the potential savings over the 120-year study period, an increase in material cost of up to 2180% could be justified for the use of a self-healing concrete capable of multiple healing cycles.

- A sensitivity analysis was carried out by altering key variables within the model and observing the change in outputs. This analysis found that the model is very sensitive to the exposure class used; a self-healing concrete deck slab is most viable for structures subject to severe exposure conditions, with no cost benefits seen in mild exposure conditions. The calculated cost savings are also sensitive to changes in study period and discount rate, although across the range of values investigated for both of these variables, the overall conclusions of the study remain the same.

This life cycle cost assessment has given an indication that a self-healing concrete, capable of multiple healing cycles, would yield a positive cost benefit when used for the concrete deck of contemporary bridges in severe exposure conditions over the design life of the structure. Suggestions on how to improve upon this model are discussed in section 7.2.

Chapter 7. Conclusions and Recommendations for Future Work

This chapter reviews the general conclusions of the work presented within this thesis, along with suggestions for future areas of investigation. Conclusions related to each section of work are included at the end of each individual chapter.

7.1. THESIS CONCLUSIONS

The research objectives, as outlined in Chapter 1, are repeated below:

1. Refine and develop a high shrinkage shape memory polymer material to enable it to be used in concrete.
2. Refine and develop an SMP system to close cracks and enhance autogenous self-healing in structural concrete elements.
3. Test the SMP system and its ability to enhance autonomous self-healing at full scale.
4. Complete a life cycle cost comparison of self-healing concrete in a real-world application.

With respect to these objectives, the following conclusions were drawn from the research:

1. A series of experiments was carried out on shape memory PET samples manufactured by Bradford University, comparing these to the commercially available PET strip samples that had been used previously. Samples were tested in restrained shrinkage, free shrinkage, Young's modulus, tensile strength and alkalinity resistance. The main conclusions drawn were:

- PET *solid filament* and *filament tube* samples, die-drawn at a rate of 1000mm/min to a draw ratio of 4.0, were found to be the most suitable polymer for a concrete crack closure system from those tested. These samples produced approximately double the restrained shrinkage stress and exhibited 1.7 times the tensile strength of the commercially available PET *strip*.

- Both *filament* samples also exhibited a higher level of free shrinkage (indicative of lower sensitivity to relative movement when placed within concrete samples), a higher Young's modulus and can be bundled into tendons in a more practical manner than the *strip* samples.

- PET *solid filament* samples submerged within a high alkalinity synthetic concrete pore solution at 60°C for 1 month exhibited a loss of mass of between 15-18%, attributed to alkaline hydrolysis. It was recognised therefore that the *filaments* would need to be protected from the concrete environment within the final system.

2. The commercially available *strips* were used to enhance autogenous self-healing within concrete beam samples of size 500x100x100mm over 1, 3 and 6-months of healing. The *solid filament* samples were then incorporated into shape memory polymer tendons. These tendons consisted of 200 filaments and an electrical activation system protected by an injection moulded sleeve. The tendons were tested both individually and within unreinforced and reinforced concrete beam samples to close cracks induced through 3-point bending. The following conclusions were drawn:

- The *strip* samples successfully closed cracks in the unreinforced concrete beams and enhanced the autogenous self-healing. A 78% reduction in surface crack width of

the concrete beams was observed upon polymer activation at 90°C in an oven. This improved to 95% after 28 days healing in water. Load recovery, measured as a comparison between the final (healed) peak load and the initial peak load, taking into account the residual load capacity of the beams, was 33% after six months of healing for samples in which the polymer was removed prior to final loading. An apparent load recovery of 98% (including the compressive force of the polymer) was observed for beam samples in which the polymer was not removed.

- The *solid filament* tendons produced a restrained shrinkage stress of 17.79-19.19MPa when activated to 90°C using the wire heating system. Within unreinforced concrete beam samples, activation of the tendons produced a crack closure of up to 85% and a significant increase in concrete beam stiffness upon reloading. Within reinforced beams, the measured crack closure was 26-39% despite challenges in reaching the desired activation temperature within the tendons.

- The shape memory polymer tendon system has resulted in the closure of cracks in structural concrete beams. However, there were challenges associated with fully activating the tendons and achieving successful crack closure within the reinforced samples. It is suggested that the tendons may be best suited as a method to replace crack control steel within reinforced concrete members, as discussed in Section 7.2.1.

3. A full-scale site trial of the shape memory polymer concrete crack closure system was undertaken, along with three autonomous self-healing techniques investigated as part of the Materials 4 Life project. Five reinforced concrete test panels were designed and constructed on the A465 Heads of the Valleys section 2 project, one of which contained

ten SMP tendons. The panels were loaded to induce cracking, the tendons were activated and the panels monitored over six months before a final loading stage was completed. The main findings were:

- The polymer tendons resulted in an increase in stiffness during initial loading (before activation) of panel B compared to control panels D and E. Activation of the tendons resulted in an average crack closure of 10-16% on panel B, applying an estimated compressive stress of 0.24MPa across the crack. Upon reloading after activation, a reduction in crack displacement at peak load was observed, compared to the results of loading immediately before activation.

- A reduction in crack width was observed from microscope images in all panels except panel C. This suggested that some crack healing had occurred. However, the crack healing observed for panels A and B containing autonomous self-healing techniques was minor and did not exceed the healing observed within the control panel D.

- Upon final loading, an improvement in load capacity at small crack displacement, indicative of crack healing, was observed for panels B and E into which sodium silicate solution had been introduced through flow networks, compared to panel A containing microcapsules.

4. A life cycle cost model for self-healing concrete bridge decks was developed by adapting material deterioration profiles in the existing Structures Asset Management Planning Toolkit. Concrete capable of varying numbers of self-healing cycles was modelled over a 120-year study period compared to conventional reinforced concrete. A single-span

bridge structure on the A465 Heads of the Valleys section 2 project was used as a case study. The main conclusions drawn were:

- Multiple healing cycles are required for self-healing concrete to be cost effective within the application investigated. A conventional reinforced concrete bridge deck with waterproofing has lower life cycle costs than a self-healing alternative capable of just one healing cycle. A theoretically 'perfect' self-healing concrete capable of indefinite healing cycles, however, could reduce the life cycle costs of the case study structure by up to 11.7%.

- A self-healing concrete bridge deck is only economically justifiable in severe exposure conditions. With mild or moderate exposure, the potential life cycle cost savings are significantly reduced or non-existent.

7.2. RECOMMENDATIONS FOR FUTURE WORK

7.2.1. Shape memory polymer system to replace crack control steel

Within previous studies (Isaacs et al., 2013, Hazelwood et al., 2015) as well as in the current thesis, shape memory polymers have been proposed as a method to enhance the autogenous or autonomous self-healing of concrete structures by producing a compressive stress across crack faces. While this has been demonstrated successfully within unreinforced mortar beams (Isaacs et al., 2013) and unreinforced concrete beams in the current study, it is apparent that the system has limited effect within reinforced concrete beams.

It is proposed by the author that the SMP system may be better employed as a replacement for steel reinforcement in the case where this steel is not required for load bearing, i.e. the steel is included purely for the purpose of controlling crack widths. In this way, the SMP could produce a low level pre-stress on the concrete member to restrict crack widths to below the levels

required by current design standards, while enhancing the autogenous healing where water is present. This approach could also reduce material costs by replacing the expensive steel bars.

Future experimental work could introduce varying amounts of steel reinforcement and SMP tendons into concrete structures to justify this approach. A study into the potential applications in the real world and the relevant industry standards for those applications would also be very beneficial.

The electrical activation system used within the current study was not completely successful, particularly within the reinforced concrete beams and when applied during the full-scale trial. A more robust activation system is vital for the next generation of SMP tendons, to ensure that all filaments within the tendon are fully activated. The literature suggests alternative activation methods, for example using microwave radiation (Yakacki et al., 2009), which may be more reliable or suitable for on-site use than using resistance heating wires. However, this would require additions to the polymer material which would add complexity and cost to the manufacturing process and change the material properties.

A lower restrained shrinkage stress was observed with increasing number of filaments per tendon, attributed to misalignment and differing levels of slack between the filaments. An improved tendon manufacturing method for large numbers of filaments would produce higher stresses in the finished tendons. One possibility is for the filaments to be wound in a similar way to steel wire rope strands, as shown in Figure 7.1, which would also make the filaments easier to handle prior to placement within concrete. However, this would require specialist manufacturing equipment and there may be challenges associated with ensuring all of the filaments are loaded equally and not over-stressed during the stranding process.

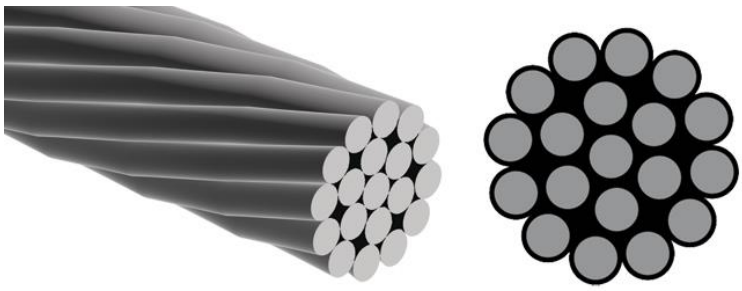

Figure 7.1: Steel wire rope strand example (1x19) (SWR, 2016).

A drop in restrained shrinkage stress was observed for the PET filament samples upon cooling. It is suggested that this drop is related to a reduction in the thermal coefficient of expansion in the direction of drawing. However, this has not been verified by experimental data. In addition, the long-term performance of the tendons within concrete beams both in terms of loss of stress over time and resistance to the alkaline environment have not been investigated in detail. Adaptations to the numerical model developed by Hazelwood et al. (2015) to include the SMP filament tendon behaviour, supported by experimental data, would contribute to the knowledge of how the system performs.

7.2.2. Self-healing concrete

The ability for structures to sense and diagnose damage, to then regulate an appropriate healing response multiple times over the structure's lifespan is the ultimate aim of self-healing concrete research. This would then allow a 'damage management' approach to structural design, as suggested by Van der Zwaag (2007), leading to improved resilience and reduced life cycle costs for concrete structures.

The outcomes of the site trial in Chapter 5 indicated that the autonomous self-healing concrete techniques investigated, while showing some success within a laboratory environment, are currently not sufficiently robust to produce significant healing within full-scale structures. The lack of full-scale applications of self-healing techniques within the literature also reflects this.

Further work is therefore required to ensure that the self-healing techniques under investigation can function within real structures outside the laboratory. Larger scale testing using structural concrete mixes is required. A focus on particular applications would allow more realistic testing regimes and an improved justification of the value of self-healing. This will depend on the type and severity of the damage that the structure is expected to experience. For example, in highway bridge decks the primary damage method may be chloride attack leading to corrosion of the reinforcement, with autonomous healing techniques designed to counteract this process.

The ability to place self-healing techniques into targeted areas of the structure is an important future development, as this will reduce the additional cost of self-healing concrete while providing the same extension in service life. This may be achieved through sequential pouring or specialist pre-casting methods and will depend on the structure under consideration.

As indicated by the life cycle cost assessment, techniques which enable repeated healing cycles to occur within concrete are preferable to those which allow only a single healing cycle. While theoretically possible through the use of bacteria or flow networks, a robust system demonstrating repeated autonomous self-healing has yet to be developed.

In addition, sensing techniques which can diagnose damage and initiate an appropriate healing response have not yet been investigated. It is envisaged by the author that research into combined autonomous sensing and healing techniques for concrete capable of producing multiple healing cycles will be a long-term focus for experts within the field.

7.2.3. Life cycle costing of self-healing concrete

A life cycle cost assessment is vital to justify any additional construction or material costs associated with self-healing concrete, based on future cost savings. The LCC model presented in Chapter 6 made use of general deterioration curves to predict costs for concrete bridge deck slabs over a 120-year study period. However, this model is only applicable for highways

structures and would need to be adapted to take into account different conditions or damage scenarios. This would enable a more in-depth assessment of the potential savings related to self-healing concrete. The effect of each self-healing concrete technique on the assumed material deterioration profile could also be studied and justified based on experimental evidence.

The environmental sustainability of self-healing concrete should be assessed through the addition of carbon and embodied energy calculations into the LCC model. The model could also be expanded to take into account manufacturing and end of life processes, which would need to be based on specific self-healing techniques.

The uncertainty within the LCC model should be assessed in more detail through the use of a Monte Carlo analysis. This allows the assessment of the consequences of simultaneous uncertainties and can take into account correlations between these inputs. By replacing single value entries for the key variables with probability distributions, the LCC model can be run multiple times to produce a range of output costs with associated probabilities. In this way, a range as well as an expected value for the LCC of various options can be generated. This method is particularly useful when there are many variables with significant uncertainties (Treasury, 2011, BSI, 2008b), which is to be expected when modelling the cost benefit of a variety of self-healing techniques.

Appendix A Polymer restrained shrinkage at 90°C repetitions

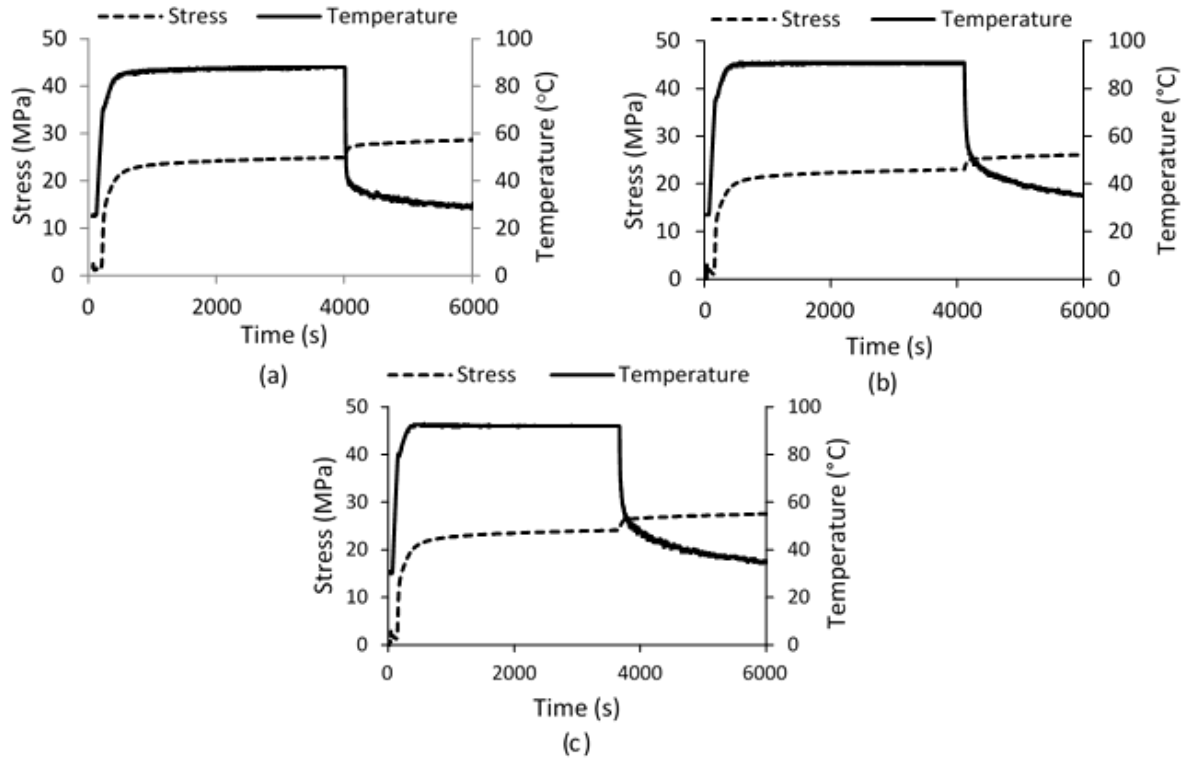

Figure A.1 (a)-(c): PET strip shrinkage at 90°C experiment repetitions.

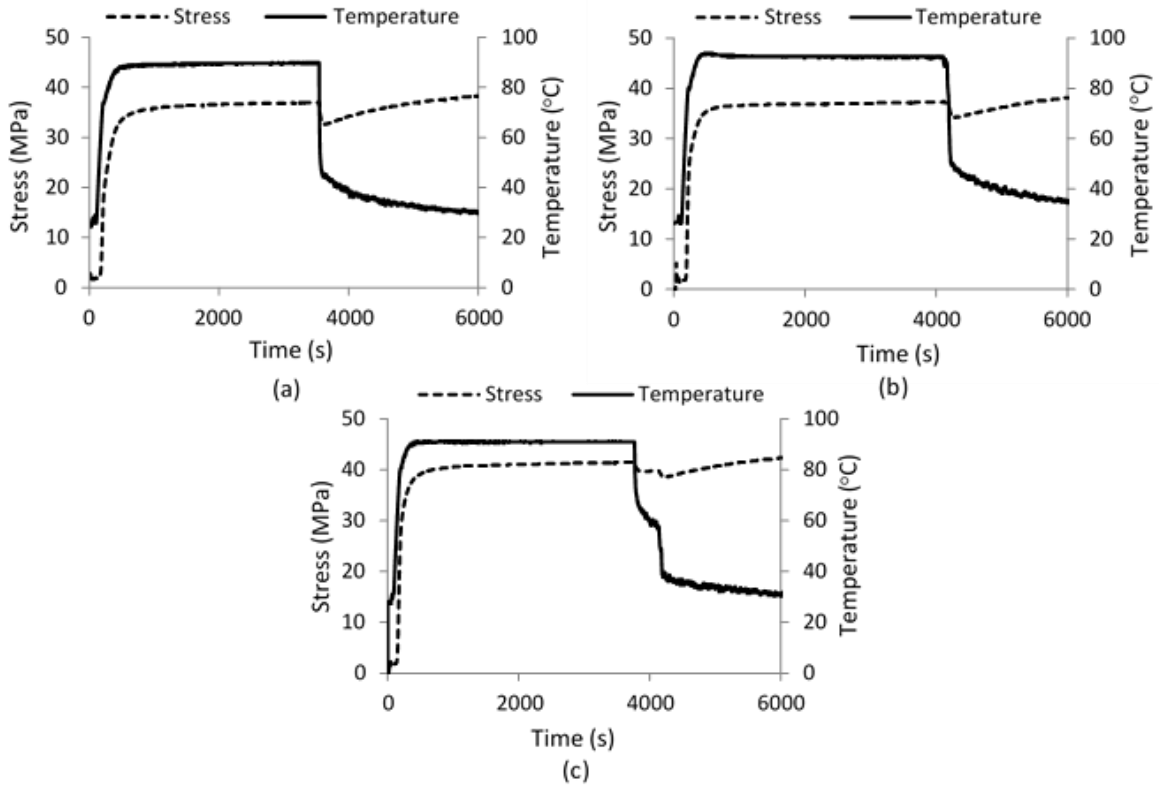

Figure A.2 (a)-(c): PET solid filament shrinkage at 90°C experiment repetitions.

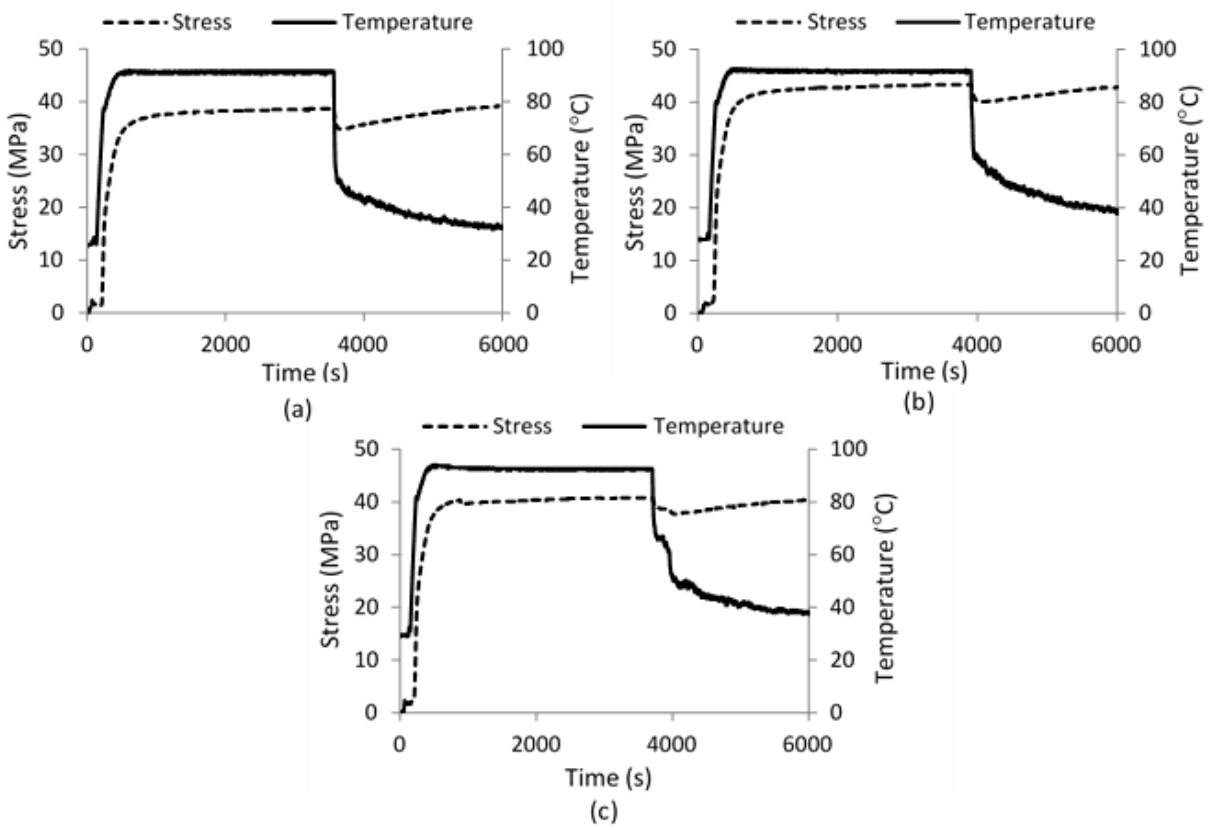

Figure A.3: (a)-(c): PET filament tube shrinkage at 90°C experiment repetitions.

Appendix B Aggregate gradation (sieve analysis) results

Table B.1: Results from 10 separate gradation tests of 4-10mm limestone coarse aggregate (testing carried out and data supplied by material supplier).

20mm % pass	16mm % pass	14mm % pass	12.5mm % pass	10mm % pass	8mm % pass	6.3mm % pass	4mm % pass	2.8mm % pass	2mm % pass	63µm % pass
100	100	100	100	98	64	15	3	3	3	3
100	100	100	100	90	43	10	3	3	3	2
100	100	100	100	93	48	8	3	3	3	2
100	100	100	100	96	85	4	3	3	3	2
100	100	100	100	85	41	14	6	6	5	4
100	100	100	100	86	35	8	3	3	2	2
100	100	100	100	89	39	6	2	2	2	2
100	100	100	100	89	41	7	3	2	2	2
100	100	100	100	91	37	4	1	1	1	1
100	100	100	100	95	50	13	4	3	3	2

Table B.2: Results from 10 separate gradation tests of 0-4mm sand (testing carried out and data supplied by material supplier).

8mm % pass	6.3mm % pass	4mm % pass	2mm % pass	1mm % pass	500µm % pass	250µm % pass	63µm % pass
100	100	98	96	71	50	2	1
100	100	99	96	88	65	1	0
100	100	99	99	76	60	9	1
100	100	99	95	85	60	20	0
100	100	97	92	87	57	7	1
100	100	97	93	71	65	34	3
100	100	96	89	83	48	5	2
100	100	95	90	82	39	4	2
100	100	96	93	91	63	7	2
100	100	95	92	89	56	6	1

Table B.3: Results from 10 separate gradation tests of 0-4mm limestone aggregate, from which 0-2mm limestone dust was sieved for use within the concrete mix (testing carried out and data supplied by material supplier).

8mm % pass	6.3mm % pass	5mm % pass	4mm % pass	2.8mm % pass	2mm % pass	1mm % pass	500µm % pass	250µm % pass	125µm % pass	63µm % pass
100	100	98	94	85	75	53	38	28	21	16
100	100	99	97	87	74	50	35	25	19	15
100	100	100	97	86	71	49	35	26	20	15
100	100	100	98	89	77	51	35	25	18	14
100	100	99	97	91	78	52	37	26	19	14
100	100	99	97	88	72	52	34	25	18	14
100	100	99	97	88	74	49	34	24	19	15
100	100	99	97	92	79	57	39	26	21	15
100	100	99	97	89	72	48	35	24	18	14
100	100	99	96	88	72	55	34	25	18	15

Appendix C Autogenous healing load-CMOD results for all beams

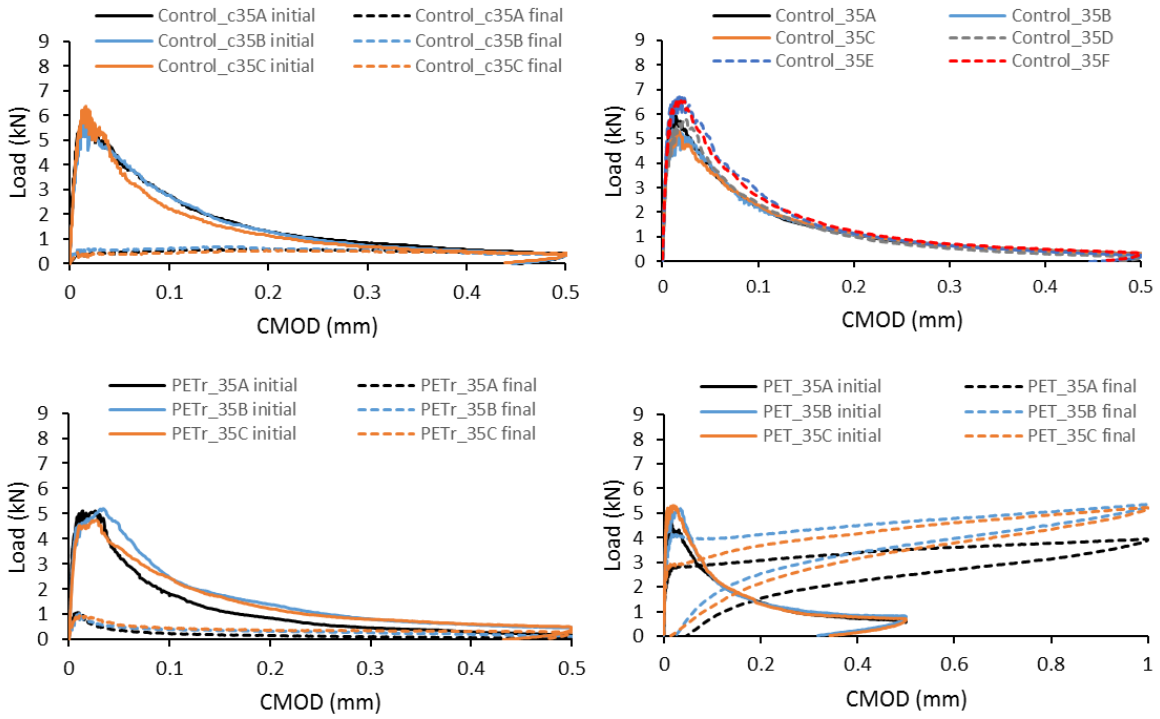

Figure C.1: Load-CMOD graphs for 1-month autogenous healing (a) Control_c35 samples; (b) Control_35 samples (where A-C are 7-day and D-F are 35 day tests); (c) PETr_35 samples and (d) PET_35 samples.

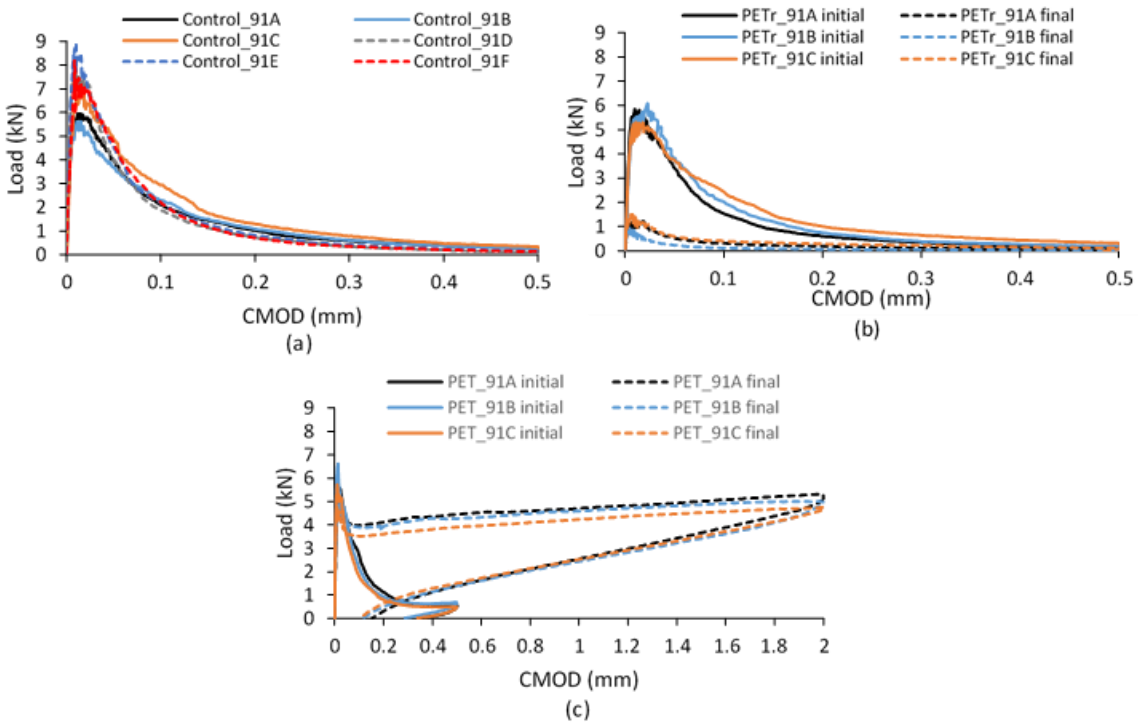

Figure C.2: Load-CMOD graphs for 3-month autogenous healing (a) Control_91 samples (where A-C are 7-day and D-F are 91 day tests); (b) PETr_91 samples and (c) PET_91 samples.

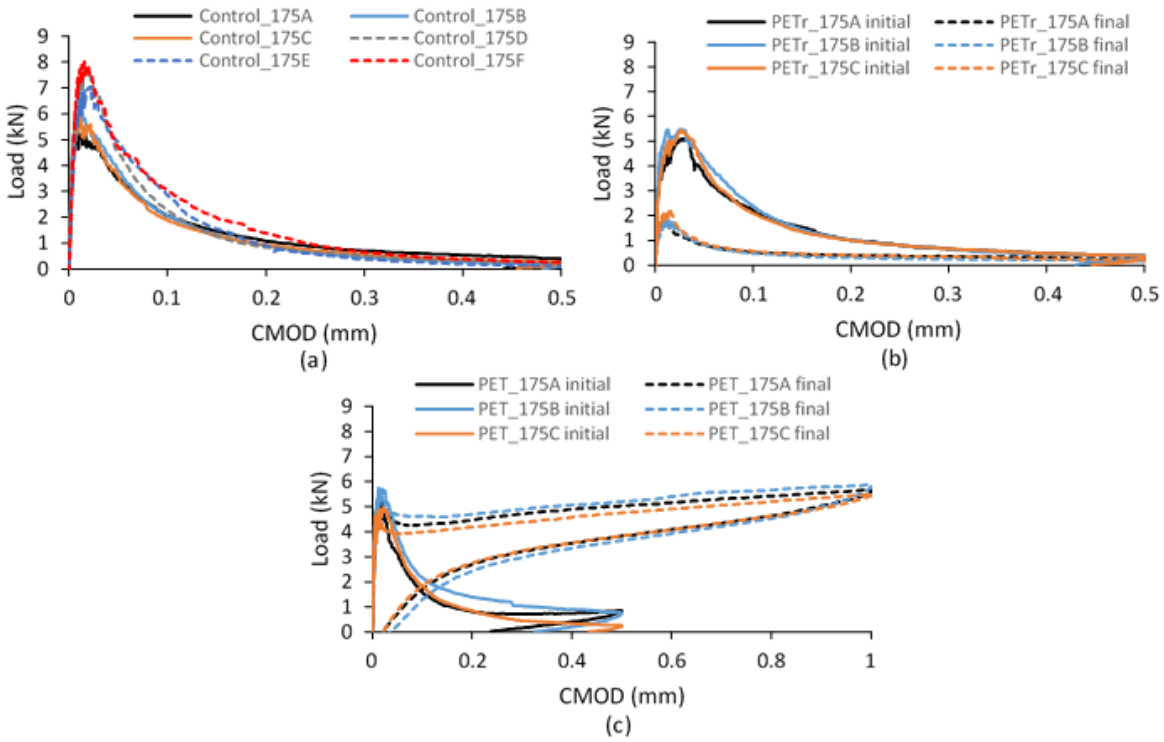

Figure C.3: Load-CMOD graphs for 6-month autogenous healing (a) Control_175 samples (where A-C are 7-day and D-F are 175 day tests); (b) PETr_175 samples and (c) PET_175 samples.

Appendix D Site trial structural design drawings

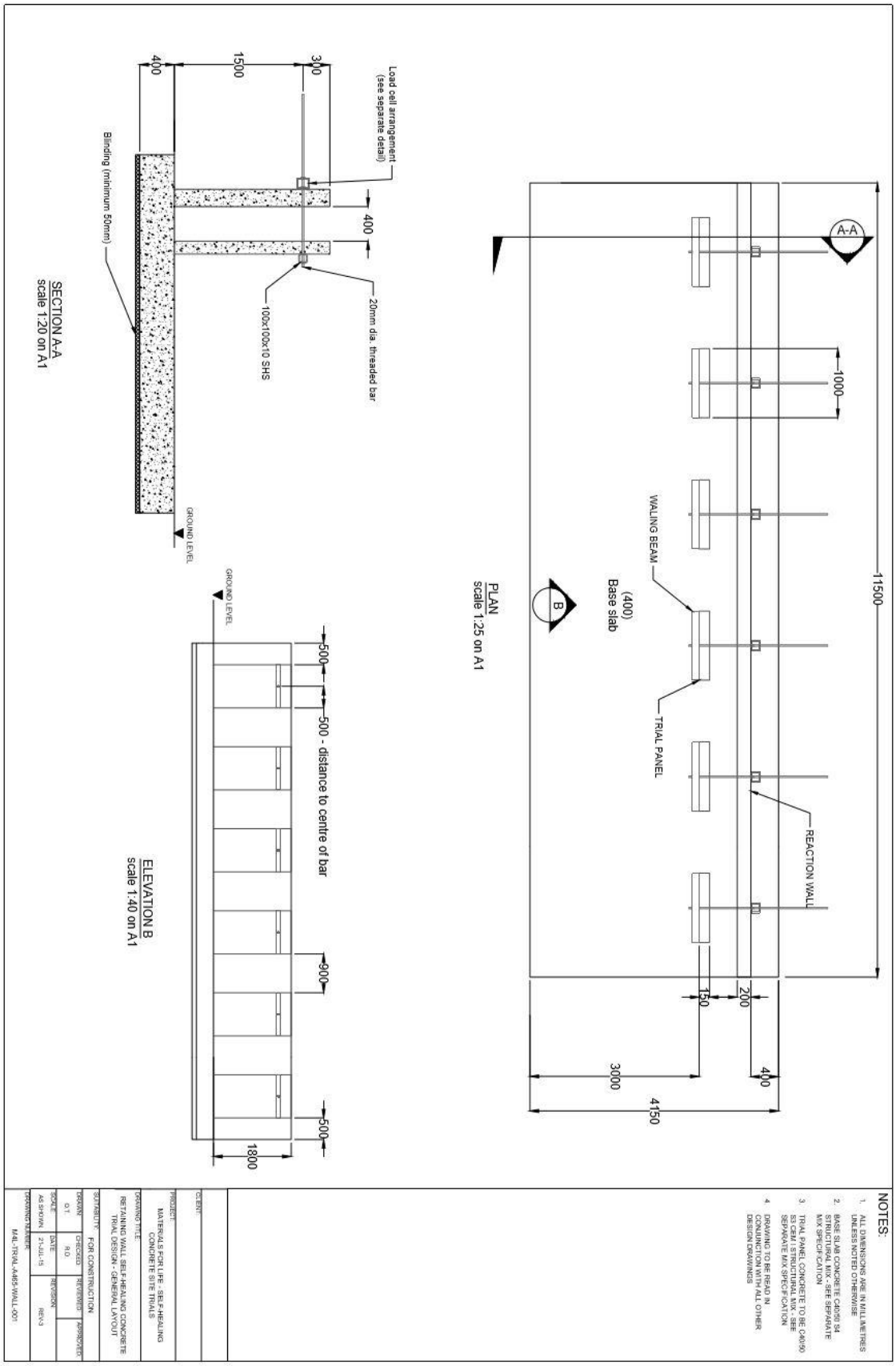

Figure D.1:General arrangement drawing for site trial structure.

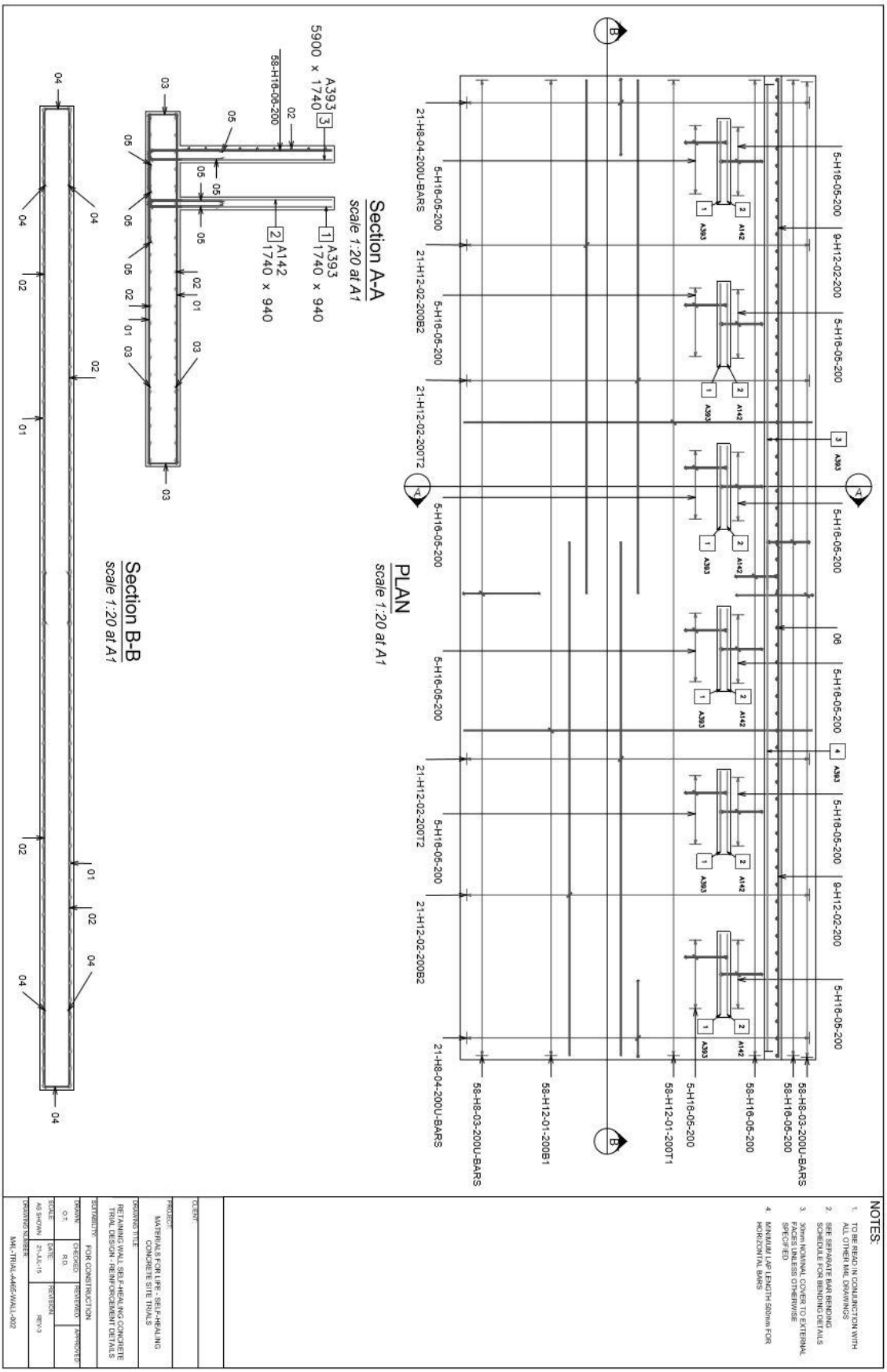

Figure D.2: Reinforcement drawing for site trial structure.

Appendix E Supporting information for Life Cycle Cost assessment model

Table E.1: Deterioration profiles used within the LCC model, from Atkins (2015c).

Deterioration profile	Exposure class	1A	2B	2C	2D	2E	3B	3C	3D	3E	4B	4C	4D	4E	5B	5C	5D	5E	Mean time to failure (without routine maintenance)
In-situ concrete	Severe	0.000	0.375	0.500	0.542	0.583	0.625	0.750	0.792	0.833	0.875	0.938	0.958	0.979	1.000	1.025	1.050	1.075	30
In-situ concrete	Moderate	0.000	0.438	0.594	0.646	0.698	0.750	0.844	0.875	0.906	0.938	0.969	0.979	0.990	1.000	1.025	1.050	1.075	60
In-situ concrete	Mild	0.000	0.250	0.375	0.417	0.458	0.500	0.625	0.667	0.708	0.750	0.875	0.917	0.958	1.000	1.025	1.050	1.075	180
Fabricated steel	Severe	0.000	0.375	0.563	0.625	0.688	0.750	0.844	0.875	0.906	0.938	0.969	0.979	0.990	1.000	1.025	1.050	1.075	30
Fabricated steel	Moderate	0.000	0.375	0.563	0.625	0.688	0.750	0.844	0.875	0.906	0.938	0.969	0.979	0.990	1.000	1.025	1.050	1.075	60
Fabricated steel	Mile	0.000	0.417	0.583	0.639	0.694	0.750	0.833	0.861	0.889	0.917	0.958	0.972	0.986	1.000	1.025	1.050	1.075	90
Internal drainage	Severe	0.000	0.267	0.383	0.422	0.461	0.500	0.633	0.678	0.722	0.767	0.883	0.922	0.961	1.000	1.025	1.050	1.075	22.5
Internal drainage	Moderate	0.000	0.250	0.375	0.417	0.458	0.500	0.625	0.667	0.708	0.750	0.875	0.917	0.958	1.000	1.025	1.050	1.075	45
Internal drainage	Mild	0.000	0.250	0.375	0.417	0.458	0.500	0.625	0.667	0.708	0.750	0.875	0.917	0.958	1.000	1.025	1.050	1.075	90
Aluminium	Mild	0.000	0.533	0.667	0.711	0.756	0.800	0.867	0.889	0.911	0.933	0.967	0.978	0.989	1.000	1.025	1.050	1.075	56.25
Handrail (other)	Severe	0.000	0.581	0.710	0.753	0.796	0.839	0.903	0.925	0.946	0.968	0.984	0.989	0.995	1.000	1.025	1.050	1.075	23.25
Handrail (other)	Moderate	0.000	0.500	0.650	0.700	0.750	0.800	0.870	0.893	0.917	0.940	0.970	0.980	0.990	1.000	1.025	1.050	1.075	37.5
Handrail (other)	Mild	0.000	0.500	0.662	0.716	0.770	0.824	0.885	0.905	0.926	0.946	0.973	0.982	0.991	1.000	1.025	1.050	1.075	55.5
Blockwork	Moderate	0.000	0.400	0.550	0.600	0.650	0.700	0.800	0.833	0.867	0.900	0.950	0.967	0.983	1.000	1.025	1.050	1.075	75
Blockwork	Mild	0.000	0.167	0.333	0.389	0.444	0.500	0.667	0.722	0.778	0.833	0.917	0.944	0.972	1.000	1.025	1.050	1.075	225
Spray systems	N/A	0.000	0.625	0.750	0.792	0.833	0.875	0.913	0.925	0.938	0.950	0.975	0.983	0.992	1.000	1.025	1.050	1.075	30

$$SC = \sum WC + TMC + PC + DC + OC$$

SC = Scheme cost

∑WC = Total works cost, i.e. the sum of all individual maintenance activities works cost for a structure calculated as described in the previous section.

TMC = Traffic Management Cost
PC = Preliminaries Cost
OC = Other Costs
DC = Design Cost

Table C.9.A: Preliminaries Cost	$PC = f_P \times \sum WC$
Works Cost	f_P (Factor for Preliminaries Cost)
< £50k	0.2
≥ £50k and < £250k	0.15
≥ £250k and < £1m	0.125
≥ £1m	0.1

Table C.9.B: Other Costs	$OC = f_O \times \sum WC$
Works Cost	f_O (Factor for Other Costs)
< £50k	0.2
≥ £50k and < £250k	0.15
≥ £250k and < £1m	0.125
≥ £1m	0.1

Table C.9.C: Traffic Management Cost	TMC = WD x TMR
TM Arrangement Description	TM Rate (£/hour)
Shuttle Working / Lane Closure	£259
Contraflow	£519
Hardshoulder Closure	£138
Waterway Possession	£305
Railway Possession	£864
Retaining Wall TM	£417

WD = Works Duration, See Equation 6 in Part A: Methodology

Table C.9.D: Design Cost	$DC = f_D (\sum WC + TMC + PC + OC)$
Works Cost + TM + Prelims + Other Costs	f_D (Factor for Design Cost)
< £50k	0.4
≥ £50k and < £250k	0.2
≥ £250k and < £1m	0.15
≥ £1m	0.12

Table C.9.E: Bridge - Works Location and TM Arrangements						
CSS Elements List	Works Location	Permissible TM Arrangement				
		Shuttle Working / Lane Closure	Contraflow	Hardshoulder Closure	Waterway Possession	Railway Possession
Br01 - Primary deck element	Below Deck	✓			✓	✓
Br02 - Transverse Beams	Below Deck	✓			✓	✓
Br03 - Secondary deck element	Below Deck	✓			✓	✓
Br04 - Half Joints/Hinge Joints	Below Deck	✓			✓	✓
Br05 - Tie beam/rod	Below Deck	✓			✓	✓
Br06 - Parapet beam or cantilever	Below Deck	✓			✓	✓
Br07 - Deck bracing	Below Deck	✓			✓	✓
Br08 - Foundations	Exclude	✓			✓	✓
Br09 - Abutments (incl. arch springing)	Below Deck			✓	✓	✓
Br10 - Spandrel wall/head wall	Below Deck	✓			✓	✓
Br11 - Pier/column	Below Deck	✓			✓	✓
Br12 - Cross-head/capping beam	Below Deck	✓			✓	✓
Br13 - Bearings	Below Deck		✓		✓	✓
Br14 - Bearing plinth/shelf	Below Deck	✓			✓	✓
Br15 - Superstructure drainage	Above Deck	✓				
Br16 - Substructure drainage	Below Deck	✓			✓	✓
Br17 - Waterproofing	Above Deck		✓			
Br18 - Expansion joints	Above Deck	✓				
Br19 - Finishes: deck elements	Below Deck	✓			✓	✓
Br20 - Finishes: substructure elements	Below Deck	✓			✓	✓
Br21 - Finishes: parapets/safety fences	Above Deck			✓		
Br22 - Access/walkways/gantries	Below Deck	✓			✓	✓
Br23 - Handrail/parapets/safety fences	Above Deck			✓		
B24 - Carriageway surfacing	Exclude					
Br25 - Footway/verge/footbridge surfacing	Exclude					
Br26 - Invert/river bed	Below Deck				✓	
Br27 - Aprons	Below Deck			✓	✓	✓
Br28 - Fenders/cutwaters/collision protection	Below Deck	✓			✓	
Br29 - River training works	Below Deck				✓	
Br30 - Revetment/batter paving	Below Deck				✓	
Br31 - Wing walls	Below Deck			✓	✓	✓
Br32 - Retaining walls	Below Deck	✓			✓	✓
Br33 - Embankments	Below Deck					
Br34 - Machinery	Exclude					
Br35 - Approach rails/barriers/walls	Above Deck					
Br36 - Signs	Above Deck			✓		
Br37 - Lighting	Exclude					
Br38 - Services	Exclude					

Figure E.1: Equation and factors used to calculate repair costs within the LCC model, from Atkins (2015c).

References

AHN, T. & KISHI, T. 2010. Crack Self-healing Behavior of Cementitious Composites Incorporating Various Mineral Admixtures. *Journal of Advanced Concrete Technology,* 8**,** 171-186.

AJJI, A., COLE, K. C., DUMOULIN, M. M. & WARD, I. M. 1997. Orientation of amorphous poly(ethylene terephthalate) by tensile drawing, roll-drawing, and die-drawing. *Polymer Engineering & Science,* 37**,** 1801-1808.

ALVES, N. M., MANO, J. F., BALAGUER, E., MESEGUER DUEÑAS, J. M. & GOMEZ RIBELLES, J. L. 2002. Glass transition and structural relaxation in semi-crystalline poly(ethylene terephthalate): a DSC study. *Polymer,* 43**,** 4111-4122.

ARYA, C. & VASSIE, P. R. 2004. Whole life cost analysis in concrete bridge tender evaluation. *Proceedings of the ICE - Bridge Engineering* [Online], 157. Available: http://www.icevirtuallibrary.com/content/article/10.1680/bren.2004.157.1.9.

ATKINS 2011. Whole Life Costing for Option Appraisal of Maintenance Schemes for Local Highway Authorities. www.ukroadsliaisongroup.org: UK Roads Liaison Group.

ATKINS 2015a. Structures Asset Management Planning Toolkit – Part A: Methodology. 2.01 ed.: UK Bridges Board.

ATKINS 2015b. Structures Asset Management Planning Toolkit – User Guide to Computerised Model

ATKINS 2015c. Structures Asset Management Planning Toolkit; Part C: Supporting Information. *In:* TRANSPORRT, D. F. (ed.).

AZHDARPOUR, A. M., NIKOUDEL, M. R. & TAHERI, M. 2016. The effect of using polyethylene terephthalate particles on physical and strength-related properties of concrete; a laboratory evaluation. *Construction and Building Materials,* 109**,** 55-62.

BEDI, R., CHANDRA, R. & SINGH, S. P. 2013. Mechanical Properties of Polymer Concrete. *Journal of Composites,* 2013**,** 12.

BEHL, M. & LENDLEIN, A. 2007. Shape-memory polymers. *Materials Today,* 10**,** 20-28.

BOGUE, R. 2014. Smart materials: a review of capabilities and applications. *Assembly Automation,* 34.

BONNER, M., MONTES DE OCA, H., BROWN, M. & WARD, I. M. 2010. A novel approach to predict the recovery time of shape memory polymers. *Polymer,* 51**,** 1432-1436.

BORG, R. P., BALDACCHINO, O. & FERRARA, L. 2016. Early age performance and mechanical characteristics of recycled PET fibre reinforced concrete. *Construction and Building Materials,* 108**,** 29-47.

BOUSSABAINE, A. & KIRKHAM, R. 2004. *Whole Life Cycle Costing: Risk and Responses*.

BSI 1992. BS 3843:1992 Guide to terotechnology (the economic management of assets).

BSI 2008a. BS EN 13411-5:2003+A1:2008 Terminations for steel wire ropes. Safety. U-bolt wire rope grips.

BSI 2008b. BS ISO 15686-5:2008; Buildings & constructed assets – Service life planning. *Part 5: Life cycle costing.*

BSI 2008c. Standardized Method of Life Cycle Costing for Construction Procurement. *A supplement to BS ISO 15686-5 Buildings & constructed assets – Service life planning – Part 5: Life cycle costing.*

BSI 2013. BS EN 206:2013. *Concrete - Specification, performance, production and conformity.* London: British Standards Institute.

BSI 2014. Eurocode 2: Design of Concrete Structures. *Part 1-1: General rules and rules for buildings.* British Standards Institute.

CABLEORGANISER.COM. 2014. *How To Use Heat Shrink Tubing* [Online]. http://www.cableorganizer.com/learning-center/how-to/how-to-use-heat-shrink-tubing.htm. [Accessed].

CARRAHER, C. E. J. 2005. *Seymour/Carraher's Polymer Chemistry*, Taylor & Francis e-Library.

CHEN, H. H. & SU, R. K. L. 2013. Tension softening curves of plain concrete. *Construction and Building Materials,* 44**,** 440-451.
CHEN, W., LOFGREN, E. A. & JABARIN, S. A. 1998. Microstructure of amorphous and crystalline poly(ethylene terephthalate). *Journal of Applied Polymer Science,* 70**,** 1965-1976.
CHOI, Y. W., MOON, D. J., KIM, Y. J. & LACHEMI, M. 2009. Characteristics of mortar and concrete containing fine aggregate manufactured from recycled waste polyethylene terephthalate bottles. *Construction and Building Materials,* 23**,** 2829-2835.
CHURCHER, D. 2008. *Whole-Life Costing Analysis*, BSRIA.
CIPFA 2010. Code of Practice on Transport Infrastructure Assets. *Guidance to Support Asset Management, Financial Management and Reporting.* London: THE CHARTERED INSTITUTE OF PUBLIC FINANCE AND ACCOUNTANCY.
CIPFA. 2016. *Code of Practice on Local Authority Transport Infrastructure Assets – supporting documents* [Online]. http://www.cipfa.org/policy-and-guidance/highways-network-asset-briefing/local-authority-transport-infrastructure-assets-supporting-documents: The Chartered Institute of Public Finance & Accountancy. [Accessed 25/08/16 2016].
COATES, P. D. & WARD, I. M. 1981. Die drawing: Solid phase drawing of polymers through a converging die. . *Polymer Engineering and Science,* 21**,** 612-618.
COMPANY, T. S. W. 2016. *Nickel Chrome wire* [Online]. http://www.wires.co.uk/acatalog/nc_bare.html. [Accessed 11/07/2016 2016].
CONSTRUCTION, C. 1985. How Microsilica Improves Concrete. [Accessed 31/03/2016].
CYTEC. 2015. *Solvay Successfully Completes the Acquisition of Cytec and Launches Integration Plans* [Online]. https://www.cytec.com/company/news/press-release/solvay-successfully-completes-acquisition-cytec-and-launches-integration: Cytec. [Accessed 18/08/2016 2016].
CYTEC. 2016. *Cytec Solvay Group* http://www.cytec.com [Online]. [Accessed April 2016].
DAVIES, R. 2014. *Micromechanical modelling of self-healing cementitious materials.* Doctor of Philosophy, Cardiff University.
DAVIES, R., JEFFERSON, A. D., LARK, R. J. & GARDNER, D. R. 2015. A novel 2D vascular network in cementitious materials. *fib Symposium 2015.* Copenhagen, Denmark.
DE ROOIJ, M. R., VAN TITTELBOOM, K., DE BELIE, N. & SCHLANGEN, E. 2013. Self-Healing Phenomena in Cement Based Materials. *State-of-the-Art Report of RILEM TC 221-SHC*.
DE WILDER, K., LAVA, P., DEBRUYNE, D., WANG, Y., DE ROECK, G. & VANDEWALLE, L. 2015. Experimental investigation on the shear capacity of prestressed concrete beams using digital image correlation. *Engineering Structures,* 82**,** 82-92.
DRY, C. 1994. Matrix cracking repair and filling using active and passive modes for smart timed release of chemicals from fibers into cement matrices. *Smart Materials and Structures,* 3**,** 118.
DRY, C. 2001. In-Service Repair of Highways Bridges and Pavements by Internal Time-Release Repair Chemicals. Washington D.C., USA: Transportation Research Board of the National Academies.
DRY, C. & MCMILLAN, W. 1996. Three-part methylmethacrylate adhesive system as an internal delivery system for smart responsive concrete. *Smart Materials and Structures,* 5**,** 297.
DUNN, S. C. 2010. *A Novel Self-Healing Shape Memory Polymer-Cementitious System.* PhD, Cardiff University.
DUNN, S. C., JEFFERSON, A. D., LARK, R. J. & ISAACS, B. 2011. Shrinkage behavior of poly(ethylene terephthalate) for a new cementitious-shrinkable polymer material system. *Journal of Applied Polymer Science,* 120**,** 2516-2526.
DUSUNCELI, N. & COLAK, O. U. 2008. Modelling effects of degree of crystallinity on mechanical behaviour of semicrystalline polymers. *International Journal of Plasticity,* 24**,** 1224-1242.
EDVARDSEN, C. 1999. Water Permeability and Autogenous Healing of Cracks in Concrete. *ACI Materials Journal,* 96-M56**,** 448-454.
EMCOCABLES. 2016. Wires and strands for Prestressed concrete.
FIB 2010. fib Model Code for Concrete Structures 2010. Berlin, Germany: Wilhelm Ernst & Sohn.

FIB 2012. Structural concrete textbook on behaviour, design and performance, 2nd edition Vol 5: Through-life care and management of concrete structures - assessment, protection, repair and strengthening. FIB.

FLANAGAN, R. & JEWELL, C. 2005. *Whole Life Appraisal for Construction*.

FOWLER, D. W. 1999. Polymers in concrete: a vision for the 21st century. *Cement and Concrete Composites,* 21**,** 449-452.

GHOSH, S. K. 2009. Self-Healing Materials: Fundamentals, Design Strategies, and Applications. *Self-Healing Materials.* Wiley-VCH Verlag GmbH & Co. KGaA.

GIANNAROS, P., KANELLOPOLOUS, A. & AL-TABBAA, A. 2016. Sealing of cracks in cement using microencapsulated sodium silicate. *Smart Materials and Structures,* Paper accepted, in press.

GORLIER, E., HAUDIN, J. M. & BILLON, M. 2001. Strain-induced crystallisation in bulk amorphous PET under uni-axial loading. *Polymer,* 42**,** 9541-9549.

GÖSCHEL, U. 1996. Thermally stimulated structural changes in highly oriented glassy poly(ethylene terephthalate). *Polymer,* 37**,** 4049-4059.

GOVERNMENT, H. 2013. Construction 2025. *In:* DEPARTMENT FOR BUSINESS, I. A. S. (ed.).

GRANGER, S., LOUKILI, A., PIJAUDIER-CABOT, G. & CHANVILLARD, G. 2007. Experimental characterization of the self-healing of cracks in an ultra high performance cementitious material: Mechanical tests and acoustic emission analysis. *Cement and Concrete Research,* 37**,** 519-527.

GREY, E. 2016. *Gotthard Base Tunnel: inside the world's longest railway tunnel* [Online]. http://www.railway-technology.com/features/featuregotthard-base-tunnel-inside-the-worlds-longest-railway-tunnel-4770271/: Railway Technology. [Accessed 07/09/2016 2016].

GROMICKO, N. & SHEPARD, K. 2016. *The History of Concrete* [Online]. https://www.nachi.org/history-of-concrete.htm#ixzz31V47Zuuj: InterNACHI. [Accessed 07/09/2016 2016].

HA 2007. *Inspection Manual for Highway Structures Volume 1: Reference Manual,* London, The Stationary Office (TSO).

HA 2014. Structures Management Information Systems (SMIS) database. *In:* AGENCY, H. (ed.).

HAGEN, R. 2009. Basics of PLA. *Bioplastics magazine.*

HAMRAT, M., BOULEKBACHE, B., CHEMROUK, M. & AMZIANE, S. 2016. Flexural cracking behavior of normal strength, high strength and high strength fiber concrete beams, using Digital Image Correlation technique. *Construction and Building Materials,* 106**,** 678-692.

HAZELWOOD, T., JEFFERSON, A. D., LARK, R. J. & GARDNER, D. R. 2014. Long-term stress relaxation behavior of predrawn poly (ethylene terephthalate). *Journal of Applied Polymer Science,* 131.

HAZELWOOD, T., JEFFERSON, A. D., LARK, R. J. & GARDNER, D. R. 2015. Numerical simulation of the long-term behaviour of a self-healing concrete beam vs standard reinforced concrete. *Engineering Structures,* 102**,** 176-188.

HEARN, N. 1998. Self-sealing, autogenous healing and continued hydration: What is the difference? *Materials and Structures,* 31**,** 563-567.

HEIDE, N. T. & SCHLANGEN, E. Self-healing of early age cracks in concrete. First international conference on self healing materials. Springer, Dordrecht, 2007.

HILLOULIN, B., TITTELBOOM, K. V., GRUYAERT, E., BELIE, N. D. & LOUKILI, A. 2014. Design of polymeric capsules for self-healing concrete. *Cement and Concrete Composites,* 55**,** 298-307.

HOFF, M. & PELZBAUER, Z. 1990. Relationship between thermal shrinkage and morphology of zone-drawn polyethylene. *Polymer,* 32**,** 3317-3321.

HOMMA, D., MIHASHI, H. & NISHIWAKI, T. 2009. Self-healing capability of fibre reinforced cementitious composites. *Journal of Advanced Concrete Technology,* 7**,** 217-228.

HORNER, R. M. W. 2005. Whole-life costing in construction. *In:* CIRIA (ed.) *Funders Report CP/106.* London.

HUANG, H. & YE, G. 2011. Application of sodium silicate solution as self-healing agent in cementitious materials. *International RILEM Conference on Advances in Construction Materials Through Science and Engineerin.* Hong Kong.

HUANG, W. M., DING, Z., WANG, C. C., WEI, J., ZHAO, Y. & PURNAWALI, H. 2010. Shape memory materials. *Materials Today,* 13**,** 54-61.

IMAGEJ. 2016. *ImageJ* [Online]. http://imagej.net/ImageJ. [Accessed 12/07/2016 2016].

IMBABI, M. S., CARRIGAN, C. & MCKENNA, S. 2012. Trends and developments in green cement and concrete technology. *International Journal of Sustainable Built Environment,* 1**,** 194-216.

ISAACS, B. 2011. *Self-Healing Cementitious Materials.* Doctor of Philosophy, Cardiff University.

ISAACS, B., LARK, R., JEFFERSON, T., DAVIES, R. & DUNN, S. 2013. Crack healing of cementitious materials using shrinkable polymer tendons. *Structural Concrete,* 14**,** 138-147.

ISAACS, B., LARK, R. J., JEFFERSON, A. D., DAVIES, R. & DUNN, S. C. 2012. Crack Healing of Cementitious Materials Using Shrinkable Polymer Tendons. *Structural Concrete*.

JEFFERSON, A., JOSEPH, C., LARK, R., ISAACS, B., DUNN, S. & WEAGER, B. 2010. A new system for crack closure of cementitious materials using shrinkable polymers. *Cement and Concrete Research,* 40**,** 795-801.

JOHNSON, N. 2015. *Self-healing concrete solves cracking problems in Dutch lifeguard station* [Online]. http://www.architectureanddesign.com.au/news/self-healing-concrete-solves-cracking-problems-in: Architecture and Design. [Accessed].

JOSEPH, C. 2008. *Experimental and Numerical Study of the Fracture and Self-Healing of Cementitious Materials.* PhD, Cardiff University.

JOSEPH, C., JEFFERSON, A. & CANTONI, M. Issues relating to the autonomic healing of cementitious materials. Proceedings of the 1st International Conference on Self-Healing Materials, Noordwijk, the Netherlands. CD-ROM, 2007.

JOSEPH, C., JEFFERSON, A. D., ISAACS, B., LARK, R. J. & GARDNER, D. R. 2010. Experimental investigation of adhesive-based self-healing of cementitious materials. *Magazine of Concrete Research,* 62**,** 831-843.

JSCE 1995. Standard Test Methods for Continuous Fiber Reinforcing Materials. *JCSE-E-538-1995 Test Method for Alkali Resistance of Continuous Fiber Reinforcing Materials.* Japan Society of Civil Engineers.

KAN, L.-L., SHI, H.-S., SAKULICH, A. R. & LI, V. C. 2010. Self-Healing Characterization of Engineered Cementitious Composite Materials. *ACI Materials Journal,* 107**,** 617-624.

KANELLOPOLOUS, A., GIANNAROS, P. & AL-TABBAA, A. 2016a. The effect of varying volume fraction of microcapsules on fresh, mechanical and self-healing properties of mortars. *Construction and Building Materials* under review.

KANELLOPOLOUS, A., LITINA, C., GIANNAROS, P. & AL-TABBAA, A. 2016b. Effect of Different Types of Polymeric Microcapsules on the Self-Healing Efficiency of Cement Based Composites. *9th International Conference on Fracture Mechanics of Concrete and Concrete Structures* University of California, Berkeley USA.

KANELLOPOULOS, A., QURESHI, T. S. & AL-TABBAA, A. 2015. Glass encapsulated minerals for self-healing in cement based composites. *Construction and Building Materials,* 98**,** 780-791.

KIM, J. J., PARK, C., LEE, S., LEE, S. W. & WON, J. 2008. Effects of the geometry of recycled PET fiber reinforcement on shrinkage cracking of cement-based composites. *Composites Part B: Engineering,* 39**,** 442-450.

KOERNER, H., PRICE, G., PEARCE, N., ALEXANDER, M. & VAIA, R. 2004. Remotely actuated polymer nanocomposites--stress-recovery of carbon-nanotube-filled thermoplastic elastomers. *Nature Materials,* 3**,** 115-120.

LAVISION. 2016. *Digital Image Correlation* [Online]. http://www.lavision.de/en/techniques/digital-image-correlation.php: LaVision. [Accessed 17-08-2016 2016].
LENDLEIN, A. & KELCH, S. 2002. Shape-Memory Effect.
LI, V. C. & HERBERT, E. 2012. Robust Self-Healing Concrete for Sustainable Infrastructure. *Journal of Advanced Concrete Technology,* 10**,** 207-218.
LI, V. C., LIM, Y. M. & CHAN, Y.-W. 1998. Feasibility study of a passive smart self-healing cementitious composite. *Composites Part B: Engineering,* 29**,** 819-827.
LI, W., JIANG, Z., YANG, Z., ZHAO, N. & YUAN, W. 2013a. Self-healing efficiency of cementitious materials containing microcapsules filled with healing adhesive: Mechanical restoration and healing process monitored by water absorption. *PLoS ONE,* 8.
LI, W., JIANG, Z., YANG, Z., ZHAO, N. & YUAN, W. 2013b. Self-Healing Efficiency of Cementitious Materials Containing Microcapsules Filled with Healing Adhesive: Mechanical Restoration and Healing Process Monitored by Water Absorption. *PLoS ONE,* 8**,** e81616.
LIBERATO, F., VISAR, K. & FABIO, M. 2016. On the use of crystalline admixtures in cement based construction materials: from porosity reducers to promoters of self healing. *Smart Materials and Structures,* 25**,** 084002.
LIFE-365. 2016. *Life-365 Software Overview* [Online]. http://www.life-365.org/overview.html: Life-365. [Accessed 25/08/16 2016].
LIU, C., QIN, H. & MATHER, P. T. 2007. Review of progress in shape-memory polymers. *Journal of Materials Chemistry,* 17**,** 1543-1558.
LIU, Y., DU, H., LIU, L. & LENG, J. 2014. Shape memory polymers and their composites in aerospace applications: a review. *Smart Materials and Structures,* 23**,** 023001.
LOOS, M. R. 2011. Is It Worth the Effort to Reinforce Polymers With Carbon Nanotubes? *Macromolecular theory and simulations,* 20**,** 350-362.
LOOS, M. R. 2016. *CNT composites: Cost and production* [Online]. https://sites.google.com/site/cntcomposites/cost-and-production. [Accessed 27/07/16 2016].
LU, H., LIANG, F., YAO, Y., GOU, J. & HUI, D. 2014. Self-assembled multi-layered carbon nanofiber nanopaper for significantly improving electrical actuation of shape memory polymer nanocomposite. *Composites Part B: Engineering,* 59**,** 191-195.
LU, X. F. & HAY, J. N. 2001. Crystallization orientation and relaxation in uniaxially drawn poly(ethylene terephthalate). *Polymer,* 42**,** 8055-8067.
LUO, M., QIAN, C. X. & LI, R. Y. 2015. Factors affecting crack repairing capacity of bacteria-based self-healing concrete. *Construction and Building Materials,* 87**,** 1-7.
MAHAL, M., BLANKSVÄRD, T., TÄLJSTEN, B. & SAS, G. 2015. Using digital image correlation to evaluate fatigue behavior of strengthened reinforced concrete beams. *Engineering Structures,* 105**,** 277-288.
MATHER, P. T., LUO, X. & ROUSSEAU, I. A. 2009. Shape Memory Polymer Research. *Annual Review of Materials Research,* 39**,** 445-471.
MATTHEWS, R., AJJI, A., COLE, K. C. & DUMOULIN, M. M. Roll and Tensile Drawing of PET: Effect of Process Conditions on Structure and Properties. Industrial Materials Institute, Canada, 1998 Atlanta, Georgia. Society of Plastics Engineers.
MCCORMICK, N. & LORD, J. 2010. Digital Image Correlation. *Materials Today,* 13**,** 52-54.
MENG, Q. & HU, J. 2009. A review of shape memory polymer composites and blends. *Composites Part A: Applied Science and Manufacturing,* 40**,** 1661-1672.
MIAUDET, P., DERRE, A., MAUGEY, M., ZAKRI, C., PICCIONE, P. M., INOUBLI, R. & POULIN, P. 2007. Shape and temperature memory of nanocomposites with broadened glass transition. *Science,* 318**,** 1294-6.
MIHASHI, H. & NISHIWAKI, T. 2012. Development of Engineered Self-Healing and Self-Repairing Concrete-State-of-the-Art Report. *Journal of Advanced Concrete Technology,* 10**,** 170-184.

MITCHELL CROW, J. 2008. The concrete conundrum. *Chemistry World.* www.chemistryworld.org: Chemistry World.
MODY, R., LOFGREN, E. A. & JABARIN, S. A. 2001. Shrinkage Behavior of Orientedpoly(Ethylene Terephthalate). *Journal of Plastic Film and Sheeting,* 17**,** 152-163.
NEVILLE, A. M. 2002. Autogenous Healing: A Concrete Miracle? *Concrete International,* 24.
NEVILLE, A. M. 2012. *Properties of Concrete*, Pearson Education.
NEVILLE, A. M. & BROOKS, J. J. 2010. *Concrete Technology*, Prentice Hall.
NIGRO, E., CEFARELLI, G., BILOTTA, A., MANFREDI, G. & COSENZA, E. 2014. Guidelines for flexural resistance of FRP reinforced concrete slabs and beams in fire. *Composites Part B: Engineering,* 58**,** 103-112.
ONS 2015. Output in the Construction Industry. *In:* STATISTICS, O. F. N. (ed.).
PACHECO-TORGAL, F., DING, Y. & JALALI, S. 2012. Properties and durability of concrete containing polymeric wastes (tyre rubber and polyethylene terephthalate bottles): An overview. *Construction and Building Materials,* 30**,** 714-724.
PALIN, D., WIKTOR, V. & JONKERS, H. M. 2015. Autogenous healing of marine exposed concrete: Characterization and quantification through visual crack closure. *Cement and Concrete Research,* 73**,** 17-24.
PELISSER, F., MONTEDO, O. R. K., GLEIZE, P. J. P. & ROMAN, H. R. 2012. Mechanical properties of recycled PET fibers in concrete. *Materials Research,* 15**,** 679-686.
PEREIRA, J. R. C. & PORTER, R. S. 1984. Extrusion drawn amorphous and semicrystalline poly(ethylene terephthalate): 3. Linear thermal expansion analysis. *Polymer,* 25**,** 869-876.
PETRA 2014. An Introduction to PET. *In:* ASSOCIATION, P. R. (ed.). http://www.petresin.org/.
PJSC, E. 2016. *Building a global icon* [Online]. http://www.burjkhalifa.ae/en/the-tower/construction.aspx. [Accessed 07/09/2016 2016].
PTI. 2011. *History: PET Industry* [Online]. Plastic Technologies Inc. Available: http://www.plastictechnologies.com/company/history/pet_industry [Accessed 03-03-14 2014].
QUOTES, H. 2016. *A guide to concrete prices* [Online]. http://householdquotes.co.uk/a-guide-to-concrete-prices/: Householdquotes.co.uk. [Accessed 07/09/2016 2016].
RASTOGI, R., VELLINGA, W. P., RASTOGI, S., SCHICK, C. & MEIJER, H. E. H. 2004. The three-phase structure and mechanical properties of poly(ethylene terephthalate). *Journal of Polymer Science Part B: Polymer Physics,* 42**,** 2092-2106.
REBEIZ, K. S. 1995. Time-temperature properties of polymer concrete using recycled PET. *Cement and Concrete Composites,* 17**,** 119-124.
REINHARDT, H.-W. & JOOSS, M. 2003. Permeability and self-healing of cracked concrete as a function of temperature and crack width. *Cement and Concrete Research,* 33**,** 981-985.
RIETSCH, F., DUCKETT, R. A. & WARD, I. M. 1979. Tensile drawing behaviour of poly(ethylene terephthalate). *Polymer,* 20**,** 1133-1142.
RYALL, M. J. 2010. CHAPTER 9 - Whole-Life Costing, Maintenance Strategies and Asset Management. *In:* RYALL, M. J. (ed.) *Bridge Management (Second Edition).* Oxford: Butterworth-Heinemann.
SAHMARAN, M., YILDIRIM, G. & ERDEM, T. K. 2013. Self-healing capability of cementitious composites incorporating different supplementary cementitious materials. *Cement and Concrete Composites,* 35**,** 89-101.
SALEM, O., ABOURIZK, S. & ARIARATNAM, S. 2003. Risk-based Life-cycle Costing of Infrastructure Rehabilitation and Construction Alternatives. *Journal of Infrastructure Systems.*
SARIBIYIK, M., PISKIN, A. & SARIBIYIK, A. 2013. The effects of waste glass powder usage on polymer concrete properties. *Construction and Building Materials,* 47**,** 840-844.
SCHWARTZ, S. A. & SARAF, A. W. 2003. PET modification with MPDiol glycol. *Chemical Fibres International,* 53**,** 445-449.
SCIENCES, P. 2011. Hot Melt Extrusion. *Technical Brief 2011.* http://www.particlesciences.com/docs/technical_briefs/TB_2011_3.pdf.

SELVARAJOO, T. 2015. *Experimental investigation into a novel form of self-healing cementitious material.* Master of Engineering: Third-year research project., Cardiff University.

SHAEFFER, R. E. 1992. *Reinforced Concrete: Preliminary Design for Architects and Builders* Mcgraw-Hill College.

SHARMA, T., ALAZHARI, M., COOPER, R., HEATH, A. & PAINE, K. 2015. The Requirements for Autonomic Microbiologically-Induced Calcite-Precipitation in Concrete. *Fifth International Conference on Self-Healing Materials.* Duke University, South Carolina, USA.

SILVA, D. A., BETIOLI, A. M., GLEIZE, P. J. P., ROMAN, H. R., GÓMEZ, L. A. & RIBEIRO, J. L. D. 2005. Degradation of recycled PET fibers in Portland cement-based materials. *Cement and Concrete Research,* 35**,** 1741-1746.

SOCIETY, C. 2010. Non-structural cracks in concrete. *Technical Report No. 22.* 4 ed. Surrey, UK: The Concrete Society.

SOURI, M., LU, Y. C., EROL, A., PULLA, S. S. & KARACA, H. E. 2015. Characterization of unconstraint and constraint shape recoveries of an epoxy based shape memory polymer. *Polymer Testing,* 41**,** 231-238.

SUN, L., HUANG, W. M., WANG, C. C., ZHAO, Y., DING, Z. & PURNAWALI, H. 2011. Optimization of the shape memory effect in shape memory polymers. *Journal of Polymer Science Part A: Polymer Chemistry,* 49**,** 3574-3581.

SWEENEY, J., BONNER, M. & WARD, I. M. 2014. Modelling of loading, stress relaxation and stress recovery in a shape memory polymer. *Journal of the Mechanical Behavior of Biomedical Materials,* 37**,** 12-23.

SWR. 2016. *1x19 (12/6/1) - Steel Wire Rope Specification* [Online]. http://www.steelwirerope.com/WireRopes/Constructions/GeneralEngineering/1x19-wire-strand-core-wire-rope.html#.V87QxZgrKCo. [Accessed 06/09/2016 2016].

THAO, T. D. P., JOHNSON, T. J. S., TONG, Q. S. & DAI, P. S. 2009. Implementation of self-healing in concrete – Proof of concept. *The IES Journal Part A: Civil & Structural Engineering,* 2**,** 116-125.

TODAY, C. 2012. *Cytec completes Umeco acquisition* [Online]. http://www.compositestoday.com/2012/07/cytec-completes-umeco-acquisition/: Composites today. [Accessed 18/08/2016 2016].

TORRES, N., ROBIN, J. J. & BOUTEVIN, B. 2000. Study of thermal and mechanical properties of virgin and recycled poly(ethylene terephthalate) before and after injection molding. *European Polymer Journal,* 36**,** 2075-2080.

TREASURE, L. 2016. *Wire rope clip* [Online]. http://b2bbazar.com/supplier/Wire-Rope-Clip-8079-307.html. [Accessed 24/06/2016 2016].

TREASURY, H. 2011. THE GREEN BOOK: Appraisal and Evaluation in Central Government. London.

UGWU, O. O., KUMARASWAMY, M. M., KUNG, F. & NG, S. T. 2005. Object-oriented framework for durability assessment and life cycle costing of highway bridges. *Automation in Construction,* 14**,** 611-632.

UMECO. 2012. *The one name in composites* [Online]. http://html.investis.com/u/umeco/: Umeco. [Accessed 18/08/2016 2016].

VAN BREUGEL, K. Is there a market for self-healing cement-based materials. Proceedings of the first international conference on self-healing materials, 2007.

VAN DEN HEEDE, P., MAES, M. & DE BELIE, N. 2014. Influence of active crack width control on the chloride penetration resistance and global warming potential of slabs made with fly ash + silica fume concrete. *Construction and Building Materials,* 67, Part A**,** 74-80.

VAN DER ZWAAG, S. (ed.) 2007. *Self-Healing Materials: An Alternative Approach to 20 Centuries of Materials Science*.

VAN TITTELBOOM, K., ADESANYA, K., DUBRUEL, P., VAN PUYVELDE, P. & DE BELIE, N. 2011. Methyl methacrylate as a healing agent for self-healing cementitious materials. *Smart Materials and Structures,* 20**,** 125016.

VAN TITTELBOOM, K. & DE BELIE, N. Self-healing concrete by the internal release of adhesive from hollow glass fibres embedded in the matrix. 2nd International conference on Self-Healing Materials (ICSHM 2009), 2009.

VAN TITTELBOOM, K. & DE BELIE, N. 2013. Self-healing in cementitious materials-a review. *Materials,* 6**,** 2182-2217.

VAN TITTELBOOM, K., GRUYAERT, E., RAHIER, H. & DE BELIE, N. 2012. Influence of mix composition on the extent of autogenous crack healing by continued hydration or calcium carbonate formation. *Construction and Building Materials,* 37**,** 349-359.

VIGNY, M., TASSIN, J. F. & LORENTZ, G. 1999. Study of the molecular structure of PET films obtained by an inverse stretching process. Part 2: crystalline reorganization during longitudinal drawing. *Polymer,* 40**,** 397-406.

VOLK, B. L., LAGOUDAS, D. C. & MAITLAND, D. J. 2011. Characterizing and modeling the free recovery and constrained recovery behavior of a polyurethane shape memory polymer. *Smart Mater Struct,* 20**,** 940041-9400418.

WANG, J. Y., SOENS, H., VERSTRAETE, W. & DE BELIE, N. 2014. Self-healing concrete by use of microencapsulated bacterial spores. *Cement and Concrete Research,* 56**,** 139-152.

WANG, N. 2011. Multi-criteria decision-making model for whole life costing design. *Structure and Infrastructure Engineering,* 7**,** 441-452.

WARD, I. M. & SWEENEY, J. 2013. *Mechanical properties of solid polymers,* Chichester, UK, Wiley.

WEATHERANALYTICS, M. O. 2016. Data delivery: daily min and max air temperature, daily rainfall and daily min and max relative humidity for the TREDEGAR (BRYN BACH PARK NO 2) and USK NO.2 sites for 1st June 2015 to 31st May 2016. *In:* OFFICE, M. (ed.).

WIKTOR, V. & JONKERS, H. M. 2011. Quantification of crack-healing in novel bacteria-based self-healing concrete. *Cement and Concrete Composites,* 33**,** 763-770.

WIKTOR, V. & JONKERS, H. M. 2015. Field performance of bacteria-based repair system: Pilot study in a parking garage. *Case Studies in Construction Materials,* 2**,** 11-17.

XIE, T. 2011. Recent advances in polymer shape memory. *Polymer,* 52**,** 4985-5000.

XU, J. & SONG, J. 2011. Thermal Responsive Shape Memory Polymers for Biomedical Applications. *Biomedical Engineering - Frontiers and Challenges*.

YACHUAN, K. & JINPING, O. 2008. Self-repairing performance of concrete beams strengthened using superelastic SMA wires in combination with adhesives released from hollow fibers. *Smart Materials and Structures,* 17**,** 025020.

YAKACKI, C. M., SATARKAR, N. S., GALL, K., LIKOS, R. & HILT, J. Z. 2009. Shape-memory polymer networks with Fe3O4 nanoparticles for remote activation. *Journal of Applied Polymer Science,* 112**,** 3166-3176.

YANG, Y., LEPECH, M. D., YANG, E.-H. & LI, V. C. 2009. Autogenous healing of engineered cementitious composites under wet–dry cycles. *Cement and Concrete Research,* 39**,** 382-390.

YANG, Y., YANG, E.-H. & LI, V. C. 2011. Autogenous healing of engineered cementitious composites at early age. *Cement and Concrete Research,* 41**,** 176-183.

YU, Y. J., HEARON, K., WILSON, T. S. & MAITLAND, D. J. 2011. The effect of moisture absorption on the physical properties of polyurethane shape memory polymer foams. *Smart Mater Struct,* 20.

ZHAO, Q., QI, H. J. & XIE, T. 2015. Recent progress in shape memory polymer: New behavior, enabling materials, and mechanistic understanding. *Progress in Polymer Science,* 49–50**,** 79-120.